# Kent Academic Repository

# Developing high-speed scatterometry tools to detect early events during Nucleotide Excision Repair

**Robert James Charman**

**Submitted to the University of Kent for the Degree of Doctor of Philosophy in**

**Biochemistry**

**School of Biosciences, January 2022**

# Table of Contents

## *2  Novel implementations of Dark-Field and Interference-*

## *Reflection Microscopy* _____ *58*

# Table of Figures

# Abstract

Exposure of DNA to ultraviolet (UV) radiation results in the formation of numerous lesions which threaten genome integrity. The nucleotide excision DNA repair pathway detects and repairs a range of such UV-induced DNA lesions. In bacteria, initial damage detection and verification is carried out by two proteins: UvrA and UvrB. Despite decades of study, the process of how these proteins locate damage remains unclear. Here we first demonstrate implementations of novel versions of both conventional dark-field microscopy, and interference reflection microscopy (IRM) for the imaging of gold nanoparticle (AuNP) labelled proteins. We then develop these into an implementation of interferometric scattering (iSCAT) microscopy to allow for high-speed imaging of protein-DNA interactions, including a method that can be used to achieve accurate active stabilisation of an iSCAT microscope in 3-axes using a software-based 3D localisation routine to extract the X, Y, and Z positions of a particle. Combining iSCAT microscopy with a novel, highly customisable, surface-bound-DNA assay, we investigate early damage detection by UvrA. Through this method we have discovered that UvrA interacts with DNA in two phases; a slow phase (~1.3/s) that correlates with an ATP-consuming state previously identified, and a second, much faster search mode. These faster interactions persist for ~130 ms and using ATP analogues we determine this phase does not require ATP consumption. Additionally, by modelling the rate at which UvrA is able to search the *E. coli* genome, we demonstrate that these rapid interactions allow for basal levels of UvrA to explore 99% of the *E. coli* genome within a single division cycle. Altogether, this work uncovers the presence of a rapid, energy-efficient search mechanism, which allows UvrA alone to search the entirety of the *E. coli* genome within a single division cycle and highlights the exciting potential for use of iSCAT microscopy for the study of protein-DNA interactions

# 1 Introduction

## 1.1 DNA Damage and Repair

DNA is often known as the molecule of life, containing all the genetic information required for the growth, development, and maintenance of all living organisms. As such, preserving genomic integrity is key for the continued survival of any organism. DNA within living cells is constantly threatened by a myriad of endogenous and exogenous damaging agents which are able to induce abnormal chemical modifications within DNA, preventing crucial cellular processes, such as transcription and replication, from performing correctly (Köhler *et al.*, 2016).

These damaging agents are ever present within the cell, and can arise from endogenous metabolic and hydrolytic processes, such as the formation of reactive chemical species, including reactive oxygen or reactive nitrogen species (Bont and Larebeke, 2004). It has been shown that alone these endogenous oxidative agents are responsible for ~10000 sites of DNA damage within each human cell per day (Ames, Shigenaga and Hagen, 1993). Exogenous sources of DNA damage can take many forms, such as Ultraviolet and ionizing radiation, or genotoxic chemical agents (Hakem, 2008).

If the sites of damage induced by both these endogenous and exogenous agents are not repaired, they can lead to uncontrolled cellular division, apoptosis, or senescence. These abnormal cellular processes can then lead to rapid ageing, reduced life span, and will predispose an organism to diseases such as cancer, or neurological disorders (Rao, 2007; Madabhushi, Pan and Tsai, 2014; Alhmoud *et al.*, 2020).

To combat this continual threat, organisms have developed a number of biochemical and molecular pathways which are focused on the detection, removal, and repair of these sites of DNA damage, known as the DNA damage response (DDR) (Chatterjee and Walker, 2017). These pathways are tasked with maintaining the genomic integrity of living cells and are present across both Prokaryotes and Eukaryotes. There are a number of known DNA repair pathways, such as nucleotide excision repair (NER), base excision repair (BER), mismatch repair, homologous recombination (HR), and non-homologous end joining (NHEJ). Each of these pathways targets different forms of DNA damage in a substrate-dependent manner, with other mechanisms such as direct repair and interstrand-crosslink repair (ICL) targeting specific lesions within the cell (Chatterjee and Walker, 2017). Disruption or deficiency in these pathways decreases genomic stability, and increases the propensity of cells to undergo unregulated replication and become cancerous (Bouwman and Jonkers, 2012; Wolters *et al.*, 2013). As such, improving our understanding of how these pathways function to effectively maintain genomic stability, and crucially how they can be disrupted, is hugely important in furthering our understanding of the progression of conditions such as cancer and early-onset ageing.

A common feature of a number of these pathways is the requirement for the location and verification of single sites of DNA damage in an environment potentially containing billions of undamaged nucleotides. The identification of these sites of DNA damage is the rate-limiting step within these pathways, yet our understanding of the exact molecular mechanisms through which these sites of damage can be effectively detected and verified is still lacking.

## 1.2 How do sequence-specific proteins locate their target sites?

The search for damaging lesions by DNA repair systems presents a considerable challenge, due to the vast quantity of non-target DNA which has to be searched concurrently by a relatively small number of proteins, this also applies more broadly to all proteins that bind specific nucleotide sequences. Yet proteins can rapidly locate DNA lesions/target sites, more rapidly than can be accounted for by random diffusion and collision with DNA (Riggs, Bourgeois and Cohn, 1970; von Hippel and Berg, 1989a). For example, the 3D diffusion constant of a protein with diameter *d* can be estimated using the Stokes-Einstein equation, as given by:

Equation. 1
$$D = \frac{k_B T}{3\pi\eta d}$$

Where $k_B$ is the Boltzmann constant, *T* is temperature, and η is the viscosity of the buffer. From this we can estimate the diffusion-limited rate for bimolecular interactions using the Smoluchowski equation, which in the case of protein-DNA interactions takes the form (Mirny *et al.*, 2009):

Equation. 2
$$k_{Smol} = 4\pi D b a$$

Where *D* is the diffusion constant estimated above, *b* is the cross-section of the binding reaction, and *a* is the proportion of the protein that contains a binding interface. Using this it was calculated that the lac repressor should have an association rate of ~$10^8$ M$^{-1}$ s$^{-1}$, however it was found that experimentally the lac repressor actually displayed and association rate of ~$10^{10}$ M$^{-1}$ s$^{-1}$ by Riggs et al. in 1970 (Riggs, Bourgeois and Cohn, 1970), a rate which is orders of magnitude larger than what would be theoretically possible due to random associations resulting from 3D diffusion and collisions. This is further evidenced when considering the number of searches a protein must undertake of a

genome whilst undertaking a search based on only 3D diffusion. For example, when searching for a specific site, it is expected that a protein will make $N$ incorrect interactions with the DNA, where $N$ is the number of base pairs within the DNA molecule. As such, we would expect that as $N$ increases, the association rate of the protein with the correct site will decrease. However, it has been shown that rather than decreasing the association rate with the correct complex, it has actually been shown that increasing the number of non-specific sites around the target site can actually increase the proteins rate of association (von Hippel and Berg, 1989b). This suggests that whilst a number of cellular factors, such as the localisation of DNA into small regions, can improve the association rate of proteins beyond that expected in bulk solution, there must be a number of alternative search mechanisms which allow for a more targeted, or rapid, search of vast quantities of non-specific DNA sites to aid in location of DNA damage/specific sequences. These mechanisms have been labelled 'facilitated diffusion', generally involving an initial random 3D-search within the cell leading to sequence-independent interactions with DNA, followed by a 1-dimensional translocation along the DNA molecule to the target site, upon dissociation from the DNA this search cycle repeats (Berg and Blomberg, 1976; von Hippel and Berg, 1989b; Shimamoto, 1999; Halford, 2004).

## Facilitated Diffusion

As described above, the underlying principle behind facilitated diffusion is that a protein undergoes a random 3D diffusional search, and upon collision with a non-specific DNA site it switches mode to a 1D search, translocating along the DNA via either sliding or hopping, before dissociating and returning to the original 3D diffusional search (Berg and Blomberg, 1976; Berg, Winter and von Hippel, 1982; von Hippel and Berg, 1989b). Since it is known that the 3D search alone cannot account for the rate at which specific sites are located (Riggs et al., 1970), the key matter to focus on is the switch to the 1D search. Facilitated diffusion primarily consists of 3 components, 1D diffusion along the DNA backbone of a protein without dissociation, rapid micro-dissociations and reassociations

on the same DNA strand known as 'hopping', or transfer between two distant sections of the same DNA molecules, known as 'intersegmental transfer' (Halford, 2004; Bonnet *et al.*, 2008).

## The Kinetics of 1D Sliding

Sliding involves linear translocation along the DNA molecule without dissociation, this functions to increase the rate of base pairs searched by a protein by reducing the dimensionality of the search (Richter and Eigen, 1974). This 1D search can take one of a number of forms on the DNA, these can be divided into random walk (random variation in position), paused motion (periods of diffusion separated by pauses in location), and directed motion (proteins which exhibit directionality in their movement), (Kad *et al.*, 2010). Directed motion is driven by the hydrolysis of ATP, whilst both random and paused motion are driven by thermal fluctuations within the cellular environment. These fluctuations are due to random variations in microscopic parameters of a biomolecular system due to thermal noise (i.e., the random diffusion of molecules which constitute a cell, such as lipids, peptides, water molecules, and proteins) (Nelson, 2008; Imashimizu and Lukatsky, 2017).

Protein-DNA binding is mediated by two types of interactions: non-specific electrostatic interactions and specific hydrogen bonding interactions. Non-specific interactions occur between the negatively charged phosphate backbone of the DNA molecule and the positively charged DNA binding regions within proteins (Lohman *et al.*, 1996; Misra *et al.*, 1998; O'Brien *et al.*, 1998; Bergqvist *et al.*, 2004; Hargreaves and Schleif, 2008), with increasing salt concentration leading to weakened electrostatic interactions and disruption of protein-DNA interactions and translocation (Record, Anderson and Lohman, 1978). Specific interactions occur between the protein and DNA bases, which arise from the relative position of the protein to the DNA (von Hippel and Berg, 1989a). For a protein to be able to slide along the DNA backbone the total binding energy of these two

components needs to be small compared the thermal energies in the local environment (von Hippel and Berg, 1989a).

We can incorporate 1D sliding into the diffusion-limited rate for bimolecular interactions ($k_{Smol}$) that was detailed above, allowing us to extract an association rate for a DNA-binding protein to its target site (Mirny *et al.*, 2009), as given by:

Equation. 3
$$k_s \approx k_{Smol} \left( \frac{\tau_{3D}}{\tau_{1D} + \tau_{3D}} \right) \tilde{n}$$

Where $\tau_{3D}$ and $\tau_{1D}$ are the average durations of 3D diffusion and 1D translocation in one round of 3D and 1D search, respectively. $\tilde{n}$ is the average number of base pairs moved during a single round of 1D search, and is equivalent to 1D Brownian motion, as given by:

Equation. 4
$$\tilde{n} = \sqrt{D_{1D}\tau_{1D}}$$

Interestingly this demonstrates that upon binding to non-specific DNA, the search rate is actually slowed down by a factor of $\tau_{3D}/\tau_{1D}+\tau_{3D}$, however this is compensated for by the sliding term ($\tilde{n}$). As previously described, the maximum rate constant is achieved when $\tau_{3D}$ = $\tau_{1D}$, which differs greatly from theoretical estimates which range from $10^{-1}$-$10^{-4}$ (Mirny et al., 2009). This clearly indicates that our understanding of protein motion on DNA is still greatly lacking.

## Rotation-Coupled diffusion of proteins on DNA

Due to the helical structure of DNA, it would be expected that proteins would translocate along the major groove of the DNA helix, following the natural curve of the DNA (Fig. 1) – the first theoretical equation for rotation-coupled diffusion of proteins was developed by Schurr in 1979 (Schurr, 1979).

This model accounts for the fact that as a DNA-binding protein travels the distance of 10 base pairs, it rotates 2π and considers translational and rotational friction, with the centre

of mass of the protein remaining on axis with the DNA. This model was further developed on by Bagchi, Blainey, and Xi culminating in the BBX model. This furthers the original model developed by Schurr by considering the off-axis rotational diffusion of proteins, and is given by:

$$D_{1D} = \frac{k_B T}{6\pi\eta r + (\frac{2\pi}{10BP})^2 (8\pi\eta(r)^3 + 6\pi\eta r (R_{OC})^2)}$$

Where $r$ is the radius of the protein, $BP$ is the distance between 2 base pairs (equivalent to 0.34 nm), and $R_{OC}$ is the separation between the centre of mass and the longest axis of the DNA (Fig. 1). The key addition in the BBX model is the incorporation of the 3rd term ($6\pi\eta r(R_{OC})^2$) which accounts for the friction associated with the off-axis translation around the central axis of the DNA. Additionally, this model results in a $1/r^3$ size dependence of diffusion, in contrast to the $1/r$ size dependence of diffusion which arises from the Stokes-Einstein equation, which more closely matches experimentally derived results based off the diffusion of transcription factors (Bagchi, Blainey and Xie, 2008; Blainey *et al.*, 2009).
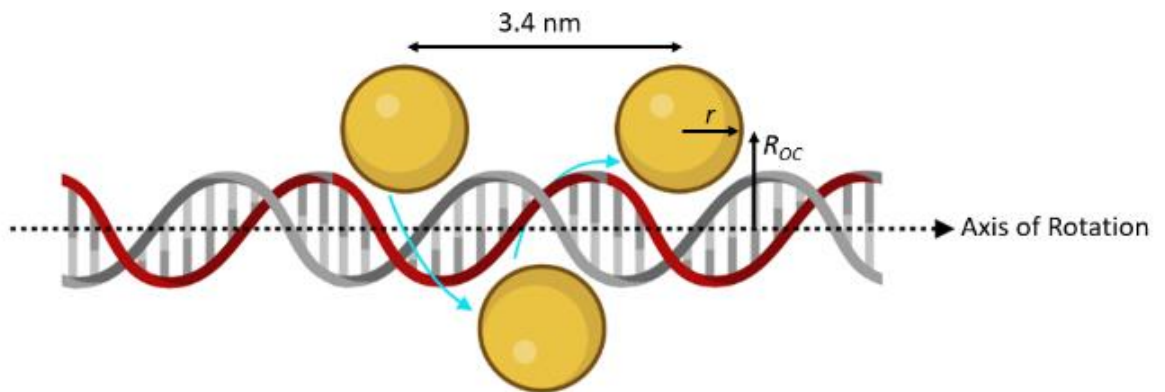


*Figure 1 – Rotation-coupled diffusion of proteins on DNA*

Due to the helical structure of DNA, proteins are thought to translocate along the major groove of the DNA helix, meaning that a protein will undergo a full 2π rotation every 10 base pairs (equivalent to 3.4 nm) keeping its DNA-binding site oriented towards the DNA helix at all times. As the protein rotates around the DNA helix it experiences friction associated with off-axis translation around the central axis of the DNA, which is influenced by the viscosity of the local solution, the radius of the protein ($r$), and the distance between the proteins centre of mass and its primary axis of rotation around the DNA helix ($R_{OC}$). Created with BioRender.com.

Interestingly, whilst this equation more accurately model's diffusion of DNA-binding proteins, it has been found that it still overestimates the diffusion constants of some transcription factors. For example, the experimentally measured diffusion constant of the Lac repressor is $(4.6\pm1.0)\times10^{-14}$ m$^2$ s$^{-1}$ (Elf, Li and Xie, 2007). Schurr's original model for the rotation-coupled diffusion of proteins predicts a value of $4.04\times10^{-13}$ m$^2$ s$^{-1}$, whilst the BBX model predicts a value of $2.09\times10^{-13}$ m$^2$ s$^{-1}$ (Bagchi, Blainey and Xie, 2008). It can be seen that whilst the BBX model provides a value closer to the experimentally obtained diffusion constant, it still overestimates diffusion constants of proteins. This indicates there is still much left that needs to be understood to resolve a clearer view of exact protein motion on DNA. It is likely that these differences arise from factors such as the free energy profile of DNA within the cell, conformation of DNA *in vivo*, the helical path taken by the protein, and the dynamic effects arising from a crowded intracellular environment (Bagchi et al., 2008; Blainey et al., 2009).

## Intersegmental Transfer

Intersegmental transfer involves the movement from one site of non-specific DNA to another on the same DNA strand, via an intermediate loop with an average distance of 400 bp. This average jump distance is a result of the 'bending persistence length' of DNA, which is a measure of the structural rigidity of a polymer chain, along with the energy cost required to deform it (Manning, 1986; Nelson, 2008). Persistence length (P) is given by:

Equation. 6
$$P = \frac{B_s}{K_b T}$$

Where $K_b$ is the Boltzmann constant, $T$ is temperature, and $B_s$ is the bending stiffness of the polymer chain. DNA's persistence length has been estimated to be ~50 nm (150 bp) at 0.1 M salt (Porschke, 1986), however it should be noted that changes within the local ionic environment dramatically affect the flexibility of DNA, with neutralisation of phosphate backbone charges dramatically increasing its flexibility (Baumann *et al.*, 1997; Podestà *et*

*al.*, 2005). The result of this persistence length is that DNA sites are most commonly juxtaposed when they are 400 bp apart. Intersegmental transfer is only relevant in the cases of proteins/protein complexes which have multiple DNA binding regions (Krepel and Levy, 2017) – with one DNA-binding domain remaining associated with the original location on the DNA, whilst the other DNA-binding domain associates itself with the newly presented DNA strand and is able to bridge the gap between the two.

## Ionic Charge and its relationship to DNA search mechanisms

Within interactions between proteins and DNA, electrostatic interactions between the positively charged DNA binding domains of proteins, and the negatively charged phosphate backbone of DNA molecules (Manning, 1978; Record, Anderson and Lohman, 1978), with computational studies indicating that the majority of interactions between proteins and nucleic acids revolve around the phosphate backbone of the DNA molecule (Jones, 2001; Luscombe, 2001). These phosphates allow for shape recognition of nucleic acids by interacting proteins (Yu, Pettitt and Iwahara, 2020), with distortion of the phosphate backbone playing a large role in the recruitment of certain proteins and protein complexes. Because of the importance of these interactions the ionic environment surrounding proteins and DNA hugely affects their interactions, and as such the search for specific DNA binding sites.

It has been noted in the past that increasing salt concentration leads to an increase in the observed rate of 1D diffusion of proteins along the DNA backbone (Record et al., 1978), it is thought that the increase in positively charged ions creates a shielding effect around the DNA backbone – hindering interactions between proteins and DNA.

## The effect of intracellular crowding on DNA search mechanisms

An additional consideration that needs to be considered when probing our understanding of DNA search mechanisms, is that of intracellular crowding. A large proportion of studies

which investigate facilitated diffusion, and the action of individual proteins are carried out, necessarily, in *in vitro* conditions – as many of these spectroscopic techniques are unable to carry out *in vivo* studies. These investigations are crucial to expand our understanding of DNA search mechanisms, however additional considerations of conditions within the cell highlights the need for additional considerations and may help to explain why results from *in vitro* studies, may not always closely match what is observed *in vivo*.

Within cells 20-40% of the total volume is taken up by additional macromolecules and proteins – whilst one would expect that the presence of these additional components would hinder the diffusion of proteins and slow down the search for DNA damage, studies have found it actually accelerates location of target DNA sites and enzymatic function (Cravens *et al.*, 2015; Singh *et al.*, 2017). Exactly how molecular crowding achieves this remains unclear, however recent increased interest has led to a number of new developments which help to un-obfuscate this process. For example, whilst increased molecular crowders would expectedly increase the viscosity of the bulk solution (macroscopic viscosity), however concurrently regions of constant microscopic viscosity occur around DNA molecules (due to depletion force, where smaller crowding particles are excluded from the local area surround larger molecules (Asakura and Oosawa, 1958)) – meaning that DNA search proteins experience a duality of viscosity between 3D and 1D searches, which functions to simultaneously increase the association time during 1D-translocation as well as increasing the hopping frequency during this translocation (Dey and Bhattacherjee, 2018). However, there remains a certain amount of ambiguity with studies finding that intracellular crowding actually has no effect on search times in certain instances (Brackley, Cates and Marenduzzo, 2013), whilst others report the enhancing effect of crowding molecules on facilitated diffusion (Cravens *et al.*, 2015). Together, these intracellular effects may provide mechanisms through which the association rate of proteins undergoing 3D-diffusion, could be increased past what would be expected based on the estimated 3D-diffusion constants for these proteins in bulk solution.

In addition to the molecular crowding that occurs in the cell, the 1D diffusion of proteins along DNA can be impeded by factors such as other proteins bound to DNA, or the tertiary/quaternary structure of the DNA. For example, in the case that two proteins which remain in constant contact with DNA encounter each other during translocation, they will be unable to pass each other due to steric hindrance (Gorman, Chowdhury, *et al.*, 2010). As such, within a cell where numerous DNA-binding proteins are concurrently searching for their targets on DNA, the diffusion of these proteins will effectively be bounded by the activity and motion of the surrounding proteins. Additionally, within Eukaryotes, the remodelling of DNA into structures such as nucleosomes or chromatin can also dramatically limit the 1D diffusion of proteins, with large sections of the DNA being rendered inaccessible (Kampmann, 2005; Gorman *et al.*, 2011; Hager, McNally and Misteli, 2019).

## Further work is needed to fully understand how sequence-specific proteins locate their targets

The exact processes through which sequence-specific proteins are able to locate their targets sites remains one of the most pressing questions within biology and biophysics. Developing our understanding of how relatively few proteins are able to search such vast quantities of non-specific sequence would have dramatic impacts on our understanding of a number of systems, including the dynamics surrounding gene regulation and DNA repair. Whilst considerable progress has been made, there remain a number of gaps in our understanding. More recent developments in the field of Single-Molecule biophysics have begun to allow us to explore more deeply into these questions, moving us from the more traditional bulk phase ensemble methodologies (Riggs, Bourgeois and Cohn, 1970; Berg, Winter and von Hippel, 1982; von Hippel and Berg, 1989a, 1989b) which investigate the average characteristics of these protein populations, to understanding the functions,

dynamics, and kinetics of single proteins, providing a level of detail which has not been achieved previously (Bonnet *et al.*, 2008; Tafvizi *et al.*, 2011; Van Houten and Kad, 2014).

## 1.3 Single-Molecule Biophysics

The emergence of Single-Molecule methods over the last few decades has been revolutionary in the field of biophysics and has provided a completely novel approach to studying biological questions. Previously all biological systems were studied using bulk/ensemble methods. With these methods it is only possible to look at the average characteristics across an entire population, however for these results to be truly representative they rely on the assumption that the population being studied is truly homogenous. However biological systems are largely heterogeneous, with populations of biomolecules displaying innate intermolecular variations which cannot be detected via bulk/ensemble methods as these nanoscale variations will be averaged out across the population (Xie and Trautman, 1998). In contrast Single-Molecule techniques revolve around monitoring a single biomolecule from a larger population, allowing us to directly probe its function, dynamics, and kinetics. This provides a novel viewpoint from which we can gain a greater understanding on how individual biomolecules, and their variations, can influence and affect a biological system. Over the past 60 years the field of Single-Molecule biophysics has progressed at an unprecedented pace, from the first measurement of a Single-Molecule of β-D-Galactosidase in 1961 (Rotman, 1961), to now weighing Single-Molecules using only light (Young *et al.*, 2018) and direct observation of the activity of single unlabelled proteins (Ortega Arroyo *et al.*, 2014).

Single-Molecule methodologies can take many forms, including electrical-based detection methods, force-based approaches, and optical-based approaches. Electrical-based detection for investigating Single-Molecules include methods such as patch-clamp and nanopore based techniques. Nanopores have been of particular interest recently with the development of nanopore sequencing, which involves the movement of single-stranded

DNA (or RNA) through a nanopore within a membrane – with detection of the change in an electrical current that passes through the membrane being used to accurately sequence the DNA as it passes through the pore (Deamer, Akeson and Branton, 2016). Force-based approaches are used to study the mechanical responses of biological systems under applied torsional or stretching forces. Force-based approaches mainly focus on the use of 3 different techniques: atomic force microscopy, optical trapping, and magnetic trapping. In all these methodologies one end of a biomolecule/biopolymer will be bound to the surface, and the other end to a force sensor. The displacement of the force sensor can then be measured to determine force. Optical based approaches allow for direct observation of the action of single proteins under controlled conditions, either *in vivo* or *in vitro*. Light microscopy involves the use of light to stimulate and detect Single-Molecules and is by far the most common method for optical Single-Molecule detection. Historically fluorescence microscopy has been the most prevalent light microscopy technique, however recent technological advances have paved the way for the development of new light-scattering based microscopes which have the potential to revolutionise our approach to studying a number of biological questions.

## 1.4 Single-Molecule Fluorescence Microscopy

The earliest reports of fluorescence microscopy date back to the early 20th century, having been initially developed by the physicists Otto Heimstaedt and Heinrich Lehmann (Renz, 2013). Since then, they have become a staple of biological research, being used for a wide range of applications across the biological sciences due to its exceptional signal-to-noise, and high labelling specificity for biomolecules of interest, allowing for straightforward detection of Single-Molecules.

The physical process of fluorescence involves the absorption of a photon by a 'fluorophore' (which may be a molecule, atom, or nanostructure), causing an orbital electron to enter an excited singlet state. This excited electron then undergoes vibrational

energy loss, relaxing it to the lowest possible energy level of the excited singlet state. Finally, upon relaxation to the ground state, it emits a photon with a red-shifted wavelength (due to vibrational energy loss whilst the electron is in the excited singlet state). This process is commonly described with a Jablonski diagram (Fig. 2), which describes the different energy states and the transitions that occur between them in a visual form (Jablonski, 1933).

The first use of fluorescence to detect Single-Molecules was carried out by Boris Rotman in 1961, in which the monosaccharide products of β-D-Galactosidase were fluorescently labelled and detected (Rotman, 1961). From then the direct detection of Single-Molecules of labelled globulin was achieved in 1976 (Hirschfeld, 1976), and the first direct detection of Single-Molecules labelled with single fluorescent dyes was achieved in 1990 (Brooks Shera *et al.*, 1990). Continued technological developments allowed for the development of
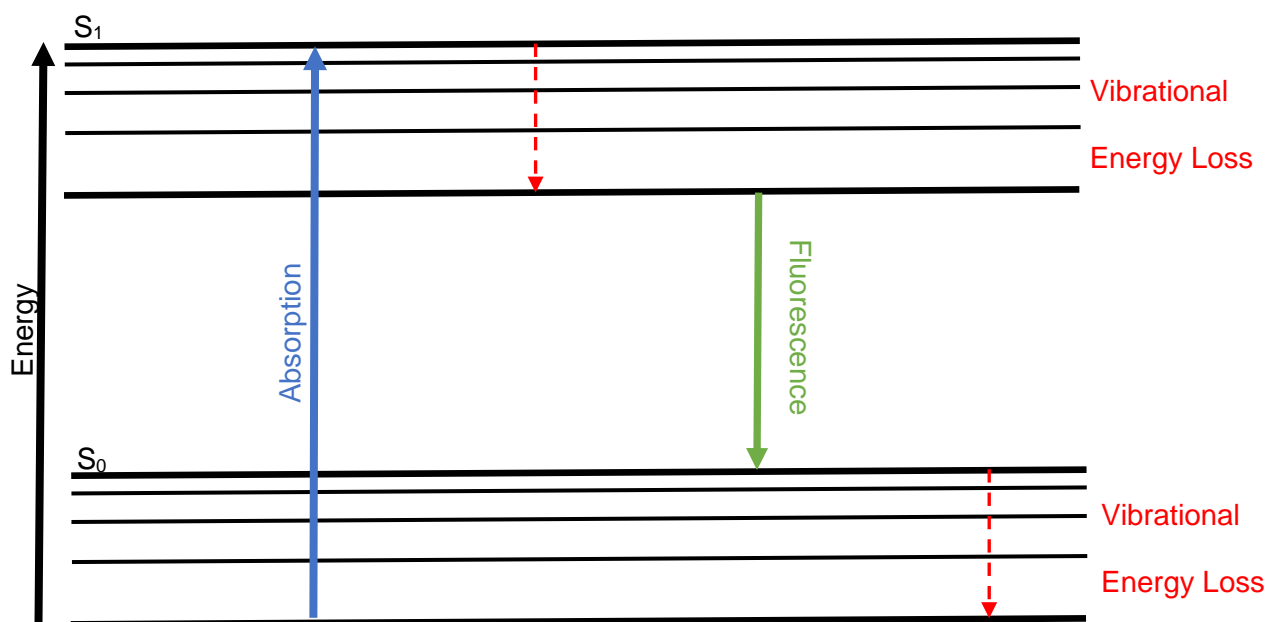


*Figure 2 - Jablonski Diagram*

Energy profile of an electron during fluorescence. The absorption of a single photon by the fluorophore leads to excitation of the electron from ground state ($S_0$) to the excited singlet state ($S_1$). Vibrational energy losses, caused by oscillation from the interruption of the negatively charged electron charge distribution around the positively charged nucleus, means that when the electron relaxes back to its ground state the released photon has lower energy (e.g., a longer wavelength).

systems with ever higher spatial resolution, culminating with the realization of super-resolution fluorescence microscopy.

## Photostability and Fluorescence Microscopy

A key concept which underlies fluorescence microscopy is the photostability of the fluorescent labels used for imaging. The photostability of a fluorescent label describes the likelihood of this label undergoing fluorescent inactivation, either reversibly or irreversibly. An ideal fluorophore for the majority of Single-Molecule experiments would be one that maintains a consistent stream of emitted photons without interruption for a long period of time. However, fluorophores can only undergo a finite number of cycles of photon absorption and emission. Inactivation can either be temporary (blinking), or permanent (photobleaching). Blinking of a fluorophore involves a sudden loss of photon emission, and can occur through a number of mechanisms (Dickson *et al.*, 1997), for example when a fluorophore enters an excited triplet state, rather than an excited singlet state (Ha and Tinnefeld, 2012). This excited triplet state has a lifetime roughly 1000 times longer than that of the excited singlet state, with the fluorophore unable to emit another photon until it has returned to ground state. Photobleaching involves the complete destruction/disruption of the initial π-electron configuration, a process which is better understood in organic fluorescent dyes as compared to fluorescent proteins (Ha and Tinnefeld, 2012; Mamontova *et al.*, 2017).

## Fluorescent Labels

Whilst proteins possess an innate ability to fluoresce due to certain amino acids (most notably tryptophan), these alone do not provide the brightness required to carry out even the simplest fluorescence-based experiments. Because of this a number of fluorescent labels have been developed and are used to report, either directly or indirectly, on the protein it is attached to and the environment around it.

## Types of fluorescent label

There are 3 types of fluorescent label that are commonly used for Single-Molecule fluorescence microscopy, these are: organic fluorescent dyes (which can be further subdivided into, for example, single fluorescent dyes, or fluorescent dye-based nanoparticles/materials (Svechkarev and Mohs, 2019; Niekamp, Stuurman and Vale, 2020)) , fluorescent proteins, and quantum dots. Each has their own specific advantages and limitations and are each suited to different applications.

Fluorescent proteins have long been one of the first choices for fluorescent labels within Single-Molecule biophysics since the initial purification of the Green Fluorescent Protein (GFP) from the jellyfish *Aequorea Victoria* (Shimomura, Johnson and Saiga, 1962), and the discovery that it could be functionally expressed in cells without the need for additional exogenous substrates or co-factors (Chalfie *et al.*, 1994; Inouye and Tsuji, 1994). These factors combined with improvements in molecular DNA cloning allowed for simple labelling of proteins. Since then a number of variants with numerous different properties have been developed, and are still being improved (Baird, Zacharias and Tsien, 2000; Lippincott-Schwartz and Patterson, 2003; Karasawa *et al.*, 2004; Shaner *et al.*, 2004; Lippincott-Schwartz and Patterson, 2008). They are commonly used due to the ease with which they can be recombinantly cloned onto proteins of interest, making them ideal for live cell imaging. However, whilst they are useful tools, they are not without their limitations. Direct fusion of fluorescent proteins can disrupt the structure and function of native proteins and require careful attention. They are also prone to aggregation, particularly when targeted to organelles (Costantini and Snapp, 2013), despite much work to circumvent this issue (Baird, Zacharias and Tsien, 2000).

Organic fluorescent dyes provide an appealing alternative to fluorescent proteins as a number of dyes have been developed covering a wider spectral range than fluorescent proteins, they are usually brighter, smaller in size, and more photostable. However, the

difficultly with fluorescent dyes is the conjugation to the protein of interest. The most common method of conjugation involves the linking of a chemically modified dye to a suitable amino acid within the protein. The two most common amino acids to be targeted are cysteine (via maleimide linked dyes) and lysine (or N-terminal amines, via succinimidyl—ester or isothiocyanate linked dyes). Two main problems present themselves using this method: firstly, to tag a protein with a single fluorophore requires the presence of only a single target residue – this presents a major protein engineering challenge ensuring only a single residue is present within a protein for the labelling reaction (e.g., Cysteine for Maleimide-linked dyes). Secondly, the labelling reactions will never reach 100% efficiency leading to the presence of a large amount of free dye and unlabelled protein in solution. The presence of these unwanted species leads to increased background signal, potential non-specific interactions, and limitations imposed due to the decreased signal due to a high-proportion of unlabelled proteins (which can pose a major challenge when evaluating events such as protein-protein interactions).

Protein labelling methods can broadly be split into two categories – direct or indirect conjugation. Direct conjugation involves the attachment of the fluorescent label to the protein of interest no intermediary requirements (e.g., recombinant DNA cloning to directly attach a fluorescent protein onto the N- or C-terminal of a protein). Indirect conjugation involves the use of an intermediary molecule which both the fluorescent label, and the protein of interest are attached to. These take many forms, including: the use of a biotinylated antibody targeted at a motif within the protein of interest, use of a genetic tag such as a SNAP/HALO tag, biotinylation of the protein of interest, or use of chemically modified organic dyes to target specific residues/chemical groups with proteins such as maleimide- (cysteine targeting) and NHS ester-linked dyes ($-NH_3$ targeting).

Quantum dots (Q-dots) are nanometre sized semi-conductors; they are formed of cadmium-selenide cores which are capped with zinc-sulphate. They display hugely

beneficial fluorescent characteristics, being incredibly bright whilst also incredibly photostable. They have extremely narrow emission peak, the wavelength of which can be modified by changing the size of the quantum dot (a larger the quantum dot, the longer its emission wavelength). The outer cap of Q-dots can also be functionalised with a number of different chemical groups (Chan and Nie, 1998), allowing a large degree of flexibility in the method of attachment to target proteins. Whilst Q-dots display numerous beneficial fluorescent characteristics, they also have a number of disadvantages. Firstly, they are large compared to both fluorescent proteins and fluorescent dyes (generally between 10-20 nm in diameter). This leads to a protein being labelled with a marker which can be 4-5 times its own size. Whilst Q-dots are resistant to photobleaching, they do display a propensity for blinking which can limit their use when looking at interactions/kinetic lifetimes – however there have been notable developments in the production of non-blinking Q-dots (X. Wang *et al.*, 2009).

## What makes a good fluorescent label?

For a fluorescent label to be effective it needs to possess a few key characteristics; primarily it needs to be bright enough for a single fluorophore to be detected by modern cameras, small enough to be attached to proteins of interest with minimal disturbance to their local environment, photostable enough to allow experiments to be carried out, and non-disruptive to the biological system which they are being used to study.

The relative brightness of a fluorophore is calculated by multiplying two of its intrinsic characteristics, the extinction coefficient and quantum yield (Waggoner, 1995). The extinction coefficient of a fluorophore describes its efficiency for absorbing light and entering the excited singlet state e.g., a high extinction coefficient means the fluorophore absorbs light more efficiently. The quantum yield of a fluorophore is the ratio between the number of photons absorbed, and the number of photons emitted – meaning a fluorophore with a high quantum yield will emit more photons per photon absorbed.

# Applications of Fluorescence Microscopy

## Super-Resolution Fluorescence Microscopy

Super-resolution microscopy describes any form of microscopy which breaks the limit on spatial resolution described by the Abbe diffraction limit ($\lambda$/2NA). This limit describes how the spatial resolution of any light microscope is limited by the diffraction properties of light ((Abbe, 1873); Translated in: (Masters, 2020)). The first realization of super-resolution microscopy was achieved through the use of near-field imaging (where the fluorescent source and detector are separated by less than a few wavelengths of the illumination light), as opposed to far-field imaging (where the fluorescent source and detector are separated by more than a few wavelengths of the illumination light) . This was done through the use of total internal reflection fluorescence (TIRF) microscopy (Axelrod, 1981) in which total internal reflection of an incident light source produces an evanescent field, with an axial illumination shorter than the standard spatial resolution limit, to illuminate the sample.

Whilst near-field imaging approaches allowed for early super-resolution microscopy, the most common approach now involves localization microscopy which is carried out using a far-field imaging setup. Localization microscopy involves estimating the position of distinct single fluorophores one at a time, this is achieved through fitting their individual point spread functions (PSF). Single point emitters (such as individual fluorophores) being viewed under a light microscope using a circular numerical aperture will produce a specific optical response, known as the PSF. This pattern forms when light emitted from a single point source is captured by the objective and focused onto a corresponding point in the image plane. When they are focused the light waves converge and interfere at the focal point, producing (in a 2D plane) a pattern of concentric rings of light which surround a bright central disk. This distinctive pattern is known as the Airy disk pattern (named after George Airy), the radius of which is determined by the numerical aperture of the objective

used. The centre of the PSF provides an accurate estimation of the actual position of the emitter, therefore if each emitter is separated by more than the diffraction limit for the given system, it is possible to accurately localise the centre of each. Using this method, tracking of plastic beads coated with kinesin travelling along surface-immobilised microtubules with a resolution of 1-2 nm was achieved using differential interference contrast (DIC) (Jeff Gelles, Schnapp and Sheetz, 1988). This fitting of PSFs to achieve super-resolution fluorescence microscopy was first implemented by Schmidt et al. in 1996, they found that each PSF could be adequately estimated by a 2D Gaussian function, with a full width at half maximum (FWHM) of roughly half the wavelength of the incident light – with this they were able to achieve a spatial resolution of 30 nm, well below the optical diffraction limit for the system (197 nm, NA = 1.3, 514 nm illumination wavelength) (Schmidt *et al.*, 1996).

The most commonly methods for fluorescent super-resolution microscopy are photoactivated localization microscopy (PALM) and stochastic optical reconstruction microscopy (STORM) which allow for live-cell imaging at the Single-Molecule level. Both techniques use stochastic activation of individual fluorophores, with the subsequent sub-pixel localisation of the PSFs allowing for an incredibly high spatial resolution, well beyond the diffraction limit.

PALM makes use photoactivatable fluorescent proteins, which are fluorescent proteins that are initially found in a dark state can be either reversibly or irreversibly activated by one wavelength, and then imaged using a second wavelength. PALM involves the stochastic activation of these photoactivatable fluorescent proteins, which are on average separated by more than the diffraction limit imposed by the given system. These activated molecules can then be precisely localised before they undergo photobleaching. This cycle can then be repeated until a large number of molecules have been precisely localised,

and their subsequent positions can then be used to create a super-resolution 2D image (Hess, Girirajan and Mason, 2006).

STORM functions in a similar manner, instead utilising photo-switchable fluorophores – these fluorophores can be repeatedly switched between a dark and fluorescent state using alternate wavelengths. This process was initially demonstrated using a photo-switchable Cy5 dye, which can undertake this activation and inactivation cycle many hundreds of times before photobleaching (Rust, Bates and Zhuang, 2006). During STORM a pulsed laser is used to activate only a small-subset of the photo-switchable fluorophores, whose positions can subsequently be accurately localised. These are then switched off using the inactivating wavelength. This cycle can be repeated many times to allow for a super-resolution image to be reconstructed from the calculated positions (Rust, Bates and Zhuang, 2006)

### Total-internal reflection fluorescence (TIRF) microscopy

Total internal reflection fluorescence (TIRF) microscopy has been a core Single-Molecule technique since its first demonstration in 1981 (Axelrod, 1981). It allows for near-field imaging of fluorophores with a high signal-to-background ratio and has been widely applied. TIRF is based on the principle that upon total internal reflection of an incident beam at a glass-water interface (e.g., between a coverslip and sample), an electromagnetic field known as an evanescent field, is projected into the sample. This evanescent field has the same properties as the incident light, but decays exponentially with distance from the glass-water interface. This allows for the excitation of only the fluorophores which are within a few hundred nanometres of the surface, drastically reducing background, and improving the signal-to-background ratio for the images (Hecht, 1998).

TIRF is achieved directing the incident light source at the sample with a high incident angle, if this angle is larger than the critical angle ($\theta_{critical}$) total internal reflection will occur.

The critical angle is determined by the difference between the refractive index of the coverslip glass ($n_1$), and the refractive index of the sample ($n_2$) as seen in Equation 7.

$$\theta_{critical} = sin^1(\frac{n_1}{n_2})$$

The depth of the produced evanescent wave is determined by the angle of illumination, incident light wavelength, and the difference between refractive indexes.

Because of its high signal-to-background ratio TIRF is well suited to Single-Molecule investigations, particularly in looking at biochemical interactions, such as protein-protein and protein-nucleic acid interactions (Ha *et al.*, 1999; Tanner *et al.*, 2009; Hoskins *et al.*, 2011), and even live-cell functions such as exocytosis (Schmoranzer *et al.*, 2000). It has also been commonly used to study the kinetics of binding events, and complex formation (Ulbrich and Isacoff, 2007; Hoskins *et al.*, 2011).

## Limitations of Fluorescence Microscopy

Fluorescence microscopy has become an important technique in the field of Single-Molecule biophysics, allowing for direct imaging of Single-Molecules with a high signal-to-noise ratio, whilst still being widely applicable to the study of numerous biological systems both *in vitro* and *in vivo*. However, the technique is not without its limitations, the most important of which is the inherent instability of fluorescent labels leading to blinking and eventually photobleaching under continuous illumination. This process directly limits the achievable acquisition times – posing a significant challenge which needs to be considered when utilising fluorescence microscopy.

The achievable temporal resolution for fluorescent microscopy is also limited by the inherent rate at which a fluorophore can undergo both absorption and emission of a photon. As previously discussed, the process of fluorescence can be broken down into 3 discrete steps: absorption of a photon causing excitement of the fluorophore, vibrational

energy loss relaxing excited electrons to the lowest possible energy level of the excited singlet state ($S_1$ in Fig. 1), and finally emission of a photon as the excited electrons return to ground state ($S_o$ in Fig. 1) (Jablonski, 1933). The limitation imposed by these steps is the time taken for all 3 events to occur, with the total time for a fluorophore to undergo absorption, excitation, and emission being measured on the nanosecond (ns) scale. Due to this factor the photon flux of fluorophores is inherently limited by the rate at which this cycle occurs – but visualisation of individual fluorophores during Single-Molecule fluorescence microscopy requires the detection of enough fluorescently emitted photons to allow for the fluorophore to be effectively resolved from background noise. This means that there is a fundamental limit imposed on the achievable temporal resolution, which as can be defined as the total integration time required to allow the fluorophore to emit enough photons to allow for effective resolution of the fluorophore.

Lastly, the incorporation of bulky fluorescent labels onto proteins can have disruptive effects on their function and dynamics. For example, it has been shown that the labelling of the type II restriction enzyme EcoRV with large fluorescent labels such as Q-dots directly affects the observed diffusion constant on DNA (Dikić *et al.*, 2012). It has also been observed that the fluorescent labelling of wheat germ agglutinin (WGA) significantly affects its binding with glycoprotein on the membrane of cells, altering its binding kinetics and the spatial distribution of the probe (Yin, Landick and Gelles, 1994).

Because of these limitations imposed by the inherent nature of fluorescence and fluorescent tags, the development and implementation of scattering-based microscopies have allowed for circumvention of these limitations by making using of the natural phenomenon of light scattering.

## 1.5 Scattering Based Microscopy

The easiest way to avoid the limitations imposed by the use of fluorescent tags would be to simply remove them from the system – instead relying on the direct interaction between the molecule of interest, and the illuminating light used in the optical system. Scattering occurs when a particle is illuminated with an electromagnetic wave (i.e., an oscillating electric field), the incident wave causes the electrical charges within the particle to enter a dipole moment, oscillating at the same frequency as the incident wave. These oscillating electric charges radiate electromagnetic energy in all directions, and it is this secondary radiation that is called scattered radiation (Bohren and Huffman, 1998). This scattering can either be elastic, in which the scattered light is the same wavelength as the incident light, or inelastic, in which some of the energy of the incident light is lost and thus the scattered light has a longer wavelength than the incident light (Bohren and Huffman, 1998).

The ability of sub-wavelength particles to scatter electromagnetic waves has been long-understood and is commonly used in many forms of spectroscopy (El-Kurdi and Patra, 2019; Jones *et al.*, 2019; Young and Kukura, 2019). Optical systems based on light scattering allow for theoretically unlimited imaging time, and as the photon flux is limited only by the incident light intensity and the scattering cross section of the particle, hugely increased temporal resolution (Young and Kukura, 2019).

The experimental difficulty in implementing light scattering as a contrast mechanism in optical microscopy primarily lies in the detection of the scattered light. The scattering of light by sub-wavelength particles is an extremely inefficient process, simply due to the mismatch in size between the scattering particle, and the wavelength of light/diffraction limited spot of a typical light microscope with a high NA objective. Another major limiting factor is the scattering cross section of a particle drops to the power of 6 with the particle diameter, meaning detection of nanoscopic particles requires extremely efficient detection

apparatus. For example, it has been estimated that bovine serum albumin (BSA) has a scattering cross section of $10^{-11}$ $\mu m^2$ (under 405 nm illumination wavelength, in an aqueous environment) (Piliarik and Sandoghdar, 2014b). This would mean that if an area of 1 $\mu m^2$ containing a Single-Molecule of BSA was illuminated with 405 nm light, only 1 in 1 trillion photons would be absorbed and scattered. This incredibly low efficiency means that even the smallest sources of noise within an optical system, such as: other scattering particles in the sample, imperfections in the optics, readout noise and dark noise from photon detectors, and mechanical/thermal instabilities – can cause serious deterioration in the observable signal-to-noise ratio. Because of this, scattering-based optical systems need to be incredibly sensitive, whilst also eliminating all these sources of potential noise.

Unlike fluorescence microscopy where it is possible to use optical filters to isolate the different wavelength of the fluorophore from the incident light, light scattered by a single particle will retain the wavelength of the incident light – meaning separation through the use of optical filters is not an option. To achieve this, two general approaches have been developed; purely scattering based, and interference based. The distinguishing factor between these approaches is the fate of the transmitted/reflected incident light, in purely scattering based approaches it is excluded leaving only the scattered signal, whilst in interference-based approaches it is collected and combined with a reference wave.

## Dark Field Microscopy

Dark-Field Microscopy is the term used to describe light microscopy approaches which focus on the detection of purely scattered light – achieved through the exclusion of transmitted/reflected incident light from reaching the detector. The result of this is an image in which scattering particles appear as bright spots on a dark background.

This technique was first demonstrated in 1830 by Joseph Jackson Lister, in which the standard brightfield condenser, was replaced with a double-reflecting darkfield condenser (Lister, 1830). This condenser produces a narrow, hollow cone of light which illuminates

the sample, but is not collected by the objective – allowing for observation of only scattered light. The use of oblique angle illumination to achieve dark-field microscopy was first described by Joseph Bancroft Reade in 1837 (Goring and Pritchard, 1837), with further mention by John Quekett in 1848 (Quekett, 1848). These were followed by continued developments through the 1800's, notably the development of the 'Parabolic Reflector' by Francis Wenham in 1850 allowing for 'all-around' dark-field illuminations of specimens, followed by the creation of the 'Annular Illuminator' by George Shadbolt.

Revolutionary work carried out by Zsigmondy and Siedentopf in 1902 demonstrated the visualisation of nanoscale gold colloids using a dark-field microscope that made use of orthogonal illumination and detection pathways (Zsigmondy, 1926), capturing the imagination of the wider scientific community. The most common current approaches for achieving dark-field illumination, is either the use of total internal reflection (Fig. 3) (von Olshausen and Rohrbach, 2013), a mismatch between excitation and detection apertures leading to exclusion of the transmitted/reflected incident light (Ueno *et al.*, 2010; Ando *et al.*, 2018), or use of a traditional dark-field condenser (Dunn and Spudich, 2007). However, alternative techniques such as rotating coherent scatterings (ROCS) microscopy have also been developed providing alternatives for super-resolution scattering microscopy (Jünger, Olshausen and Rohrbach, 2016). All these techniques allow for effective isolation of the scattered light; however, the sensitivity is limited with regards to unlabelled Single-Molecules, meaning that gold nanoparticles which naturally have larger scattering-cross sections are used as contrast enhancing labels. Dark-field microscopy has been used to reach nm spatial resolutions, with µs temporal resolutions

whilst allowing for unlimited imaging time making it an extremely attractive option for Single-Molecule studies.
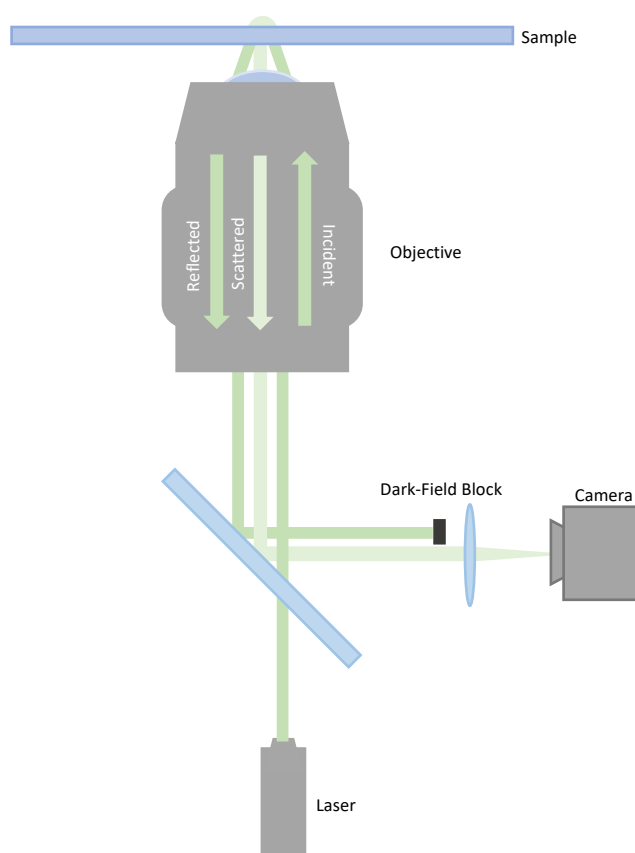


*Figure 3 - Dark-Field microscopy using a Total-Interal Reflection (TIR) illumination pathway*

The use of total-internal reflection (TIR) to achieve dark-field imaging has become commonplace due to its simple implementation and exceptional background removal. The use of TIR results in a spatial separation between the reflected component, and the scattered component – addition of a dark-field aperture/block allows for the complete removal of the reflected component, ensuring that only the light scattered by the sample reaches the camera. Dark-field microscopy using TIR allows for high signal-to-noise images with µs temporal resolution and nm spatial resolution.

## Gold Nanoparticles are efficient scattering labels

Gold nanoparticles (AuNPs) have become commonplace throughout biology and biotechnology due to their unique properties and the ease with which they can be functionalised and attached to molecules of interest. They have become widely used in areas such as biosensing (Miranda *et al.*, 2010), drug-delivery (Brown *et al.*, 2010), and imaging. These nanoparticles consist of small gold aggregates capped with labile capping ligands, such as citrates and thiols. Furthermore, AuNPs can be efficiently functionalised

with a wide range of chemical groups via a ligand exchange reaction to replace the capping ligands, making them suitable for simple labelling of biomolecules of interest (Yeh, Creran and Rotello, 2012).

It is the unique optical properties of these AuNPs which make them of particular interest in scattering-based microscopies. Spherical gold-nanoparticles display an innate physical property known as plasmon resonance, meaning they have greatly increased scattering and absorption cross sections within a size range of 500-550 nm (Jain *et al.*, 2006). This occurs due to the oscillation of conductive electrons of the nanoparticles under excitation at the resonant wavelength, known as the 'surface plasmon band' (Mie, 1908). This makes AuNPs extremely efficient scatterers, particularly when excited at their resonant wavelengths, with an 80 nm AuNP displaying a comparable scattering cross-section to a 300 nm polystyrene nanosphere (Jain et al., 2006).

## Previous Applications of Dark-Field

The use of contrast enhancing scattering labels has become commonplace in dark-field microscopy, allowing for imaging of labelled particles with incredibly high spatial and temporal resolutions (Yasuda *et al.*, 2001; Ueno *et al.*, 2010). Attachment of these scattering labels to proteins of interest has allowed for the µs tracking of $F_1$-ATPase rotation (Yasuda et al., 2001), real-time imaging of viral infection of HEp-2 cells (Wan *et al.*, 2014), and the tracking of Kinesin-1 movement on microtubules with angstrom localisation precision (Ando *et al.*, 2018). These systems can also readily be combined with fluorescence illumination and detection pathways, allowing for simultaneous scattering and fluorescence imaging (Weigel, Sebesta and Kukura, 2014). Notably a method for three-colour dark-field imaging has also recently been developed by the Iino group (Ando *et al.*, 2019), making use of the differing plasmon-resonance wavelengths for metal nanoparticles and their alloys. Using a diffraction grating combined with three-colour illumination corresponding to the plasmon-resonance wavelengths for silver nanoparticles,

silver:gold (50:50) nanoparticles, and gold nanoparticles, allowed for sub-nanometre localisation efficiency for each nanoparticle at ms exposure times (Ando et al., 2019).

Label free imaging of biomolecules using Dark-Field microscopy presents a number of challenges, primarily involving the detection of such a limited number of scattered photons, and the efficient removal of the background light. Because of these challenges, unlabelled imaging of biomolecules has been restricted to the imaging of larger biological macromolecules. One of the first demonstrations of this was in the detection of label-free microtubules, firstly examining the dynamic instability of individual microtubules (Horio and Hotani, 1986), and subsequently the observation of tubulin treadmilling and managing to corroborate previous work into the rate at which treadmilling occurs (Hotani and Horio, 1988). Subsequent investigations in a label-free manner have remained scarce, with some work being done involving label-free detection of the influenza virus (Enoki *et al.*, 2012).

## Interference-Based Microscopy

In contrast to dark-field microscopy, interference-based microscopies take an opposite approach to imaging. Rather than relying on the complete exclusion of reflected/transmitted light from the final image, interference-based approaches instead collect this light, selectively alter its phase, and then recombine it with the light that is scattered by the sample. Due to the alteration in the phase of this background light, interference occurs between the two components, enhancing the obtainable contrast. Interferometric detection also has the advantage that the interferometric signal scales linearly with the scattering particles size – as compared to the square relationship for pure scattering (Bohren and Huffman, 1998; Young and Kukura, 2019).

## Phase-Contrast Microscopy and Differential Interference Contrast Microscopy

One of the first, and most influential, demonstrations of this approach was carried out by the Nobel prize winning Frits Zernike who noted that through the use of phase plates to selectively alter the phase of the background light to match that of the scattered light led to constructive interference between the two components. The background light could then be specifically attenuated, great increasing the achievable contrast for light microscopy. This technique was named phase contrast, and has become on the most commonly used microscopy techniques in the past century (Zernike and Stratton, 1934; Zernike, 1942b, 1942a). Following on from the development of phase contrast, a number of other microscopy techniques were developed which also functioned on an interferometric basis. The first of these was Differential Interference Contrast (DIC) microscopy, which was first demonstrated by Georges Normarski in 1950 (Normarski, 1950). DIC involves the use of a specialised prism known as a Normarski prism (a modified Wollaston prism, an optical device which separates incident light into separate, orthogonal, linearly polarised beams), which separates polarised light into two rays, polarised 90° from each other – one functions as the sample ray, and the other as the reference ray. These rays are then travel through the sample adjacent to each other, and due to the different optical paths and refractive indexes in the sample their phases are further modified. The rays are recollected, and passed through a second Normarski prism, where they are recombined, leading to either constructive or destructive interference dependent on their optical path difference. The resulting image has a characteristic 3D component. However, reaching the sensitivity required for Single-Molecule experiments hugely increased the experimental complexity, as the contrast is dependent on the orientation of the sample to the Normarski prism. Because of this, other techniques instead use the reflected incident light from the glass-water interface of a microscope coverslip to create the required reference wave for interference.

## Scatterometry

This method is better suited for the detection of unlabelled Single-Molecules as only a small portion of the incident light is reflected, this in combination with the assumption that sub-wavelength particles scatter equally in both forwards and backwards directions, leads to an increase in the obtainable interferometric contrast. However, it is key to note that this does not increase the observable signal-to-noise ratio – as to obtain the increase in interferometric contrast the number of detected photons is greatly decreased (Ortega-Arroyo and Kukura, 2012; Young and Kukura, 2019). This is most commonly achieved using a common-path interferometric setup, in which the same objective is used for both illumination and detection – collecting both the reflected light (reference wave) and scattered light. Using this setup, the detected intensity, $I_{det}$, at any given point on the image is given by:

Equation 8. $$I_{det} = I_{inc}(r^2 + |s|^2 + 2r|s|\cos(\varphi))$$

In which $I_{inc}$ is the intensity of the incident light, $r$ is the reflectivity at the glass-water interface, $s$ is the scattering amplitude of the particle, and $\varphi$ is the phase difference between the reflected and scattered fields. However, for the case of sufficiently small particles (i.e., Single-Molecules) where $r >> s$ the pure scattering term can be ignored – meaning the intensity of the detected light is given by:

Equation 9. $$I_{det} = I_{inc}(r^2 + 2r|s|\cos(\varphi))$$

The obtainable signal-to-noise is given by:

Equation 10. $$SNR = \frac{2|s|\cos(\varphi)}{r}$$

And the interferometric contrast is given by:

Equation 11. $$Contrast = 1 - \frac{2|s|\cos(\varphi)}{r}$$

The scattering amplitude of a particle can be approximated using general Mie Theory, in which the scattering intensity is given by:

Equation 12. $$s(\lambda) = \eta \varepsilon_{med}(\lambda)\pi \frac{D^3}{2} \frac{\varepsilon_p - \varepsilon_m}{\varepsilon_p + 2\varepsilon_m}$$

In which $\varepsilon_p$ and $\varepsilon_m$ are the dielectric constants of the particle and the medium surrounding it, D is the diameter of the particle, and $\eta$ is a constant which describes the detection efficiency of the optical setup (Ortega-Arroyo & Kukura, 2012; Young & Kukura, 2019). It is important to note here that whilst Rayleigh scattering has typically used to describe the scattering efficiency of particles much smaller than the wavelength of the illuminating light, it remains an approximation, whereas Mie theory can be used to accurately describe the scattering of spherical particles of any size (Bohren & Huffman, 1998). These are both forms of elastic scattering.

It is clear to see the advantage of an interferometric setup for the detection of Single-Molecules in equation 9, where the scattered (i.e., interferometric) signal scales linearly compared to particle size (defined in Equation 12) – compared to the pure scattering signal ($|s|^2$) which scales with the square of the particle size, meaning that the signal drop for interferometric detection will be much lower as the detected particle size decreases. The key advantage of this is the reduced dynamic range required to detect single molecules of differing sizes. For example, if two particles with arbitrary sizes 0.1 and 0.01 were imaged with an interferometric setup, there would be a $10^3$-fold difference in detected intensity. If the same two particles were imaged via detection of purely scattered signal, there would be a $10^6$-fold difference in detected intensity.

The first example of this method was demonstrated in 1964 and was named interference reflection microscopy (IRM) (Curtis, 1964). Initially being used to study the adhesion of

cells to surface, the image in this technique is formed from the interference of the scattered light from the sample, and the reflected light from the glass-water interface of the coverslip. This leads to an image in which the sample appears as a dark shape on a bright background – dependent on its distance from the surface of the coverslip. Notably this technique has been utilised in the study of microtubules on the Single-Molecule level and is able to obtain an incredibly high signal-to-noise ratio for nanometre scale particles (Mahamdeh *et al.*, 2018). Its relatively simple implementation also makes it an attractive option for use in light-scattering based Single-Molecule microscopy. However, the achievable resolution for IRM remains limited (Mahamdeh et al., 2018) – to truly achieve Single-Molecule sensitivity using light-scattering further developments needed to be made, culminating in the development of interferometric scattering microscopy (iSCAT).

## Interferometric Scattering Microscopy

The concepts and ideas that underlie iSCAT have been in use for a long time, however the term interferometric scattering microscopy was first used in 2009, in a study tracking the movement of viral particles on a lipid bilayer membrane (Kukura *et al.*, 2009), with foundational work using super-continuum white light and confocal illumination setups being implemented earlier for the detection of single gold nanoparticles (Lindfors *et al.*, 2004; Jacobsen *et al.*, 2006). Major improvements including the introduction of a widefield illumination scheme, the addition of acousto-optic deflectors to scan the beam over the sample at kHz rates, and highly stable laser illumination allowed for shot-noise limited imaging of nano-scale particles. Using this illumination scheme the signal-to-noise for an interferometric signal (S), scales with $N^{1/2}$, where N is the number of detected photons. This means that the obtainable resolution can theoretically be continually improved (albeit not linearly) by increasing the incident light intensity, or exposure time (Kukura et al., 2009; Ortega-Arroyo & Kukura, 2012).

The first major challenge that presents itself arises from the instability that is inherent to the majority of commercial lasers, intensity fluctuations and imperfect wavefronts lead to interference fringes and unwanted background limiting the achievable resolution, alongside speckle introduced by the long coherence lengths of lasers. The most common illumination setups for iSCAT microscopy can be separated into two broad categories, wide-field illumination, and beam-scanning illumination. Both of these setups are widely used, and each have their own advantages and disadvantages. Wide-field illumination allows for a larger field of view, high temporal resolution and parallel sensing of Single-Molecules – however, it introduces the need for a high-quality laser wavefront, as any inhomogeneities will lead to deterioration of the observable signal to noise ratio (Piliarik and Sandoghdar, 2014b; Gemeinhardt *et al.*, 2018). The alternative is to use acousto-optic deflectors to achieve high-speed beam scanning across the sample, removing the requirement for high-quality wavefronts but greatly increases the experimental complexity, and limiting the achievable temporal resolution (Kukura et al., 2009).

The second challenge that presents itself is that of the background caused by reflections from the rough surface of the coverslip, the background fluctuations of which can easily obscure the contrast produced by the sample. However, in the case of background contributions that are independent of the sample, these can be removed through the subtraction of median image produced whilst the sample is translated laterally (Kukura et al., 2009). This isolates the background from features in the sample, allowing for a simple subtraction from all future images. Secondly a more powerful technique relies on the inherently dynamic nature of biological systems and can be implemented whenever a particle of interest within the sample is under constant motion. A differential image can be produced, eliminating static features of the sample from the final image – this is most commonly achieved using a rolling window method in which two batches of consecutive images are averaged, and subsequently subtracted from each other (Fig. 4). This isolates only features which have changed between the frame batches. Whilst these methods are

the most common techniques for background subtraction, new methods have been developed for background removal using iterative-estimation algorithms to isolate dynamic features within an image (Cheng and Hsieh, 2017).
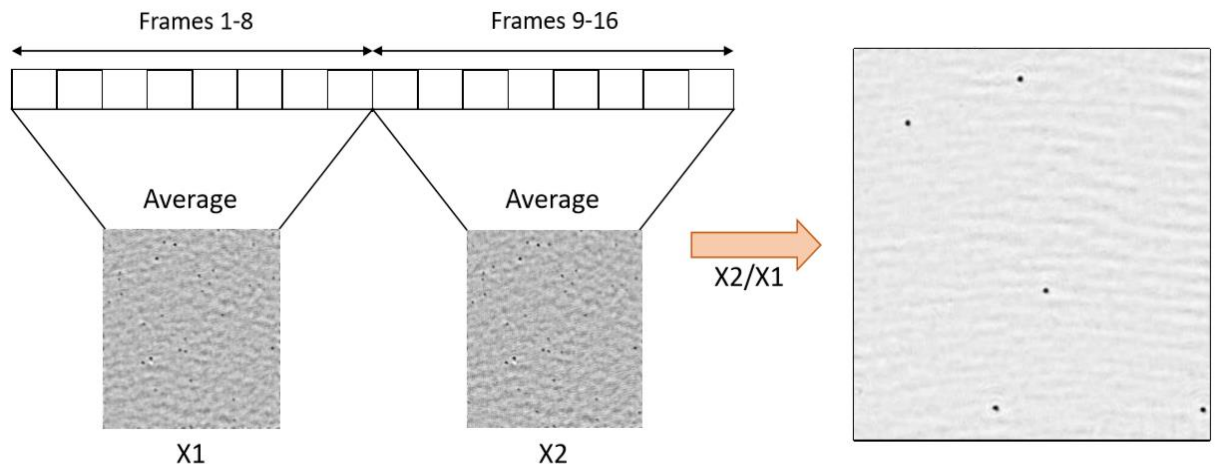


*Figure 4 - Differential Imaging of 40 nm gold nanoparticles*

Differential imaging is commonly achieved through the use of a sliding window process, in which 2 sequential batches of frames are averaged – producing the two static images X1 and X2. These images contain all the static features that are present in the sequential batches of frames, and division of X2 by X1 reveals the dynamic features within the sample that have changed between X1 and X2. In this case 40 nm gold nanoparticles were seen binding to the surface, with the particles in the differential image being particles that landed between frames 8 and 9.

## Increasing iSCAT contrast through reference wave attenuation

A recent development in improving the sensitivity of iSCAT was first demonstrated in 2017 by the Van Hulst (Liebel, Hugall and Van Hulst, 2017) and Kukura (Cole *et al.*, 2017) groups, and characterised further by the Piliarik (Jurdova *et al.*, 2019) group. The method involves the selective attenuation of the reference wave, the effect of which can be easily observed in equations 9 and 10, effectively enhancing the contrast of weaker scatterers. This can be achieved due to the spatial separation of reflected and scattered components that are collected by the objective – this separation occurs as light scattered from a particle near the glass-water interface will primarily be concentrated towards the critical angle, emerging from the objective concentrated towards the edge of the numerical

aperture. Therefore, the use of a partial reflector (glass window coated with a thin layer of reflective metal) can specifically attenuate only the reflected light – with little loss in the photons originating from the scattering particle. It should be noted that whilst this technique does improve the achievable iSCAT contrast for Single-Molecules, it does not improve the signal-to-noise ratio for shot noise limited imaging due to the reduction in photon flux caused by attenuation of the reflected light.

### A lower coherence length illumination source improves iSCAT imaging

iSCAT has the fundamental requirement for the coherence length (the distance over which a wave maintains specified level of coherency) of the illuminating source to be longer than the distance between the interface and the scatterers in the sample. Whilst the use of diode-pumped solid state (DPSS) or He-Ne lasers would provide a much cleaner beam profile, their longer coherence lengths would lead to the interference of any back reflections from optics within the system – creating additional, unnecessary imaging noise. Because of this the use of standard diode lasers is commonplace in iSCAT systems, their shorter coherence length means interference of back reflections is limited to the sample region, and some of the objective optics. To overcome the limitations created by the lower quality wavefront the illumination source can either be spatially filtered via coupling to a single mode fibre or focusing it through a pinhole. Both result in a speckle-free beam with a higher quality Gaussian profile, reducing the presence of interference fringes in the final image.

### Wide-Field vs Beam Scanning Illumination Pathways

Whilst the initial implementation of iSCAT involved the use of confocal scanning of the sample over a focused beam, however this setup greatly limits the achievable temporal resolution and is prone to noise from laser intensity fluctuations and mode-switching. To circumvent these problems two illumination schemes have become popular: a wide-field detection setup, and a high-speed beam scanning setup (Fig. 5). The wide-field

illumination scheme involves using Köhler illumination to evenly illuminate the sample, with the incident beam being focused into the back focal plane of the objective, resulting in a collimated beam illuminating the sample. This allows for incredibly high temporal resolutions; however, it is prone to laser speckle and interference patterns caused by an imperfect wavefront. These issues are largely tackled using either spatial filtering via a pinhole or coupling to an optical fibre – with both methods producing a speckle-free Gaussian beam (Thyagarajan and Ghatak, 1981). The second method which is commonly utilised is high-speed beam-scanning using acousto-optic deflectors. This setup involves raster scanning a tightly focused beam over the desired illumination area (>10 $\mu m^2$) multiple times during a single camera exposure (scanning rate usually exceeds 10 kHz). This method removes the requirement for high-quality laser wavefronts which is imposed using wide-field illumination. However, the achievable temporal resolution is limited by the rate at which the acousto-optic deflectors can scan the beam, alongside the increase in experimental complexity that arises from the use of acousto-optic deflectors in the illumination pathway. Both methods have been widely used and can achieve Single-Molecule detection with a resolution in the 20-30 kDa range (Liebel et al., 2017; Piliarik & Sandoghdar, 2014b; Young et al., 2018).
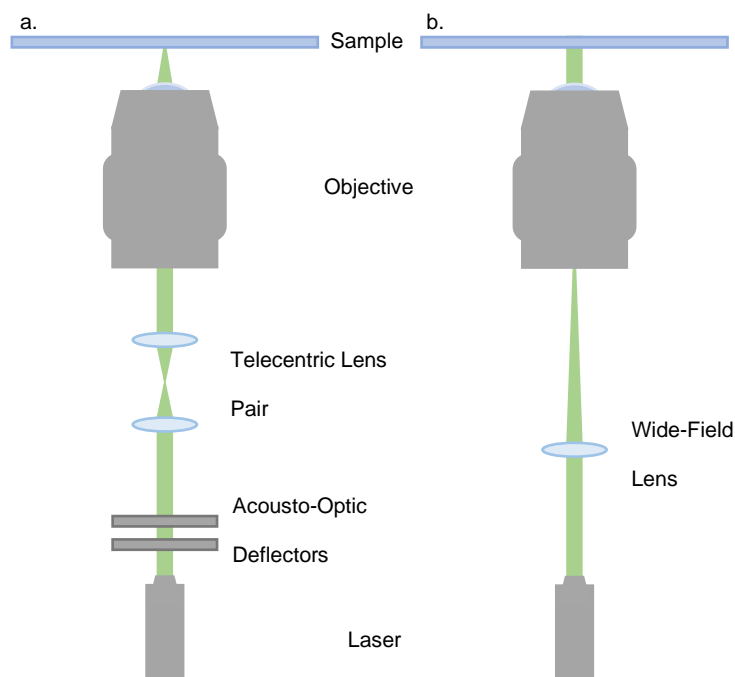
*Figure 5 - Wide-Field vs Beam Scanning Illumination Pathways*

The two most common illumination setups to achieve iSCAT imaging are the (a.) beam scanning, and (b) wide-field approaches. Beam scanning involves the use of acousto-optic deflectors to scan the laser over a 10 μm$^2$ area at kHz rates. The scanned beam passes through a telecentric lens pair and is collimated as it enters the objective. This produces a tightly focused beam illuminating a small spot on the sample. In contrast wide-field illumination uses Köhler illumination, in which the laser is focused into the back focal plane (BFP) of the objective, this results in a collimated beam emerging from the objective providing even illumination over a wider area of the sample.

## Single-Particle Tracking

Whilst fluorescence and scattering-based microscopies provides us with the tools to visualise biomolecules of interest, allowing us to gain a greater understanding of their size, stoichiometry, and conformation – these techniques alone do not allow for the tracking of dynamic processes. To account for this a number of single-particle tracking (SPT) methodologies have been developed. These techniques are used to track dynamic processes of any single particle, and in their simplest form these processes allow for 2D-tracking of particles of interest on a frame-to-frame basis, often with a spatial resolution higher than that of the diffraction limit (Yildiz *et al.*, 2003; Lowe *et al.*, 2010).

The first demonstration of SPT was in the 1980's with the development of 'Nanovid Microscopy', which made use of 40 nm gold nanoparticles injected into the cytoplasm of live PTK-2 cells. These nanoparticles were imaged using DIC, with their spatial positions then being calculated down to a nanometre level (Geerts *et al.*, 1987; De Brabander *et al.*, 1988). The most common particles used in early SPT experiments were largely polystyrene, latex, or silica beads – for example, in the tracking of kinesin-coated beads stepping along microtubules, with a precision of 1-2 nm (J Gelles, Schnapp and Sheetz, 1988). Due to the increase in sensitivity of optical setups it is now possible localise fluorescent tags, gold-nanoparticles and even unlabelled proteins with nanometre to sub-nanometre precision (Andrecka *et al.*, 2016; Ando *et al.*, 2018).

As previously described, imaging a sub-diffraction sized particle will produce an optical response known as a PSF, centred on the particle's true location. Whilst the FWHM is usually on the order of a few hundred nanometres, as defined by the diffraction limit ($\lambda$/2NA), the PSF can be accurately estimated using a 2D-Gaussian function (Schmidt *et al.*, 1996; Thompson, Larson and Webb, 2002). This allows for precise determination of the PSF's centre of mass, which describes position of the particle with a resolution greater than that set by the diffraction limit for the system. It should also be noted that whilst algorithms have been developed to resolve particles with overlapping PSFs (Huang *et al.*, 2011; Manzo *et al.*, 2014), the majority of experiments are primarily based on the localization of single, distinct PSFs. Repeating this process across a series of images produces a sub-diffraction trajectory for the particle (Fig. 6).

The localisation precision describes the scatter of locations that would be obtained if a particle was localised multiple times, which, in the case of Gaussian fitting (in a shot-noise limited system), can be defined as $\sigma/N^{1/2}$. Where $\sigma$ is the standard deviation of the Gaussian fit, and N is the number of photons that are detected (Thompson et al., 2002), meaning that nanometre precision can be achieved when $N > 10^4$ (Yildiz et al., 2003; Young & Kukura, 2019). Because of this iSCAT is an incredibly useful tool with regards to single particle tracking, with N being limited only by the illumination intensity, and the
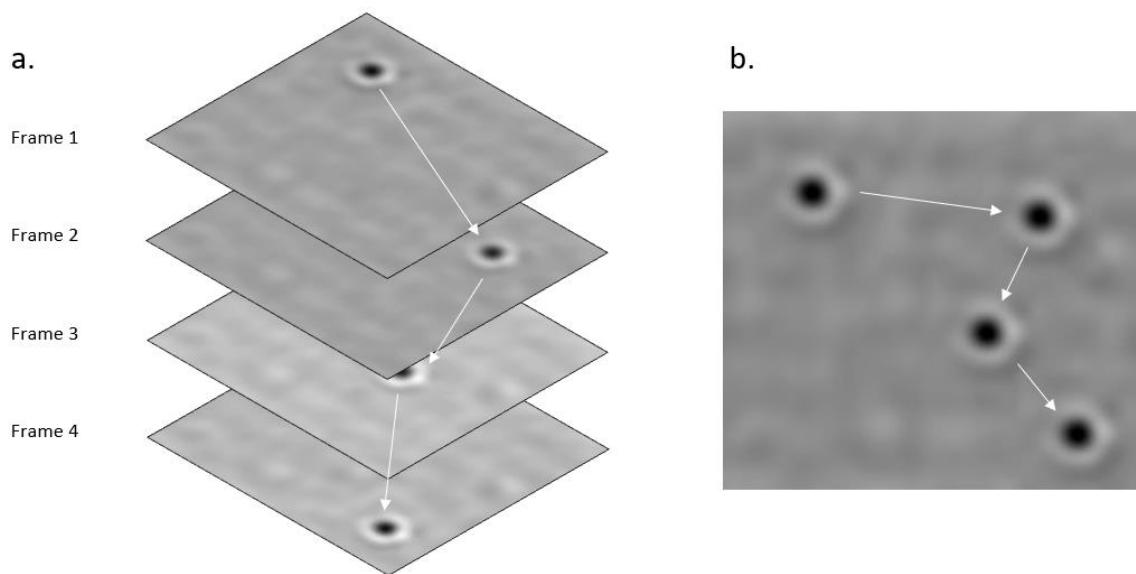


*Figure 6 - Single-Particle Tracking and Trajectory Reconstruction*

Single-particle tracking allows for a greater understanding in the dynamic processes of biological molecules, the most basic implementation of SPT involves the frame-to-frame localisation of a particles PSF using a 2D Gaussian fit to obtain its precise location (as seen in a.). This process is repeated for each frame in a stack which allows for the production of a trajectory with precision commonly within the nanometre/sub-nanometre range.

dynamic range/full well capacity of the used sensor (which is also not limited by exposure time – allowing for high-speed, and high-precision localisation).

## Applications of iSCAT

### Bacteriophages and Viral Particles

The first application of iSCAT was in the observation of the movement and orientation of single-viral particles on supported lipid bilayers (improving on previous work using a different interferometric detection system (Ewers *et al.*, 2007)) and was the first demonstration of the spatial and temporal resolutions that can be achieved using iSCAT. This study achieved a spatial resolution of 2.2 nm, and through simultaneous localisation of a conjugated Q-dot, were able to track the rotational movement of the viral particle, which allowed for visualisation of the rocking between membrane bound receptors (Kukura et al., 2009). The use of iSCAT into the study of viral particles has been greatly furthered by the work Manoharan et al. who have extensively used the technique to gain a greater understanding of various viral kinetic parameters. Initially examining the ejection of DNA from λ phages, immobilising them on the surface of a coverslip and monitoring their observable iSCAT contrast over time revealed a smooth decrease in intensity which correlated with a movement from a DNA full phage to a DNA empty phage. With this method they were able to resolve the kinetics of DNA ejection with a 4.2 kb DNA per frame resolution – providing a novel method for studying this process (Goldfain *et al.*, 2016). The same group subsequently used iSCAT to investigate the kinetics of MS2 viral capsid formation around its RNA genome. By utilising MS2 genomes linked to the surface of a coverslip they directly observed formation of the capsid by MS2 coat proteins by monitoring the observable contrast for each viral particle – allowing for measurement of the nucleation threshold, nucleation time, subcritical fluctuations, and growth time of the MS2 capsid, and further broadening the available tools for the study of viral particles (Garmann, Goldfain and Manoharan, 2019).

## Cytoskeleton

iSCAT has widely been used for the study of various components of the cytoskeleton, including both microtubules and actin-myosin systems. For example, key insights into the structural dynamics of the molecular motor, myosin 5a heavy meromyosin (HMM), have been studied in depth in both a labelled and label-free manner. Initially a 20 nm gold nanoparticle was attached to the N-terminal head of the myosin-5a head and allowed for analysis of its step size (37 nm) with nanometre resolution, 3D analysis of the movement of the free head through tracking the change in iSCAT contrast, and even small structural transitions that are characterised by a 'backstep' that occurs between myosin-5a steps (Andrecka *et al.*, 2015). This was followed by the label-free detection and tracking of HMM, which was the first demonstration of label-free detection and tracking of a single-protein using iSCAT (Ortega Arroyo *et al.*, 2014). The utilisation of differential imaging, and temporal averaging of consecutive frames allowed for a shot-noise detection limit of 60 kDa to be reached – this produced a spatial resolution of 5 nm for single HMM molecules and allowed for measurement of its 37 nm steps along actin filaments, agreeing well with previous studies. More recently iSCAT has been utilised for the label-free analysis of myosin-II binding dynamics with actin networks (Mosby *et al.*, 2020).

Alongside work into actin-myosin networks, iSCAT has proved to be a valuable tool in the investigation of kinesin-microtubule interactions, dynamics, and kinetics. Initially being demonstrated by Andrecka et al. a sub-nm resolution was achieved for unlabelled microtubules, with assembly and disassembly of microtubules being monitored with a <5 nm resolution (Andrecka *et al.*, 2016). More recently the direct observation of individual tubulin dimers binding to microtubules has been reported, making use of gold-nanoparticle labelled tubulin monomers. Allowing for direct measurement of the tubulin binding and release rates (Mickolajczyk *et al.*, 2019).

### Live Cell Imaging

The application of iSCAT to live cell imaging presents a number of problems which are not present when imaging Single-Molecules, largely dominated by the speckle like background and large interference fringes that occur due to scattering by the cell itself. However, in the face of this there have been a number of developments which have allowed for effective use of iSCAT in live cell studies. The use of gold-nanoparticles to label membrane proteins of interest within cells has been effectively demonstrated by both the Kukura (de Wit *et al.*, 2018) and Sandoghdar (Taylor *et al.*, 2019a) groups, which have allowed for nanometre spatial, and µs temporal resolutions for tracking membrane proteins. Particularly of interest is the development of 3D-iSCAT by the Sandoghdar group (Gholami Mahmoodabadi et al., 2020; Taylor et al., 2019, 2020), in which the procedural fitting and regression analysis of a particle's PSF allows for estimation of its axial position, relative to focus, with a resolution of 3 nm. This allows for an accurate 3D analysis of a membrane proteins trajectory on a live cell membrane, at a temporal resolution which greatly exceeds what has been achieved previously (Taylor et al., 2019). Interferometric imaging of type IV pili movements *Pseudomonas aeruginosa*, allowing for greater understanding into how microbes are able to interact and sense their external environment (Talà *et al.*, 2019). Another notable use of iSCAT for live cell imaging involves creating a mosaic image of a single cell, achieved by imaging a small (10 µm$^2$) field-of-view, and constantly moving the stage 5 µm between frames. Collating these images provides an incredibly detailed view of a single cell and allows for not only imaging the points of contact between the cells and the glass surface, but also the folded membrane structures of intracellular organelles (Park *et al.*, 2018).

### Mass Photometry

One of the most notable developments in the use of iSCAT is Mass Photometry, this technique, developed by the Kukura group, allows for the direct measurement of the

molecular mass of molecules using only light (Young *et al.,* 2018). This represents a breakthrough in the way in which light microscopy can be used, providing a whole new dimension to the technique. Mass photometry relies on the linear relationship between the molecular mass of a molecule, and the observable iSCAT contrast that it produces – through calibration with multiple molecules of varying mass it becomes possible to estimate the molecular weight of molecules in solution with a resolution of 19 kDa, and a precision of 1 kDa. Since its development it has been used to measure the molecular mass of nucleic acids (Yiwen, Struwe and Kukura, 2020) and membrane proteins (Olerinyova *et al.,* 2020), quantify protein-protein interactions (Soltermann *et al.,* 2020), and examine the heterogeneity of oligomeric protein complexes (Sonn-Segev *et al.,* 2020).

## 1.6 Summary

In the past decades the field of Single-Molecule biophysics has undergone a revolution, with continual progress achieved in a number of areas, producing an array of methodologies which allow for investigations into biological questions to be carried out with a level of detail and precision unseen before. Within these techniques optical-based microscopy stands out, providing tools to visualise the real-time function of individual proteins, giving further insight into their functions, dynamics, and kinetics.

Fluorescence microscopy has become a staple methodology within the field, allowing for now straightforward resolution of molecules below the theoretical diffraction limit imposed on these systems. Alongside the specificity that is conferred with the range of available fluorescent tags, it provides a powerful basis for the study of a number of biological questions. However, it is not without its challenges, largely imposed by the fundamental process of fluorescence itself, limiting the achievable photon flux and subsequently the achievable temporal resolution. Additionally, the inherent instability of fluorescent labels limits the functional acquisition times, and the labelling of proteins with fluorescent tags is

not without its own challenges, either requiring the use of bulky intermediates or non-trivial protein engineering to remove specific amino acids (e.g., cysteine).

Scattering-based microscopy provide an attractive alternative to fluorescence-based studies, allowing for high-speed investigations of protein systems, only limited by the power of the illuminating laser, alongside sub-nm spatial resolutions. These techniques also demonstrate the potential to extend these processes to unlabelled biologically relevant molecules. iSCAT in particular is a technique with a huge amount of potential to revolutionise how certain biological systems are studied – having already demonstrated its incredible sensitivity for Single-Molecule detection. However current iSCAT systems have either high experimental complexity in their setup (e.g., the use of acousto-optic deflectors and the creation of custom optical components such as partial reflectors)), or prohibitively high expenses for components such as high-speed cameras to allow for μs temporal resolution. Here we aim to outline the development of a simple, easy to implement iSCAT microscope with Single-Molecule sensitivity, μs temporal resolution, and nm spatial resolution – combined with software-based approaches to allow for accurate correction of lateral and axial drift. We will then demonstrate how these approaches can be applied to study a number of *in vitro* biological questions regarding protein-DNA interactions, highlighting the key advantages conferred through the use of iSCAT microscopy within this field.

# 2 Novel implementations of Dark-Field and Interference-Reflection Microscopy

## 2.1 Axicon-based Dark Field Microscopy for Single-Molecule Imaging

### Introduction

An axicon is a specialised type of lens with a conical surface, which converts a Gaussian laser profile to a non-diffractive Bessel-like profile (McLeod, 1954; Herman and Wiggins, 1991). The conical design of the axicon results in the incident beam deviating cylindrically towards the optical axis, this results in two well defined zones (Fig. 7). Firstly, the beam overlap region, in this area spatial interference occurs as the conically focused rays overlap – resulting in the formation of a non-diffracted Bessel-beam (Herman and Wiggins, 1991; Lei and Yao, 2004, 2008; Thériault, De Koninck and McCarthy, 2013). This interference results in the subsequent formation, and propagation of a ring-shaped beam immediately following this region. Due to these unique attributes, axicons have

previously been implemented for several applications across a number of fields, as discussed below.
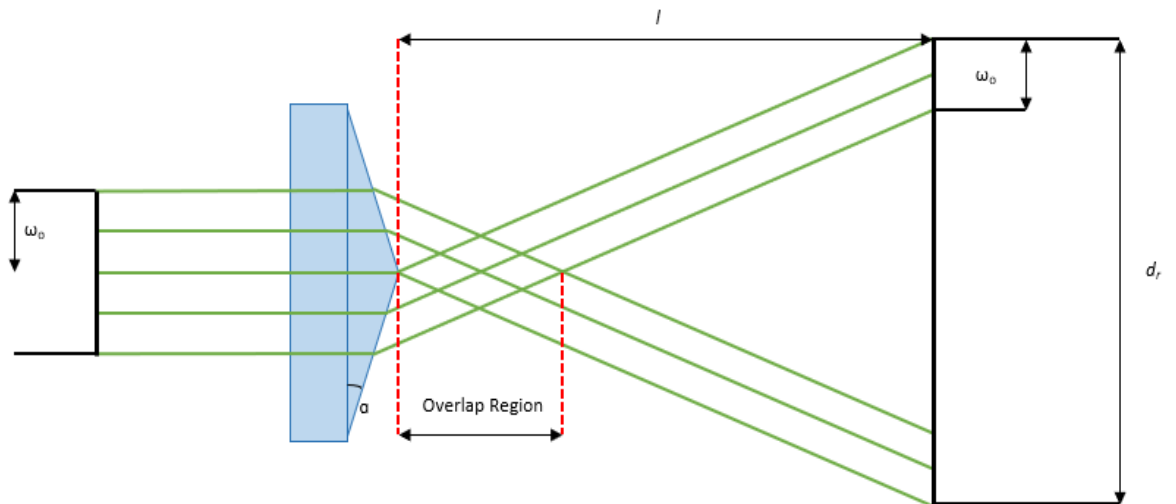


*Figure 7 - Ray tracing diagram of Bessel-beam propagation via an Axicon*

An axicon is able to create a focal line along the optical axis through interference occurring within the beam overlap region (DOF). This overlap region is known as the depth of focus (DOF), which is able to approximate a Bessel beam, which can be thought of as the interference of the conical waves formed by the axicon. This overlap region and the interference that occurs results in the propagation of a ring-shaped beam following the DOF region. This ray tracing diagram is a representation of the different paths light can take as it passes from one location to another, here each green line represents how a photon travelling along that path would move as it passes through the axicon.

The non-diffractive nature of the Bessel-like beam produced by axicons offers a key advantage for use in optical trapping (Garcés-Chávez *et al.*, 2002; Yoon and Cicuta, 2010). Optical trapping functions via the transfer of momentum from a tightly focused laser to a particle, resulting in scattering and distortion of the illuminating laser beam, the forces produced by this process trap the particle near the focal point of the beam (Ashkin, 1997; Garcés-Chávez *et al.*, 2002). Conventional use of Gaussian beams within optical trapping limits the axial range of trapping to a few µms due to the diffractive nature of the beam – this can be circumvented through the use of a non-diffractive Bessel-like beam. Additionally the reconstructive properties of Bessel-like beams allows for multiple particles to be trapped within the axial plane (Garcés-Chávez *et al.*, 2002), as portions of the beam blocked by trapped particles are able to reconstruct as the beam propagates.

Within the field of Single-Molecule imaging, a small number of implementations of dark-field microscopy have used axicons (Lei and Yao, 2008; Ando *et al.*, 2018). The key feature of the axicon which makes it well suited to dark-field microscopy is the ease through which isolation of the scattered wave can be achieved due to the ring-like beam produced as a result of the zone of spatial interference (Fig. 6). This has been applied in a number of ways, some of which involve; the use of a perforated mirror to allow for transmission of scattered light whilst removing the reflected field (Ando *et al.*, 2018), or with the axicon functioning as a dark-field condenser resulting in an oblique angle hollow beam which is not collected by the objective, isolating the scattered light (Lei and Yao, 2008). Recently this has allowed for high-precision imaging of AuNP labelled kinesin-I with a sub-nm localisation precision (Ando *et al.*, 2018).

Due to the ease of isolation of the scattered field within dark-field imaging, and the 360° illumination which can be achieved through the use of an axicon, it has provided an exciting opportunity for implementation within dark-field microscopy systems. Here we present an implementation of Dark-Field Axicon Microscopy (AXIOM), the results which can be achieved with such a system, and the benefits and drawbacks of the system design.

## Results

### Microscope Design

The collimated output of a 5 mW 535 nm standard-diode laser passes through a UV Fused Silica Axicon (ThorLabs, AX2520-A), resulting in the Gaussian-profile of the incoming beam being converted to a Bessel-like profile. The beam passes through a 2x magnification telescope, consisting of a 50 mm plano-convex NBK-7 lens (ThorLabs, L1) and a 100 mm plano-convex NBK-7 lens (ThorLabs, L2). A 3D-printed black disk with a diameter of 10 mm mounted on a piece of NBK-7 glass is mounted in the path of the beam after L1 and is placed such that the central portion of the hollow beam is blocked.

This beam is then focused by a high-NA objective (Olympus, 60x, 1.46 NA), via a 50:50 beamsplitter. This results in a tightly focused Bessel-like beam illuminating the sample. Both reflected and scattered light is recollected by the objective, passes back through the 50:50 beamsplitter and is collimated by a 200 mm plano-convex NBK-7 lens (ThorLabs, L4). The output is then focused by a 50 mm plano-convex NBK-7 lens (ThorLabs, L5) through an adjustable iris aperture, removing the reflected portion of the output signal. The scattered light is then collimated by a 150 mm plano-convex NBK-7 lens (ThorLabs, L6), resulting in a final magnification of 180x. The scattered light is imaged onto the sensor of a Basler ACE CMOS camera (Basler, acA800-510um). The system is enclosed within an optical enclosure formed from black hardboard, within internal
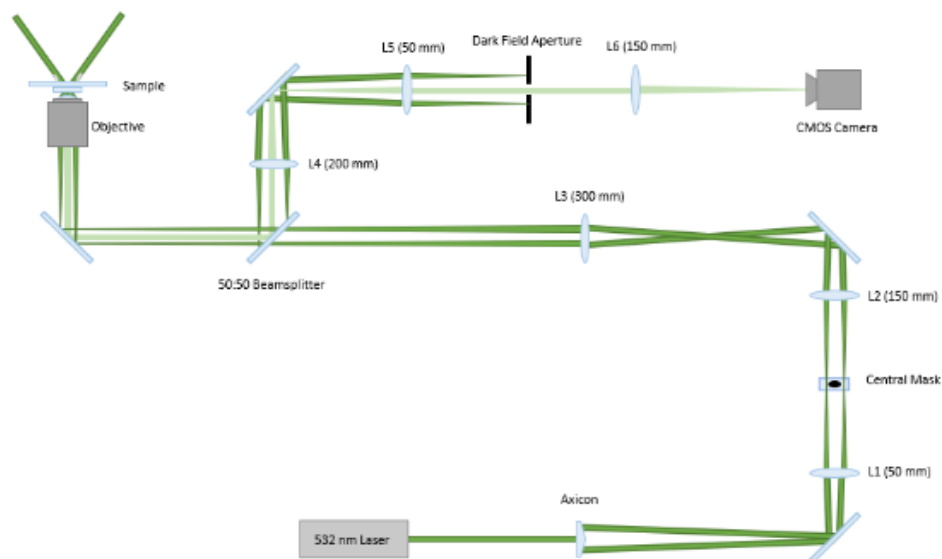


*Figure 8 - Diagram of Axicon-Based Dark-Field Microscope*

The output of a 532 nm standard-diode laser passed through an Axicon, resulting in conversion of the Gaussian-profile beam into one with a Bessel-like beam profile. This beam passes through a telescope consisting of a 50 mm lens (L1), and a 150 mm lens (L2), via the 3D-printed central mask. The beam is focused onto the back focal plane of the objective by 300 mm lens (L3), via a 50:50 beamsplitter. The scattered and reflected fields are recollected by the objective, are reflected by the 50:50 beamsplitter, and pass through a 200 mm tube lens. The scattered light is then isolated through exclusion of the reflected field, via a dark-field aperture, before being focused onto the sensor of a CMOS camera via a 150 mm lens (L6). The green line in this diagram represents the path that the laser illumination will take as it passes through the optical pathway, with expanding and contracting lines indicating focusing and expansion of the beam as it passes through the optical elements in the illumination and detection arms of the microscope.

compartmentalisation being used to mitigate the risk of thermal drift. The microscope is located in an isolated air-conditioned room.

## Central irregularities in the axion cone result in aberrant reflections and image deterioration

Clear and consistent central reflections can be seen within images from the microscope, as pictured in Fig. 9a, these dramatically reduce image quality whilst concurrently distorting signals from the sample. Previous studies modelling and measuring experimental transverse cross-sections of the ring-like beams produced by axicons have described the presence of a number of secondary rings located within the centre of the main ring produced by the axicon (Dépret, Verkerk and Hennequin, 2002), and is likely a by-product of the interference that occurs within the overlap region immediately following the cone of the axicon. This presents a major experimental challenge for dark-field
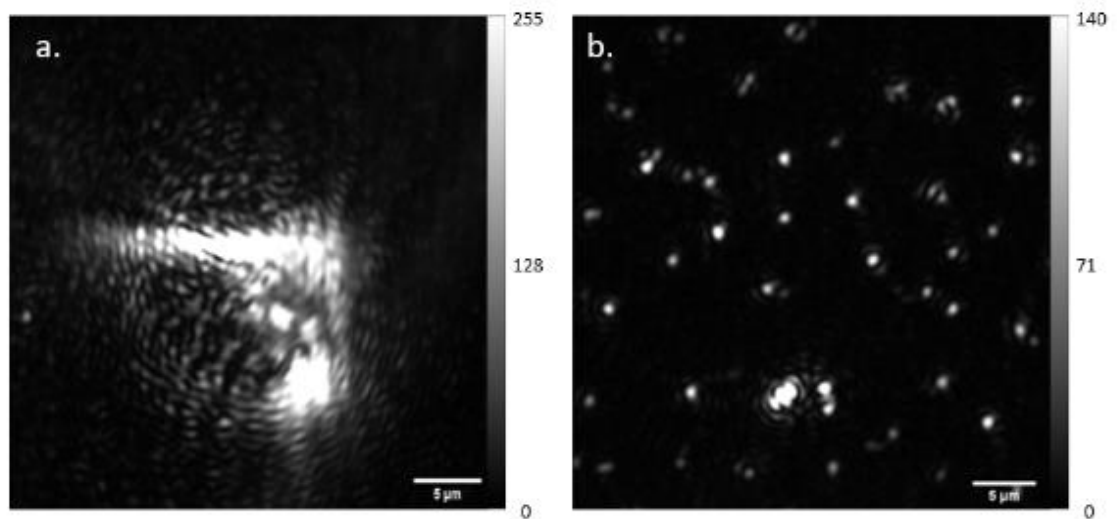


*Figure 9 - Aberrant reflections caused by imperfections in the axicon central cone can be corrected using a central mask*

Imperfections within the central cone result in aberrant reflections which cannot effectively be removed by the use of an adjustable iris aperture, as these become spatially separated from the outer Bessel-like profile and become incorporated into the final image alongside the scattered light from the sample. (a.) These reflections dramatically deteriorate the central portion of the final image, and whilst 40 nm gold nanoparticles can be observed, their PSFs become distorted and inconsistent. (b.) The use of a central mask to block these central rings and aberrations results in almost complete removal of these central reflections, resulting in dramatically reduced distortions of the sample.

microscopy, as this technique relies on the isolation of the scattered light from the core of the ring-shaped beam. The presence of these additional rings and central aberrations results in the observed reflections and distortions present in Fig. 9a.

which was used to block the central core of the illuminating ring-shaped beam after it emerges from the axicon. The 10 mm 3D printed disk was mounted on a coverslip and placed within the path of the ring-shaped beam emerging from the axicon, effectively blocking the central portion of the hollow beam, removing the secondary rings and central aberrations. Combined with the use of the adjustable iris aperture, this allowed for more effective removal of the resulting reflections from the sample. As can be seen in Fig. 9b, addition of this mask allows for dramatic reduction in the presence of central reflections and distortions from the final image.

## Axiom Imaging of Gold Nanoparticles

To assess the *in vitro* characteristics of the Axiom system, a series of images of surface-immobilised 40 nm gold nanoparticles were collected. Static images of 40 nm gold nanoparticles can be seen in Fig. 10, from which a signal-to-noise ratio was calculated using the following:

$$SNR = \frac{\mu_{signal} - \mu_{background}}{\sqrt{\sigma^2_{signal} - \sigma^2_{background}}}$$

Where $\mu_{signal}$ and $\mu_{background}$ are average signal from a 40 nm gold nanoparticle and the background respectively (both extracted from 10x10 pixel area), and $\sigma^2_{signal}$ and $\sigma^2_{background}$ are the variances of the signal and the background noise respectively (Kubitscheck *et al.*, 2000; Koyama-Honda *et al.*, 2005). From this a signal-to-noise ratio of 21.12 was achieved, with the key limiting factor being the presence of unwanted background reflections which are not adequately controlled through the use of the central beam mask. These reflections increase proportionally with the illumination intensity, limiting the

Page | 63

advantage achieved with increased photon flux from the immobilised 40 nm AuNPs. To further assess the localisation precison achievable based on 40 nm gold nanoparticles within the axiom system we used the following equation (Thompson, Larson and Webb, 2002):

$$\sigma_i = \sqrt{\frac{s^2 + a^2/12}{N} + \frac{4s^3 b^2 \sqrt{N}}{aN^2}}$$

Where $a$ is the pixel size in nm, $b$ is the standard deviation of the background, $N$ is the number of photons, and $s$ is the standard deviation of the Gaussian fit. To assess localisation precision 5000 frames were taken of a stationary 40 nm AuNP, a kymograph was produced from this image, and each slice of the kymograph was fit to a 1D Gaussian function, as given by:

$$f(x) = a * \exp\left(\frac{(x - b)^2}{2c^2}\right)$$

Where $a$ is the height of the peak, $b$ is the mean position of the peak, and $c$ is the standard deviation of the Gaussian. The standard deviation of these Gaussian fits is then used to calculate the spatial precision for the slice – the final localisation precision is calculated as the average of all measured localisation precisions. From this method we are able to extract localisation precision of 11.57±0.4 nm, demonstrating the fine spatial precision that can be achieved with temporal resolutions up to 3 kHz. It should be noted, that whilst presented method of determining localisation precision has been demonstrated to be accurate at determining the localisation precision for super-resolution probes (Thompson, Larson and Webb, 2002), the localisation precision may be limited in cases such as this where the gaussian-like shape of the PSF is distorted. An alternate experimental method for assessing the localisation precision for these systems would be to track the position of stationary two particles simultaneously, and measure the deviations in their position relative to one another on a frame-by-frame basis (J Gelles,

Schnapp and Sheetz, 1988). These deviations describe the intrinsic noise present within the system, as such the standard deviation of these deviations provides an accurate experimental measure of the localisation precision for a system (Ortega Arroyo, Cole and Kukura, 2016).
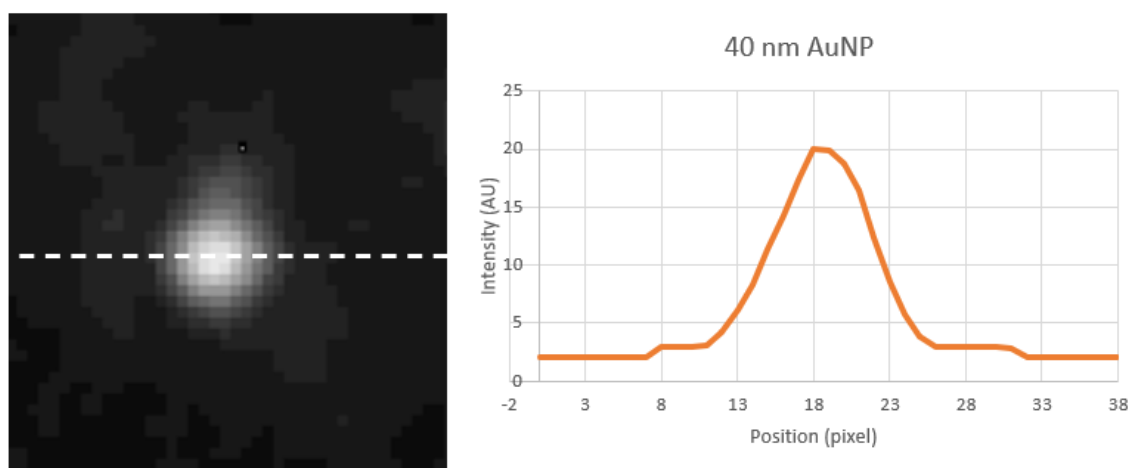


*Figure 10 - 40 nm Gold Nanoparticle image and intensity profile imaged using Axicon Dark-Field Microscopy (AXIOM)*

Use of an axicon to create spatial separation between scattered and reflected fields allows for straightforward implementation of dark-field microscopy, allowing for Single-Molecule imaging of single 40 nm gold nanoparticles with an achievable signal-to-noise ratio of 21.12, and spatial localisation precision of 11.57 ±0.4 nm.

## Discussion

The primary challenge presented through this implementation are the central rings present within axicon hollow beams (Dépret, Verkerk and Hennequin, 2002), which are a result of both unwanted curvature at the tip of the axicon, and the interference that occurs within the overlap region that immediately follows the tip of the axicon (Curry, Hwang and Wax, 2006; Lei and Yao, 2008).We have shown that these central rings can effectively be controlled using a central mask, which is mounted in such a way that the central portion of the hollow beam is blocked, dramatically improving the resulting image quality through the elimination of these unwanted reflections. Use of an axicon alongside this central mask

allows for effective imaging of single gold nanoparticles at high-frame rates, with a high level of spatial localisation precision.

## Use of an axicon permits straightforward exclusion of reflected light, and isolation of scattered light

An axicon provides an ideal methodology to allow for isolation of scattered light from reflected light that emerges from the objective, due to the resulting spatial separation between scattered and reflected fields. This has been achieved via a number of methods, here we make use of an adjustable iris aperture, however other methods such as the use of a perforated mirror to allow for transmission of scattered light whilst removing the reflected field (Ando *et al.*, 2018), or with the axicon functioning as a dark-field condenser resulting in an oblique angle hollow beam which is not collected by the objective, isolating the scattered light (Lei and Yao, 2008). Here we have presented an implementation of axicon-based dark field microscopy which could provide a powerful tool for Single-Molecule imaging, allowing for imaging of 40 nm gold-nanoparticles with high spatial resolution (11.57 nm), whilst maintaining sub-ms temporal resolution (3 kHz). This presents an ideal base for *in vitro* studies of a number of biological systems, such as high-speed imaging of DNA repair proteins on DNA, or the function of cytoskeletal components such as actin/myosin, and microtubules/kinesin. More recent work has further developed the technique demonstrated here, and highlighted its application to high-speed tracking of gold-labelled Kinesin-I, achieving a sub-nm spatial resolution using 40 nm gold nanoparticles (Ando *et al.*, 2018). Together this demonstrates the exciting potential for the use of axicon-based dark field microscopy for the study of Single-Molecule investigations.

## 2.2 Interference Reflection Microscopy using a laser-diode and rotating ground-glass diffuser

### Introduction

As previously discussed, Interference Reflection Microscopy (IRM) was first implemented in 1964 (Curtis, 1964), to study cell surface contacts. The underlying concept is like that of iSCAT microscopy, in which a reference wave (produced by light reflected by at the glass-water interface within the sample), and the light scattered by particles within the sample interfere at the camera to produce an image in which the background is bright, with dark spots corresponding to scattering particles within the sample. The primary difference between IRM and iSCAT is the illumination source, with IRM involving the use of a non-coherent light source (for example, an LED), and iSCAT using a coherent light source (e.g., laser diode).

### Coherence

Coherence is used a descriptor of the correlation between all physical properties of waves and can be split into two categories: spatial coherence, and temporal coherence. If both types of coherence are present between two waves, they can interfere. Two waves are perfectly coherent if they display identical waveforms, frequencies, and a constant phase difference (Hecht, 1998; Wolf, 2007).

Spatial coherence describes the correlation between waves at different points in space, for example if a wave has a constant amplitude value over an infinite length it is considered to be perfectly spatially coherent. Two waves with a strong spatial coherence will have a nearly fixed phase-relationship, allowing for interference to occur. Spatial coherence within lasers is an essential requirement for strong directionality.

Conversely temporal coherence describes the correlation between waves at one single point in space, but at different times – and is a measure of the time interval in which the wave resembles a sinusoidal wave (Fig. 11) . This means temporal coherence can also effectively be used as a measure of monochromatism of a light-source. Perfectly temporally coherent light sources will be monochromatic producing waves with one fixed frequency, whilst a white light source produces waves which vary greatly in frequency and amplitude – because of this they have incredibly low temporal coherence (coherence time) and are often described as incoherent.
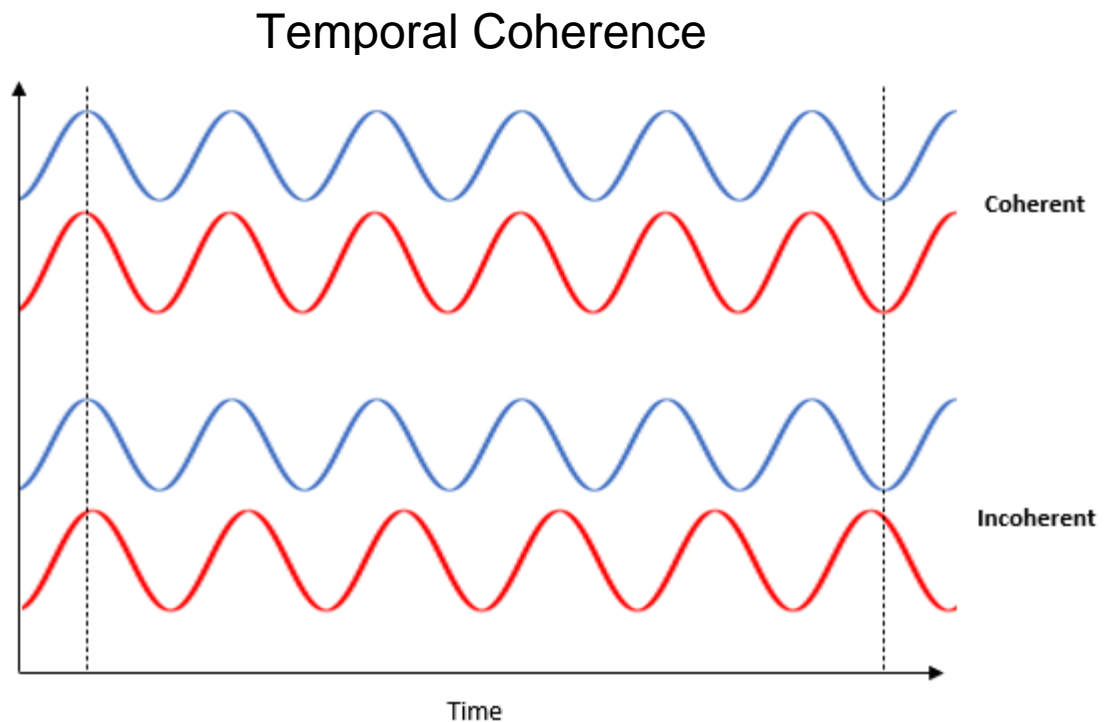


*Figure 11 - An example of Temporal Coherence*

Temporal coherence describes the correlation between waves at a single point in time, two perfectly temporally coherent waves will resemble perfectly sinusoidal waves. Temporal coherence effectively functions as a measure of monochromatism of a light source, as a perfectly temporally coherent light source will produce waves with a single fixed frequency. The temporal coherence of a light source also describes its coherence length, which is equivalent to the coherence time (the time over which a wave remains perfectly sinusoidal) multiplied by the speed of light.

The coherence length of a light source describes the distance over which a coherent wave is able to maintain a specific degree of coherence, and notably describes the degree of temporal coherence not spatial coherence. The coherence length ($L_c$) of a light source is equivalent to:

$$L_c = c\tau_c$$

Where $c$ is the speed of light, and $\tau_c$ is the coherence time of the light source. A wave with a longer coherence length more closely resembles a perfectly sinusoidal wave. Waves interfere most effectively when the paths taken by all interfering waves are shorter than their coherence length (for example, in an interferometric microscope, the distance between the sample and the detector).

The coherence length of a light source used within an interferometric system is a key consideration, as it will play a serious role in the final image that is produced. For example, lasers with long coherence lengths may detract from the achievable signal-to-noise ratio of the final image, as any small reflections within the system arms (particularly optics within the objective) will interfere at the detector – producing additional interference fringes within the image. Because of this, it is common practice to use standard-diode lasers, as opposed to higher coherence solid-state pumped laser diodes as the presence of interference fringes is dramatically reduced within the final image. Alternatively, within interferometric reflection microscopy, light sources with a coherence length that is shorter than the distance between the sample and the detector are used. This results in dramatically reduced presence of interference fringes and reflections resulting from optical elements further down the imaging and detection pathways, requiring less background removal and total post processing to produce an effective final image. The coherence length of the light source should always be a key consideration in the implementation of any interferometric system – as it will have major impacts of the functionality and final result.

Here we present the implementation of an Interference Reflection Microscope which makes use of a standard laser diode, along with a rotating ground-glass diffuser to disrupt the coherence length of the illuminating beam, allowing for imaging of gold nanoparticles with minimal post-processing whilst maintaining a spatial resolution in the nanometre range for frame rates up to 100 Hz.

## Results

### Microscope Design

The output of a 445 nm diode laser (Roithner-Lasertechnik ULV-445-300), which is modulated at 20 kHz, controlled by custom-written software on an Arduino Uno Rev3, is first focused by 200 mm a plano-convex NBK-7 lens (L1) – and is passed through a ThorLabs P50HD 50 μm pinhole filter, resulting in an output beam with a Gaussian profile. The beam is recollimated using a 100 mm plano-convex NBK-7 lens (L2) and passes through the rotating ground glass diffuser – this rotating diffuser disrupts the coherence length of the laser, dramatically reducing it. This resulting beam is focused into the back focal plane the objective (Nikon CFI Apochromat TIRF 60x Oil Immersion Objective Lens, NA 1.46) by a 200 mm plano-convex NBK-7 lens (L3). The illumination and detection pathways are separated by a 50:50 beamsplitter. The scattered and reflected fields emerging from the objective travels back through the 50:50 beamsplitter, and through a 200 mm plano-convex NBK-7 lens (L4). Finally, the light passes through a telescope constructed from a 50 mm plano-convex NBK-7 lens (L3) and a 150 mm plano-convex NBK-7 lens (L3), resulting in a final magnification of 180x. The light is then focused onto the sensor of a Flir Grasshopper USB3 CMOS camera (Point Grey Research, GS3-U3-23S6M-C). The system is enclosed within an optical enclosure formed from black hardboard, within internal compartmentalisation being used to mitigate the risk of thermal drift. The microscope is in an isolated air-conditioned room.
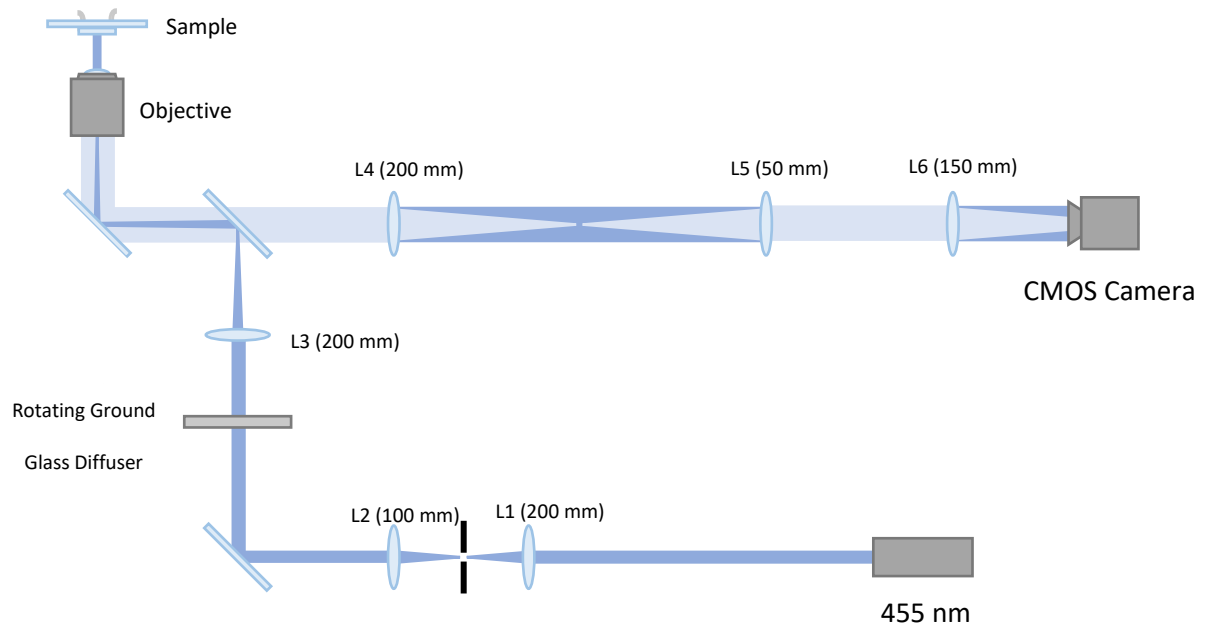
*Figure 12 - Diagram of Interference Reflection Microscope utilising a rotating ground-glass diffuser*

The output of a 455 nm standard-diode laser, modulated at 20 kHz, is focused through a 50 μm pinhole via a 200 mm focal length lens (L1), and subsequently recollimated by a 100 mm lens (L2). The beam passes through a rotating ground-glass diffuser to disrupt the coherence length of the laser. The beam is then focused into the back focal plane of the objective by a 200 mm focal length lens (L3) via a 50:50 beamsplitter which separates the illumination and detection pathways. The light emerging from the objective passes back through the 50:50 beamsplitter, and through a 200 mm tube lens (L4) before it passes through a telescope consisting of a 50 mm focal length lens (L5) and a 150 mm focal length lens (L6), which focuses the light onto the sensor of a CMOS camera.

## A Rotating Ground-Glass Diffuser disrupts the coherence of the illuminating standard diode-laser

The rotating ground-glass diffuser is used to dramatically reduce the coherence length of the illuminating standard laser-diode. The rotating ground-glass diffuser is made using a 2.8 V Stepper Motor, with a 5 mm shaft diameter – mounted on the shaft is a 3D printed adapter, which consists of a 20 mm diameter cylinder, with a length of 40 mm. The centre of the cylinder contains a 5 mm cylindrical hole with a depth of 10 mm. The adapter is glued to the shaft of the stepper motor. A ThorLabs Ø2" Unmounted N-BK7 Ground Glass

Diffuser, 220 Grit (ThorLabs, DG20-220) is mounted onto the solid end of the 3D printed adapter.

It should be noted that the position of the ground-glass diffuser on the 3D-printed adapter is key, if it is not perfectly central unwanted vibration and movement will be introduced when rotating at high-speeds – increasing the danger of the ground-glass diffuser, or 3D-printed adapter from slipping and coming free of the motor at high-speed. Great care should be taken when attaching the diffuser – and before use at high-speeds it should be thoroughly tested to ensure that no unwanted vibration is introduced upon acceleration.

The stepper motor is controlled by an Arduino Uno REV3, running a custom written script which accelerates and decelerates the motor safely. To allow the motor to run at full speed, a ramping process is needed to slowly accelerate the motor without it missing any steps. Stepper motors are brushless DC motors, with the central rotor being moved by a series of electromagnets arranged as a stator around the central rotor. The electromagnets are turned on one-by-one, with each rotating the central rotor slightly – allowing the next to continue the movement. If the electromagnets are activated too quickly there will not be enough movement of the central rotor, meaning the next electromagnet will be unable to rotate the central rotor further. To counteract this and ensure that excess torque is avoided (as this will cause steps to be missed), we linearly ramp up the speed of the stepper motor – allowing us to successfully achieve the maximum speed available for the motor.

Fig. 13a shows an image acquired from the microscope prior to starting the rotating ground-glass diffuser, when the motor is turned on and the diffuser begins to rotate the continuous reflections average out and details within the sample become clear, such as surface-immobilised 40 nm gold-nanoparticles as seen in Fig. 13b.
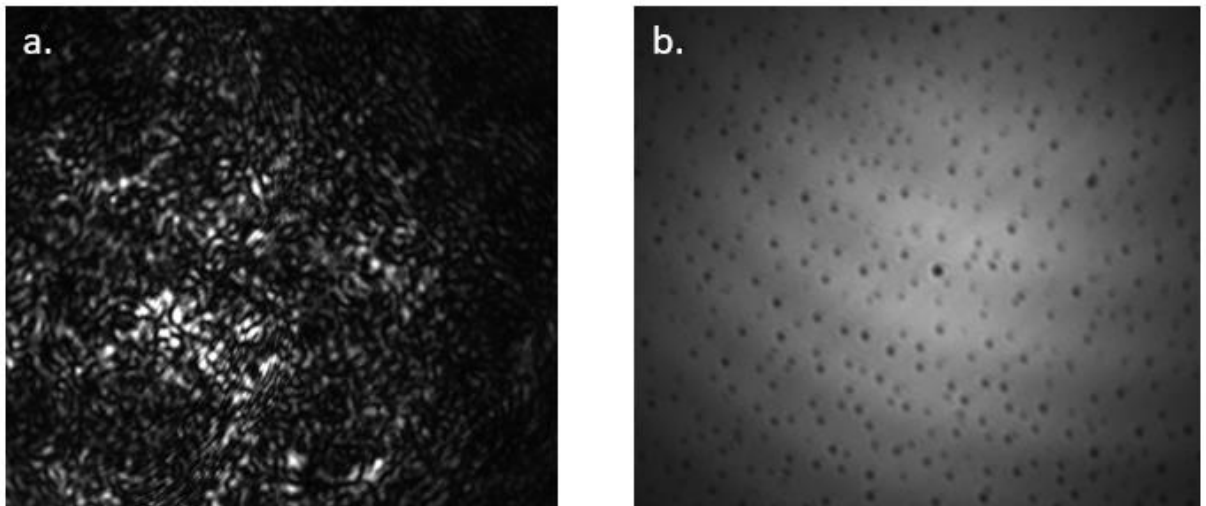


*Figure 13 - A rotating ground glass diffuser disrupts the coherence length of the illuminating laser*

Use of a ground glass diffuser in the illumination pathway leads to dramatically reduced coherence length of the illuminating laser, this reduces the coherence length of the light source to less than the distance between the sample and the detector. This produces a dramatically reduced background, revealing particles within the sample – without the requirement for flat-field correction. (a.) an image of the sample prior to use of the rotating-ground glass diffuser. (b.) the same area of sample with the ground glass diffuser rotating, the dramatic reduction in background reflections and interference can be clearly seen, allowing for 40 nm gold nanoparticles to be clearly resolved within the sample.

## Rotational speed defines the achievable temporal resolution

The most notable drawback of using the rotating ground-glass diffuser is the limit placed on the achievable temporal-resolution which arises from the speed of rotation of the ground-glass diffuser. Due to the nature of the ground-glass diffuser, a number of inhomogeneities are present on the diffuser which cause interference patterns within the final image – to avoid this the ground-glass diffuser needs to be rotate a number of times within each exposure time to ensure that these inhomogeneities are averaged out. This results in automatic flat-field correction of the interference patterns caused by areas on

the ground-glass diffuser – with the static components providing the vast majority of the signal within the final image.

This becomes a limitation when short exposure times are required, the reduction in the number of rotations occurring per exposure time results in the introduction of rotating patterns of interference into the resulting images. These greatly reduce the achievable signal-to-noise ratio for particles within the sample and cannot be corrected using flat-field processing due to their dynamic nature. This presents a serious limitation when attempting to reach frame rates exceeding 100 Hz. Examples of these interference patterns can be seen in Fig. 14. These patterns were isolated from videos recorded at 1000 fps with an exposure time of 1 ms, in which the sample remained static. A flat-field image was created using 1000 frames and used to remove the static components from the recorded video. This isolates the dynamic interference patterns that arise as a result of the combination of short exposure times, and slow rotation of the ground-glass diffuser. To avoid the introduction of these interference fringes, we limited our imaging conditions to frame rates of 100 Hz and exposure times of 10 ms.
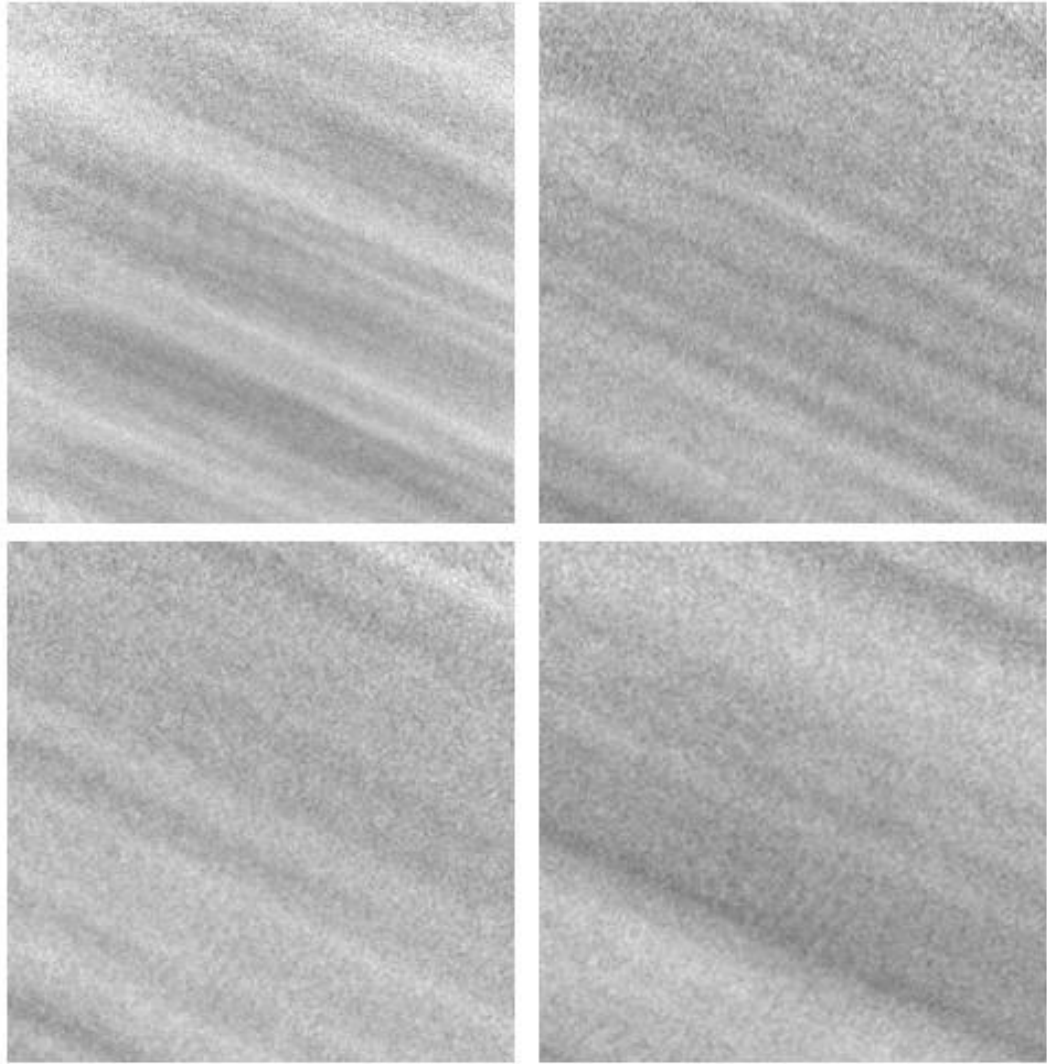
*Figure 14 - Isolated interference patterns caused by short exposure time and slow rotation of the ground-glass diffuser*

To isolate the interference patterns caused as a combination of short exposure times, and the slow rotation of the rotating ground-glass diffuser, videos were recorded at 1000 fps with an exposure time of 1 ms. Throughout the video the sample remained static, and in post-processing a stack of 100 frames was averaged to isolate the static sample. The original video was divided by this flat-field image, isolating the dynamic interference patterns which are a result of the rotating ground-glass diffuser.

## IRM using a rotating ground-glass diffuser allows for effective imaging of single gold nanoparticles

As previously discussed, gold nanoparticles are incredibly attractive contrast enhancing labels for use within scattering-based microscopy. To assess how the rotating ground-glass IRM responds to these commonly used labels, imaged surface-immobilised 40 nm gold nanoparticles, as seen in Fig. 15a. Images of 40 nm gold nanoparticles can be easily achieved with very little post-processing, at frame rates of up to 100 Hz (without introducing additional noise).
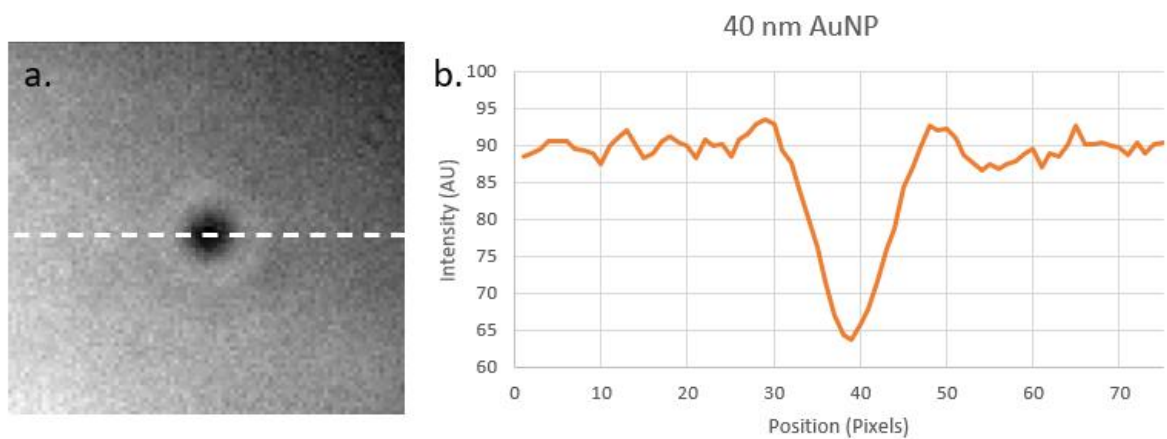


*Figure 15 - 40 nm gold nanoparticle image and intensity profile using rotating-ground glass IRM*

The implementation of IRM using a rotating ground-glass diffuser to disrupt laser coherence allows for effective imaging of single gold nanoparticles with a high signal-to-noise ratio and achievable spatial resolution.

To assess the *in vitro* characteristics of the system, a series of images of surface-immobilised 40 nm gold nanoparticles were collected. Static images of 40 nm gold nanoparticles can be seen in Fig 14, from which a signal-to-noise ratio was calculated using the following:

$$SNR = \frac{\mu_{signal} - \mu_{background}}{\sqrt{\sigma_{signal}^2 - \sigma_{background}^2}}$$

Where $\mu_{signal}$ and $\mu_{background}$ are average signal from a 40 nm gold nanoparticle and the background respectively (both extracted from 10x10 pixel area), and $\sigma^2_{signal}$ and $\sigma^2_{background}$ are the variances of the signal and the background noise respectively (Kubitscheck *et al.*, 2000; Koyama-Honda *et al.*, 2005). From this a signal-to-noise ratio of 24.52 can be extracted for 40 nm AuNPs. To assess the localisation precision of the microscope we used the following equation (Thompson, Larson and Webb, 2002):

$$\sigma_i = \sqrt{\frac{s^2 + a^2/12}{N} + \frac{4s^3 b^2 \sqrt{N}}{aN^2}}$$

Where *a* is the pixel size in nm, *b* is the standard deviation of the background, *N* is the number of photons, and *s* is the standard deviation of the Gaussian fit. To assess localisation precision 5000 frames were taken of a stationary 40 nm AuNP, a kymograph was created of the stationary AuNP, and each slice of the kymograph was fit to a 1D Gaussian function, as given by:

$$f(x) = a * \exp\left(\frac{(x - b)^2}{2c^2}\right)$$

Where *a* is the height of the peak, *b* is the mean position of the peak, and *c* is the standard deviation of the Gaussian. The standard deviation of these Gaussian fits is then used to calculate the localisation precision for the slice – the final localisation precision is calculated as the average of all measured spatial precisions. From this we extracted a final localisation precision of 9.25 ±0.02 nm for 40 nm AuNPs, imaged at a frame rate of 100 Hz with an exposure time of 10 ms.

## Discussion

### A rotating ground-glass diffuser effectively disrupts laser coherence length

The use of a rotating ground-glass diffuser effectively disrupts the coherence length of the illuminating laser, reducing it to a distance shorter than the distance between the sample and the detector resulting in dramatic reduction in background and production of an interference reflection microscopy illumination and detection pathway. Using this illumination setup, we have shown that Single-Molecule imaging of gold nanoparticles becomes an efficient and easily attainable possibility – with little requirement for post-processing to provide strong signal-to-noise characteristics and high spatial resolutions.

Previous implementations of Single-Molecule interference reflection microscopy have revolved around the use of light emitting diodes (LEDs) as an incoherent illumination source (Mahamdeh *et al.*, 2018; Simmert *et al.*, 2018). These implementations provide excellent results for imaging of larger biological macromolecules such as microtubules, allowing for accurate visualisation and analysis of microtubule polymerisation/depolymerisation whilst remaining relatively simple to implement and interpret. Here were present an alternative using a more common illumination source within a Single-Molecule microscopy setting, whilst also providing the opportunity to switch to a more sensitive imaging modality in the form of interferometric scattering microscopy (iSCAT) due to the identical imaging pathways.

### LED vs Disrupted Laser Illumination

There are a number of key differences between LED illumination, and the use of a coherence-disrupted laser diode – largely within the achievable temporal resolutions between the two implementations, and the relative simplicity of implementation.

The key drawback to the use of a rotating ground-glass diffuser within the illumination pathway is the speed of rotation which can comfortable be achieved using the stepper

motor. To ensure that no distortions are present within the image, the ground-glass diffuser needs to rotate a sufficient number of times within a single exposure time to average out inhomogeneities on the surface of the diffuser itself. If the diffuser rotates too slowly, these inhomogeneities will be incorporated into the final image, reducing the achievable signal-to-noise ratio and image quality. Using a more powerful motor with increased torque, and thus increase revolutions per minute (rpm) would allow for increased temporal resolution – but requires additional safety precautions to ensure a safe operating environment whilst operating at such high speeds. In practice, our exposure times were limited to a maximum of 10 ms, functionally limiting the frame rate to 100 fps. In contrast, LEDs do not present such issues, they allow for high temporal resolutions which are ever increasing due to the rapid developments being made within LED technology. Increasing illumination intensities continue to allow for increased frame rates and additionally, use of a fibre coupled LED removes the challenge of effectively collimating such an incoherent light source.

However, previous studies using LED-based implementations of IRM for unlabelled imaging of microtubules and gold nanoparticles limited their acquisition frame rates to 100 fps (Mahamdeh *et al.*, 2018; Mahamdeh and Howard, 2019), meaning the achievable results with this methodology match well with those previously achieved – whilst additionally matching the achievable spatial resolution of previous implementations.

## 2.3 Conclusions

We have demonstrated and characterised the novel implementation of two scattering-based Single-Molecule microscopies: Dark-Field Axicon Microscopy (AXIOM), and Disrupted Laser Diode (DLD) IRM. Both these methodologies allow for straightforward implementation of scattering-based microscopy and demonstrate a high-levels of spatial and temporal resolution, providing an attractive alternative to fluorescence microscopy.

The use of axicons within dark-field microscopy presents an interesting alternative to conventional methods (such as the use of a dark-field condenser/mismatch between excitation and detection apertures, or TIRF) and a number of clear advantages, including the ease with which the scattered light can be isolated from the reflected/transmitted light. We have demonstrated the high-level of spatial resolution that can be achieved with this setup using 40 nm gold nanoparticles, which can be maintained whilst imaging with a high temporal resolution ($3x10^3$ Hz). However, this method poses a number of additional challenges, such as the presence of central aberrations in the core of the hollow cone produced by the axicon, a result of the interference that occurs within the overlap region which immediately follows the central cone of the axicon. We have demonstrated that these aberrations can be effectively controlled through the use of a central block, which is used to eliminate these central aberrations, dramatically reducing unwanted reflected light and the distortions they introduce.

Implementation of IRM through the use of a rotating ground-glass diffuser presents an interesting alternative to conventional LED illumination which has been previously used to achieve Single-Molecule sensitivity (Mahamdeh *et al.*, 2018; Simmert *et al.*, 2018). We have described a simple method which allows for effective imaging of gold-nanoparticles, with the potential to image biological macromolecules such as microtubules. They key drawback presented is the achievable temporal resolution, which has the capacity to be expanded through the use of more powerful stepper motors, but not without the introduction of additional complexities and challenges – but achieves comparable results to previous LED-based implementations of IRM.

Whilst both these imaging modalities provide a number of notable advantages (for example, ease of implementation and high-level of spatial resolution), they are do impose certain limitations on the achievable results. To achieve an even higher level of spatial and temporal resolution, with the potential for unlabelled detection of Single-Molecules, a

movement to an iSCAT based approach presents a number of exciting possibilities which would be hugely beneficial in the study of protein-DNA interactions.

# 3 Interferometric Scattering Microscopy and software-based 3-axis active stabilisation

## 3.1 Introduction

iSCAT microscopy has been demonstrated to be an incredibly effective tool for studying a wide range of biological questions, ranging from cytoskeletal dynamics (Andrecka *et al.*, 2015; Mickolajczyk *et al.*, 2019; Mosby *et al.*, 2020), to the diffusion of membrane proteins within live cells (Taylor *et al.*, 2019b). However, implementing an iSCAT microscope which is able to achieve the high-level of experimental stability to allow for high-speed imaging and detection of unlabelled proteins presents a major experimental challenge. To aid in this, we have developed an iSCAT microscope which allows for high-speed imaging of proteins, with high spatial precision. This system was also designed to be easy to implement, providing an accessible iSCAT microscope which can be built by those with limited experience in the construction of optical systems. This implementation includes an optical pathway containing minimal components, with the option to add a fluorescence pathway with the addition of only a dichroic mirror and imaging camera. Using only a single illumination laser in a wide-field imaging scheme, avoiding the use of additional hardware such as acousto-optic deflectors. Additionally, to complement this we have built a method which can be applied to the lateral and axial stabilisation of an iSCAT microscope in a software-based manner. Reducing experimental cost and complexity, and hopefully creating an accessible base to allow for straightforward adoption and implementation of iSCAT microscopy.

# iSCAT Microscopy and Stability

Stability is key in any interferometric scattering microscope with an ideal system running in a shot-noise limited regime. Because of this any vibration or drift in any axis will lead to deterioration of the image, reducing the achievable resolution. This is particularly important in the z-axis, where even nanometre drift will cause a change in the reference



*Figure 16 – Axial drift of a non-stabilised iSCAT microscope over 2 minutes*

To highlight the effect of axial drift on resulting iSCAT image quality, a 2-minute time series of images was taken of a clean coverslip on a non-stabilised iSCAT microscope. These images were then flat field corrected using an average of initial 100 frames. (a.) The initial flat-fielded frame and (b.) the flat-fielded frame after 2 mins shows drastically different levels of noise. The standard deviation of the background noise over the 2-minute time period can be seen in (c.).

wave (arising from the reflection of the incidence light at the glass-water interface) – this causes significant deterioration of flat-field corrected images (as seen in Fig. 16), and a gradual change will introduce significant noise to ratiometric images and can be the difference which prevents a system from reaching Single-Molecule sensitivity. There are several factors that can cause sample drift, including thermal drift, vibrational drift, mechanical instability, coverslip flex, and sample instability:

Thermal Drift**:** Temperature changes within a microscopy system can have major effects on focal position – the effect of temperature on a material is given by its thermal expansion coefficient, given by:

$$\frac{\Delta L}{L} = \alpha_L \Delta T$$

Where $\Delta L$ is the change in focal length, $L$ is the original focal length, $\alpha_L$ is the material's coefficient of thermal expansion, and $\Delta T$ is the change in temperature. Given this, a 1$^{\circ}$C change would cause a change in focal length of 355 nm for a 50 mm NBK-7 lens. This focal drift compounded across an entire system would cause serious deterioration of an iSCAT image. Thermal drift should be avoided by locating the system in an air-conditioned room with constant temperature, and by sealing and compartmentalising the system to avoid thermal currents affecting the optics. Heatsinks and cooling systems (e.g., fan, or Peltier cooling system) should be used to actively cool the camera and lasers to prevent overheating and further degradation of image quality.

Vibrational Drift: Due to the scales on which iSCAT systems function even incredibly small-scale vibrational movements can cause significant deviation in all 3-axes. Sources of vibration can arise from any number of sources, such as movement within the dark room, external building work, or even air currents against taller buildings (if the system is located above the ground floor). Isolating the system from vibration is largely done through the use of a heavy optical table – either passively isolated or actively isolated

(Rivin, 1995). The most common methods of passive isolation involve the use of a heavy breadboard style table mounted on air bags to absorb vibrational energy – or suspending the table from the ceiling using flexible cords. Active stabilisation can involve the use of piezo accelerometers to record vibration and provide an active feedback loop to counteract this motion (Kerber *et al.*, 2007).

Mechanical Instability**:** Mechanical instability primarily arises from optics which are not mounted correctly, or not sufficiently attached to the optical table. All optics should be firmly bolted to the optical table – specific care should also be taken when mounting the objective. Large, heavy-set objective mounting turrets should be used to prevent any possible slip or movement in the objective. Conversely the stage needs to be mounted in such a way to reduce any potential movement or vibration.

Coverslip Flex**:** Coverslip flex results from two primary sources, being thermal fluctuations resulting from changes in temperature within the sample, and the second being artefacts arising from a diaphragm effect which is result of fluids being forced through the flow chamber during an experiment. This may not affect experiments which do not require high-temporal resolution, however for temporal resolutions of < 1 second, it is important to control for these effects. Reducing thermal instability within the flow chamber can be controlled through the installation of an objective heater, maintaining a stable temperature across experiments. Secondly the diameter of the perfusion tubing leading into the flow cell can be reduced, doing so will limit the diaphragm effect produced when introducing fluids into the flow cell.

Whilst each of these sources of instability can tackled in passive ways, active methods have been developed to counteract sample drift, improving stability in all three axes (Carter *et al.*, 2007; McGorty, Kamiyama and Huang, 2013; Schmidt *et al.*, 2018). Most commonly within iSCAT systems is the use of an additional illumination laser with a large spectral separation from the primary imaging laser. This laser is aligned such that total

internal reflection occurs upon incidence with the coverslip – this results in an emerging beam which displaces laterally upon sample movement in the Z-axis. This movement can either be detected using a quadrant photodiode, or a secondary imaging camera – in which an active feedback loop converts the displacement into a signal which is sent to the stage allowing it to move and account for this drift. This method is highly accurate and allows for constant Z-axis stabilisation within a few nanometres (< 10 nm) (Ortega Arroyo, Cole and Kukura, 2016). However, the hardware requirements for this method may be limiting in some circumstances, requiring a secondary laser, an additional dichroic for separation of the stabilisation and iSCAT signals, and a signal-detection method (either a camera or a quadrant photodiode) - increasing experimental complexity and cost.

Alternative methods for axial stabilisation are able to provide even greater levels of stability, even achieving up to 0.1 nm precision in 3 axes (Carter *et al.*, 2007). These implementations primarily rely on back-focal plane imaging of fiducial markers and measurement of their position relative to that of the objective, from which a position can be extracted and a positive feedback loop can be used to correct the axial and lateral positions (Carter *et al.*, 2007; Schmidt *et al.*, 2018). This extreme level of axial and lateral stabilisation potentially allows for the realisation of incredibly sensitive Single-Molecule surface-based experiments, however achieving this level of sensitivity presents huge experimental complexity – requiring nanofabrication of fiducial markers, a number of additional optical and computational components, and ideal environmental conditions (Carter *et al.*, 2007).

To overcome these limitations an ideal system would involve a software based 3-axis active stabilisation system, achieving a similar level of stability whilst reducing the hardware and experimental requirements imposed by alternative approaches. To approach this problem, we have made use of a number of recent advances in our understanding of the iSCAT PSF – and the level of positional detail it describes alongside

methods to accurately measure and model experimentally derived iSCAT PSFs. This method examines the change in the structure of the PSF as the particle travels through focus but remains at a constant level relative to the interface that gives rise to the reference wave, meaning there is little to no change in the $\phi$ term in equation 9.

Here we describe the implementation of a wide-field interferometric scattering microscope, alongside software-based procedure for which would allow for accurate stabilisation of an iSCAT microscope stage in 3 axes. This method exploits the inherent positional data that is encoded within the PSF of a scattering particle in an iSCAT system to accurately measure the position of a stationary particle with an precision of 1.7 nm – allowing for continual active stabilisation which requires minimal modification to experimental procedure, and no additional optical components within the iSCAT pathway – simplifying construction and development.

## 3.2 Methods

### Microscope Design

The iSCAT microscope design is illustrated in Fig. 16 and comprises a 300 mW 445 nm diode laser (Roithner-Lasertechnik ULV-445-300) TTL modulated at 20 kHz using an Arduino Uno Rev3. Due to the elliptical nature of the output beam of the ULV-445-300, it is first focused by 200 mm a plano-convex NBK-7 lens (L1) – and is passed through a ThorLabs P50HD 50 µm pinhole filter, resulting in an output beam with a Gaussian profile and reduced fringing (to improve image quality). The beam is recollimated using a 100 mm plano-convex NBK-7 lens (L2), before being focused into the back focal plane of the objective (Nikon CFI Apochromat TIRF 60x Oil Immersion Objective Lens, NA 1.49) by a 200 mm plano-convex NBK-7 lens (L3). The beam is redirected to the objective using a 50:50 beamsplitter, providing separation between the illumination and detection pathways. The resulting reflected and scattered fields are recollected by the objective, before travelling back through the 50:50 beamsplitter, and undergo collimation by a 200 mm

plano-convex NBK-7 lens (L4). A 490 nm longpass dichroic mirror **(**ThorLabs, DMLP490R) is used to separate the scattering and fluorescence channels. The reference and scattered waves pass through a telescope constructed from a 50 mm plano-convex NBK-7 lens (L3) and a 150 mm plano-convex NBK-7 lens (L3), resulting in a final magnification of 180 x. The light is then focused onto the sensor of a Flir Grasshopper USB3 CMOS camera (Point Grey Research, GS3-U3-23S6M-C). The fluorescence channel is imaged using a Basler ACE CMOS camera (Basler, acA800-510um). The system is enclosed within an optical enclosure formed from black hardboard, within internal compartmentalisation being used to mitigate the risk of thermal drift. The system is housed within an isolated air-conditioned room.
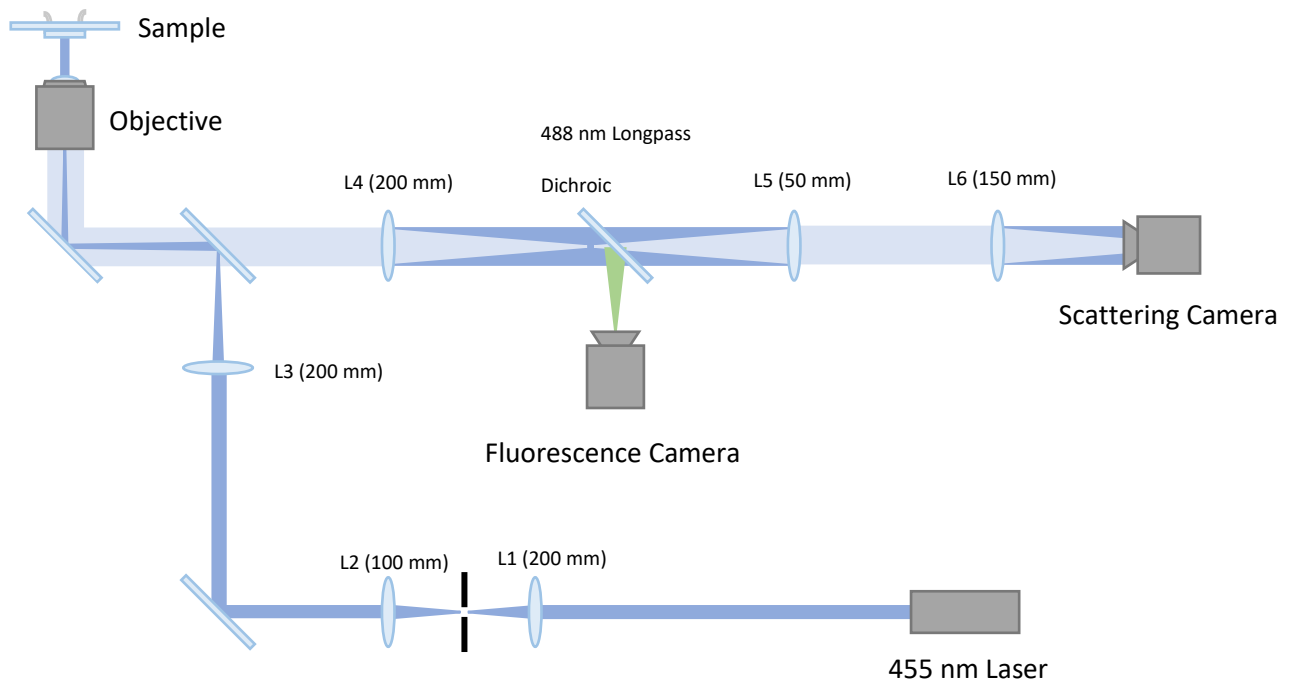


*Figure 17 - Diagram of Interferometric Scattering Microscopy with Fluorescence Channel*

The output of a 455 nm standard-diode laser, modulated at 20 kHz, is focused through a 50 µm pinhole via a 200 mm focal length lens (L1), and subsequently recollimated by a 100 mm lens (L2). The beam is then focused into the back focal plane of the objective by a 200 mm focal length lens (L3) via a 50:50 beamsplitter which separates the illumination and detection pathways. The light emerging from the objective passes back through the 50:50 beamsplitter, and through a 200 mm tube lens (L4). A 488 nm longpass dichroic mirror separates the fluorescence and scattering channels. The scattering channel passes through a telescope consisting of a 50 mm focal length lens (L5) and a 150 mm focal length lens (L6), which focuses the light onto the sensor of a CMOS camera. The fluorescence light is focused by L4 onto the sensor of a CMOS camera, via the 488 nm longpass dichroic mirror.

## Illumination power is matched to the full-well capacity of the primary imaging camera to reduce shot-noise

Output power of the illumination source is closely matched to the full-well capacity of the iSCAT pathway imaging camera (Flir Grasshopper USB3 GS3-U3-23S6M-C CMOS camera (Point Grey Research). The full-well capacity of this camera is 33 ke$^-$, meaning for saturation of the imaging area 33000 photons need to reach each individual pixel (given a gain and offset of 0). Given an illumination spot size of 20 μm$^2$, the total illumination area is given by:

$$A = \pi r^2$$

Where $A$ is the area, and $r$ is the radius of the illumination spot – resulting in a total area of 314 μm. The final pixel size after magnification at the camera is 37.5 nm, meaning the total number of pixels being illuminated is 8374, giving a requirement of 276342000 photons reaching the sensor per exposure. Given an exposure time of 1 ms, allowing a frame rate of 1000 fps, the total number of photons needing to reach the sensor per second is $2.76 \times 10^{11}$.

The energy of a photon at a given wavelength can be calculated using the photon energy equation:

$$E = \frac{hc}{\lambda}$$

Where E is photon energy, $h$ is the Planck constant, $c$ is the speed of light in a vacuum, and λ is the photons wavelength. Given this equation the energy of a single photon with a wavelength of 445 nm is 2.86 eV, meaning per second the total energy requirement is $7.9 \times 10^{11}$ eV. Converting this to Joules gives us an energy requirement of $1.27 \times 10^{-7}$ J s$^{-1}$. Given that 1 J/s is equivalent to 1 W of energy, this gives an energy requirement of 127 uW (in 1 ms). However only a fraction of this incoming light is reflected at the glass-water

interface, forming the reference wave for the iSCAT system. The reflectance of glass is given by:

$$R = \frac{(n_o - n_g)^2}{(n_o + n_g)^2}$$

Where R is the reflectance, $n_o$ is the refractive index of the medium other than glass, and $n_g$ is the refractive index of the glass. Given the refractive index of glass is 1.515, and the refractive index of water is 1.333, the reflectance at this interface is 0.004. Considering the reflectance at the glass water interface, and the 25% total transmission from the 50:50 beamsplitter, and a quantum efficiency of 72% for the imaging camera, the required output power of the illumination source is 236 mW. With the full-well capacity of the camera being 33 ke[-], and the 2x2 binning that occurs in post processing, the total number of events per pixel at the camera are 132 ke[-]. This results in a signal-to-noise, given a shot-noise limited imaging regime, of 363.16, which is further increased upon temporal-averaging theoretically allowing for detection of unlabelled Single-Molecules. Here we use a 300 mW 445 nm diode laser (Roithner-Lasertechnik ULV-445-300) to achieve the illumination intensity required to allow for shot-noise limited imaging using the Flir Grasshopper USB3 GS3-U3-23S6M-C CMOS camera (Point Grey Research). For applications utilising AuNPs, use of illuminating wavelengths between 500 nm and 550 nm may be advantageous due to the increased scattering cross-sections seen at these wavelengths as a result of plasmon resonance (Mie, 1908; Jain *et al.*, 2006).

## Lower coherence length lasers provide improved image quality

The choice of illumination source within an iSCAT system is key to its functionality and stability, for example it is possible to use incoherent light sources (such as LEDs) for iSCAT imaging – as long as the coherence length of the light source is longer than the distance between the scattering particle, and the interface which gives rise to the reference wave. Therefore, low coherence length light sources can be used when

experiments are confined to the surface of the coverslip. However, once the distance between the scattering particle and the reference wave becomes larger than the coherence length of the light source, the interferometric term within Equation 9. becomes negligible. Because of this, the most common illumination source within iSCAT systems are standard laser diodes, these diodes have relatively long coherence lengths, however they do not reach the scale of coherence length achieved with Helium-Neon lasers, or diode-pumped solid-state lasers. Whilst these lasers provide much cleaner illumination profiles, the extended coherence length leads to interference of nearly any reflection within an experimental setup – leading to unwanted speckle and noise within images. This speckle and noise would not pose an issue if it remained static throughout acquisitions, however this would require a perfectly interferometrically stable system – which in itself provides extreme experimental challenges (Jacobsen *et al.*, 2006; Piliarik and Sandoghdar, 2014a; Ortega Arroyo, Cole and Kukura, 2016).

## Laser modulation dramatically improves image quality with low coherence light sources

Modulation of the illuminating laser diode is achieved via TTL modulation, controlled by a custom written script executed via an Arduino UNO3. This custom written script can modulate the laser at the maximum permittable rate of 20kHz – this modulation rate allows for even illumination with sub millisecond exposure times. Modulation of the laser dramatically improves stability, and image quality – with considerably less degradation of the resulting image over long illumination periods, and reduced fringing and beating patterns within the iSCAT image. This is likely due to inhibition of mode-hopping during acquisition, which results in sudden jumps in the optical frequency.

Fig. 18 shows two frames taken of surface-immobilised 20 nm AuNPs, after undergoing flat field processing. Fig.18a shows an image taken whilst the laser is being modulated at 20 kHz, whilst Fig.18b shows an image taken whilst the laser is not undergoing

modulation. The differences are clear to see, the fringing pattern that appears within the unmodulated image is a result of a consistent beating pattern that occurs whilst the laser is not being modulated. This beating pattern constantly changes meaning that it cannot be accounted for within flat-field imaging/ratiometric imaging, which results in the signals being dramatically amplified, obscuring other particles within the sample.
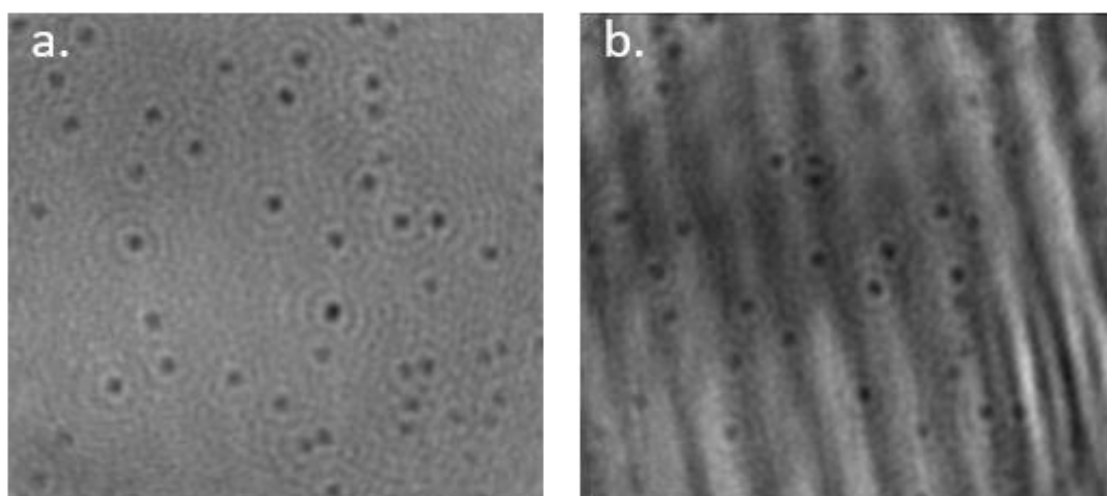


*Figure 18 - Laser-Modulation dramatically reduces noise post flat-field processing*

Single frames of surface-immobilised 20 nm AuNPs, take whilst the laser is (a.) being modulated and (b.) not being modulated. 20 kHz modulation of the laser leads to dramatically reduced noise post flat-field processing. This is due to the persistent beating pattern that is present whilst the laser is not undergoing modulation. Since these patterns are constantly changing they cannot be accounted for during flat-field processing, additionally this constant movement renders ratiometric images completely unusable – as the signal from this beating pattern is amplified and becomes significantly larger than any other signal present within the images.

## Stage Design

The flow cell is mounted on a customised recessed specimen holder – mounted on a MadCityLabs LPS200 3-axis nanopositioning stage via 4 adjustable brass spacers. The flow cell is oil coupled to the objective (Nikon CFI Apochromat TIRF 60x Oil Immersion Objective Lens, NA 1.49). The focal position of the flow cell is controlled by the MadCityLabs LPS200, allowing for precise nanometre control of X, Y and Z axes. The position of all axes is controlled via the use of a joystick, and custom-written LabView

software – with all axes being monitored and stabilised using custom-written LabView/MatLab programs. The design of the stage is key in the construction of an iSCAT system, any mechanical instability or fault in design will lead to increased noise within the system, limiting the achievable spatial resolution and removing the key advantage of iSCAT: shot noise limited imaging.

## Stage Assembly Design

The stage described here is repurposed from a previous system and is not a requirement for stable iSCAT microscopy, the key requirement is that the sample stage provides a stable base which is ideally isolated from any form of mechanical or vibrational instability. The core of the stage consists of a Mad City Labs 3-axis Nano-LPS200, which is controlled by a Mad City Labs 3-Drive Nano-Drive. The Nano-Drive is controlled via a custom-written LabView program which allows for nanometre positioning in all 3-axes using a Logitech Gamepad. A modified specimen holder is mounted on the Nano-LPS200 in a drop through-fashion, with 4 brass spacers maintaining the position of the flow-cell relative to the objective. As detailed in Fig. 19, the Nano-LPS is mounted to a backplate with 2 aluminium struts running underneath the body of the Nano-LPS. The backplate contains two 7 mm grooves, allowing for the whole structure to be mounted to a ThorLabs PT3 XYZ translation stage via 4 M6 screws. The PT3 XYZ translation stage allows for coarse adjustment of all three axes, with the X and Y adjustments being controlled by ThorLabs ZST225B Stepper Motor Actuators which themselves are driven by two ThorLabs TDC001 T-Cube DC Servo Motor Controllers, allowing for remote adjustment without physical interaction with the stage construction. All cables emerging from the stage assembly (Nano-LPS200, and ThorLabs ZST225B Stepper Motor Actuators), are attached to the side of the optical table – ensuring that no external force is applied along these cables to the stage assembly.

To provide extra stability during imaging the stage is mounted above an optical breadboard, with a central hole through which the objective is mounted. During imaging, the entire stage is lowered, with the 2 aluminium struts of the backplate resting directly on the optical breadboard. The coarse Z-axis control of the ThorLabs PT3 translation stage is used to provide downward pressure, pushing the stage assembly onto the optical breadboard, effectively coupling the stage assembly to the optical table. This process dramatically reduces the mechanical instability inherent with a free-floating stage design, allowing the passive compensation of the optical table to extend to the complete stage assembly.
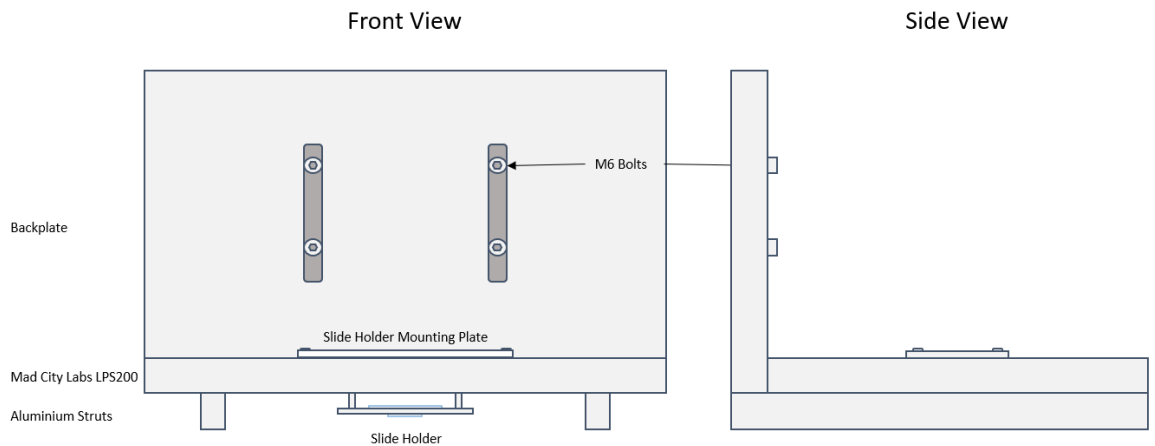


*Figure 19 - Design of the iSCAT Stage Assembly*

The iSCAT stage assembly is designed to provide a stable base, aiming to reduce noise and maintain the shot-noise limited regime of iSCAT imaging. The design consists of a backplate with two 7 mm grooves, with two aluminium struts bolted to the bottom. The Mad City Labs LPS200 rests on these two struts and is bolted to the backplate. This assembly is then attached to a ThorLabs PT3 XYZ translation stage via 4 M6 bolts. This XYZ translation block allows for coarse Z-focusing, with the X and Y adjustments being controlled by ThorLabs ZST225B Stepper Motor Actuators driven by two ThorLabs TDC001 T-Cube DC Servo Motor Controllers. This allows for coarse movement of the entire stage assembly. During imaging the Z-axis control of the PT3 XYZ translation stage is used to lower the stage assembly onto the optical breadboard below, with the aluminium struts providing a point of contact. Active pressure provided by the Z-axis coarse focus is used to couple the stage assembly to the optical breadboard below.

## Modified Specimen Holder Design

To compensate for the loss of coarse Z-axis focus resulting from the design of the stage assembly, a modified stage holder (Fig. 20) is used to allow for accurate positioning of the flow cell within the 200 µm Z-axis range of the Mad City Labs Nano-LPS200. The modified specimen holder consists of a specimen mounting plate, 4 adjustable brass spacers, and a mounting plate allowing for attachment to the Nano-LPS200. The brass spacers consist of an M2 10 mm male-to-female standoff spacer, an M2 10 mm female-to-female spacer, and an M2 nut. This construction allows for fine-adjustment of the final position of the flow-cell relative to the objective. This has the additional benefit of allowing for adjustments to ensure that the flow-cell remains parallel to the optical table during imaging, ensuring that X-Y displacements do not cause changes in the relative position of the coverslip surface in relation to the focal point of the objective – preventing unwanted noise arising from a changing background and allowing for accurate flat-field correction.
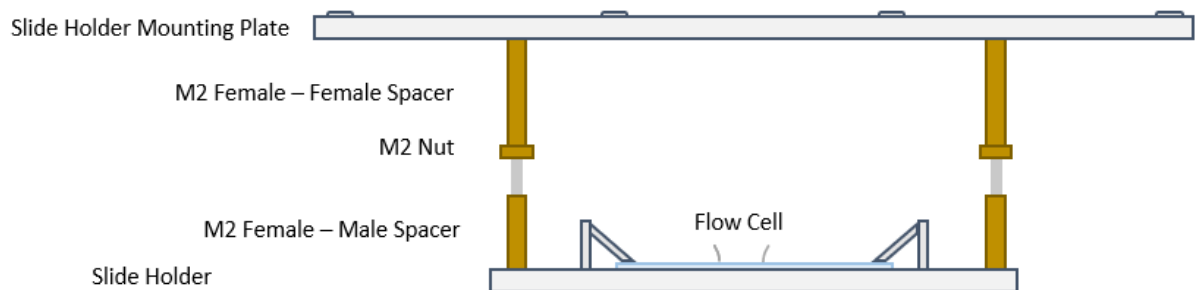


*Figure 20 - Design of the modified specimen holder*

The modified specimen holder allows for fine adjustment of the position of the flow cell once the stage assembly has been lowered onto the optical breadboard below. This is achieved through the use of 4 adjustable brass spacers, consisting of an M2 Female-Female Spacer, an M2 Nut, and an M2 Female-Male Spacer – allowing for fine adjustment of the resulting Z-axis position. This also allows for fine adjustment of the level of the flow cell, ensuring that no deviations in the X and Y axis occur upon lateral translation – which would result in the effective focal position, dramatically reducing the effectiveness of flat-field

# Image Processing

## Real-Time Image Processing

Control of the camera and all real-time image processing is carried out within a custom written LabView program, utilising LabView's NI-IMAQdx package to allow for real-time control of all camera attributes. The program is interfaced within the imaging camera via it's USB 3.0 connection to allow for high-speed data transfer. Camera attributes are controlled via the numerical entry forms on the user interface, these are then updated via LabView property nodes upon retrieval of the following frame. This provides the user full control over the functional attributes that need to be controlled during experiments, such as exposure time, frame rate, field of view, binning, acquisition frame rate, and the number of frames to be acquired. Image acquisition, real-time flat field processing, and real-time ratiometric image processing can each be carried out and controlled in real time whilst running experiments, and are achieved as follows:

### Image Acquisition

The image acquisition algorithm was designed for image acquisition at frame rates exceeding 1000 Hz, without need for additional hardware such as frame grabbers. To allow image acquisition at this frame rate the real-time processor makes use of a circular buffer - to ensure that the frame rate is not limited by the speed at which frames can be written to file. A circular buffer is a data structure, which uses a pre-defined fixed size ($n$) buffer as if one end were connected to the other. The primary advantage of using such a buffer is that frames do not have to be moved within the buffer whenever a new frame is added/remove. Two pointers are used to define the position of the writing and reading processes – new frames are read sequentially into the buffer until the maximum position of the array is reached ($n$), at which point the reading process returns to position 1 within the buffer (if this position is filled it will be overwritten with the new data). Concurrently the writing pointer is continually writing the frames to physical memory, following the same

pattern as the reading pointer – continuing till $n$ is reached, and then looping back to position 1 within the array. To further increase the speed at which this process can occur, two regions of contiguous virtual memory (with size $n$) are mapped to the physical memory in which the buffer is stored – this allows both the read and write processes to occur at the same time, further increasing the frame rate at which frames can be saved to physical memory without loss. Together, this process allows for effective image acquisition at high-frame rates (up to 4 kHz), without loss of frames, and without excessive memory usage.

*Flat-Field Processing*

The background is isolated via recording of a pre-defined number of frames ($x$), whilst the sample is being laterally translated – since the background formed from the reflected reference field remains static during this process it is effectively isolated from the sample. To limit the computational demand of this process, flat-field correction is carried out at the maximum refresh rate of the monitor being used to control the system. Since conventional monitors largely are limited to 60 Hz refresh rates, it would be unnecessary to apply flat-field correction to every frame when acquiring images at 1000 Hz – instead the frame rate is divided by the refresh rate on the monitor, and the resulting number is used to define an interval at which frames are flat-field corrected and displayed.

*Ratiometric Image Processing*

A pre-defined batch size, $R$, is used to create two sequential batches of frames (each with size $R$). The second of these frame batches is divided by the first, producing a ratiometric image, which removes all static components whilst dramatically increase the signal-to-noise ratio of dynamic components of the image. This temporal averaging also has the added effect of reducing shot-noise within the image, allowing greater detection resolution and imaging of particles which are not usually visible using flat-field correction. A similar

process is used during the real-time ratiometric image processing to reduce computational complexity, where the effective frame rate of the resulting ratiometric image is capped to the refresh rate of the monitor being used.

## Software based 3-Axis Active Stabilisation of an iSCAT Microscope

### XY Stabilisation

Stabilisation in the XY axis is achieved using a repeated 2D Gaussian fit of a stationary particle – providing a sub-pixel location, deviations from which can be used as an active feedback loop to constantly correct the position of the stage. Initial detection of the particle is achieved using a sub-pixel weighted centroid algorithm in which the centre of mass of the image is calculated using pixel intensities as weightings – this position is used as an estimate for the initial position of the stationary particle.

The particle is then fit to a 2D Gaussian function, as given by:

$$f(x,y) = A \, exp\left(-\left(\frac{(x-x_o)^2}{2\sigma^2_x} + \frac{(y-y_o)^2}{2\sigma^2_y}\right)\right)$$

Where A is the amplitude, $x_o, y_o$ is the centre of the Gaussian, $\sigma_x$ and $\sigma_y$ are the *x* and *y* intensities at these positions of the signal. As a further measure to ensure the fit is arising from the particle of interest, the $\sigma_x$ and $\sigma_y$ are used to calculate the eccentricity of the fit. The smallest of the two is taken and divided by the larger – this gives a measure of eccentricity (sphericity) of the fit, any fits with a value < 0.8 are excluded. Upon the initial fit the sub-pixel position of the particle is recorded, all subsequent fits are compared to these values. Differences in position are taken and used to correct the XY positions of the stage.

To achieve this process effectively it is ideal to use a pre-processed iSCAT image, in our case the real-time image processing is carried out during image acquisition, before the 2D-localisation algorithm. However, this can also be achieved via collection of a flat-field correction frame before starting image acquisition/localisation – this can then be applied during the localisation procedure.
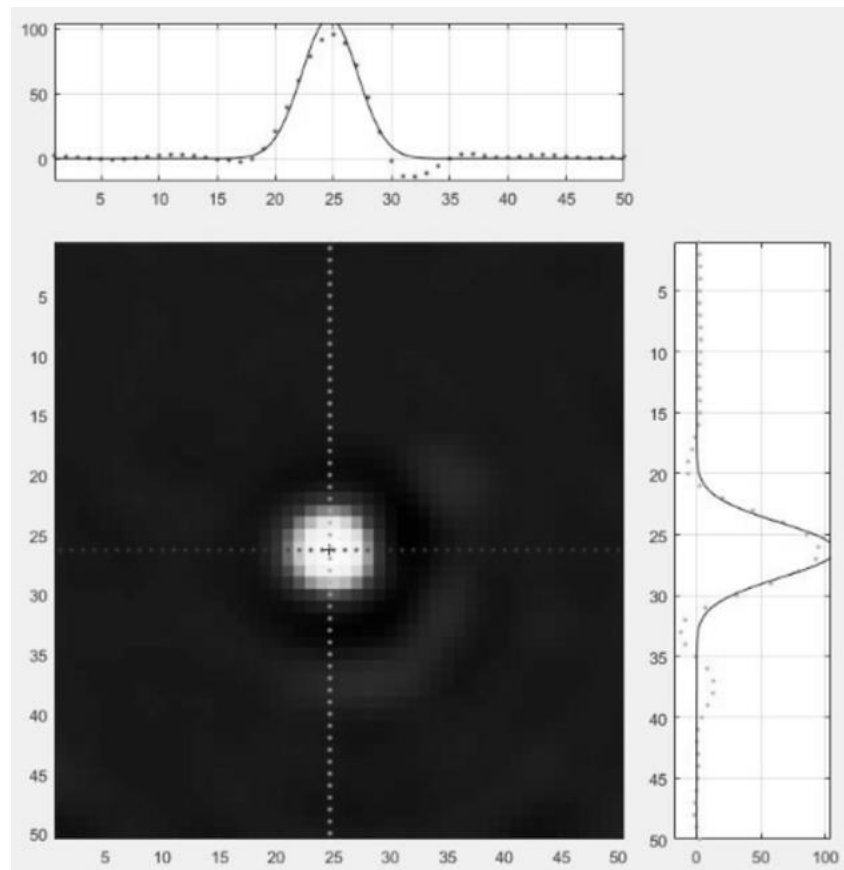


*Figure 21 - 2D Localisation of an iSCAT particle*

The 2D Gaussian of a scattering particle within an iSCAT system is demonstrated in, this 2D Gaussian fit allows for sub-pixel localisation of the scattering particle – this sub-pixel position can be used within an active feedback loop which corrects the position in relation to the original particle position. To ensure the signal is arising from a particle with a true iSCAT PSF, rather than noise, the ellipticity of the particle is estimated to ensure that the signal is arising from a particle with a spherical PSF, adding an extra layer of precision into the particle detection routine.

## PSF Estimation

The PSF of a scattering particle within an iSCAT system displays an interferometric diffraction pattern which encodes accurate positional details about the particle, understanding and decoding this pattern allows for high-precision estimation of the

position of the particle relative to the focal plane of the system (Gholami Mahmoodabadi et al., 2020).

The iSCAT PSF is characterised by a central core of oscillating contrast, surrounded by a series of rings which increase and decrease in diameter based on the particles position relative to focus and has been accurately described using a vectorial diffraction model, as previously described (Gholami Mahmoodabadi et al., 2020). Estimation and analysis of this diffraction pattern is the basis of Z-axis stabilisation within an iSCAT system.

Estimation of the experimental iSCAT PSF is achieved in a similar way to previous methods (Taylor et al., 2019a, 2020; Gholami Mahmoodabadi et al., 2020). The central position of the PSF is extracted using the methods outlined above, with the sub-pixel position returned from the 2D Gaussian fit is used as the origin for estimation. In brief, as seen in Fig 22. a radial series of 360-line profiles are taken (with 1° of separation between each), extending out from the centre of the PSF. These profiles give an estimation of the fine outer rings of the iSCAT PSF, they are averaged together to provide a single profile which describes the PSF at the current focal position. In practice, coordinates around the origin are calculated using the following:

$$x = x_o + rcos(\theta)$$

$$y = y_o + rsin(\theta)$$

Where x and y are the coordinates around the circumference of the circle, $x_o$ and $y_o$ are the central coordinates of the circle, r is the radius of the circle, and θ is the angle from the centre in radians. Using these equations profiles are calculated for all 360° around the circle, which are subsequently normalised to the maximum intensity within each profile. These profiles are then averaged together to produce an accurate profile for the iSCAT PSF at the current focal position.
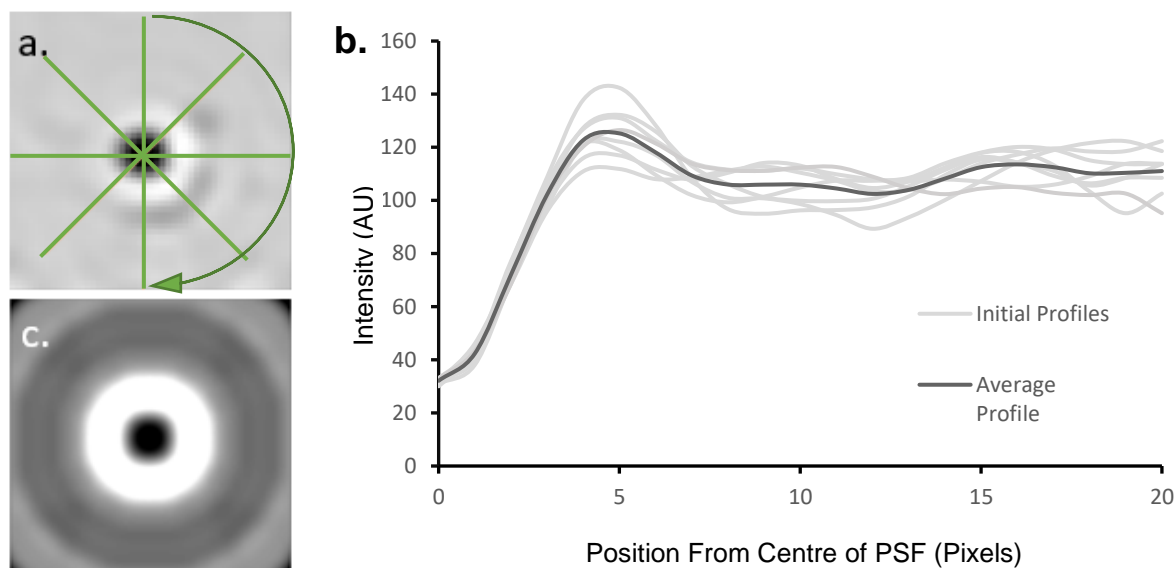
*Figure 22 - Estimation of an iSCAT PSF*

The PSF of a scattering particle in an iSCAT system can be accurately estimated (a), even without flat-field correction, by plotting a series of profiles for all 360 degrees of the PSF – the intensity profiles (b.) of each of these 360 profiles can be averaged together to produce a median profile which accurately describes the PSF and the fine outer rings of the particle. Reproducing the PSF by replotting this profile (c.) gives us a template PSF for a scattering particle at its position relative to focus. This PSF can be upscaled using cubic interpolation (c), with the resolution of the PSF being increased 4x to reveal the fine detail within the outer rings of the estimated PSF. These fine outer rings contain the accurate positional data of the estimated PSF, and with the use of a template stack can be used to accurately measure the position of the PSF relative to

## Template Z-Stack Creation

Estimation of Z-positions of experimentally derived iSCAT PSFs is achieved via fitting PSF profiles to a previously measured stack of iSCAT PSFs at 1 nm intervals – fitting the experimentally measured iSCAT PSF to this stack allows for accurate measurement of its position relative to focus.

To create the template stack, an image stack is first taken of a single 40 nm gold nanoparticle immobilised on a coverslip – the coverslip is moved in 10 nm steps from 100 nm below focus, to 100 nm above focus, with 500 frames being captured at each focal position. This video is taken and the PSF at each frame is estimated using the method described above. This provides a stack of 500 extracted PSFs for each focal position,

these are averaged together to create a template stack with one experimentally measured PSF for each 10 nm step. This stack is up-sampled 4 times in the X and Y axes, revealing the finer details of the rings surrounding the iSCAT PSF. The stack then undergoes 10x up-sampling in the Z-axis, providing an accurate estimation of the position of the rings surrounding the iSCAT PSF for 1 nm steps relative to the focal plane.

## Cubic Spline Interpolation accurately models the iSCAT PSF and surrounding diffraction rings

Cubic spline interpolation is a method which allows for accurate prediction of the sub-pixel intensities, providing a method to increase the resolution of extracted PSFs. This has previously been applied to the PSFs of fluorescent molecules, allowing for accurate super-resolution microscopy through detailed measurement of the X, Y and Z position of the 3D PSF (Babcock and Zhuang, 2017). Cubic spline interpolation involves the use of piece-wise cubic polynomials which pass through a set of control points (equivalent to pixel intensity values), as defined by a 1D function Fig. 22. A cubic spline is given in the form:

$$f_i(x) = a_i(\frac{x - t_i}{\Delta t})^3 + b_i(\frac{x - t_i}{\Delta t})^2 + c_i \left(\frac{x - t_i}{\Delta t}\right) + d_i(t_t \leq x \leq t_{i+1}, \Delta t = t_{i+1} - t_i)$$

Where $f_i$ is valid on small equal length intervals. This plots a cubic polynomial between 2 individual pixels – this function can then be used to estimate the sub-pixel values which are used for interpolation, as seen in Fig 23. Using cubic spline interpolation, it is possible to up-sample images in all 3 axes, this serves two purposes: firstly, it allows for greater detail to be resolved in the faint outer rings of the iSCAT PSF that can be used to estimate the position of the particle relative to the focal plane, and secondly it allows for estimation of the position of these rings between experimentally measured iSCAT PSFs at set positions relative to focus. With this method, PSFs are experimentally measured at 10 nm intervals relative to focus and using cubic interpolation is used to estimate the shape of the PSF outer rings for the values between.

## Cubic Interpolation
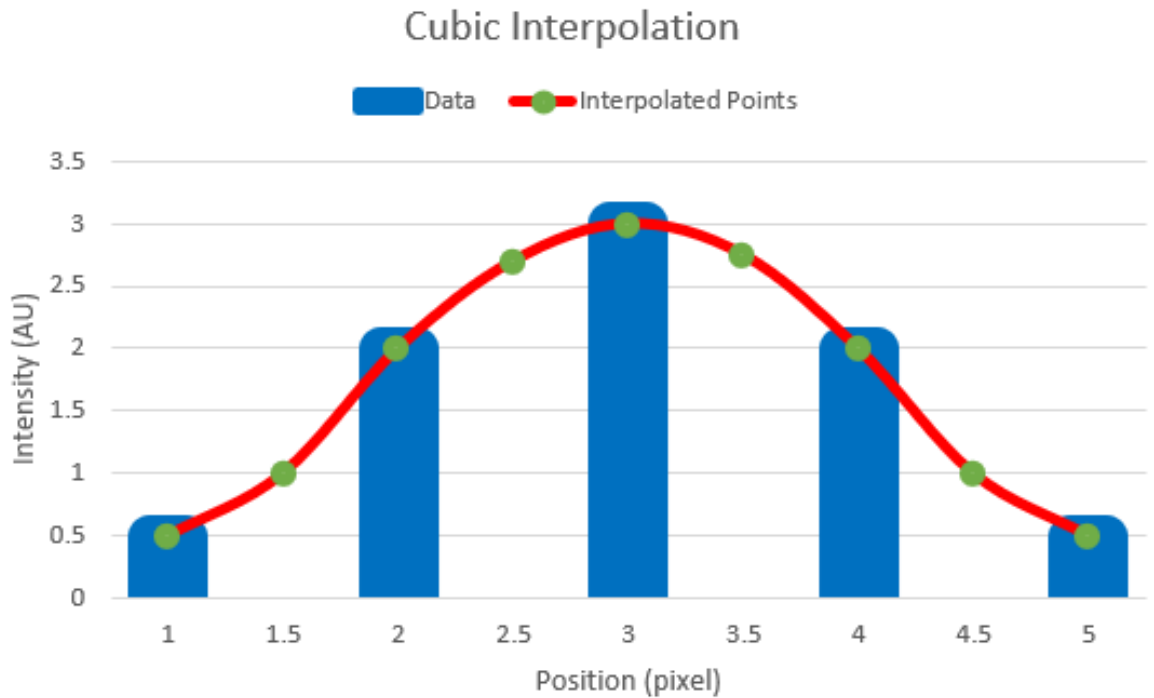
*Figure 23 - Cubic Spline Interpolation*

Cubic interpolation is a method which makes use of piece-wise polynomials to interpolate data points located between experimentally measured data points. These piece-wise polynomials pass through a set of control points (e.g. the experimentally extracted data), the resulting cubic functions can be used to estimate points at set intervals along the function. This method allows us to upscale the resolution of experimentally measured PSFs, revealing the fine outer detail of the surrounding rings – which encode the positional data of the PSF.

As seen in Fig 24**.** this method reveals finer details of the outer rings of the iSCAT PSF, allowing for the fitting of experimentally extracted PSFs. As the particle travels through the Z-axis in relation to the focal plane the rings shift in a way resembling that of an Airy Ring, with a smooth movement of interference patterns which are symmetrical both above and below the focal plane – as previously demonstrated (Gholami Mahmoodabadi *et al.*, 2020). This is due to the relative position of the particle to the interface which gives rise to the reference wave – at μm distances above this interface these interference patterns show an asymmetrical profile relative to the focal plane. Whilst this is a key consideration, when a particle is likely to travel over distances of > 100 nm, for this application the symmetry of these rings does not present an issue, as it is improbable that the system will

drift such a large distance between frames. Since this is the case, the direction of drift relative to focus can be inferred from previous positional movements. Additionally, it is key to note that during assessment of sample drift relative to the focal plane, the position of the immobilised particle in relation to the reference plane stays constant. This means that our measurement considers the change in PSF structure due to the change in relative focal position, not the change in the position of the particle relative to the reference plane.

The template stack of iSCAT PSFs produced through cubic interpolation in 3 dimensions is then used as a reference table for future fitting of experimental data, allowing for accurate measurement of the current position of the experimental PSF. Each pixel-to-pixel distance within the interpolated PSFs are described by 4 coefficients (*a, b, c,* and *d*), equivalent to the variables in the following equation:

$$y = ax^3 + bx^2 + cx + d$$
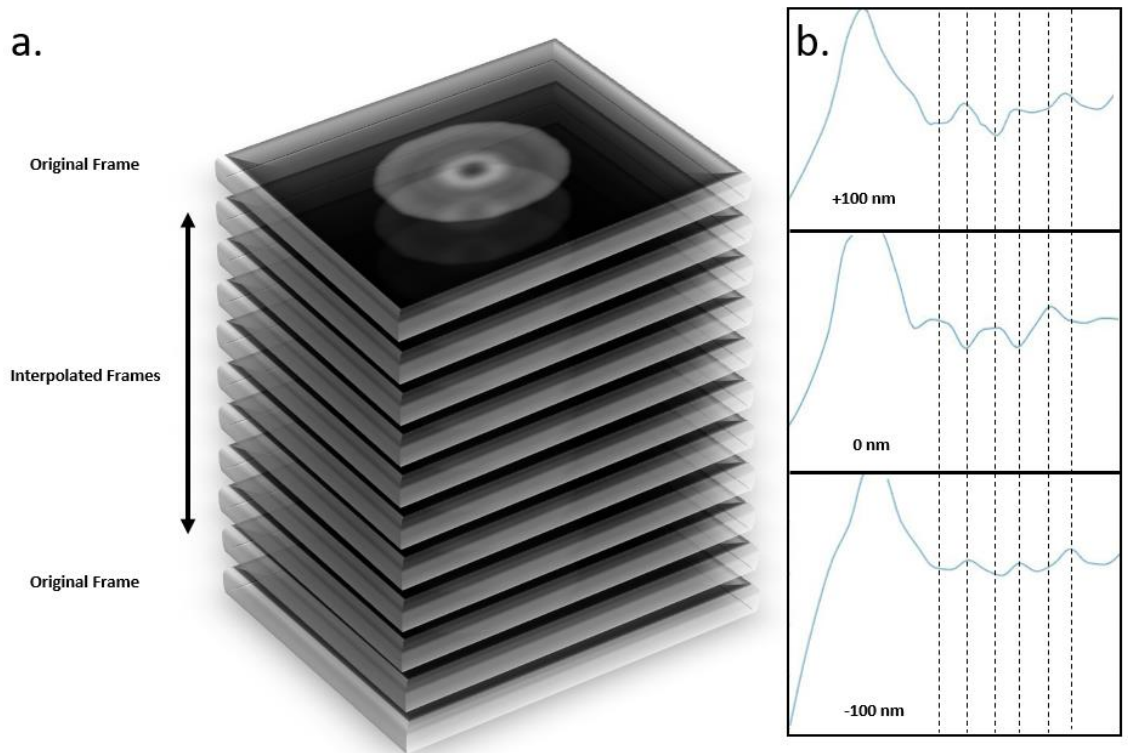
*Figure 24 - Cubic Interpolation accurately models the outer rings of iSCAT PSFs*

Cubic interpolation is used to upscale the experimentally measured PSFs 4 times in the X and Y axes, doing this increases the resolution of the experimentally measured PSFs to reveal the detail in the outer rings. Alongside this the template stack, PSFs measured from a particle at 10 nm steps relative to focus, is upscaled 10 times in the Z axis – doing this uses the cubic splines to estimate the position of the outer iSCAT rings through 1 nm steps (a). Comparison of these PSFs in the template stack reveals how the outer rings change as the particle travels relative to focus – with a smooth movement through a series of profiles which closely resemble those of the Airy rings. Since this movement is occurring close to the source of the reference wave, the movement is symmetrical, meaning as you travel through focus in the range of 100 nm these diffraction patterns repeat. This inversion of peaks is highlighted in (b.)

## Fitting extracted PSFs to the Z-Template

To assess the similarity between the extracted PSF, and template PSFs within the Z-template stack, the discrete Fréchet distance is used. The Fréchet distance is a measure of the similarity between two parametric curves, which considers the continuity of shapes within the curve (Fréchet, 1906). Given two curves, $P$ and $Q$ in a metric space, the Fréchet distance ($d_F$(P,Q)) is defined as:

$$d_f(P, Q) = \inf_{\alpha,\beta} \max_{t \in [0,1]} \{ d\left(P(\alpha(t)), Q(\beta(t))\right)\}$$

Where α and β range over all reparameterizations, d($x, y$) is the Euclidian distance between two points, and *inf* is infimum. Since there is a finite number of reparameterizations, the Fréchet distance is equivalent to the maximum distance within the reparameterization that results in the smallest distance between points P(α(t)) and Q(β(t)). It is key to note here, that the Fréchet Distance is calculated between two polygonal approximations of curves (Fig. 25).

However, since the comparison between extracted PSF and template PSF relies on the distance between pre-defined points along the curves, we instead use the discrete Fréchet distance (also known as the coupling distance) (Eiter and Mannila, 1994). The discrete Fréchet distance allows for approximation of the Fréchet distance for two arbitrary curves, as opposed to polygonal approximations of curves. This allows for accurate estimation of the discrete Fréchet distance with dramatically reduced computational complexity (on the order of *O(nm)* vs *O(nmlog$_2$(nm))*). The discrete Fréchet distance between two polygonal curves, $P$ [0,m] and $Q$ [0, n], is defined as:

$$d_f(P, Q) = \min_{\alpha:[1:m+n] \to [0:m], \beta:[1:m+n] \to [0:n]} \max_{s \in [1:m+n]} \{ d\left(P(\alpha(s)), Q(\beta(s))\right)\}$$

This method allows for the calculation of the discrete Fréchet distance in polynomial time – allowing for rapid fitting of experimentally extracted PSFs to the Z-template stack.
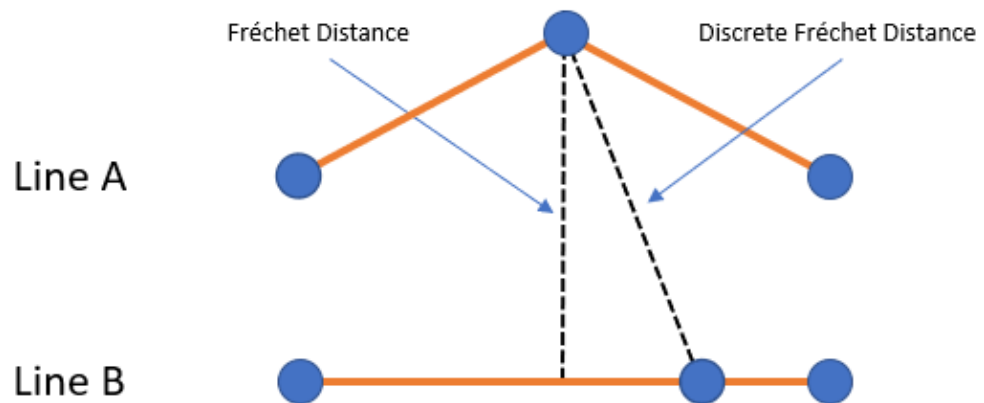
*Figure 25 - Visual Comparison of Fréchet Distance and Discrete Fréchet Distance*

Here we apply the discrete Fréchet distance to assess the similarity between the experimentally extracted PSFs, and the Z-template PSF stack – allowing for accurate assessment of the Z-axis position of a scattering particle. The discrete Fréchet distance is used due to the reduction in required computational complexity, complexity of calculating the true Fréchet distance being on the order of $O(nm\log_2(nm))$, as compared to the complexity of calculating the discrete Fréchet distance which is on the order of $O(nm)$. A visual comparison between the true Fréchet distance and the discrete Fréchet distance can be seen here, with the true Fréchet distance being calculated with polygonal approximations of lines A and B, whilst the discrete Fréchet distance only considers the distance between two arbitrary curves.

## 3.3  Results

### Axial tracking of a stationary particle

To assess the precision of the tracking of a stationary 40 nm AuNP, held at a constant axial position – videos of static 40 nm AuNPs were collected, at a frame rate of 500 fps for a total time of 10 seconds. The 2D position of these stationary nanoparticles were extracted via 2D Gaussian fit as described previously, these 2D coordinates were then used as the central point for the extraction of PSFs. The deviation of the fit from the true axial position can be seen in Fig. 26a, with a histogram of measure deviations seen in Fig.26b. The root mean square deviation (RMS) of the axial fits results in an estimation error of 1.92 nm.
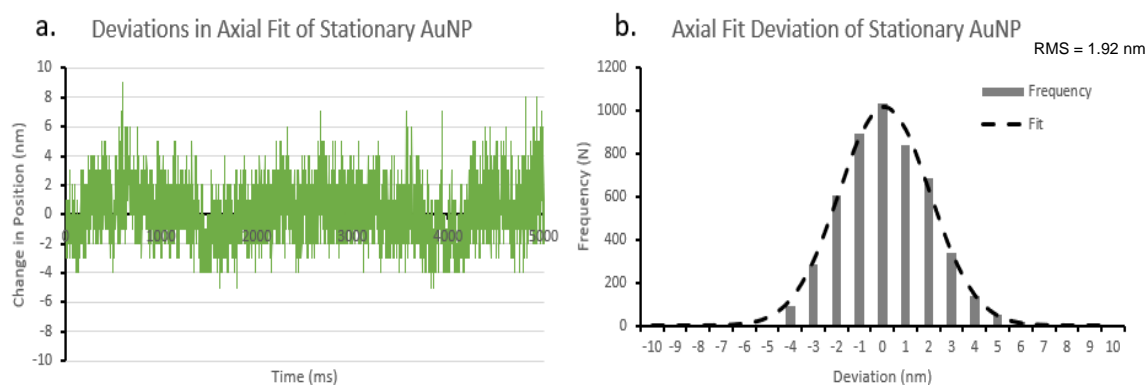
*Figure 26 - Axial tracking of a stationary particle*

Axial tracking of a stationary 40 nm AuNP, with (a.) calculated deviations from the true position over a time period of 500 ms. (b.) These deviations are compiled into a histogram, which is subsequently fit to a 1D Gaussian, which results in a standard deviation of ±1.98 nm for the deviation in axial fit for a stationary particle. Additionally, the root means square deviation (RMS) achieved was 1.92 nm, indicating the high level of axial precision that can be achieved with this approach

## Axial tracking of a dynamic particle

To assess the precision of this methodology in detecting the axial movement of a particle relative to the current focal position – videos were recorded of surface-immobilised 40 nm AuNPs being axially translated 50 nm relative to the current focal position via 10 nm steps every 500 ms. These steps are recorded at a frame rate of 1000 fps, resulting in 500 frames per focal position. The 2D position of the AuNPs were extracted using a 2D Gaussian fit as previously described, these extracted positions were then used as the central position for extraction of the experimental PSFs. The extracted focal positions can be seen in Fig. 27, it can be seen that whilst axial motion of the particle is resolved, the individual 10 nm steps cannot be clearly resolved. Some deviation would be expected as the stepping of the stage takes place over a period of ~50 ms, however would not account for the constant movement that is present in the extracted localisation trace. To assess the rate of axial displacement, the trace was fitted to a straight line, as given by:

$$y = mx + c$$

Where $m$ is the gradient, and $c$ is the point at which the line intersects the $y$ axis. This fit

reveals a gradient of 0.018, which is equivalent to a change of 0.18 nm ms$^{-1}$. This is

equivalent to a change of 18 nm s$^{-1}$, with an expected stepping rate of 20 nm s$^{-1}$. To

identify the individual steps taken by the 40 nm AuNP, a step-fitting routine previously

described by Kerssemakers et al. (Kerssemakers *et al.*, 2006; Loeff *et al.*, 2021) was

applied. The routine involves an iterative routine in which a Chi$^2$ calculation is used to

detect steps. Using a constrained fit in which a set number of steps are located, we can

see in Fig.27 that the routine isolates a series of steps with an average step size of 10.21

±2.19 nm with an average dwell time of 435 ±47.1 ms, and an R$^2$ value of 0.92 for the fit of

the steps to the extracted axial position. The root mean square error (RMSE) was

calculated to be 4.03, indicating that on average predicted step positions differ from the

extracted axial position by 4.03 nm. This suggests that whilst on average the step size

extracted (10.21 nm) is similar to that of the true step size (10 nm), there is significant

background variation present in the estimated axial positions. This may also be a
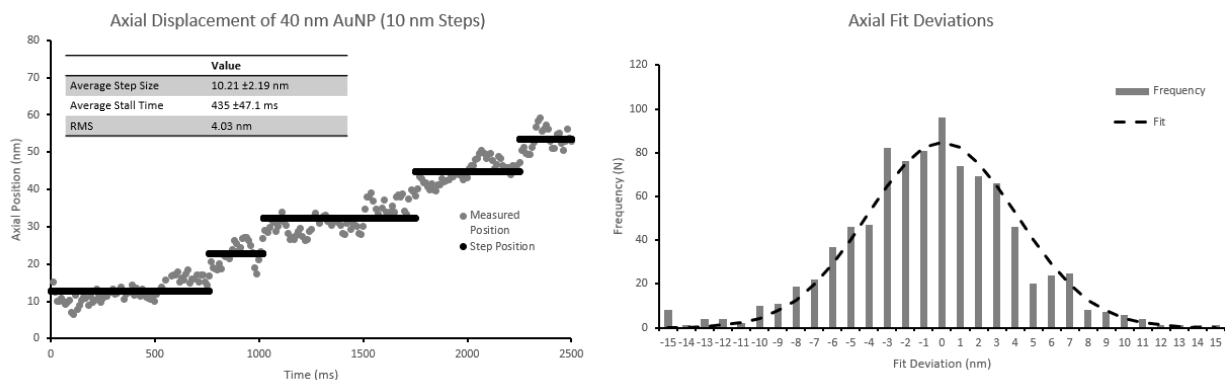


*Figure 27 - Axial tracking of a dynamic particle (10 nm Steps)*

a.) Axial tracking of a dynamic 40 nm AuNP taking 10 nm steps within the Z-axis, with (b.) calculated deviations from the true

position over a time period of 500 ms. The direct steps taken by the nanoparticle are resolve through the use of a step-finding

routine, extracting a series of steps with an average step size of 10.21 ±2.19 nm, and an average dwell time of 435 ±47.1 ms. (b.)

The deviations of the fit from the estimated step positions are compiled into a histogram, which is subsequently fit to a 1D

Gaussian. From this an RMS deviation indicates an estimation error of 4.03 nm.

contributing factor in the observed difference between the extracted average stall time (435 ±47.1 ms) and the true stall time (500 ms), and the variation noted in the range of observed stall times (250 ms to 750 ms). This suggests that the current limiting factor may lie in the background variation present in the Z-axis localisation routine

To further assess this, the above experiment was repeated with a 40 nm AuNP taking 5 nm steps through the Z-axis. As can be seen in Fig. 28, individual steps are not resolvable, however linear fit of the extracted fits reveals a gradient of 0.012 nm ms$^{-1}$, equivalent to a rate of 6.18 nm per 500 ms, compared to an expected rate of 0.01 nm ms$^{-1}$ (5 nm per 500 ms). Additionally, application of the constrained step finding routine isolates a series of steps with an average step size of 5.54 ±1.77 nm and an average dwell time of 490 ±27.89 ms. An R$^2$ value of 0.96 was calculated for the fit of the steps to the extracted axial positions, whilst the RMSE was calculated to be 2.35 nm. Once again a large amount of variation was observed in the estimated dwell times, with dwell times ranging
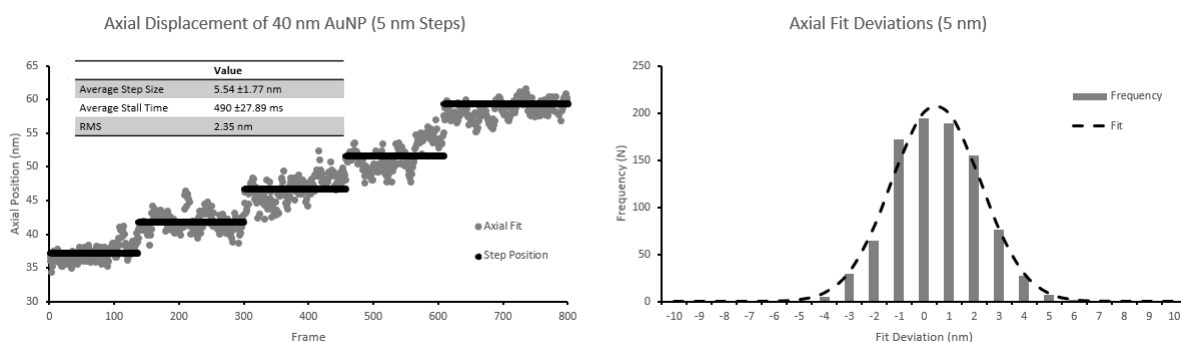


*Figure 28 - Axial tracking of a dynamic particle (5 nm Steps)*

(a.) Axial tracking of a dynamic 40 nm AuNP taking 5 nm steps within the Z-axis, with (b.) calculated deviations from the true position over a time period of 500 ms. The direct steps taken by the nanoparticle are resolve through the use of a step-finding routine, extracting a series of steps with an average step size of 5.54 ±1.77 nm, and an average dwell time of 490 ±27.89 ms. (b.) The deviations of the fit from the estimated step positions are compiled into a histogram, which is subsequently fit to a 1D Gaussian. From this an RMS deviation indicates an estimation error of 2.35 nm.

between 340 ms and 780 ms, consistent with the variation observed in the estimated dwell times for a 40 nm AuNP taking 10 nm steps through the Z-axis. Again, with the RMSE being equivalent to 47% of the expected step size, it is likely that this large

background variation in extracted axial positions limits the effectiveness of the step-finding routine.

## Increasing PSF profile size increases achievable axial resolution but increases processing time

To assess the effect of increasing the PSF profile size that is used to create the Z-template stack and the experimental PSF for axial-position assessment, multiple Z-template stacks were created with a range of PSF profile sizes (from 5-75 pixels) and used to fit images of a stationary 40 nm AuNP. As can be seen in Fig.29, continual improvements in the achievable axial position can be achieved with a continually increasing PSF profile size, with a maximum RMS deviation of 0.538 nm being achieved
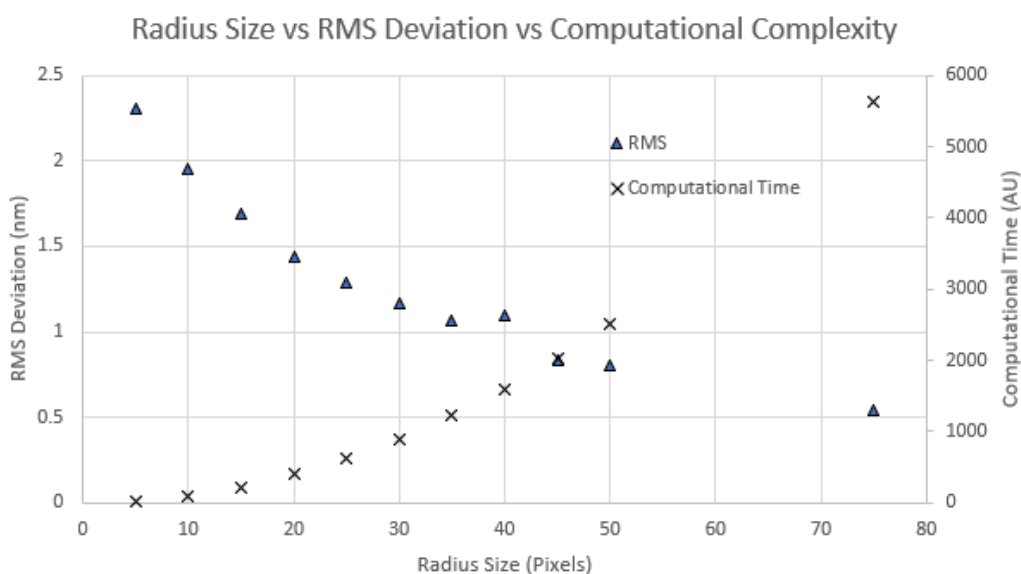


*Figure 29 - The effect of PSF profile size on achievable axial precision and processing time*

Assessment of experimental PSFs is achieved through the averaging of multiple line profiles of the immobilised particle sampled from the experimental images. The length of the PSF profile used to assess the experimental and template PSFs has a dramatic effect on the achievable axial resolution, with a maximum RMS deviation of 0.538 nm being achieved with a profile size of 75 nm. However due to the polynomial computational complexity associated with the calculation of the discrete Fréchet distance, there is a square relationship between the profile size and the required processing time. Additionally, increased profile sizes results in a requirement for increased experimental fields of view to allow for complete assessment of the experimental PSF profile.

with a profile size of 75 pixels. Minimum RMS deviation of 2.306 is achieved using a profile size of 5 nm – indicating the high-level of axial precision that can be achieved even with minimal assessment of the outer regions of the iSCAT PSF.

Due to the polynomial time complexity of the discrete Fréchet distance calculation, the time taken for processing grows with the square of the profile size in pixels. This results in a dramatic increase in processing time as profile size increases, however this is potentially offset by the improvement in achievable axial resolution that can be achieved using larger profile sizes. Modulation of the profile size used to assess the experimental PSF could be utilised to achieve either faster correction rates, or higher levels of axial resolution. Alongside the increasing processing time that is associated with increase profile sizes comes the requirement for larger fields of view being recorded, to allow for a total diameter of 2x the profile size. This increase in field of view could lead to dramatic decreases in the achievable frame rates within experimental conditions and increases the chance of external noise being included from other scattering particles within the sample.

## Adjusting the sampling rate for the iSCAT PSF dramatically affects processing time

Continual axial fitting of an image stack of 1000 frames results in a final run-time of 201.86 s, equivalent to a one axial fit per 201.86 ms, or ~5 axial fits per second. The key bottleneck on the achievable rate is measurement of the PSF profiles, running for a total time of 185.35 s due to the requirement extracting 360 profiles per slice – meaning over 1000 fits this routine needs to be run 36000 times, acting as the rate-limiting step for the axial fitting routine. This results in a final achievable rate for axial-localisation of 4.96 Hz. To assess how the number of profiles used to create the experimental average profile affects both the accuracy of the resulting fit, and the processing time multiple template stacks were created using alternative sampling values (36, 72, 180, and 360). These were then used to sample and fit a stationary gold nanoparticle, from which the RMS deviation

can be calculated (Fig. 26). As seen in Fig. 30 , maximum RMS deviation is achieved at 360 samples, with an RMS of 0.538, however limits the achievable correction rate to 4.95 Hz. However, assessing the PSF using a total of 180 samples results in an RMS deviation of 0.541, highlighting the minimal gain that is achieved with double the sampling rate. Due to the linear relationship between profile sampling and processing time, this means that using 180 samples a maximum correction rate of 9.18 Hz (after accounting for additional processing time). Using lower sampling rates leads to a rapid drop in the achievable RMS deviation, with 72 samples and 36 samples achieving 1.27 nm and 5.11 nm respectively. These sampling levels still maintain a high level of localisation precision, however does not match the fine resolution that is achieved using the higher sampling values. However, the reduction in sampling values results in higher achievable correction rates of 18.66 Hz for 72 samples, and 28.53 Hz for 36 samples.
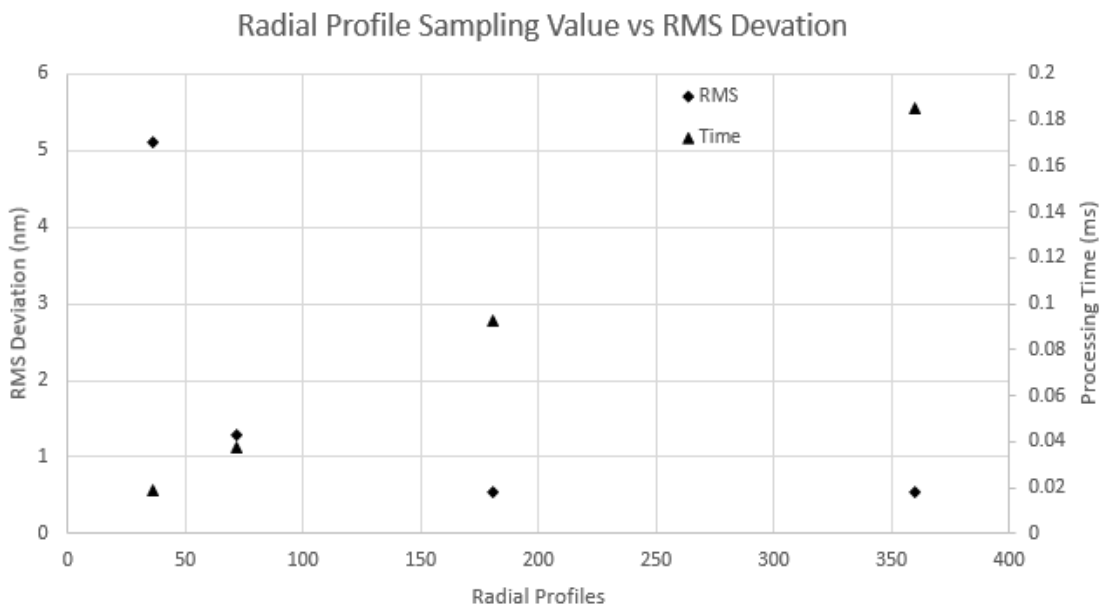


*Figure 30 - The effect of PSF sampling rate on achievable axial precision and processing time*

Assessment of experimental PSFs is achieved through the averaging of multiple line profiles of the immobilised particle sampled from the experimental images. The number of profiles sampled dramatically affects both the achievable axial resolution and processing time. It can be seen the beyond a sampling rate of 180 profiles, there is minimal increase in achievable axial precision, but almost a twofold increase in required processing time. Conversely, a decrease in the sampling rate leads to increased correction rates but decreased axial precisions. Modification of the sampling rate could provide an additional control, allowing for increased correction rates with a trade-off in achievable axial resolution.

These results suggest the optimum sampling level to maintain a high level of axial precision, whilst allowing for more rapid assessments of drift and a higher rate of correction is 180 samples for assessment of the experimental PSF. However, this can be modified as per experimental requirements, with lower sampling levels resulting in reduced accuracies but increased correction rates.

## Noise-limited Resolution of iSCAT microscopy

One of the key advantages of iSCAT microscopy is that it is a shot-noise limited imaging regime, to assess the noise-limitation of the system a series of images were collected and increasing levels of frame binning was applied (with a range of 1-7500 frames). The resulting standard deviation of the background noise is then calculated, and when plotted on a logarithmic scale reveals the background noise limit (Fig. 31). It can be seen that the resulting standard deviation of background noise follows a linear relationship between 1 and 750 frame bin sizes, matching well with the theoretical shot-noise limit (dashed line). However, bin sizes of ≥ 1000 frames, results in a deviation from this linear relationship, this is likely a result of external noise sources such as vibrational noise, thermal expansion of optical components, or mechanical instabilities within the system. This results in a limit being reached at ~1000 frames and a standard deviation in the background noise of ~0.00003, with diminishing returns with longer temporal averaging.

## Standard Deviation of Noise vs Frame Binning
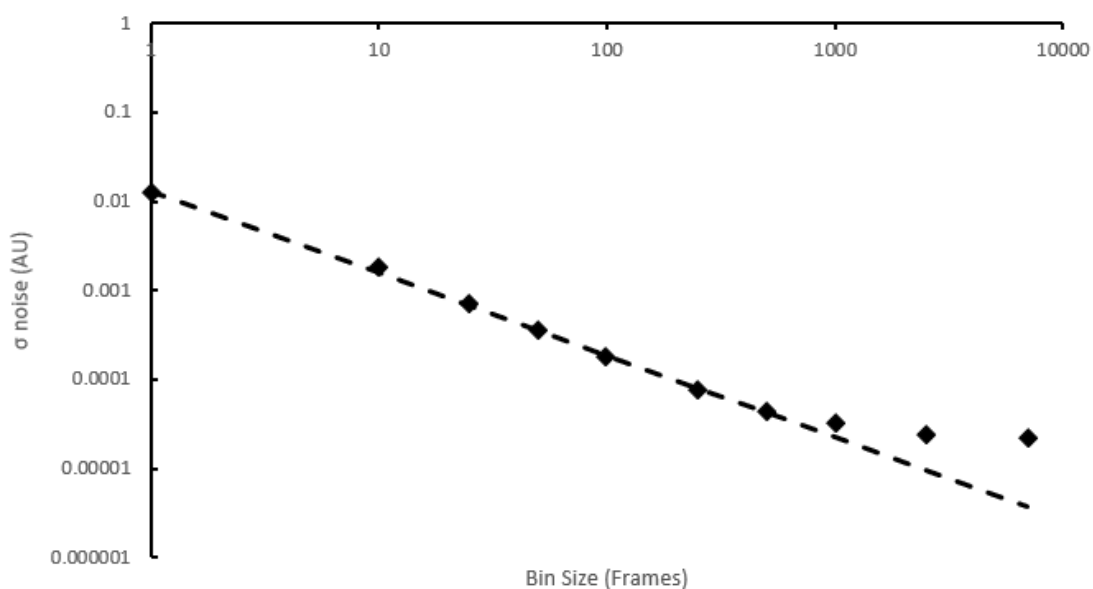


*Figure 31 - Shot-Noise limitation of iSCAT imaging*

The standard deviation of the background noise of images with increasing frame averages (ranging from 1 frame, to 7500 frames) – when plotted on a logarithmic scale the linear relationship can be seen between resulting standard deviation of the background noise, and the level of frame averaging. The theoretical shot-noise limit can be seen as the dashed black line, it can be observed that the resulting standard deviations of background noise for frame averages of < 1000 match well with the theoretical shot-noise limit. However, when frame averaging reaches ≥ 1000, the resulting standard deviation of background noise begins to deviate from the theoretical shot-noise limit. This is likely due to external noise sources, arising from factors such as thermal expansion, or mechanical instability – which become incorporated when averaging over long imaging periods.

## Gold Nanoparticle Calibration Curve

To characterise the response of the iSCAT system to AuNPs, we created a calibration curve of a range of AuNP sizes versus measured contrast. This calibration curve allows for easy measurement of AuNP size and stoichiometry in future assays, whilst also simplifying image analysis by provide thresholds for binder contrast when using AuNPs. This was achieved using a landing assay in which 25 nM of streptavidin-functionalised AuNPs (20 nm, 40 nm, and 80 nm) were added to an APTES-treated flowcell, blocked

with biotin-mPEG-SVA and mPEG SVA with a ratio of 0.5:24.5 mg/ml. Flow cells were
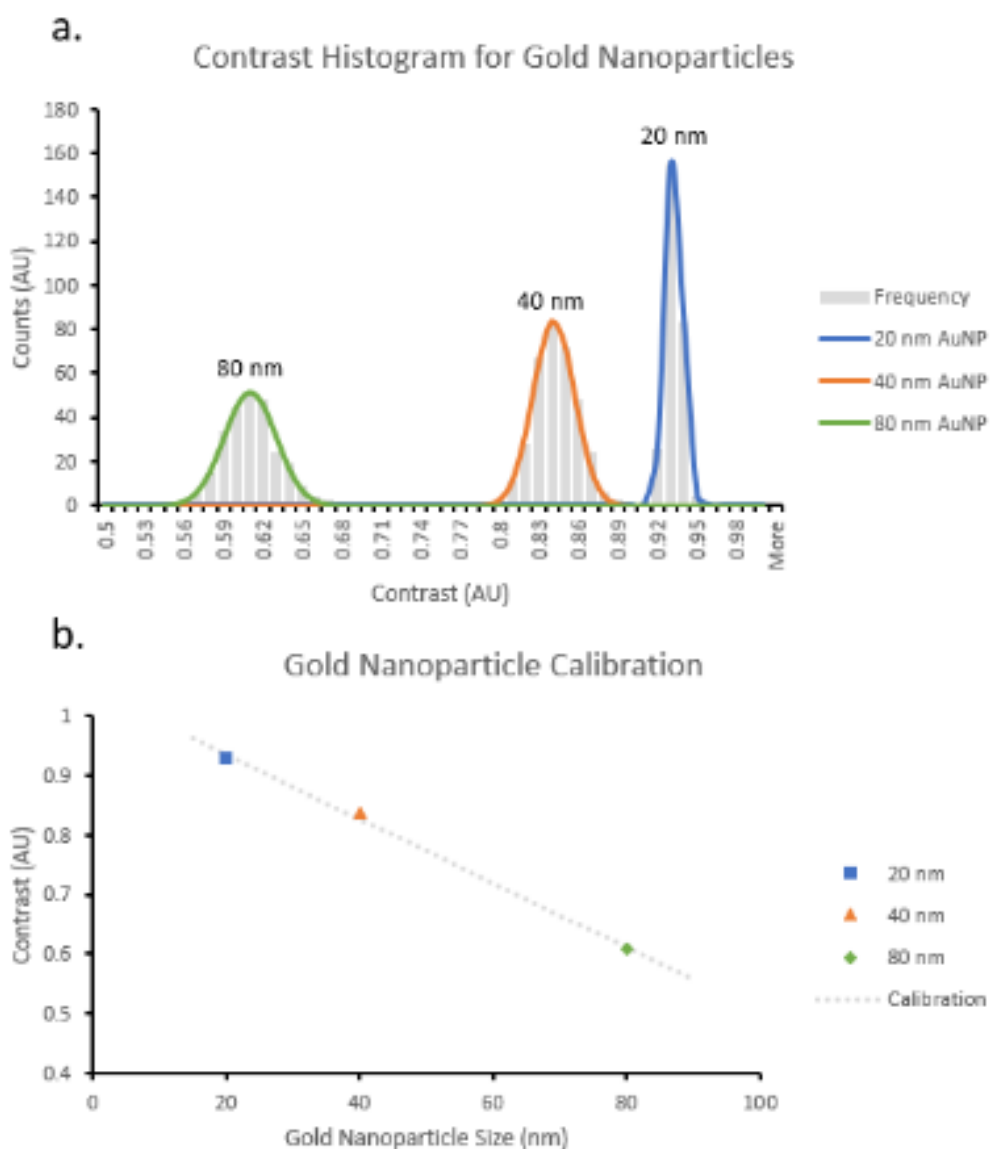


*Figure 32 - Gold Nanoparticle Contrast Histograms and Calibration Curve*

(a.) Histogram of  observed contrasts for 3 populations of gold nanoparticles, with sizes of 20 nm, 40 nm, and

80 nm, with their respective gaussian fits. (b.)Calibration curve for the average contrast detected for AuNPs

with diameters of 20 nm, 40 nm, and 80 nm. The average contrasts for these particles are 0.928, 0.838, and

0.608 respectively, and c learly demonstrate the linear relationship between contrast and particle size. Using

this calibration curve, it becomes possible to estimate the stoichiometry and size of AuNPs when used in future

assays. The larger variation present in larger nanoparticle populations is likely due to the larger inherent

variability in nanoparticle sizes as given by the manufacturers.

then immediately imaged, 30000 frames were recorded for each video at a frame rate of 500 fps, giving a total time imaging time of 1 minute per flow cell. Prior to ratiometric imaging, all videos underwent 10-fold temporal averaging to reduce noise and decrease processing time. All videos then underwent ratiometric processing with a bin size of 10 frames, and the contrast of all binding events observed were recorded and collated into histograms. The average contrast was then calculated for each AuNP size, and when plotted (Fig. 32) clearly displays the linear relationship between contrast and particle size as described previously.

When creating a calibration curve for gold nanoparticles, a range of at least 4 sizes should be used – as use of only three points can result in a large difference between the resulting linear fit, and the true relationship. This curve was limited by the availability of gold nanoparticles, and prior to future use an additional size should be incorporated. It was noted that the spread of the contrasts achieved for the 80 nm and 40 nm populations was much greater than that of the 20 nm populations. As defined by manufacturers it is likely that this results from the heterogeneity of nanoparticle sizes within synthesised products – with more variation being present in the larger nanoparticle populations, resulting in a wider range of detected contrasts for these populations (Coefficient of Variance for 80 nm AuNPs, >= 8%). Additionally, the interferometric signal for 80 nm AuNPs may begin to depart from the linear relationship observed between particle diameter and interferometric contrast. As the particle size begins to approach the size of the illuminating wavelength, the scattering term for eqn. 8 is no longer negligible, and the observed signal will begin to deviate from the linear relationship observed for smaller particles. However, this does not present an issue as there is no overlap in detected contrast between populations, meaning it is possible to clearly define which population a nanoparticle belongs to based purely on contrast.

## Localisation Precision

To assess the *in vitro* characteristics of this iSCAT implementation, a series of images of surface-immobilised 20 nm gold nanoparticles were collected. Static images of 40 nm gold nanoparticles can be seen in Fig 33, from which a signal-to-noise ratio was calculated using the following:

$$SNR = \frac{\mu_{signal} - \mu_{background}}{\sqrt{\sigma_{signal}^2 - \sigma_{background}^2}}$$

Where $\mu_{signal}$ and $\mu_{background}$ are average signal from a 20 nm gold nanoparticle and the background respectively (both extracted from 10x10 pixel area), and $\sigma^2_{signal}$ and $\sigma^2_{background}$ are the variances of the signal and the background noise respectively (Kubitscheck *et al.*, 2000; Koyama-Honda *et al.*, 2005). This results in an achievable signal-to-noise ratio of 128.75 for 20 nm AuNPs.
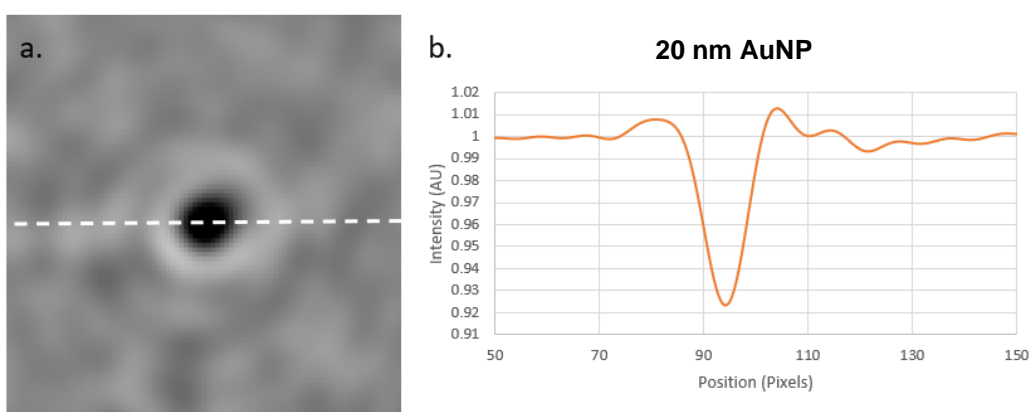


*Figure 33 - 20 nm gold nanoparticle image and intensity profile using iSCAT microscopy*

The implementation of iSCAT microscopy allows for effective imaging of single gold nanoparticles with a high signal-to-noise ratio and achievable spatial resolution, achieving a localisation precision of 4.11 ±0.02 nm.

To assess the localisation precision of the microscope we used the following equation (Thompson, Larson and Webb, 2002):

$$\sigma_i = \sqrt{\frac{s^2 + a^2/12}{N} + \frac{4s^3 b^2 \sqrt{N}}{a N^2}}$$

Where $a$ is the pixel size in nm, $b$ is the standard deviation of the background, $N$ is the number of photons, and $s$ is the standard deviation of the Gaussian fit. To assess localisation precision 5000 frames were taken of a stationary 20 nm AuNP, a kymograph was created of the stationary AuNP, and each slice of the kymograph was fit to a 1D Gaussian function, as given by:

$$f(x) = a * \exp\left(\frac{(x - b)^2}{2c^2}\right)$$

Where $a$ is the height of the peak, $b$ is the mean position of the peak, and $c$ is the standard deviation of the Gaussian. The standard deviation of these Gaussian fits is then used to calculate the localisation precision for the slice – the final spatial precision is calculated as the average of all measured spatial precisions. From this we extracted a final localisation precision of 4.11 ±0.04 nm for 20 nm AuNPs, imaged at a frame rate of 1 kHz with an exposure time of 1 ms.

To assess the localisation precision of particles in motion we made used of 2D-positional tracking of surface-immobilised AuNPs. 25 nM 20 nm streptavidin-labelled AuNPs were immobilised on an APTES-treated glass coverslip, blocked with biotin-mPEG-SVA and mPEG SVA at a ratio of 0.5:24.5 mg/ml. The AuNPs were incubated in the flow cell for 30 minutes prior to imaging. Upon imaging, several videos were taken of the lateral translation of the slides, with step sizes ranging between 50 nm and 2.5 nm, at a frame rate of 500 fps. All then underwent flat-field processing and 10-fold temporal averaging prior to image analysis. Initial spot detection was carried out using a weighted centroid routine to detect the sub-pixel centre of the particle being tracked, the particle was then fit to a 2D Gaussian to accurately detect the sub-pixel position of the particle, using the initial weighted centroid position as the initial prediction for the Gaussian fit:

$$f(x,y) = A * \exp\left(-\left(\frac{(x-x_o)^2}{2\sigma_x^2} + \frac{(y-y_o)^2}{2\sigma_y^2}\right)\right)$$

Where A is the amplitude, $x_o$ and $y_o$ is the centre of the Gaussian, $\sigma_x$ and $\sigma_y$ are the x and y spreads of the Gaussian. The central coordinates are recorded as the spatial position and used as the initial estimate of the fit for the next frame of the stack.

As can be seen in Fig. 34, step sizes ranging between 50 nm and 10 nm are clearly resolvable with no additional image processing required, from these we were able to resolve average steps sizes of 48.08 ±1.61 nm, 19.18 ±0.44 nm, and 9.43 ±0.75 nm for 50 nm, 20 nm, and 10 nm steps respectively. This highlights the fine spatial precision that
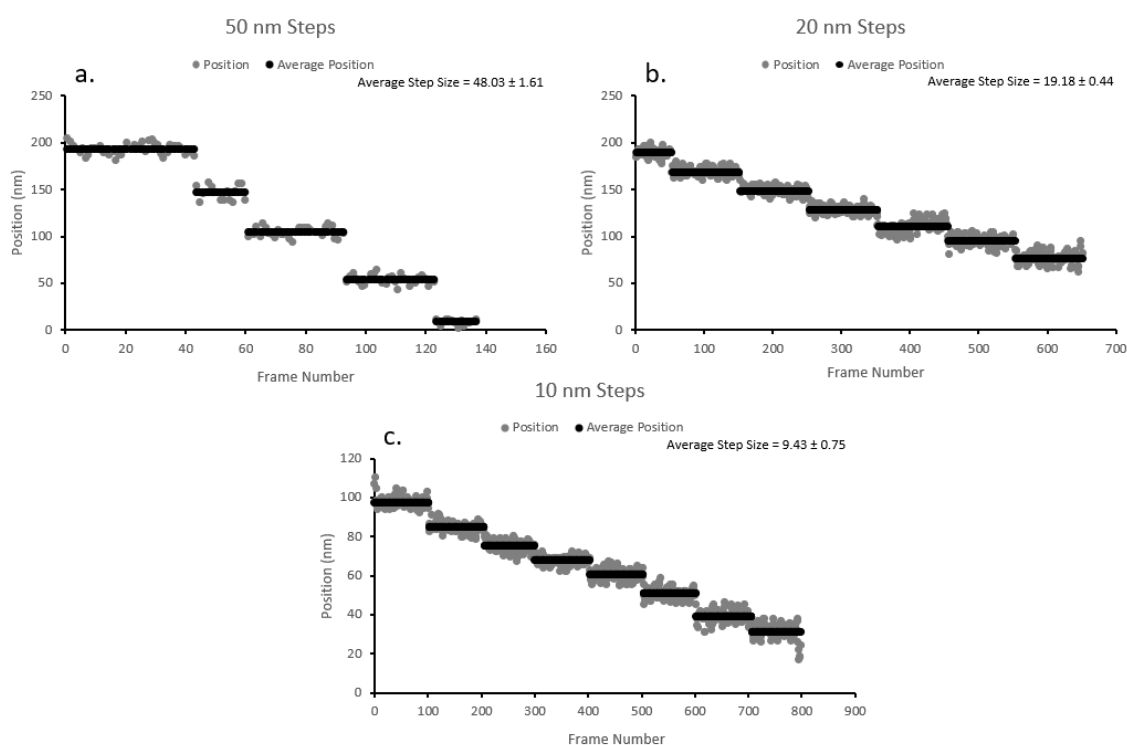


*Figure 34 - Positional tracking of AuNPs undergoing lateral translation of fixed step size*

To assess the positional and tracking precision of the iSCAT system, surface-immobilised 20 nm AuNPs were imaged undergoing lateral translation with a range of fixed step sizes (ranging from 50 to 3 nm). 50 nm (a.) steps are clearly resolvable, with an average step size of 48.03±1.61 nm extracted from the video. This is consistent for 20 nm (b.) steps, in which an average step size of 19.18±0.44 nm was extracted, and similarly for 10 nm (c.) steps in which an average step size of 9.43±0.75 nm was extracted. This displays the localisation precision displayed by the iSCAT system, allowing for super-resolution of steps well beneath the diffraction limit of the system.

can be reached with the system, with an precision well below the diffraction limit of the system being achieved with no need for additional image processing.

For step sizes below 10 nm, individual steps became harder to clearly resolve – whilst remaining visible in the 5 nm steps, they became partially obscured by noise for the 2.5 nm steps. To overcome this issue, we made use of a method in which a sliding window paired T-test is applied to the localisation data, similar to that used in ratiometric image processing. Sequential batches of size $n$ were extracted and underwent a paired T-test to assess the similarity of the frame batches. The T-value was given by:

$$T = \frac{m_1 - m_2}{(\frac{\sigma_{diff}}{\sqrt{n}})}$$

Where $m_1$ and $m_2$ are equivalent to the means of the first and second windows respectively, $\sigma_{diff}$ is the standard deviation of the differences between the two groups, and $n$ is the sample size. This process then sequentially moves through the positional data one frame at a time, this produces a new trace which can be overlaid the original which displays the similarity within that region of the localisation data. Individual steps are highlighted due to the shift in positional data, leading to negative peaks in the values extracted from the T-test – this allows us to extract the positions at which steps take place, and from this can work out an average step size across the video. As seen in

Fig.35a and Fig.35b 5 nm and 2.5 nm steps, respectively, taken by a 20 nm AuNP are able to be resolved.
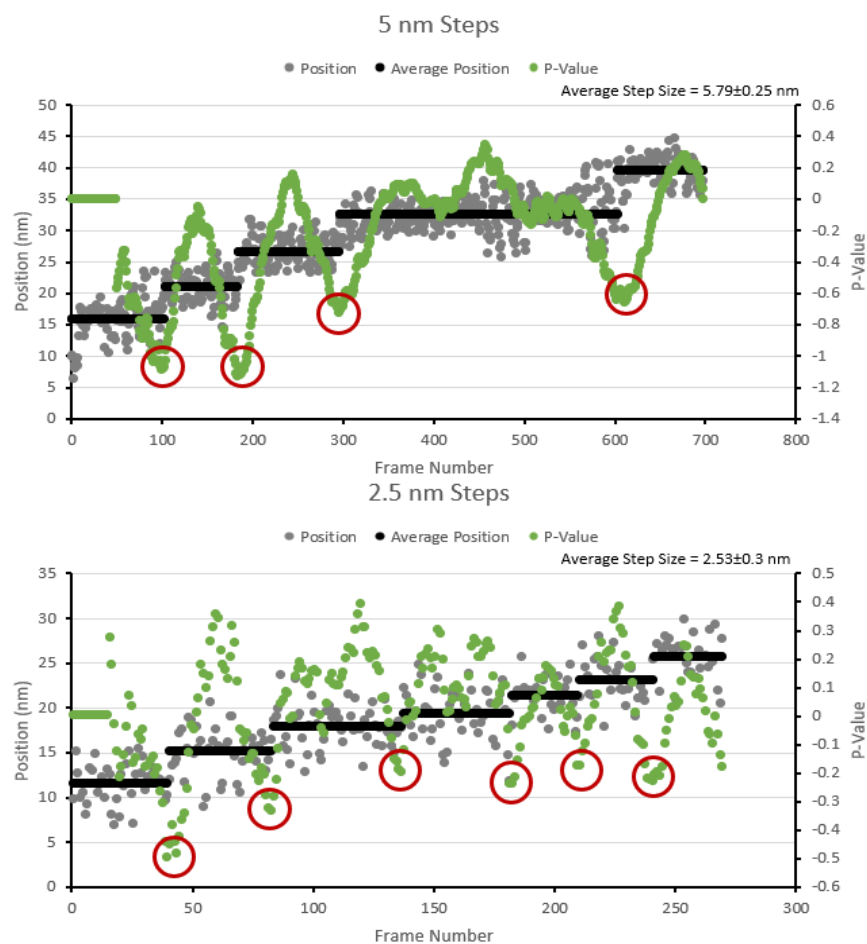


*Figure 35 - A sliding-window T-test reveals ≤ 5 nm steps of a 20 nm AuNP*

To further resolve smaller lateral steps taken by 20 nm AuNPs, we made use of a sliding window T-test, in which sequential batches of positions undergo a T-test to reveal the similarity between them. This then repeats as the window slides along the data point by point. This creates a new data series which can be overlaid on the original positional data, where larger T-values correspond to regions in which the positional values are similar, and negative values correspond to regions in which there is a large amount of dissimilarity between positional locations. These dips in the P-values correspond to the points at which the 20 nm AuNP takes a lateral step, as there will be a large change in the positional values within the T-test windows. (a.) Shows the extracted T-values overlaid on the original localisation data from the 5 nm step dataset, the dips correspond to steps taken by the AuNP – using this we outline the average position of the AuNP after each step and extract an average step size of 5.79±0.25 nm. (b.) shows the same process applied to an AuNP undertaking 2.5 nm steps, this once again reveals dips within the calculated T-value which correspond to steps taken by the AuNP, returning an average step size of 2.53±0.3 nm.

Together these results display the achievable spatial precision for our implementation of iSCAT, allowing us to resolve 2.5 nm steps taken by 20 nm AuNPs (equivalent to 7.14 DNA base-pairs), as simulated with lateral translation of the piezo stage. This allows for fine-spatial tracking and provides a strong platform for the study of a wide-range of biological systems.

## 3.4 Discussion

### iSCAT allows for high-speed imaging the fine spatial-resolution and tracking precision

A key benefit of iSCAT microscopy is the high spatial resolutions that can be achieved, due to the shot-noise limited regime, and the ability to increase photon flux through increased illumination intensities (Ortega Arroyo *et al.*, 2014; Young and Kukura, 2019). Due to this, previous implementations have achieved sub-pixel localisation accuracies for AuNPs (Andrecka *et al.*, 2016) – here we describe the level of spatial resolution that can be achieved with our simple, wide-field implementation of iSCAT microscopy, allowing for the resolution of AuNPs undergoing lateral steps of 2.5 nm and a localisation precision of 4.11 nm. As can be seen this does not reach the level of lateral resolution previously achieved by others (Andrecka *et al.*, 2015, 2016), it is likely that this is due to underlying sources of noise which are not fully compensated for via the active stabilisation methods that are employed. It is likely that these are due to low frequency vibrations which are not stabilised functionally through the use of a supported optical table as defined by the manufacturer, possible sources of these vibrations could be external factors such as building works in the nearby area or even wind currents around the building the system is housed in due to its location on the 4th floor. However, the level of localisation precision achieved still allows for a high-level of experimental accuracy, with a resolution of 2.5 nm this would allow for resolution of movements equivalent to 7.14 DNA base pairs, or steps along single actin monomers in an actin filament (~2.71 nm) (Dominguez and Holmes,

2011). This spatial resolution, combined with the ability to achieve it at frame rates reaching 3 kHz provide a strong platform for the study of a wide range of biological systems.

## Real-time software based axial tracking of immobilised AuNPs could allow for highly accurate 3-axis stabilisation

Active stabilisation plays a key role in maintaining the shot-noise limited sensitivity of iSCAT microscopy, with any deviations in axial or lateral position contributing non-significant levels of noise. To achieve this a number of methods have been used previously, including the use of an additional laser in a TIR illumination regime, with displacement of the resulting reflected beam indicating the change in focus (Ortega Arroyo, Cole and Kukura, 2016), or lateral correction being achieved using a 2D Gaussian fit of a surface immobilised AuNP (Garmann, Goldfain and Manoharan, 2019). Alternative implementations have widely made use of nanofabricated fiducial markers, in combination with back-focal plane imaging, allowing for high-speed monitoring of the position of the fiducial marker relative to the objective (Carter *et al.*, 2007; Schmidt *et al.*, 2018). These methods allow for incredibly sensitive stabilisation, reaching an accuracy of 0.1 nm at kHz rates, but importantly demand a huge increase in experimental complexity, requiring custom nanofabricated fiducial markers, additional hardware, and an already stable optical setup to achieve. Whilst these methods are able to achieve incredible levels of sensitivity, they remain difficult to implement, and require a not-insignificant amount of additional monetary investment. To provide an attractive alternative, we sought to develop a solely software-based approach to achieve high-precision 3D stabilisation of an iSCAT microscope.

We describe a 3D-localisation routine which could be applied to achieve active axial stabilisation via extraction and fitting of experimental PSFs to a previously measured stack of model PSFs. Estimation of the iSCAT PSF was achieved as previously described

(Taylor *et al.*, 2019a, 2020; Gholami Mahmoodabadi *et al.*, 2020), in which multiple profiles are taken and averaged to produce an estimated PSF profile. These then undergo upscaling via cubic spline interpolation, a method that has been previously applied for use in 3D super-resolution fluorescence microscopy (Babcock and Zhuang, 2017), allowing the fine positional data encoded in the outer rings of the iSCAT PSF to be revealed (Gholami Mahmoodabadi *et al.*, 2020). Use of the discrete Fréchet distance allows for accurate fit of experimentally extracted PSFs to the template Z stack, resulting in an axial estimation error of 1.92 nm for a stationary particle. When applied to particles travelling through the Z axis at 20 nm s$^{-1}$ and 10 nm s$^{-1}$, equivalent displacement rates were measured to be 23.21 nm s$^{-1}$ and 11.3 nm s$^{-1}$ respectively, with an RMS error of 4.84 nm and 2.35 nm respectively.

It is key to note that the observed dwell times (between 250 ms and 750 ms) showed considerable variation around the true dwell time of 500 ms, which may be caused by the significant noise present in the extracted axial positions limiting the effectiveness of the step-finding routine. This in particular highlights the need for further work to be carried out to refine this method further. An alternative 3D localisation method could be achieved by detecting the specific position of the outer rings of the iSCAT PSF (Fig. 24), and their relative position to one another and the central core of the PSF. As the particle travels through the Z-axis these rings invert in a linear fashion over a range of ~100 nm, as such by measuring the change in the relative intensity of these rings one could create a calibration curve against which experimentally extracted intensities for these rings could be fit. This would require considerably less processing time compared to fitting of the entire PSF using the discrete Fréchet distance and could also allow for automated generation of this calibration curve at the start of each experiment.

Previous implementations of Z-axis active stabilisation (Ortega Arroyo, Cole and Kukura, 2016) require additional hardware, and increases the experimental complexity of

implementing iSCAT microscopy – but are able to achieve high levels of active stabilisation (< 10 nm). In comparison a purely software-based method for achieving this removes a number of these additional requirements, only requiring the presence of a surface immobilised AuNP within the imaging field of view, whilst still maintaining an axial precision of 1.92 nm which aligns well with the localisation precision achieved through hardware based approaches (Ortega Arroyo, Cole and Kukura, 2016). Together these data highlight the potential high axial precision that could be achieved with this method, and when combined with lateral active stabilisation via 2D Gaussian fit of the stationary AuNP could provide an accessible alternative to the commonly implemented methods of 3D active stabilisation.

## Future Developments

### Partial Reflector

A key future addition would be the implementation of a partial reflector within the detection arm of the system. Partial reflectors were initially described in 2017 by the Kukura and Van Hulst labs (Cole *et al.*, 2017; Liebel, Hugall and Van Hulst, 2017). These components consist of a clear glass window, with a small layer of deposited gold/silver with varying thickness (~100-200 nm) – this layer attenuates any light that passes through it (usually by a factor of > 90%). As scattered light is collected by the objective it is concentrated to edge of the numerical aperture, leading to spatial separation between the scattered and reflected fields. Partial reflectors specifically attenuate the reference field, whilst allowing the scattered field to pass through (largely) unchanged. This results in particles within the iSCAT system having increased contrasts, further increasing the potential mass resolution of a system – it is important to note that shot-noise remains constant, only the observed contrasts of molecules changes (Cole *et al.*, 2017; Liebel, Hugall and Van Hulst, 2017).

The addition of a partial reflector could vastly improve the achievable mass resolution of the system, with implementation being incredibly simple – it can be placed between

lenses 4 and 5 in the current system, as the reflected field becomes focused to a tight point upon passing through lens 4. To maintain the observed signal at the camera it is likely this change would have to be accompanied with an increase in output power of the 445 nm laser, as the >90% attenuation of the reflected field would result in vastly decreased signal reaching the sensor of the camera – resulting in an increase in shot-noise.

## Fibre-Coupling of Laser Diodes

Additional improvements would also take the form of a fibre-coupled laser diode, as in the current implementation the poor beam quality has to be corrected through the use of a 50 µm pinhole filter – leading to a reduction in illumination intensity, limiting the maximum achievable frame rate whilst maintaining minimal shot noise. An alternative is to use a pair of cylindrical lenses to correct the ellipticity of the beam, however this would not confer the advantages of using a pinhole filter/fibre-coupling, being the production of a clean speckle-free Gaussian profile.

## Combining iSCAT and Fluorescence Microscopy

Whilst iSCAT alone provides a powerful tool for the study of several biological systems, it does present a few limitations when compared to fluorescence microscopy. One primary feature being the lack of specificity in detection, beyond the contrast provided by the particle of interest – unlike fluorescence where a specific wavelength can be used to confirm the presence of a particle of interest, iSCAT is unable to provide the same level of specificity.

Because of this combining iSCAT and fluorescence measurements within one system provides the benefit of both methods, and opens a variety of alternate experimental procedures, providing an additional level of flexibility. Introducing a fluorescence pathway into a pre-existing iSCAT system is incredibly straightforward at its most basic level but

can be expanded to include any required level of experimental complexity. This can be functionally achieved with the addition of an additional imaging pathway, and no modification to the iSCAT illumination pathway.

The fluorescence imaging pathway makes use of a 488 nm long-pass dichroic mirror (ThorLabs DMLP490R), placed after the tube lens (Fig. 16, Lens 4) – as all the required information for the iSCAT image is encoded in the 455 nm light emerging from the objective, this isolates all wavelengths above this arising from fluorescence signals within the sample. The fluorescent signal is then focused by a 50 mm plano-convex NBK-7 lens onto a Basler ACE CMOS camera (Basler, acA800-510um). This results in a final pixel size of 72.5 nm.

The limitation of this implementation of a fluorescence pathway is the use of only one illumination wavelength, however this can be overcome with the use of quantum-dots as the fluorescence label used within experiments. These are available in several wavelengths and can all be excited using the same illumination source. Additionally, quantum-dots can also be used as a scattering label, as they have a sufficient scattering cross-section to allow for detection via scattering within the iSCAT channel (with diameters between 10-20 nm).

An extension of this fluorescence pathway would be to include a further series of dichroic bandpass mirrors, allowing for further separation of fluorescence signals, allowing for multiple fluorescence labels to be used within the same system, allowing for further discrimination of the functional components within the experiment. This can be effectively achieved using the OptoSplit III (Cairn Research), with the additional benefit of being able to make use of the same imaging camera. This would allow for discrimination of labelled species within iSCAT microscopy, via correlation of binding species with their fluorescent signatures if each is labelled with a spectrally distinct Q-dots. This would allow for efficient use of the advantages conferred by both iSCAT microscopy (high-spatial and temporal

resolutions) and fluorescence microscopy (straightforward discrimination of labelled species).

## 3.5 Conclusions

We have developed and presented a simple interferometric scattering microscope, which can comfortably be constructed by persons with limited previous experience in the construction of optical systems. This microscope is able to achieve unlabelled imaging of Single-Molecules, whilst demonstrating spatial tracking and localisation down to step sizes of 2.5 nm. Alongside this we have developed software-based routines for the detection, and correction, of axial and lateral drift within such microscopes, achieving an axial localisation precision of 4.11 nm – providing an alternative to previous hardware-based solutions which led to increased experimental complexity and cost. For the further application of this form of microscopy to new fields we have developed new assays for the study of protein-DNA interactions, with a particular focus on the study of DNA repair pathways.

# 4 High-speed Single-Molecule imaging reveals a fast, energy efficient search mode for the DNA repair protein UvrA

## 4.1 Introduction

### UV-Induced DNA Damage

UV is a form electromagnetic radiation with wavelengths ranging between 10 nm and 400 nm. The full spectrum of UV radiation is emitted by the sun, with the majority of the more harmful shorter wavelengths being absorbed by Earth's atmosphere. Due to this, UV-A and UV-B are the primary source of UV-induced lesions resulting from solar radiation. The exposure of DNA to UV radiation results in the formation of numerous cytotoxic DNA lesions which can pose a serious threat to genome integrity.

UV-induced DNA lesions are primarily formed through direct interactions between UV-B (Yoon *et al.*, 2000; Cadet *et al.*, 2001; Jones and Baxter, 2017). The majority of UV-A wavelengths are poorly absorbed by DNA, however these wavelengths are associated with DNA damage through the generation of reactive oxygen species (ROX) (Cadet *et al.*, 2001; Kawanishi and Hiraku, 2001). Three helix-distorting lesions are induced via direct interaction of UV-B with DNA nucleotides, these are; cyclobutane pyrimidine dimers (CPDs), 6-4 photoproducts (6-4 PP), and Dewar valence isomers (Boyce and Howard-Flanders, 1964; Setlow and Carrier, 1964; Yoon *et al.*, 2000; Sinha and Häder, 2002; Cadet, Sage and Douki, 2005; Douki and Sage, 2016; Jones and Baxter, 2017) (Fig. 36). Upon exposure of DNA to UV radiation CPDs and 6-4 PPs are able to form between adjacent pyrimidine bases, with the exception of 5'-CT-3' sequences between which only CPDs fom (Sinha and Häder, 2002; Jones and Baxter, 2017). Dewar valence isomers

form via UV-B induced photoisomerization of 6-4 photoproducts (Mitchell and Rosenstein, 1987). Cyclobutane pyrimidine dimers are the most prevalent lesions being induced at a 3:1 ratio relative to 6-4 photoproducts under solar radiation (Sinha and Häder, 2002).
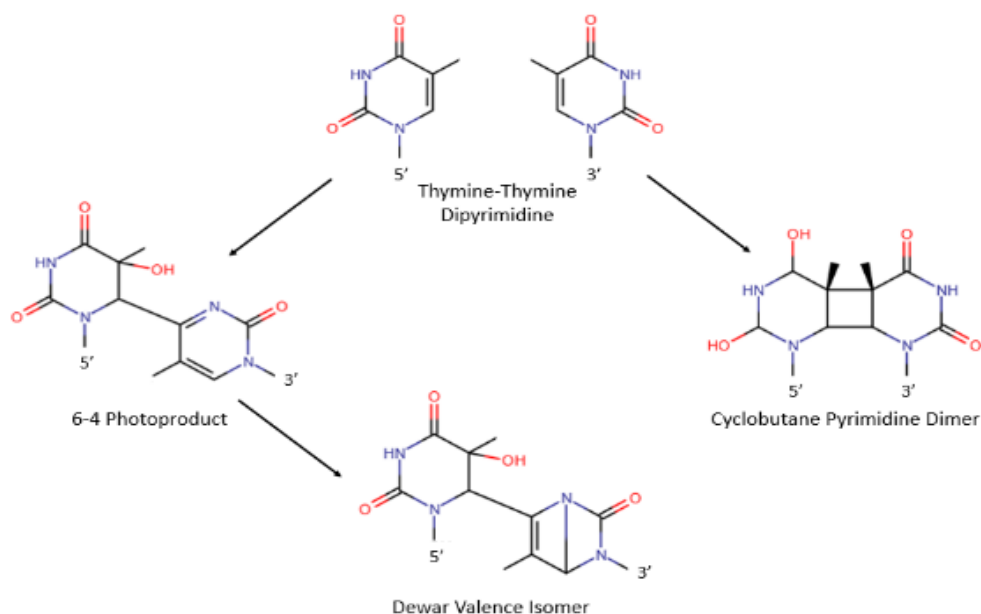


*Figure 36 – UV-induced dipyrimidine lesions*

Direct interaction of UV-B with dipyrimidine nucleotides can lead to the formation of direct chemical linkages between the adjacent pyrimidines, resulting in bulky cytotoxic lesions known as Cyclobutane pyrimidine dimers and 6-4 photoproducts. Further exposure of 6-4 photoproducts can lead to photoisomerization and the formation of Dewar Valence Isomers.

Whilst UV-A is not as effective as UV-B at inducing the formation of dipyrimidine lesions, it is still associated with DNA damage through the generation of reactive oxygen species and induction of oxidative stress (Mouret *et al.*, 2006; Jones and Baxter, 2017). These reactive oxygen species may be produced by the activation of endogenous photosensitizers such as porphyrins and flavins via absorption of UV-A or UV-B (El-missiry and Abou-seif, 2000). This oxidative stress can directly result in the formation of lesions such as 8-oxo-7,8-dihydro-2'-deoxyguanosine (8-oxodGuo), or lead to DNA double strand breaks (Mouret *et al.*, 2006; Jones and Baxter, 2017). UV-A has also been shown to inhibit eukaryotic NER through its interaction with 6-formylindolo[3,2-*b*]

carbazole (FICZ), a UV-B induced photoproduct of tryptophan. In combination with UV-A, FICZ generates reactive oxygen species which causes oxidative damage to the proteins involved in eukaryotic NER (Brem *et al.*, 2017).

Due to the ubiquitous nature of UV-radiation, it poses a persistent threat to genome integrity, being able to both directly and indirectly cause cytotoxic DNA lesions. To combat this ever-present threat number of DNA repair pathways have evolved to directly tackle these UV-induced lesions, one such pathway being Nucleotide Excision Repair.

## Prokaryotic Nucleotide Excision Repair

Nucleotide excision repair (NER) is a DNA repair pathway which is primarily focused on the removal of UV induced DNA damage; however, it is particularly notable due to its promiscuity regarding substrate sensitivity. NER involves a multi-step process in which DNA lesions are recognised, removed, and repaired using the opposite DNA strand as a template. NER can be split into two further sub-pathways; transcription coupled NER, and global genomic NER – with the defining difference between these sub-pathways being the detection of the DNA lesions.

NER and its repair of UV-induced photoproducts was first described in 1964 by Richard Setlow and Bill Carrier (Setlow and Carrier, 1964), and separately by Richard Boyce and Paul Howard-Flanders (Boyce and Howard-Flanders, 1964). Both of these studies focused on the removal of a UV-induced cyclobutane pyrimidine dimers. Subsequent breakthroughs followed with the discovery of the responsible genes (*uvr* genes), and the purification of their products (Sancar *et al.*, 1981; Thomas, Levy and Sancar, 1985) and the reconstitution of the UvrABC enzyme complex (Sancar and Rupp, 1983). This allowed for the first studies into the function and structures of the *Uvr* proteins (Yeung *et al.*, 1983).

## Overview of Prokaryotic NER

The process of NER can be dissected into discrete steps, with these being damage detection, damage verification, incision, excision, DNA synthesis, and ligation. As mentioned previously the two sub-pathways of NER differ only at the damage detection step. Global genome NER damage detection involves the collaborative work of the UvrA and UvrB proteins, whilst transcription coupled NER damage detection is initiated upon stalling of RNA polymerase at a DNA lesion, leading to the recruitment of Mfd (or Transcription-repair coupling factor, TRCF) which is able to remove the RNA polymerase and recruit the UvrAB complex to the damage site. From here the pathways merge and follow identical steps. The UvrB helicase separates the two strands and inserts a beta-hairpin for damage verification, leading to the release of UvrA. UvrC is then recruited to the damage site and using its two nuclease domains is able to make incisions either side of the DNA lesion (Orren and Sancar, 1989). UvrBC (the post-incision complex) is then displaced by UvrD and DNA Polymerase I, excising the nicked fragment, and subsequently resynthesizing the strand using the opposite strand as a template. DNA ligase is then recruited to ligate the fragment, completing the pathway (Van Houten *et al.*, 2005).

## UvrA

UvrA is the primary damage sensing protein in the NER pathway and is a member of the ATPase-Binding Cassette (ABC) superfamily. The UvrA protein (Fig. 37) consists of 2 ATP-binding domains, with each containing an A-Walker motif site, a Q-loop for nucleotide binding, a B-Walker motif, a D-loop, an ABC signature domain, and a his-loop. Additional domains are also located within the N-terminal ATP-binding domain, with one being involved in UvrB-binding (Pakotiprapha *et al.*, 2008, 2009), and the other being the insertion domain allowing for DNA binding (Timmins *et al.*, 2009). UvrA also coordinates three zinc ions per monomer, with one located between signature-domain I and the UvrB-

binding domain, one between the signature-domain I and the insertion domain, and the last connecting the signature-domain II to the dimer interface. These three zinc ions are thought to play important structural roles (Croteau *et al.*, 2006; Wagner, Moolenaar and Goosen, 2011; Kisker, Kuper and Van Houten, 2013).Additionally, whilst zinc-finger domains are commonly utilised DNA-binding motifs, it has been shown that the C-terminal
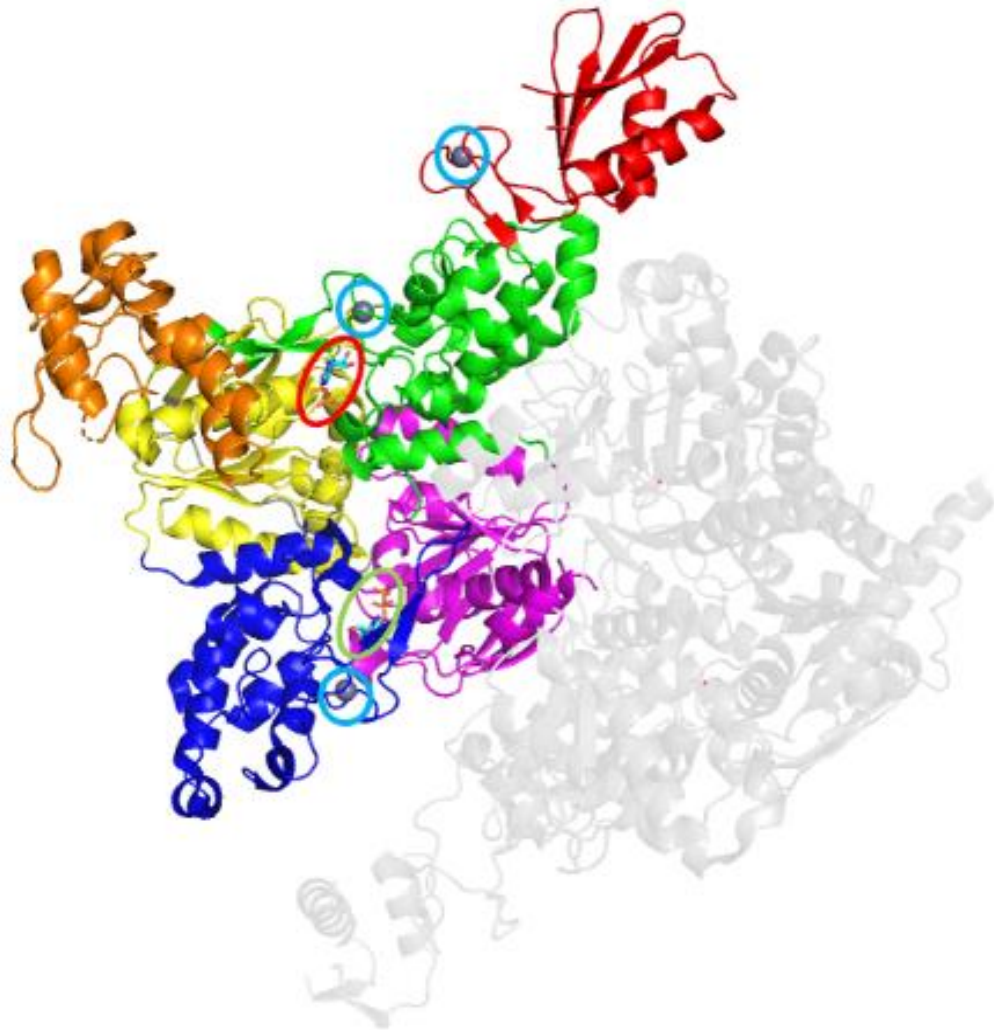


*Figure 37 – The structure of Geobacillus stearothermophilus UvrA*

The overall structure of the UvrA dimer of *Geobacillus stearothermophilus* UvrA, with one of binding partner greyed out. The protein is colour by domain, with ATP-binding domain I in magenta, Signature domain I in green, the UvrB binding domain in green, the Insertion domain in orange, ATP-binding domain II in yellow, Signature domain II in blue. The three coordinated zinc atoms are circled in blue, whilst the ADP bound in the proximal ATPase site is circled in red, and the ADP bound in the distal ATPase site is circled in light green.

zinc-finger domain is not actually involved in DNA binding, instead seemingly being required for effective discrimination of damaged DNA (Croteau *et al.*, 2006). Upon initial binding to DNA the respective alpha-helices of the zinc-finger domains for both protomers in the UvrA dimer are positioned in such a way that ATP in the distal ATPase site cannot be hydrolysed. Once a lesion is encountered, the DNA binding regions of both protomers are thought to be rearranged, resulting in the movement of the zinc-finger alpha helices which allows for subsequent ATP hydrolysis at the distal ATPase (Wagner, Moolenaar and Goosen, 2011).

UvrA is able to dimerize in the presence of nucleotides, bring the N-terminal and C-terminal ATPase sites of the separate UvrA molecules into close proximity (Pakotiprapha et al., 2008). The UvrA ATPase mechanism is complex with a number of intermediates (Case *et al.*, 2019), including allosteric communication between sites, which couples the binding of UvrA to the lesion to the recruitment of UvrB, most likely as a consequence of turnover at the proximal ATPase site – demonstrating a tight-coupling model due to negative cooperativity between the UvrA ATPase sites (Stracy *et al.*, 2016; Barnett and Kad, 2019; Case *et al.*, 2019; Kraithong *et al.*, 2021).

Whilst extensive structural studies have been carried out trying to gain insight of how UvrA binds DNA, and more importantly, detects and discriminates DNA damage – these mechanisms remain unclear. It is thought that upon binding of a UvrA dimer to dsDNA, the DNA is bound in a cleft formed by the UvrA dimer, interacting only with the phosphate backbone of the DNA. Interactions primarily occur with 4 nucleotides around the signature-II (demonstrated in *T. maritima* UvrA), however other points of contact along the DNA binding path include the signature-I domain, the insertion domain, and the three Zinc-binding domains (Pakotiprapha *et al.*, 2009, 2012; Timmins *et al.*, 2009). Residues within the signature-II domain seem to particularly contribute to DNA binding, as demonstrated by Croteau et al. using *Bacillus caldotenax* UvrA, in which mutation of Lys-

680 and Arg-691 reduces UvrA binding to a 50bp dsDNA fragment 37-fold (Croteau *et al.*, 2008). This interaction, which involves only the phosphate backbone, could explain NER's promiscuity with regards to its wide range of substrates – damage detection relies on the detection of distortions within the backbone which affect the rigidity and stability of the helix. A dynamic model has been proposed in which the signature-domain IIs of the two UvrA monomers are able to probe for lesions by bending the DNA and assessing the rigidity of the helix in-between.

Within signature-domain II resides a conserved structural element, which is a β-hairpin within the 3$^{rd}$ Zinc-binding module (Zn3hp); recent studies have begun to elucidate the larger role this element plays within early damage detection by UvrA. It is thought that UvrA binds DNA in two separate modes. The first is thought to involve interactions with both undamaged and damaged DNA as described above, via interactions through the signature-I and signature-II domains, the insertion domain, and the 3-zinc binding-modules (Pakotiprapha et al., 2009, 2012; Timmins et al., 2009). Upon interaction with damaged DNA the binding mode switches to a Zn3hp-dependent interactions, in which a stable interaction is formed between Zn3hp and the damaged DNA. The exact molecular mechanism through which UvrA is able to discriminate damaged DNA and induce this change in binding modes currently remains unclear. However due to large distorting nature of NER's target lesions it is possible UvrA is able to probe for distortion of the backbone. This movement of the Zn3hp element is required for subsequent loading of UvrB, with this movement being controlled by ATP hydrolysis within the distal-ATPase of UvrA (Kraithong *et al.*, 2017).

UvrB is the key link within prokaryotic NER which connects damage detection and verification, with the downstream processes of lesion excision, removal, and resynthesis. UvrB is a superfamily-2 DEAD-box helicase, exhibiting both weak helicase and ATPase activity (only activated upon interaction with UvrA, or upon removal of the autoinhibitory domain 4) (Theis *et al.*, 2000; Wang *et al.*, 2006).



*Figure 38 – The structure of Bacillus caldotenax UvrB*

The crystal structure of UvrB, with domains 1a, 1b, 2, and 3 showing in red, yellow, green, and purple respectively. The important β-hairpin is shown in cyan and bridges the gap between domains 1a and 1b. Domain 4 of UvrB is not shown here as it is disordered.

The structure of UvrB is well characterised, both in its apo form (Machius *et al.*, 1999; Nakagawa *et al.*, 1999; Theis, 1999; Truglio *et al.*, 2004), and in complex with DNA (Eryilmaz *et al.*, 2006; Waters *et al.*, 2006). It consists of two SF-2 Rec-A-like domains (1A, and 3), alongside 3 auxiliary domains (1B, 2, and 4) with each contributing to additional functions of UvrB (Fig. 38). Domain 1B is involved in additional interactions with

Page | 137

DNA, domain 2 interacts exclusively with UvrA, and domain 4 acts in combination with domain 2 to interact with both UvrA and UvrC. One key component of UvrB is the β-hairpin which connects domains 1A and 1B (K. Theis, 1999), containing a number of key structural residues which have been shown to be involved in DNA damage verification (Skorvaga *et al.*, 2002; Malta, Moolenaar and Goosen, 2006).

The exact mechanism through which UvrB is able to verify damage is currently unclear, however a number of models have been proposed which could elucidate this process. The most supported mechanism is the base-flipping model (Malta, Moolenaar and Goosen, 2006; Malta *et al.*, 2008); upon binding DNA, one strand is threaded behind the β-hairpin, with the other remaining on the surface of the protein. This causes two bases to become extrahelical, with one flipping into a hydrophobic pocket. The bases that become extrahelical are the base-pairing partner of the damaged nucleotide, along with its direct 3' nucleotide neighbour (Malta et al., 2006). It is unclear where the damaged strand is located (on the surface of the protein, or behind the hairpin), with experiments pointing to both positions being possible (Malta et al., 2006; Skorvaga et al., 2002; Waters et al., 2006). Both would position the lesion in a position in which it could interact with tyrosine residues either on the surface of the hairpin (Sancar, Franklin and Sancar, 1984), or with Tyr92 via stacking interactions (Skorvaga et al., 2002).

### The UvrA$_2$B$_2$ Complex

Damage detection by NER revolves around the action of UvrA and UvrB, with these proteins forming a complex consisting of two UvrA molecules, and 2 UvrB molecules (Malta, Moolenaar and Goosen, 2007; Kad *et al.*, 2010). This complex is able to form in the absence of DNA, as well as in the presence of un/damaged DNA – with both UvrA and UvrB being in an ATP-bound state (Malta, Moolenaar and Goosen, 2007; Pakotiprapha *et al.*, 2008).

It has been previously suggested that within the complex UvrA is able to facilitate the wrapping of DNA around UvrB (Van Houten *et al.*, 1987; Shi *et al.*, 1992; Hsu *et al.*, 1994; Verhoeven, 2002), a process which is potentially coupled to the helicase activity of UvrB as a β-hairpin mutant of UvrB showed a lower degree of wrapping than the wild-type (H. Wang *et al.*, 2009). Recent models of the $UvrA_2B_2$ complex suggest that the core of the complex is formed from the UvrA dimer, being flanked on both sides by UvrB molecules (Jaciuk *et al.*, 2020) with a distance of 145 Å between them (Pakotiprapha et al., 2012).
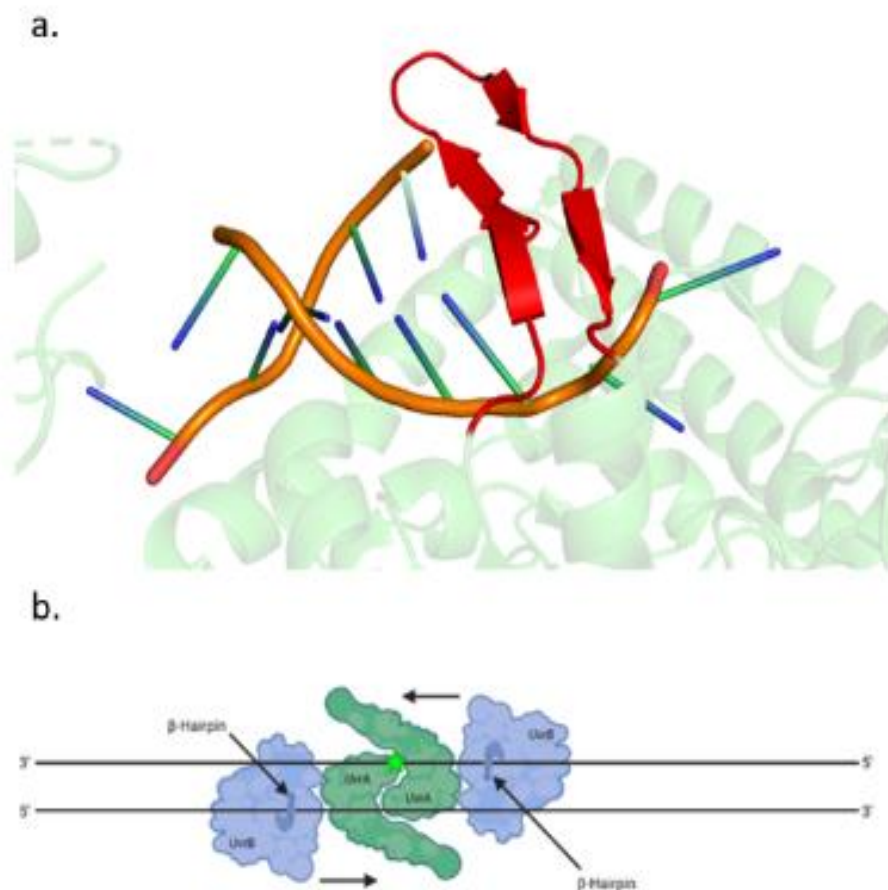


*Figure 39 – Diagram showing UvrB's β-hairpin clamping the DNA emerging from UvrA*

(a.) Crystal structure of the insertion of the β-hairpin of UvrB into the bound DNA molecule. (b.) Tt is thought that upon suspicion of DNA damage UvrB's β-hairpin clamps the 5' side of the DNA emerging from it's adjacent UvrA molecule, both UvrB's then translocate in the 3' direction until the UvrB clamping the damaged strand stalls at the lesion. This results in the dissociation of the other UvrB, prior to recruitment of UvrC to form the pre-incision complex. Created with BioRender.com.

UvrA and UvrB are contacted at 2 points, with the first being formed by the UvrB-binding domain of the first UvrA and domain 2 from its contacting UvrB. The second is formed between the signature II domain of the second UvrA and domain 1b of its contacting UvrB molecule. There is also potential for additional contacts to be formed between domain 4 of UvrB and the DNA-binding domain of UvrA due to their close proximity (Jaciuk et al., 2020).

Within this model the DNA is clamped by the β-hairpin of the UvrB, on the 5' side of the double-stranded DNA emerging from each side of the UvrA dimer, meaning each UvrB clamps a different strand of the DNA (Fig. 39). Both UvrB molecules are thought to translocate in the 3' direction (Jaciuk et al., 2020; Pakotiprapha et al., 2012) until the UvrB clamping the damaged DNA strand stalls at the lesion. The other UvrB dissociates, allowing for subsequent recruitment of UvrC to form the pre-incision complex.

## NER Damage Detection and Verification

It has been demonstrated that UvrA alone is able to form a function dimer and perform a 3D search of the DNA in the presence of ATP, characterised by purely static interactions with DNA for an average of ~2s (Barnett & Kad, 2019; Case et al., 2019), and is also able to hop between nearby DNA strands with an average distance of 1.2 μm (Barnett & Kad, 2019; Kad et al., 2010; Stracy et al., 2016). These hops involve the dissociation of UvrA from the DNA, followed by a short period of 3D diffusion, before reassociating with the same or a different section of DNA. This rapid reassociation is likely due to the high concentration of DNA present within the local environment (Houten and Kad, 2014). However, it has been noted that this 3D search alone would be wholly incapable of searching a large proportion of the *E. coli* genome within a single division cycle (Kad et al., 2010). Addition of UvrB results in the formation of the UvrA$_2$B$_2$ complex, collapsing UvrA's search mechanism into a 1D search whilst dramatically increasing DNA residence time (6-fold), characterised by random walks, directed motion, and paused motion (Kad et

al., 2010). Upon interaction of the $UvrA_2B_2$ complex with DNA, only 17% of complexes enter a motile state (Kad *et al.*, 2010). The complexes that remain static display lifetimes consistent with that of UvrA alone, suggesting that in the case of static $UvrA_2B_2$ complexes, UvrB does not significantly modify UvrA's mode of interaction with the DNA (Kad *et al.*, 2010). The complexes that enter the motile state display a 6-fold increase in their residence time on DNA, suggesting that in these cases UvrB is able modify UvrA's mode of interaction with the DNA. However, it is not currently clear what triggers this change (Kad *et al.*, 2010).

Interestingly, the experimentally derived 1D diffusion constant for the $UvrA_2B_2$ complex ($4.4 \times 10^{-4}$ $\mu m^2$ $s^{-1}$) is significantly slower than the theoretical maximum rate for rotation coupled diffusion ($2.1 \times 10^{-2}$ $\mu m^2$ $s^{-1}$) (Kad *et al.*, 2010). This suggests that whilst, in the case of motile complexes, UvrB modifies UvrA's mode of interaction with DNA, the $UvrA_2B_2$ complex still forms relatively stable non-specific interactions with the DNA backbone. Under the assumption that the $UvrA_2B_2$ steps along the DNA 1 bp at a time, it has been calculated that the energy barrier for diffusion for this complex would be 3.9 $K_BT$ (Kad *et al.*, 2010), significantly higher than the predicted energy barrier for efficient target location of 2 $K_BT$ (Slutsky and Mirny, 2004). It is currently not known why the $UvrA_2B_2$ complex faces such a large energy barrier, but it has been suggested that this may be due to the $UvrA_2B_2$ complex causing significant structural alterations to the DNA as it probes for damage (Kad *et al.*, 2010).

Whilst it was previously thought that the $UvrA_2B_2$ complex was the primary driver of damage detection during NER, *in vivo* studies found that within undamaged *E. coli* cells the majority of UvrB molecules remain diffusive within the cell (Stracy et al., 2016), indicating that the majority of UvrB molecules remain monomeric in solution during the search for DNA damage. This suggests, the seemingly more efficient search carried out by the $UvrA_2B_2$ is not the primary search mechanism within Prokaryotic NER, and hint at

the presence of an alternative DNA damage detection mechanism within Prokaryotic NER. Due to the diffusive nature of UvrB within undamaged *E.coli* cells this search is likely carried out by UvrA, with recruitment of UvrB from solution occurring upon location of DNA damage. To investigate this, we utilised a surface-based DNA assay to image high-speed UvrA-DNA interactions using iSCAT microscopy.

## 4.2 Methods

### Oligonucleotide List and Construct Design

The Damaged_98bp and Undamaged_98bp constructs are formed from 3 oligonucleotides: Digoxigenin-Labelled Oligonucleotide, Bridge Oligonucleotide, and either F26,50 Oligonucleotide or Undamaged F26,50 Oligonucleotide (for damaged and undamaged respectively). The Bridge Oligonucleotide is complementary to both the Digoxigenin-Labelled Oligonucleotide and the (undamaged) F26,50 Oligonucleotide, providing a 96 bp region of dsDNA. The fluorescein modification on the F26,50 Oligonucleotide is flanked by 25 nucleotides on either side, allowing room for the UvrA dimer to bind with a footprint size of 33 bp (Van Houten *et al.*, 1987; Jaciuk *et al.*, 2011). The undamaged_49bp construct is formed from the Digoxigenin-Labelled Oligonucleotide, and the Reverse Digoxigenin-Labelled Oligonucleotide, providing a 49 bp region of dsDNA for binding. All oligonucleotides were purchased from Eurofins Genomics, Germany.

| Oligonucleotide Name | Sequence |
|---|---|
| Digoxigenin-Labelled Oligonucleotide | 5'-[DIG]GCAGCGCAGGAATTCATCTGGGTGCGAGTAGGATGGGTAGTCCGACTCA-3' |
| F26,50 | 5'-GACTACGTACTGTTACGGCTCCATC[FlcdT]CTACCGCAATCAGGCCAGATCTGC-3' |
| Undamaged F26,50 | 5'-GACTACGTACTGTTACGGCTCCATCCTACCGCAATCAGGCCAGATCTGC-3' |
| Bridge Oligonucleotide | 5'-GCAGATCTGGCCTGATTGCGGTAGCGATGGAGCCGTAACAGTACGTAGTCTGAGTCGGACTACCCATCCTACTCGCACCCAGATGAATTCCTGC-3' |
| Reverse Digoxigenin Oligonucleotide | 5'-TGAGTCGGACTACCCATCCTACTCGCACCCAGATGAATTCCTGCGCTGC-3' |

| Construct Name | Constituent Oligonucleotides |
|---|---|
| Damaged_98bp | Digoxigenin-Labelled Oligonucleotide |
|  | Bridge Oligonucleotide |
|  | F26,50 Oligonucleotide |
| Undamaged_98bp | Digoxigenin-Labelled Oligonucleotide |
|  | Bridge Oligonucleotide |
|  | Undamaged F26,50 Oligonucleotide |
| Undamaged_49bp | Digoxigenin-Labelled Oligonucleotide |
|  | Reverse Digoxigenin-Labelled Oligonucleotide |

## Oligonucleotide Annealing

Equimolar concentrations of the constituent oligonucleotides for each construct were diluted to 1 μM in 1x TE buffer (10 mM Tris, 1 mM EDTA, pH 8). The oligonucleotide mix was heated at 95°C for 10 minutes, before being allowed to cool slowly to room temperature.

## Protein Labelling

All proteins were labelled at a 1:1:3 protein, to antibody, to Qdot ratio to maximise the probability that proteins were only singly labelled (Dunn *et al.*, 2011). UvrA (expressed and purified as previously described (Barnett and Kad, 2019)), Penta-His Mouse Antibody (Qiagen), and 605 nm quantum dots functionalized with Goat-Anti-Mouse IgG (Invitrogen) are mixed to final concentrations of 200 nM, 200 nM, and 600 nM respectively and incubated

at 4°C for 1 hr. Prior to loading into the flow chamber, labelled protein solutions were diluted to a final concentration of 5 nM. We have extensively shown previously that fluorescent labelling of UvrA does not affect its function (Kad et al., 2010; Barnett and Kad 2019).

## Experimental Setup

Prior to flow cell construction all slides and coverslips were rinsed sequentially with ethanol and water, dried under a constant stream of nitrogen, and processed for 2 mins in a Harrick Plasma PDC-32G Plasma Cleaner before subsequent treatment with 2% (3-aminopropyl)trimethoxysilane. Flow cells are constructed as described previously (Kad *et al.*, 2010). In brief, a microfluidic chamber is created from a standard glass microscope slide (with two 1 mm holes drilled 12 mm apart) and glass coverslip joined by an adhesive gasket. Polypropylene tubing is used to create an inlet and outlet tube, allowing for addition of experimental reagents to the flow chamber. This was followed by overnight incubation with 25 mg/mL mPEG$_{500}$ in 250 m NaHCO$_3$, pH 8.3. These flow cells were then washed with 400 µL 18MΩ water prior to incubation with 1x ABT buffer (50 mM Tris-HCl, pH 7.5, 50 mM KCl, 10 mM MgCl$_2$, 1 mg/mL BSA, 0.1% Tween-20, 0.02% NaN$_3$) for 1 hour. These were then washed with 400 µL 1x ABC buffer (50 M Tris-HCl, pH 7.5, 50 mM KCl, 10 mM MgCl2, 0.02% NaN$_3$) prior to incubation with 10 µg/mL anti-digoxigenin antibody (Roche) in 1x ABC buffer for 1 hour. Following a wash with 400 µL 1x ABC buffer, 1 nM annealed oligonucleotide in 1x ABC buffer was added and incubated for 30 mins, followed by a final wash with 400 µL 1x ABC buffer. 50 µL of 5 nM UvrA-Qdot and 20 nM unlabelled UvrA in 1x ABC buffer containing 1 mM nucleotide (ATP, ATPγS or ADP) was added to the flow cell and was immediately imaged on a custom-built iSCAT microscope. The maximum positional drift in X and Y was < 37.5 nm. All images were acquired at 500 fps, for a total of 30000 frames per video.

## Ratiometric and Image Processing

Ratiometric images were produced using a sliding window method, in which two sequential batches ($R_1$ and $R_2$) of N frames are averaged, normalised to their own maximum pixel intensity, and then divided ($R_2/R_1$) to produce a ratiometric image (Fig. 36b). As a result, these ratiometric images contain only features which have changed between $R_1$ and $R_2$. This process is repeated, advancing frame-by-frame through the whole image stack to produce a ratiometric movie. A bin size of 20 (N) was used for all image processing, giving a temporal resolution of 40 ms. The resulting images were convoluted with an experimentally extracted point-spread function (PSF) (Taylor *et al.*, 2019a), and a Gaussian filter (n = 2) was applied. All image processing was carried out using custom-written MATLAB software.

## Image and Data Analysis

All videos were converted into global kymographs (Fig. 36e), and a threshold applied based off the minimum measured contrast for the UvrA-Qdot complex, isolating peaks which correspond to binding and release events (single binding or release events were excluded as an accurate lifetime could not be estimated). Local minima and maxima along individual columns of the kymographs are located, and subsequently fitted to 1-D Gaussian distributions in the X and Y axis. To ensure the signal arises from a binder and not noise, the standard deviation of both axes of each peak were used to create a ratio describing the uniformity of the PSF. Any signals with a ratio of < 0.9 were excluded. Lifetimes were calculated from the difference between the peak minimum and peak maximum frames (Fig. 36f). Lifetimes for each condition were collated into a cumulative residence time distribution and were fitted as natural logarithms to a double exponential similarly transformed into linear space.

## 4.3 Results

### Digoxigenin Based DNA Surface Assay

To provide a platform for studying protein-DNA interactions, we developed a surface-based assay in which customisable DNA oligonucleotides labelled with digoxigenin are tethered to the surface via immobilised anti-digoxigenin antibodies. This assay provides an open platform through which a huge range of DNA-protein interactions can be studied effectively using iSCAT microscopy, due to the facile ability to modify the surface-tethered oligonucleotides with any commercially or in-house available DNA modifications.

#### Oligonucleotide Design

The surface oligonucleotide consists of 3 overlapping oligonucleotides, which are annealed together to form the final experimental oligonucleotide, these are the digoxigenin-labelled oligonucleotide, the bridge oligonucleotide, and the target oligonucleotide (Fig. 40). The digoxigenin-labelled oligonucleotide functions as the base of the assay, allowing for surface immobilisation of the completed oligonucleotide. The bridge oligonucleotide contains the complementary sequences for both the digoxigenin-labelled oligonucleotide, and the target oligonucleotide – bridging the two and allowing for formation of a single double-stranded oligonucleotide. Lastly, the target oligonucleotide is a fully customisable oligonucleotide which can be tailored to incorporate any modifications of interest – this provides a perfect basis for studying a huge range of protein interactions with specific DNA sequences, modifications, or synthetically introduced lesions. It should be noted however, a limitation in utilising this method lies in the inability to effectively simulate the cellular environment *in vitro*, as such the influence of factors such as molecular crowding, and obstacles on DNA (e.g., tertiary/quaternary structure, or other DNA-bound proteins) cannot be accounted for within this assay. To anneal the oligonucleotides, equimolar amounts of all three individual oligonucleotides are mixed,

these are then heated to 95°C for 10 minutes before being slowly cooled back to room temperature over 2 hours.
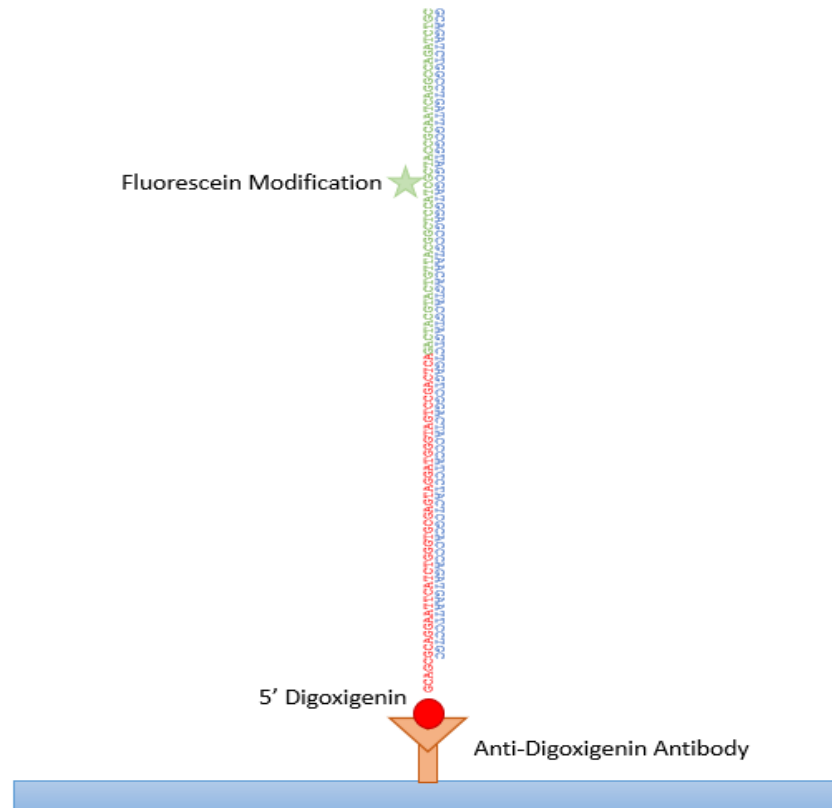


*Figure 40 - Digoxigenin labelled oligonucleotide design*

The Digoxigenin-labelled oligonucleotide is formed from 3 component oligonucleotides: the Digoxigenin oligonucleotide, the bridge oligonucleotide, and the target oligonucleotide. This system provides the facile ability to include specific DNA sequences, structures, or synthetically introduced adducts into the annealed oligonucleotide – providing a straightforward method to tailor the experiment to study a wide-range of DNA-protein interactions.

## Surface Preparation

Due to the sensitive nature of iSCAT to surface imperfections, preparation of microscope slides and coverslips is a key part of all experimental procedures. All slides and coverslips are first thoroughly rinsed with acetone and ethanol, before being immersed in 100% ethanol, and left shaking at 180 rpm for a minimum of 2 hours. Slides and coverslips are then removed from the ethanol, and sequentially rinsed with ethanol, $ddH_2O$, ethanol, and $ddH_2O$ before being dried under a constant stream of nitrogen. Slides and coverslips are then loaded into the chamber of a Harrick Plasma PDC-32G, and plasma cleaned at High RF for 2 minutes. This process strips the slides of all organic material, dramatically reducing the background noise present when imaged with iSCAT microscopy. Slides and coverslips are then removed from the plasma cleaner and immersed in 2% (3-aminopropyl)trimethoxysilane solution, and left shaking at 180 rpm for 2 minutes. Slides and coverslips are then immediately rinsed sequentially with ethanol and $ddH_2O$, before being dried under a constant stream of nitrogen. Slides and coverslips are then cured at 105°C for 30 minutes.

Following flow-cell assembly, all flow-cells are blocked overnight with 25 mg/mL $mPEG_{5000}$ in $NaHCO_3$ (pH 8.2) overnight – the SVA-labelled $mPEG_{5000}$ is able to covalently attach to the silanised glass surface, dramatically reducing non-specific binding of proteins. The following day, all flow-cells are rinsed thoroughly with water before being incubated with 1 mg/mL BSA, 0.1% Tween-20, 50 mM Tris-HCl, pH 7.5, 50 mM KCl, 10 mM $MgCl_2$. The addition of BSA further passivates the surface, and the Tween-20 works in combination with the $mPEG_{5000}$ to prevent non-specific binding. We have found that this combination of passivation methods significantly reduces non-specific binding of protein, whilst simultaneously providing a clean base for all experimental procedures.

# Interferometric Scattering Microscopy reveals protein-DNA interactions on a millisecond timescale

We were able to directly image the binding and release of Qdot labelled UvrA dimers from both damaged and undamaged DNA using iSCAT. This approach combines light scattering from labelled proteins in the sample with reflected light at the glass-water interface of the flow cell, leading to interference. Our *in vitro* surface-based assay (Fig. 41a) provides a target for UvrA dimer binding; digoxigenin-labelled dsDNA oligonucleotides (either labelled with a fluorescein moiety, or unlabelled) are tethered to the surface via an anti-digoxigenin antibody. Ratiometric imaging (Fig. 41b) allows us to
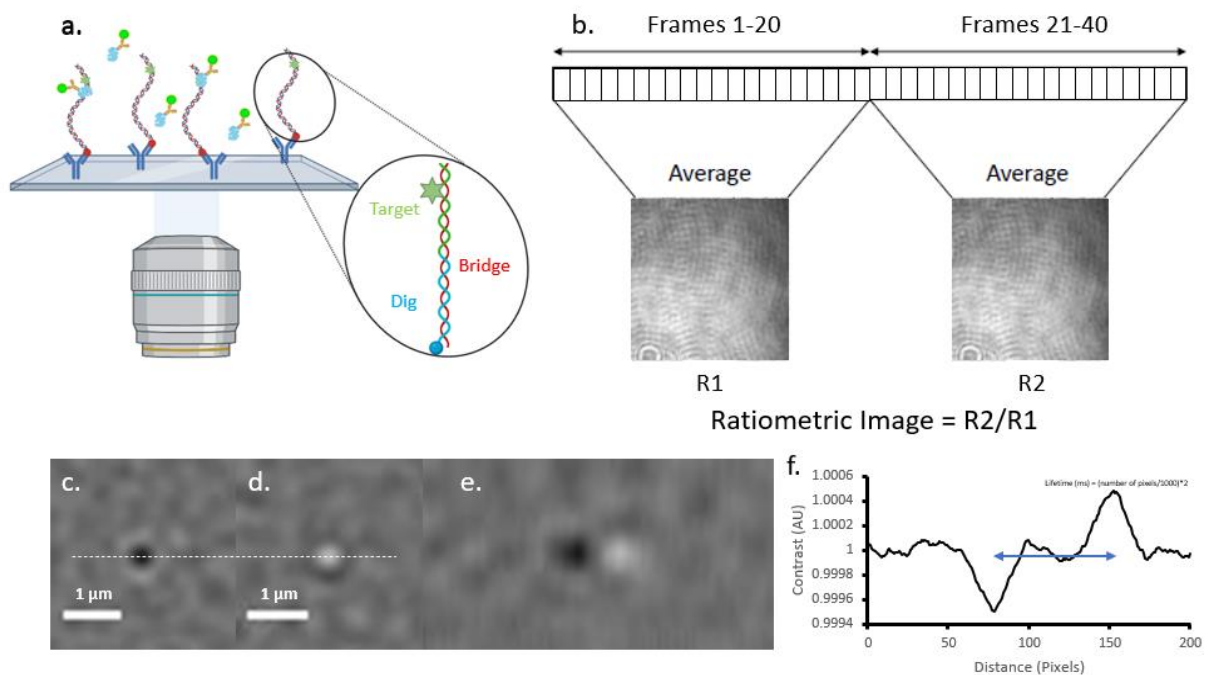


*Figure 41 - Ratiometric imaging reveals rapid binding and release events*

(**a**) The experimental setup used in this experiment, in which surface immobilised DNA oligonucleotides are targets for UvrA-Qdot protein complexes. Binding and release events are revealed through the use of (**b**) ratiometric imaging, a process in which dynamic features are revealed by dividing sequential batches of n frames – isolating features which change between frames n and n+1. (**c**) Binding and (**d**) release provide differential signals allowing for clear differentiation of lifetimes, as seen in (**e**) a kymograph of UvrA labelled with a 605 nm Qdot binding and releasing from DNA tagged with a fluorescein moiety. (**f**) The difference between peak contrast of binding and release provides the frames in which molecules bind and release, respectively. Lifetime is calculated from the 2*pixel difference/1000.

clearly resolve differential signals for binding (Fig. 41c) and release (Fig. 41d) of labelled-protein from DNA by isolating dynamic features within the sample, allowing for direct visualisation of UvrA dimer-DNA interactions and lifetimes (Fig. 41e) with an achievable temporal resolution down to 1 ms. In this study the temporal resolution is limited to 40 ms with a 20-frame bin to maximise the achievable signal-to-noise ratio when utilising Qdots as a scattering label. Since UvrA binds DNA as a dimer we henceforth use the term UvrA to describe the dimer.

## Quantum dots do not interact with DNA in isolation

To ensure that no lifetimes arise from non-specific interactions of Q-dots with the surface-tethered DNA molecules, we carried out the full experimental setup in the absence of UvrA, for both damaged and undamaged DNA. For both conditions a total of thirty 30000 frame videos were taken (500 fps) across 3 flow cells, equivalent to 10 minutes imaging time in each flow cell, and 30 minutes total imaging time. Across all videos no lifetimes were recorded, demonstrating that Q-dots in isolation do not display non-specific interactions with DNA within our experimental timescales. This aligns with previously reported observations (Dunn et al., 2011; Kad et al., 2010).

## UvrA-Qdot conjugates displays minimal interactions with the passivated coverslip surface

Due to the minimal spatial separation between the tethered DNA and the surface, it is possible that during imaging UvrA-Qdot conjugates could non-specifically interact with the surface of the coverslip – leading to the incorporation of erroneous lifetimes into our final analysis. To ensure that all lifetimes arise purely from protein-DNA interactions we added 5 nM of UvrA-Qdot conjugates to fully passivated flow cells containing no DNA tethers, recording thirty 30000 frame videos (500 fps), across 3 flow cells, equivalent to 10 minutes imaging time within each individual flow cell, and 30 minutes total imaging time. Whilst a small number if UvrA-Qdot conjugates were observed binding to the surface of the coverslip, there were no recorded lifetimes (binding and release from the same spatial

position, within one full 30000 frame video) across all recorded videos. This indicates that whilst the passivation of the surface does not fully prevent non-specific binding of UvrA-Qdot conjugates, it is effective in preventing repeated binding and release events on the time scales that are recorded within our experiments.

## Ratiometric imaging can artificially extend observed lifetimes

Due to the nature of ratiometric imaging oversampling within bin sizes can lead to artificial extension of observed lifetimes, as binding and release events are incorporated into an extended number of bin windows. To ensure no artificial extension of lifetimes occurred, a series of videos were taken of UvrA-Qdot conjugates interacting with surface-immobilised DNA, at a frame rate of 500 fps. The resulting videos were then processed with a series of different ratiometric bin sizes (ranging from 10-150 frames), these were then analysed to find binding and release events, and the lifetimes were extracted from these to allow for comparison between bin sizes.

As can be seen in Fig. 42, the minimum lifetime observed was 146 ms – which was observed with bin sizes between 10 and 50 frames. It can be seen that excessive ratiometric imaging starts to artificially extend the observed lifetimes, with bin sizes of 100 frames and 150 frames leading to extended lifetimes of 200 ms and 232 ms respectively. This can also be seen within the binding and release kymographs, where the centre of the binding and release events become artificially extended – resulting in the increased lifetime. For all following UvrA experiments a ratiometric bin size of 25 frames was used, with an acquisition frame rate of 500 fps. These conditions were selected as no lifetimes below 75 ms were observed, and these conditions did not artificially extend the observed lifetimes whilst allowing sufficient signal-to-noise ratio to allow for effective lifetime detection.

| Bin Size | Binder Kymograph | Extracted Lifetime |
|:---:|:---:|:---:|
| 10 | | 146 ms |
| 25 | | 146 ms |
| 50 | | 146 ms |
| 100 | | 200 ms |
| 150 | | 232 ms |
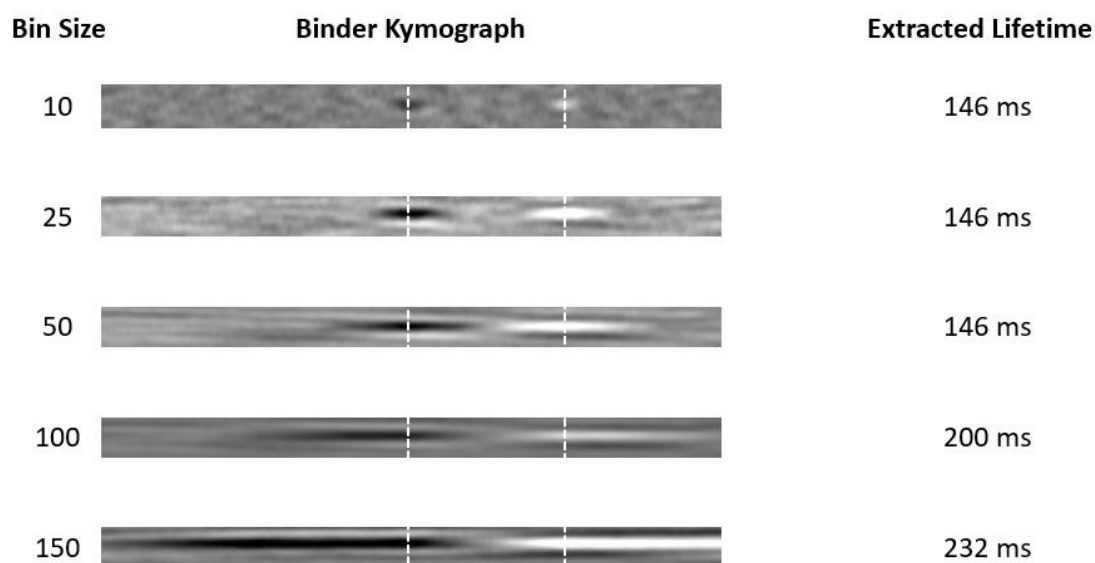
*Figure 42 - Excessive ratiometric imaging artificially extends lifetimes*

To ensure correct preservation of all lifetimes, we have to ensure that the correct bin size for ratiometric imaging is used to avoid artificial extension of lifetimes. A sample binding and release event of UvrA-Qdot from undamaged DNA was process with 5 different bin sizes, 10-150 frames. When the lifetime is plotted as a kymograph it is clear to see the artificial extension that occurs with extreme ratiometric processing, with the lifetime being extended at bin sizes of > 50 frames. The lifetime becomes artificially increased by 54 ms between 50 and 100 bin sizes, and 32 ms between 100 and 150 bin sizes. This highlights the need for ratiometric imaging to be carefully tailored to the observed lifetimes. Due to this we limit our ratiometric image processing to a bin size of 25, in combination with 500 fps frame rates we are able to clearly resolve lifetimes with no artificial

## Lifetime Detection

To aid with efficient lifetime detection and computational processing, we developed a custom written MatLab program which automates detection of lifetimes after ratiometric image processing. Following image processing, videos are converted into global kymographs – where each row within the image is projected into a kymograph, resulting in each frame being a kymograph of one row from the original image (see Fig. 44a). An upper and lower threshold is then applied to these images based on the upper and lower values for the observed contrasts of individual Q-dots (Fig. 43). This isolates signals which are likely to be the result of a Q-dot binding/releasing from the surface-immobilised DNA.
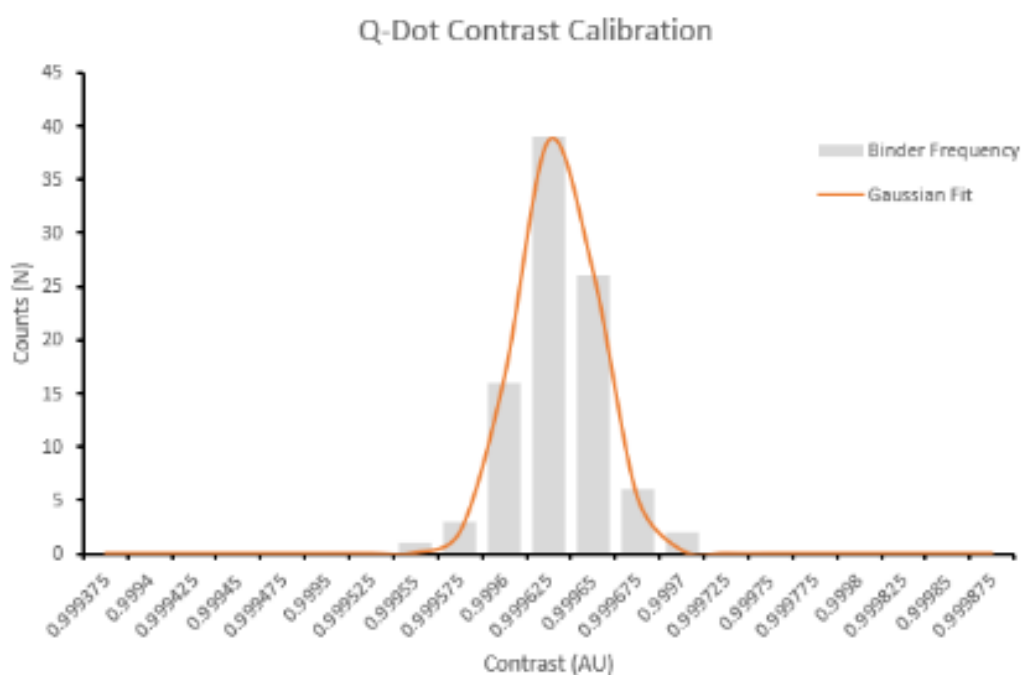


*Figure 43 – Q-dot Contrast Calibration*

Histogram of observed contrasts for individual Qdots landing on the surface of a glass coverslip, from this distribution we are able to set the threshold values for lifetime detection. The upper and lower thresholds are taken as the maximum and minimum detected contrasts for single Qdots.

To detect binding events, local minima are detected within each column of the kymograph (equivalent to one pixel across the entire video). Upon detection of a point of local minima, the X-axis is fit with a 1D Gaussian, as given by:

$$f(x) = a * \exp\left(\frac{(x - b)^2}{2c^2}\right)$$

Where $a$ is the height of the peak, $b$ is the mean position of the peak, and $c$ is the spread of the peak. This returns the centre of the PSF of the binder in the X-axis – this position is then used to fit a 1D Gaussian to the Y-axis, which combined together with the original fit provides the central coordinates of the binder (Fig. 44c). To ensure that the signal arises from a binder, a ratio is created from the smallest $c$ value (spread of the peak), to the largest – this ratio describes the uniformity of the PSF. Any detected signals with a uniformity ratio of < 0.9 are rejected, as the signal likely arises from random noise within the image, rather than binding of a particle.

If the signal is confirmed to arise from a binding event, local maxima events are then detected in the remainder of the kymograph for the corresponding spatial position. If an event is found, the same process as above is carried out – fitting X and Y Gaussians to the detected release event, and confirming the uniformity of the PSF. If a release event is
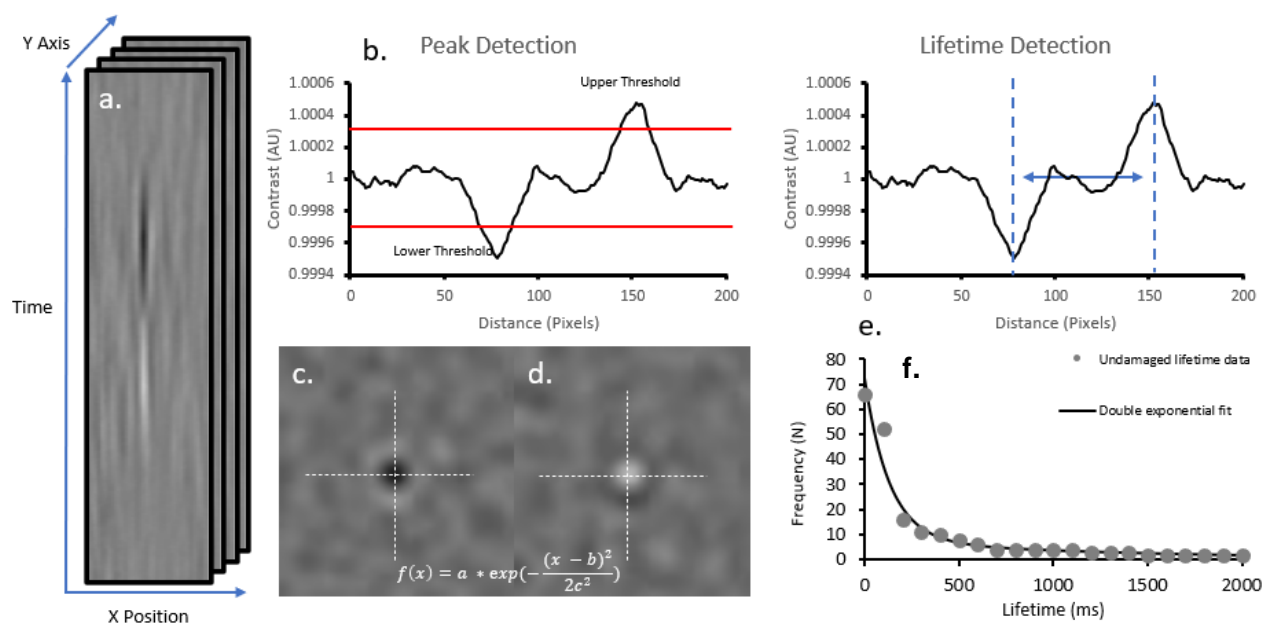


*Figure 44 - Lifetime detection and analysis*

The image stack undergoing analysis is first converted into a global kymograph (**a**) in which the x-axis represents one row of pixels from the ratiometric image, and the y-axis represents time – whilst the y-axis of the ratiometric image stack is converted into the z-axis of the global kymograph (i.e., every frame of the global kymograph represents how one row of pixels from the ratiometric video changes over time). For each pixel along the x-axis an intensity profile is plotted (**b**), and local points of maxima and minima are identified, with a lower and upper threshold being applied for binding and release respectively. These threshold values are calculated based on experimentally extracted contrasts for individual Qdots. Upon location of points of maxima and minima, the PSFs for the particles at those times are extracted (**c**), and a 1D Gaussian is fit in the X and Y axes for both binding and release PSFs. To assess the ellipticity of the particle causing the binding/release signal, a ratio of the smallest to the largest c value (the spread of the Gaussian fit) is created, and signals with a ratio < 0.9 are rejected as arising from noise. The lifetime of confirmed binding and release events (**e**) is then calculated as the distance between the frames at which the local minima, and subsequent local maxima are reached. Lifetimes are then collated and used to create a cumulative residence time distribution, which subsequently undergoes a natural logarithmic transformation. This is then fit to a double exponential in linear space (**f**) to extract the dissociation rate constant and respective amplitudes of the two populations.

found and confirmed to arise from a particle with a contrast corresponding to that of the binding event - a lifetime is recorded as the distance between the points at which maximum contrast is reached upon binding and release (Fig. 44d). This process is then repeated across all columns within the global kymograph (excluding events that occur in the same spatial position as previously recorded events, ensuring lifetimes are not recorded multiple times). Following lifetime detection, all detected lifetimes are collated and plotted as a cumulative residence time distribution. This cumulative residence time distribution then undergoes a natural logarithmic transformation and is fit to a double exponential equation in linear space, as given by:

$$f(x) = (a_1 * e^{(-k_1 * x)}) + (a_2 * e^{(-k_2 * x)})$$

Where $a_1$ and $a_2$ are the amplitudes of the two populations, and $k_1$ and $k_2$ are the dissociation rate constants of the two populations. The amplitudes represent the size of each population, whilst the dissociation rate constants give the number of dissociations occurring per second within each population; this can be converted to lifetime in seconds by taking the reciprocal of the $k$ for each population.

## UvrA displays rapid interactions with both damaged and undamaged DNA

It is known that UvrA uses a 3D mechanism, where it attaches to DNA and then leaves without sliding, to search DNA for damage (Kad *et al.*, 2010; Stracy *et al.*, 2016; Barnett and Kad, 2019), however, given the lifetimes of interaction and footprint size this search mechanism would not be sufficient to search the entirety of an *E. coli* genome within a single division time (Kad *et al.*, 2010). Additionally, it has been suggested that rather than the more efficient UvrA$_2$B$_2$ complex being the primary damage-sensing species within NER, UvrA instead recruits UvrB from solution upon location of damage (Stracy *et al.*, 2016). Therefore, to search effectively UvrA may locate damage first using an alternative, faster, mechanism of search.

To investigate this, we analysed high-speed UvrA interactions with both damaged (Damaged_98bp, using fluorescein-dT, which is a well-established damage analogue (DellaVecchia *et al.*, 2004)) and undamaged DNA (Undamaged_98bp). 5 nM Qdot-labelled UvrA was mixed with 20 nM unlabelled UvrA (resulting in a final concentration of 25 nM) in the presence of 1 mM ATP, leading to the formation of UvrA dimers that are mostly labelled with a single Qdot. Post ratiometric processing, UvrA-DNA lifetimes appear as a black spot (with a contrast similar to that of a single Qdot, consistent with the single-labelling of UvrA dimers described above), followed by a white spot in the same spatial location. Lifetimes are calculated by taking the distance between the frame in which peak contrast is reached upon binding, and the frame in which peak contrast is reached upon release. Individual lifetimes were plotted as cumulative residence time distribution and fit to double exponentials following natural logarithmic transformation to linear space (Fig. 45). The use of the cumulative residence time distribution rather than a histogram, allows for bin-width independent assessment of the rate constants and relative amplitudes and provides better sensitivity for small populations (Kastantin and Schwartz, 2013). Single exponential fits did not adequately describe the data (Fig. 45 dotted lines), nor did triple exponential fits, consistently providing two identical populations. These fits provide DNA dissociation rate constants ($k$), and amplitudes corresponding to relative populations for each rate constant.

The rate constants for UvrA release on undamaged DNA (Fig. 45a) was 7.6 ±1.69 $s^{-1}$ and 1.4 ±0.46 $s^{-1}$, versus 7.8 ±2.27 $s^{-1}$ and 1.3 ±0.18 $s^{-1}$ on damage-containing DNA (Fig. 45b). The relative proportions of fast to slow lifetimes were 90.25 ±14.44 to 9.75 ±1.95 for undamaged DNA, and 78.13 ±20.13 to 21.87 ±5.32 for damage-containing DNA, indicating the dominant form of UvrA interactions with DNA are the fast lifetimes. The difference between relative amplitudes of the slower lifetime populations between damaged and undamaged DNA is shown to be statistically significant (p < 0.00 The $r^2$ values for the double

exponential fits were 0.97 and 0.96 for the undamaged and damagaed fits respectively, as opposed to $r^2$ values of 0.71 and 0.67 for single exponential fits.
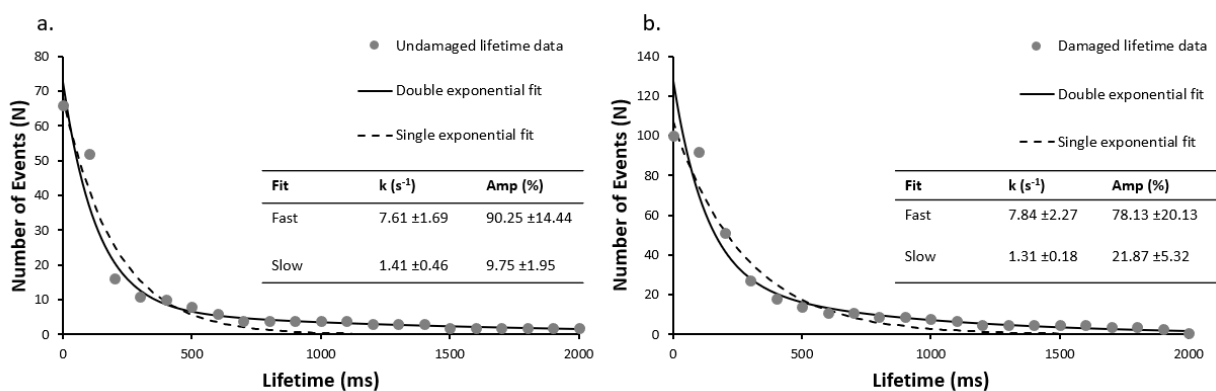


*Figure 45 - Rapid Single-Molecule kinetics of UvrA on damage and undamaged DNA*

Attached lifetimes obtained from ratiometric images were compiled into cumulative residence time distributions. In the absence of damage (Undamaged_98 bp) (**a**) two clear populations are seen with a predominant fast rate constant of 7.61 ±1.69 s$^{-1}$, and a slower rate constant of 1.41 ±0.46 s$^{-1}$ ($r^2$ = 0.97 vs 0.71, for double and single exponential fits respectively). With fluorescein-damage (Damaged_98 bp) (**b**), two populations ($r^2$ = 0.96 vs 0.67, for double and single exponential fits respectively) are again seen with the faster population predominant again, at 7.84 ±2.27 s$^{-1}$, matching well with the fast population observed on undamaged DNA.

We hypothesised that these faster events could include a localised diffusive search. Unfortunately, the architecture of this assay means a signal for movement along the DNA is not present; therefore, we reduced the length of the undamaged DNA oligonucleotide from 98 bp to 49 bp (Undamaged_49 bp). As seen in Fig. 46a, the double exponential fit of the lifetime cumulative residence time distribution for the shorter DNA construct results in a fast dissociation rate constant of 7.5 ±0.93 s$^{-1}$ in good agreement with the rate constant for the 98 bp undamaged DNA (7.6 s$^{-1}$), and a slow rate dissociation constant of 0.68 ±0.12 s$^{-1}$. The $r^2$ value for the double exponential fit was 0.98, versus the $r^2$ value of 0.55 for single exponential fit. This suggests that the lifetime of UvrA's interaction with DNA is not limited by the DNA length. The observed slow dissociation rate constants are consistent with UvrA:DNA interactions in which UvrA hydrolyses 2 ATP molecules, with an ATP turnover rate constant of ~1-2 ATP/s (Barnett and Kad, 2019; Case *et al.*, 2019) – however, these

are more challenging to assign due to the low number of observed slow events and limited acquisition times. Herein lies the primary limitation within these data, with the difficulty posed in accurately assigning populations with the low count statistics. A key advantage presented with the use of iSCAT microscopy is the theoretically unlimited imaging times that are permitted due to the non-degradative nature of scattering. As such, these data would greatly benefit from vastly increased imaging time, to increase the number of
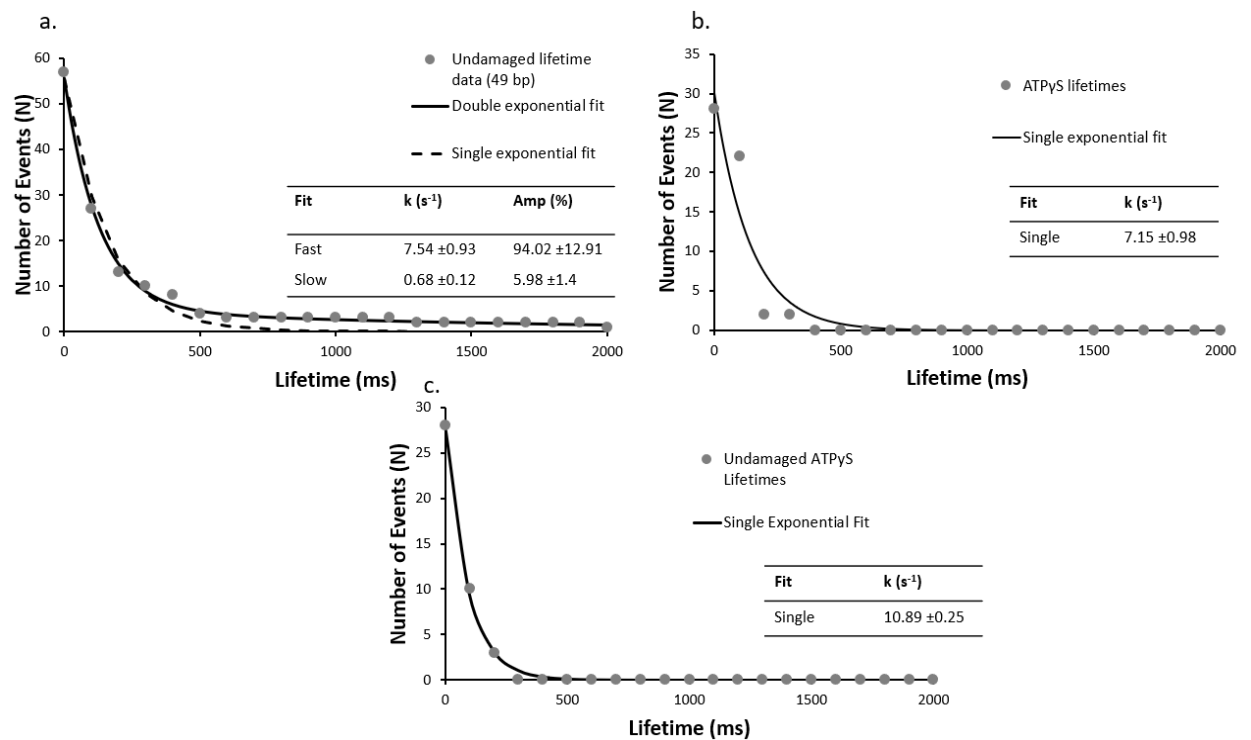


*Figure 46 - DNA length has no impact on fast lifetimes, but in the presence of ATPγS UvrA loses the slow phase*

Cumulative residence time distributions with a shorter (Undamaged_49 bp) undamaged DNA construct (**a**), are unchanged kinetically from the 98 bp construct suggesting the lifetimes are not limited by sliding off the DNA ($r^2 = 0.98$ vs 0.55, for double and single exponential fit respectively). UvrA interactions were also studied on (**b**) 98 bp damaged DNA (Damaged_98 bp) and (**c**) 98 bp undamaged DNA (Undamaged_98 bp) in the presence of 1 mM ATPγS where no slow events were seen. The observed interactions fit well to a single exponential with a detachment rate constant of 7.15 ±0.98 s$^{-1}$ and 10.89 ±0.25 s$^{-1}$ for damaged and undamaged DNA respectively ($r^2 = 0.99$ and 0.91 for single exponential fit on undamaged and damaged DNA respectively).

recorded events and allow for a more accurate assignment of the populations observed. This is a key limitation in the within this study, and future investigations should ensure that this feature of iSCAT microscopy is utilised to its fullest.

## ATP analogues dramatically reduce UvrA damage detection

Use of alternative nucleotides, ATPγS (a non-hydrolysable ATP analogue) and ADP, dramatically affected the interaction of UvrA with DNA containing a fluorescein lesion (Damaged_98bp) and undamaged DNA (Undamaged_98bp). In the presence of ATPγS only fast events were seen, with a detachment rate constant of 7.15 s$^{-1}$ (139 ms interaction lifetime) and 10.89 s$^{-1}$ (92 ms interaction lifetime), on damaged (Fig 46b.) and undamaged DNA (Fig. 46c) respectively. Furthermore a ~5-fold reduction in the average number of observed events in the presence of ATPγS relative to ATP with a damage-containing DNA construct was observed. This indicates that ATP turnover is necessary for loading UvrA
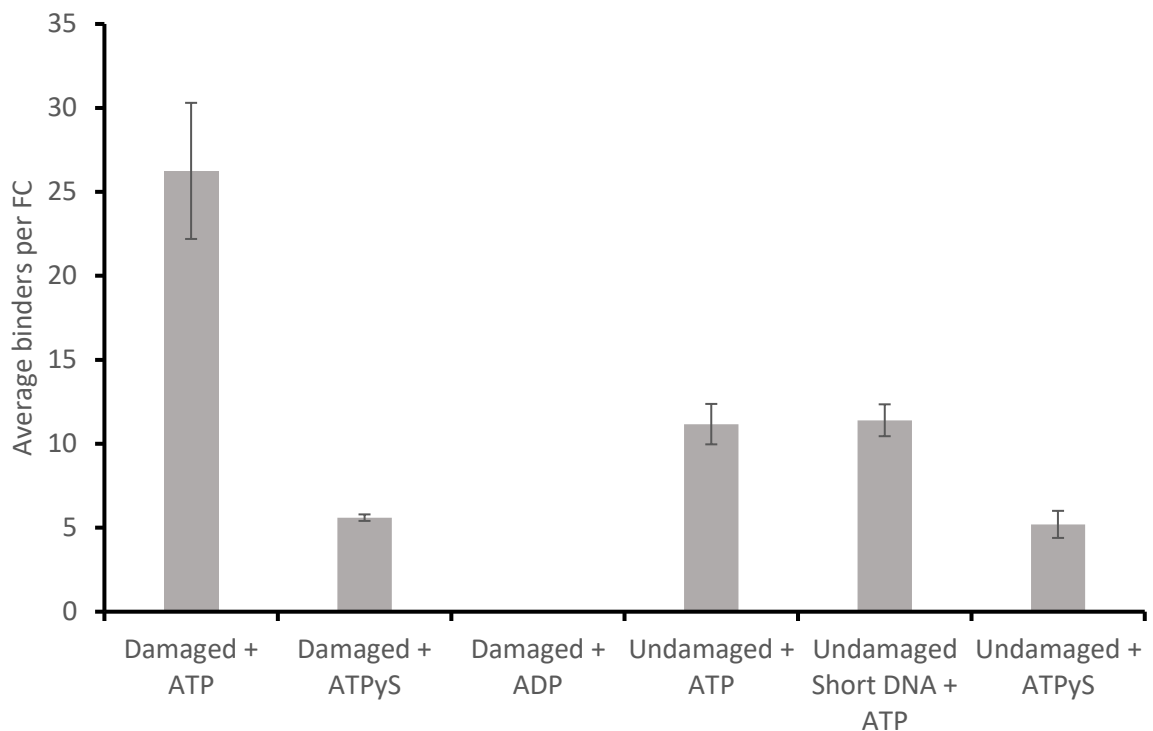


*Figure 47 - ATP hydrolysis precedes DNA binding of UvrA*

A comparison of average number of binders, n, per flow cell in different experimental conditions. All averages were calculated from equivalent numbers of observations (10 videos per flow cell, across 6 flow cells, equal to a total 60 minutes of imaging per experimental condition). ATPγS significantly reduces the number of binders in the presence of fluorescein-damaged DNA (27 per flow cell vs 6 per flow cell), and in the presence of undamaged DNA (12 per flow cell vs 5 per flow cell), whilst ADP completely eradicates observable attachments to fluorescein-damaged DNA.

onto the damage. In addition, the presence of ADP eradicates all interactions of UvrA with damaged DNA (Fig. 47). It has been previously found that ADP inhibits the interactions of UvrA with DNA due to its affinity for the distal UvrA ATPases (Case et al., 2019), suggesting that in the presence of ADP fewer UvrA dimers are present in solution (Seeberg and Steinum, 1982). Additionally, in the absence of ATP, no interactions were seen between UvrA and DNA.

## 4.4 Discussion

Due to the vast quantity of non-target DNA, the search for damaging lesions by DNA repair systems presents a considerable challenge. A number of mechanisms have been proposed to accelerate the search (von Hippel & Berg, 1989b), however the search is limited by the lifetime of each visit to the DNA and number of proteins. UvrA is a dimeric molecule that has been implicated in searching DNA for damage (Croteau et al., 2006; Orren & Sancar, 1989) in bacteria. However, its long-attached lifetime (Barnett & Kad, 2019; Kad et al., 2010; Stracy et al., 2016), small footprint (B Van Houten et al., 1987), and relatively low abundance (Karsten Theis et al., 2000) suggest it cannot search the entire genome before cell division. Here we use interferometric scattering microscopy (iSCAT) to determine the lifetime of UvrA's (the term UvrA is used here to describe the dimer form) interaction with DNA. We find UvrA's interaction consists of two phases, one consistent with that expected from ATPase measurements (Barnett & Kad, 2019; Case et al., 2019), and a faster phase with an average interaction time of 130 ms. This is supported by our observation that UvrA's lifetime in the presence of the non-hydrolysable analogue ATPγS eliminates the slower phase, but not the rapid lifetimes. Furthermore, the length of the target DNA molecule does not affect this rapid lifetime suggesting UvrA exclusively uses a 3D search rather than a limited 1D search. Altogether, these data suggest UvrA searches the genome efficiently using an ATP-independent rapid search, followed by ATP turnover at suspected damage sites.

## Interferometric Scattering Microscopy provides an ideal methodology for studying rapid protein-DNA interactions

iSCAT microscopy has a number of features that make it stand out as an exciting methodology in the study of a number of biological systems, such as a high temporal resolution, precise spatial resolution, the ability to track motion in the Z-axis, whilst also allowing for determination of complex stoichiometry in an unlabelled manner. All these features make iSCAT microscopy an ideal method for the study of protein-DNA interactions. We have clearly demonstrated here that iSCAT microscopy is able to reveal interactions on timescales which have not been observed previously – and believe it can be more widely applied to the study of a number of other interactions.

Utilisation of the surface-based digoxigenin-labelled DNA assay provides a perfect base for the study of these interactions, whilst remaining hugely customisable with the facile ability to modify the target DNA to introduce any synthetic labels, lesions, or DNA modifications. In combination with iSCAT microscopy we are able to reveal and understand protein-DNA interactions on a level that has not been examined before, however there is much more room to expand the potential of the assay and to further the use of iSCAT microscopy in the study of protein-DNA interactions.

The ability of iSCAT to allow for imaging of unlabelled single proteins allows for investigations not permitted via other methodologies. Direct unlabelled imaging of proteins directly interacting with DNA removes the additional complications that are imposed through the use of labels such as Quantum Dots or AuNPs. However, it should be noted that reaching this level of sensitivity presents a number of challenges. The key challenge being maintenance of the achievable temporal resolution, due to the requirement for temporal averaging of frames, followed by ratiometric processing to reduce shot noise to a point at which unlabelled proteins can be resolved (Young et al., 2018). As we detailed previously, extreme levels of ratiometric binning can lead to the artificial modification of

lifetimes – meaning that the frame rates, temporal averaging, and ratiometric binning would all need to be carefully modulated to ensure that true lifetimes were being observed. However, there are a few additional considerations that would make this more feasible. The key area which can be dramatically improved is the camera which is being utilised for imaging, our current system allows us to image a small area (64x64 pixels) at frame rates approaching 3000 fps – however, it is possible to utilise high speed cameras which can record at frame rate of 114,700 fps whilst maintaining a similar field of view (Taylor et al., 2019). This would allow for incredibly high-speed imaging of these interactions, whilst also providing more than ample frames for temporal averaging, and ratiometric imaging does have a few drawbacks. The first is the extreme cost for these cameras, and secondly the sheer volume of frames produced by cameras which are operating at these frame rates increases the computational load by many orders of magnitude meaning significant investment into this area would also be required. However, as high-speed cameras, more powerful processors, and large-scale data storage solutions become more affordable, such implementations may become more accessible to the wider research community. Opening a huge number of opportunities for even deeper investigations into protein-DNA interactions.

An alternative expansion would be to move away from a ratiometric imaging regime, instead utilising the flat-field correction of the static background  allowing us to visualise the interaction for its entire duration rather than just attachment and release. This could comfortably be achieved using proteins labelled with AuNPs due to their dramatically increased contrast versus labels of similar sizes (e.g., Quantum Dots). Of particular interest would be the application of Z-axis tracking of protein mobility of DNA – one could envision an assay in which direct attachment of processive DNA binding proteins (e.g., exo- or endonucleases) is imaged with an axial spatial-resolution reaching a handful of base-pairs – which could provide key insights on how proteins such as these are able to interact and remove/repair DNA lesions in real time. In combination with the relative

simplicity to tailor surface-immobilised target DNA with the assay we have previously described, this would provide a powerful tool for investigating specific protein interactions with their specific target sites/lesions in a way that has not been achieved before.

## UvrA alone is able to effectively search the *E. coli* genome via a 3D search mechanism

UvrA interacts statically with DNA leading to binding events with a lifetime of ~1-3 seconds (Barnett & Kad, 2019; Stracy et al., 2016). It has been previously suggested that the formation of the $UvrA_2B_2$ complex on DNA is driven by recruitment of UvrB from solution by UvrA bound to sites of damage (Stracy *et al.*, 2016). This would suggest that the time taken for locating damage by UvrA is a key factor within this process. To calculate how this lifetime relates to the proportion of the *E. coli* genome that can be searched by UvrA within a single *E. coli* division cycle we employed a simple exponential distribution of the Poisson process:

$$\% \ of \ genome \ searched = \ 1 - \ e^{(-\tau x)}$$

Where *x* is time, and ᴛ is the proportion of DNA searched by the total number of UvrA dimers within a cell per second:

$$\tau = \frac{\left( n * \left( \frac{UvrA \ footprint \ (bp)}{DNA_{tot} \ (bp)} \right) \right)}{Lifetime \ (s)}$$

Where *n* is the total number of UvrA dimers present within the cell, the *UvrA footprint* is 33 bp (Van Houten et al., 1987), *Lifetime* is the duration of interaction, and $DNA_{tot}$ is the total amount of DNA that needs to be searched. The  basal level of UvrA within a cell has been estimated from 9-129 depending on conditions (Sancar and Sancar, 1988; Schmidt *et al.*, 2016; Stracy *et al.*, 2016; Ghodke, Ho and van Oijen, 2020), here we take the canonical measurement of 20 (Sancar and Sancar, 1988) this is the equivalent to 10 dimers. During SOS response UvrA is upregulated, resulting in ~200 copies of UvrA equivalent to 100

dimers. With the average division time of an *E. coli* cell at 25ºC being 90 minutes (Kumar and Libchaber, 2013), we can see in Fig. 48a that UvrA is unable to search the majority of DNA within an *E. coli* cell, reaching a total coverage of ~18% going up to ~86% during SOS over the 90-minute period. This highlights the vast inadequacy of this 3D search mechanism with a lifetime of 2 second.

 However, incorporation of the rapid 130 ms lifetime that we have observed leads to a dramatic increase in the proportion of DNA searched by UvrA within a single division cycle, allowing UvrA to reach 94% coverage of the *E. coli* genome within ~90 minutes (Fig. 48b). Upon induction of the SOS response this search time drops again, resulting in 95% coverage of the *E. coli* genome being reached in ~9 minutes. We previously thought that the 3D search mechanism of UvrA would prove wholly incapable of providing an efficient search mechanism within *E. coli* (Kad *et al.*, 2010; Van Houten and Kad, 2014) – however these results indicate the larger role played by UvrA acting alone during the early stages of DNA damage detection within NER.
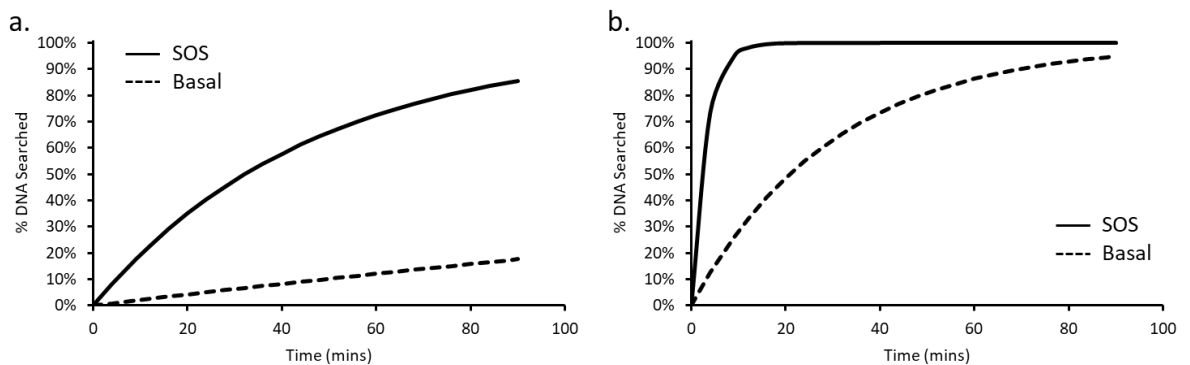


*Figure 48 - Predicting the percentage of E. coli genome searched by UvrA in a single division cycle*

The percentage of the E. coli genome searched by UvrA is plotted against time, for an average lifetime of 2 s, (**a**) showing that after 90 minutes only 18% of the genome is searched by basal levels of UvrA (dashed line) vs 86% at SOS levels (continuous line). Predicting the genome search time for the faster, 130 ms, lifetime measured here (**b**) suggests 95% of the genome is searched within 90 minutes without SOS levels of UvrA (continuous line). Whereas 95% of the genome is searched after only ~9 minutes at SOS protein levels (dashed line).

This process could work in combination with the ability of UvrB to form the UvrA$_2$B$_2$ dimer (Malta, Moolenaar and Goosen, 2007; Kad *et al.,* 2010),  collapsing the 3D search of UvrA alone into a 1D search by the UvrA$_2$B$_2$ complex. This 1D search is the most efficient form of damage detection within NER (Kad et al., 2010) – however, it has been noted that during *in vivo* experiments the vast majority of UvrB remains diffusive within solution (~90%) (Stracy et al., 2016). It is possible that the rapid search by UvrA bridges these two observations and allows for rapid search of the DNA by UvrA, leading to the recruitment of UvrB from solution upon location of DNA damage. However, further work needs to be carried out to understand how these processes are connected. Together these search mechanisms could provide an effective combination of 3D and 1D searches allowing for an entire *E. coli* genome to be effectively searched by a small number of proteins within a single division cycle.

## UvrA adopts a low energy cost search mechanism

As detailed above, it has been previously found the UvrA interactions with DNA lead to static binding events with a lifetime of ~2 seconds along with an ability to hop to nearby DNA molecules (Barnett & Kad, 2019; Kad et al., 2010; Stracy et al., 2016). During this period, 2 molecules of ATP would be consumed (Barnett & Kad, 2019; Case et al., 2019), resulting in a high energetic cost per interaction.

We confirmed that the rapid interactions we have observed do not consume ATP through the use of the non-hydrolysable ATP-analogue ATPγS, which eliminates slower lifetimes. The consequence of a non-ATP consuming process as a first means to detect DNA abnormalities results in a dramatically reduced energetic cost for the cell. Longer, ATP-consuming, interactions were detected by iSCAT in both the presence and absence of damage, consistent with previous studies (Barnett & Kad, 2019; Case et al., 2019; Stracy et al., 2016), however their prevalence was much lower. This suggests that the first step in damage detection is performed by UvrA without requiring ATP. We propose that this cursory

check is followed by an ATP-requiring second check, before the next ATP-consuming event that loads UvrB (Sancar and Rupp, 1983; Yeung *et al.*, 1983; Barnett and Kad, 2019; Case *et al.*, 2019). This means, based on the UvrA ATPase turnover rate of 1 ATP/UvrA-monomer/second, that within a typical *E. coli* doubling time at 25°C of 90 minutes (Kumar and Libchaber, 2013), the entirety of the genome, 4.6 million base pairs, could be searched with a maximum energetic cost of ~110 000 ATP molecules; however since only 10% of UvrA molecules enter the slow phase the better estimate of energetic cost is ~ 11 000 ATP molecules equivalent to $3.3 \times 10^5$ kJ/mol.

## The role of ATP in the fast-association rate of UvrA

The structure of DNA is altered by the presence of a lesion, with more distorting lesions being excised with greater efficiency (Van Houten *et al.*, 2005). UvrA plays a clear role in this recognition process since its affinity for DNA has been shown to be greater in the presence of damage (Croteau *et al.*, 2006; Jaciuk *et al.*, 2011). Here, we show that UvrA binds to DNA ~2-fold more frequently in the presence of damage, suggesting that the increased affinity of UvrA for damage is mediated by the attachment rate constant. This would suggest that UvrA binds to DNA in a conformation that stabilizes the damaged DNA (conformational selection) rather than through induced fit. The correct nucleotide occupation of the ATP-binding sites on UvrA appears crucial to permitting damage detection and even DNA binding. UvrA with ATPγS was found to bind to damaged and undamaged DNA with much lower frequency than UvrA with ATP. Indeed, the level of binding to DNA was lower than expected if only the slow phase events were absent (which was observed). This suggests ATPγS drives UvrA in a lower affinity form for DNA binding, but not as low as in the absence of ATP which showed no binding in these experiments. Recent studies of UvrA's ATPase have indicated that the proximal and distal ATP-binding sites attain an asymmetric nucleotide bound state (proximal-ATP:distal-ADP) prior to interacting with DNA; upon meeting damage the distal site is activated (Case *et al.*, 2019). In an elegant crosslinking study, ATP hydrolysis at this distal site was linked to the movement of the third

zinc finger (zinc finger 3) over the DNA (Kraithong *et al.*, 2017), that was previously implicated in damage recognition (Croteau *et al.*, 2006; Wagner, Moolenaar and Goosen, 2011). Therefore, with ATPγS UvrA cannot assume the conformation needed to select for damaged DNA. Furthermore, once damage is located, ATP hydrolysis at the distal site would be needed to confirm its presence before recruiting UvrB.

## A model for DNA damage detection by UvrA

Here we present a model for the early, ATP-independent, damage detection of UvrA (Fig. 49). UvrA utilises a 3D search mechanism and upon binding DNA remains statically bound for ~130 ms. During this time, no ATP is hydrolysed but the DNA is inspected, possibly by the movement of zinc finger 3 (Kraithong *et al.*, 2017). If no damage is detected the UvrA dimer is able to dissociate from the DNA, from here it returns into solution with an increased probability of reassociating on another nearby DNA strand due to the high-local concentration of DNA within a cell. However, if zinc finger 3 detects a site of suspected damage, UvrA hydrolyses ATP to lock it onto DNA for subsequent damage verification, which if detected leads to UvrB loading, in preparation for subsequent processing by downstream NER proteins. This offers a much more parsimonious model of DNA damage recognition by the NER apparatus.

## 4.5 Conclusions

Using high speed imaging we have discovered a previously unseen component of UvrA's search for damage. UvrA rapidly binds for ~130 ms without consuming ATP before releasing from DNA. These interactions probe for damage and offer a first step in a kinetic proofreading mechanism of damage detection. By employing an initial rapid search, this enables native levels of UvrA to reliably scan the entirety of an *E. coli* genome during a single division cycle without triggering the SOS response. We propose a model for early

damage detection for NER by UvrA and detail the close association of ATP hydrolysis for further damage verification and subsequent UvrB recruitment.
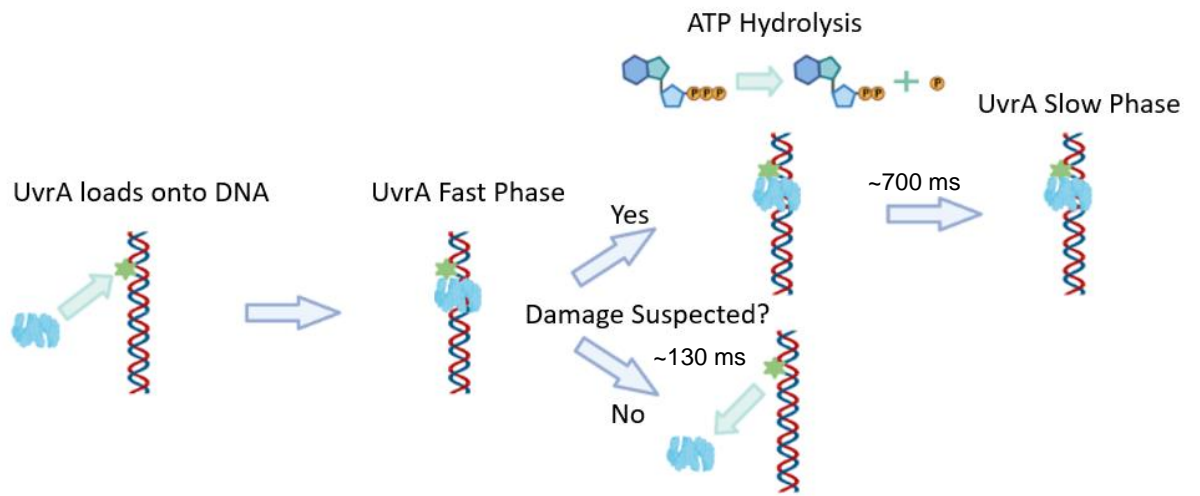


*Figure 49 - A model for early NER damage detection by UvrA*

UvrA randomly binds to DNA with a footprint of 33 base pairs. If DNA damage is not found at this site UvrA dissociates with a lifetime of ~130 ms, and no ATP is consumed. If DNA damage is located, the UvrA dimer hydrolyses ATP (~700 ms) to confirm the presence of damage (Barnett and Kad, 2019) followed by loading of UvrB and subsequent DNA repair. This figure is created without UvrB, in its presence UvrA may be bound to UvrB throughout the search phase. Created with BioRender.com.

# 5 Discussion

## A simple to implement, stabilised iSCAT system provides an accessible base for Single-Molecule experiments

Interferometric scattering (iSCAT) microscopy has provided a powerful tool for the study of a number of biological systems in recent years (De Wit et al., 2015; McDonald et al., 2018; J. Ortega Arroyo et al., 2014; Piliarik & Sandoghdar, 2014; Talà et al., 2019; Taylor et al., 2019), with advances allowing for high-speed imaging of Single-Molecules, with incredibly fine spatial resolution (Andrecka et al., 2015, 2016), and the ability to detect unlabelled Single-Molecules with molecular weights down to 14 kDa (Young et al., 2018). This makes it a promising and exciting new tool which has the potential to be expanded and applied to a wider range of biological systems and questions in the coming years.

To further develop this potential, we developed and constructed a simple and easy-to-implement wide-field interferometric scattering microscope, which allows for sub-ms temporal resolution and an achievable spatial resolution in the single nanometre range. This provides a strong base for Single-Molecule studies, tailored particularly to the use of gold-nanoparticles as contrast enhancing labels. This level of sensitivity and precision can be achieved using standard optical components and equipment, allowing for accessible implementation of this system by individuals with little experience in the construction of optical systems.

Alongside this we have developed the underlying processes for a software-based method of achieving nanometre-level stabilisation of an iSCAT microscope stage in 3 axes. Previous implementations of Z-axis and 3-axes stabilisation provide incredibly high level of correction and localisation precision (down to 0.1 nm) (Carter et al., 2007). However, these implementations require extensive additional hardware, increasing the cost, and

experimental complexity that is involved in creating a highly stable interferometric system. These levels of stabilisation are achieved through a variety of different methods, however the most accurate involve back-focal plane detection of the position of a nanofabricated fiducial marker, relative to the position of the objective (Carter et al., 2007; P. D. Schmidt et al., 2018) – or alternatively via the use of an additional laser in a TIR illumination scheme, this results in an laser emerging from the objective which is displaced laterally in response to axial movements of the sample (Jaime Ortega Arroyo et al., 2016). These methods allow for high-speed (multiple kHz) and highly stable (between 0.1-10 nm) (Carter et al., 2007; Jaime Ortega Arroyo et al., 2016; P. D. Schmidt et al., 2018) levels of stabilisation, making them a gold-standard for stabilisation when feasible to implement. However, the use of these methods requires significant investment in additional hardware; for example, spectrally distinct lasers for TIR illumination, additional cameras, and optical components such as Dichroic filters to allow for effective separation of the illumination and stabilisation wavelengths. The incorporation of these components into the optical pathways increases both experimental complexity and monetary expense, which may be prohibitively limiting in some circumstances.

To align with the straightforward implementation of iSCAT microscopy that we have described, we developed a method of achieving nanometre level stabilisation via a software-based approach. This is based on the estimation of an experimental PSF of a surface-immobilised gold-nanoparticle, which contains a wealth of positional data in the fine outer rings that surround the core of the PSF (Gholami Mahmoodabadi et al., 2020; Taylor et al., 2019). To further expand and resolve these fine outer rings, the extracted PSF profile is upscaled 4x in the X axis via cubic spline interpolation (Babcock & Zhuang, 2017). Fitting and comparison of this extracted and upscaled PSF via the discrete Fréchet distance, to that of a template stack containing the PSFs of gold-nanoparticles corresponding to 1 nm steps in the Z-axis allows for accurate estimation of immobilised gold-nanoparticles, with an estimation error of 1.92 nm. This can be achieved with a

processing time which allows for a correction rate of 29 Hz. Alongside this we demonstrated the ability of this process to detect fine movements of axial displacement of gold nanoparticles, achieving similar levels of estimation error for gold-nanoparticles taking 5 nm and 10 nm steps in the Z-axis. This technique provides a potentially powerful tool, which provides a high-level of stabilisation with the only requirement being the presence of an immobilised gold-nanoparticle in the imaging field-of-view. The primary trade-off is the achievable correction rate, with hardware-based methods achieving rates exceeding 10 kHz (Carter et al., 2007; A. Schmidt et al., 2016) – which makes these more suited to experiments requiring extremely high correction rates alongside the high level of correction accuracy. However, an accessible approach to achieving a nanometre level of stabilisation in 3 axes provides an exciting opportunity for wider implementation within a number of optical systems, and the further application of iSCAT microscopy to a wider range of biological questions.

## iSCAT presents a powerful tool for the study of protein-DNA interactions

iSCAT microscopy has been applied to the study of a wide-range of biological systems, including the cytoskeleton (Andrecka et al., 2016; Mickolajczyk et al., 2019), membrane protein dynamics (De Wit et al., 2015; Hsieh et al., 2014; Spindler et al., 2018; Taylor et al., 2019), live-cell imaging (Park et al., 2018; Talà et al., 2019), and bacteriophages and viral particles (Garmann et al., 2019; Goldfain et al., 2016; Kukura et al., 2009). There are a number of characteristics that make it an attractive methodology for studying these systems, including high temporal and spatial resolutions, the ability to assess stoichiometry of protein complexes, and theoretically unlimited imaging time. All of these characteristics would make iSCAT an incredibly powerful system to apply to the study of protein-DNA interactions and DNA repair pathways. All of the above-described characteristics would allow for more detailed investigations than carried out previously with fluorescence microscopy, due to the limitations imposed by limited photon flux and photobleaching/blinking of fluorescent tags.

A number of conventional assays for Single-Molecule fluorescence microscopy, such as combination with optical tweezers, DNA tightropes, and detection of labelled-molecules under-flow, do not translate efficiently to the iSCAT modality. For example, DNA tightropes provide an ideal basis for studying protein-DNA interactions, due to the spatial separation from the surface and the suspended DNA, and ease of isolating individual DNA strands (Barnett & Kad, 2019; Kad et al., 2010). However, the use of large 5 μm beads poses a challenge when translated to iSCAT microscopy, this is due to the extensive scattering and interference patterns that are generated, particularly when making use of a wide-field imaging regime (Young & Kukura, 2019).

To aid in the application of iSCAT microscopy to the study of protein-DNA interactions, we developed assays which allow for direct *in-vitro* imaging of gold nanoparticle labelled proteins on immobilised DNA strands. We developed a customisable surface-based DNA assay, in which a custom-made DNA strand labelled with a digoxigenin moiety is immobilised onto the surface via surface-adsorbed anti-digoxigenin antibodies. This results in a surface coating on vertical DNA strands. Due to the nature of the immobilised DNA, it can be tailored to suit the requirements for the study of any biological system, with the facile ability to introduce specific sequences, structures, or commercially available chemical modifications. This provides a flexible assay which can easily be combined with ratiometric imaging to investigate protein binding dynamics, and additionally assess the stoichiometry of binding protein complexes due to the linear relationship between particle size and observed contrast. It is important to note, the primary limitation of this assay lies in the inability to accurately replicate cellular conditions *in vitro*, for example the effects of molecular crowding within the cell, or the influence of DNA-bound proteins and the tertiary/quaternary structure of DNA on the 1D diffusion of proteins. Additionally, due to the structure of the assay, the tethered DNA extends axially into solution meaning that unless combined with 3D-localisation of bound particles the 1D diffusion of proteins along the immobilised DNA cannot be detected and characterised. However, further

development such as the implementation of 3D-tracking using iSCAT microscopy (Taylor *et al.*, 2019b, 2020), and *in vitro* assays mimicking the cellular environment (Cravens *et al.*, 2015) could provide the tools to expand the flexibility of this assay even further.

We believe the combination of iSCAT microscopy with the methods detailed above (alongside alternative traditional methods of studying protein-DNA interactions such as DNA curtains (Greene et al., 2010)), provides an exciting, and currently underutilised tool, for the study of protein-DNA interactions, and DNA repair pathways.

## High-speed iSCAT imaging reveals a novel binding mode for dimeric UvrA

The early stages of damage detection within the prokaryotic NER pathway still remain uncertain, with previous studies into the damage sensing ability of UvrA suggesting that it would be incapable of checking the entirety of an *E. coli* genome in a single division cycle alone via it's 3D search mechanism (Kad et al., 2010), due to its ~2 second lifetime on DNA (Barnett & Kad, 2019). In combination with UvrB, it can form the $UvrA_2B_2$ complex, collapsing UvrA's 3D search into a 1D search (Kad et al., 2010). This search mechanism would allow for effective damage sensing, providing a mechanism through which UvrA and B could work in concert to accurately locate DNA damage (Kad et al., 2010). However, recent *in vivo* studies found that the majority of UvrB molecules (~90%) remain diffusive within the cell (Stracy et al., 2016), indicating that the $UvrA_2B_2$ complex is not the primary damage sensing component of bacterial NER. It is unclear as to why such a large number of the cells UvrB reserves remain diffusive in solution, however this may serve to improve the association rate with UvrA once it has located damage. The higher the number of UvrB molecules present in solution, the higher the probability of these molecules encountering a damage bound UvrA dimer whilst undergoing 3D diffusion. Additionally, UvrB is able to complex with UvrC at sites of damage in the absence of UvrA (Springall *et al.*, 2018), and as such a larger population may support both of these damage location mechanisms. This large population of diffusive UvrB molecules suggests

the presence of an alternative damage-sensing mechanism of UvrA, allowing for more rapid detection of DNA damage. To study this, we made use of high-speed iSCAT microscopy in combination with the previously described customisable surface-based DNA assay.

High-speed imaging of UvrA interacting with both undamaged DNA, and DNA labelled with fluorescein (a well characterised target for NER) (Croteau et al., 2008) reveals a novel binding mode displayed by UvrA dimers, characterised by a lifetime of ~130 ms. Additionally, a longer lifetime is observed consistent with UvrA-DNA interactions in which UvrA hydrolyses 2 ATP molecules, with an ATP turnover rate of ~1-2 ATP/s (Barnett & Kad, 2019; Case et al., 2019). Repeating this with a DNA construct of shorter length (50 bp), results in a rapid lifetime consistent with our previous observations (~130 ms), suggesting that UvrA remains static during this interaction. To assess how effective UvrA would be at locating DNA damage within *E. coli* during single division cycles we made use of an exponential distribution of a Poisson process, accounting for the repeated sampling of regions within the genome due to the random nature of the 3D-search. Utilising these fast interactions, native levels of UvrA (~20 copies) in an undamaged cell would be able to effectively search the entirety of the *E. coli* genome within a single division cycle, as opposed to only ~18% coverage when accounting for previously observed lifetimes (~2 s) (Barnett & Kad, 2019).

Use of ADP and the non-hydrolysable ATP analogue ATPγS demonstrated the ATP-independent nature of these lifetimes. Lifetimes are eradicated completely in the presence of ADP, which aligns well with observations suggesting that the presence of ATP results in the dissociation of UvrA dimers (Case et al., 2019). In the presence of ATPγS, long lifetimes are eradicated, with the short ~130 ms lifetimes being maintained. This highlights the presence of a low energetic cost search mechanism for NER, with an initial cursory check occurring in an ATP independent manner – with ATP hydrolysis only occurring

upon location of DNA damage. The ability for UvrA to initially bind the DNA in an ATP-independent manner, combined with previous observations that upon meeting damage ATP hydrolysis occurs in the distal ATPase (Case et al., 2019) and the link between distal ATPase hydrolysis and the movement of zinc finger 3 (Kraithong et al., 2017) suggest a mechanism for early damage detection by UvrA. The initial attachment of UvrA is able to occur in an ATP independent manner, and if no damage is detected upon the initial attachment, UvrA is able to dissociate without hydrolysing the bound ATP. The exact molecular mechanisms through which UvrA is able to discriminate between damaged and undamaged DNA currently remain unclear, however due to the DNA distorting nature of NERs target lesions it is possible that UvrA may be able to dynamically assess the distortion of the DNA backbone to check for the presence of lesions (Kisker, Kuper and Van Houten, 2013). It is thought that upon suspicion of damage, ATP is hydrolysed in the distal ATPase site (Case *et al.*, 2019). This causes a change the movement of zinc-finger 3, which tests for DNA damage and is likely required for the subsequent recruitment of UvrB to continue in the damage verification process. This process could also be an effective example of conformational proofreading (Savir and Tlusty, 2007), a method of kinetic proofreading which increases target sit recognition specificity, via a structural mismatch between a protein and its target. This has previously been demonstrated within eukaryotic NER, in which UV-DDB forms multiple kinetic intermediates on DNA prior to long-lived static loading at sites of damage (Ghodke *et al.*, 2014). This mirrors our findings, showing that UvrA is able to form a short-lived intermediate on DNA, during which time zinc finger 3 may probe the DNA for the presence of damage. If it is suspected that damage is present at bound site, UvrA is able to hydrolyse ATP and lock onto the DNA – possibly in preparation for recruitment of UvrB from solution.

This process could be an effective example of kinetic proofreading, a method for error correction within biochemical pathways which allows for highly specific reactions to occur with an accuracy higher than that suggested by the free energy differences between the

activation of two pathways (Hopfield, 1974; Ninio, 1975). This was first suggested in relation to protein synthesis by James Hopfield (Hopfield, 1974) who noted that the error rate of protein synthesis (1 in 10000) is impossible to achieve in a one-step reaction due to the minimal differences between substrates (e.g. one base difference between the correct and incorrect codons).

Additionally, these rapid ATP-independent interactions could further be enhanced by the cellular environment in which they occur *in vivo*. As previously described, 20-40% of the total volume of cells is taken up by the presence of macromolecules and proteins – with a variety of studies demonstrating this may actually enhance the abilities of DNA-binding proteins to locate their target sites (Cravens *et al.*, 2015; Singh *et al.*, 2017). It is possible that this is a result of the dichotomy in cellular viscosity that occurs due to the presence of depletion forces which result in smaller crowding particles being excluded from the area surround larger molecules (i.e., DNA) (Asakura and Oosawa, 1958). For example, these pockets of low viscosity surrounding DNA could work in concert with the rapid interactions displayed by UvrA. The association rate of UvrA and DNA *in vivo* will be limited by the rate at which UvrA can diffuse through the crowded cytoplasm of the cell to reach the DNA – as such, once UvrA reaches the region of low viscosity surrounding the DNA its 3D diffusion constant, and thus, association rate could be increased. Additionally, the gradient from low viscosity surrounding the DNA, to high viscosity further away from the DNA may impede the diffusion of UvrA back into the cytoplasm. This could effectively trap UvrA in close proximity to the DNA, further increasing its association rate and effectiveness at searching the genome for damage. These effects have been studied *in vitro* in relation to the facilitated diffusion the glycosylases hUNG and hOGG1, mimicking the molecular crowding seen *in vivo* using a buffer containing 20% polyethylene glycol 8000, with the study showing that the facilitated diffusion of both enzymes was enhanced in the presence of this crowding agent (Cravens *et al.*, 2015). Expansion and application of these methodologies to the study of UvrA, and NER as a whole, would be incredibly useful in

furthering our understanding of how the cellular environment may function to increase the effectiveness of DNA damage location and verification within NER.

It also is key to note the limitations imposed within this study, primarily being the low count statistics, and the challenges this imposes when trying to accurately assign populations. This study did not exploit a key advantage conferred via the use of iSCAT microscopy, being the theoretically unlimited imaging times that can be achieved due to the non-degradative nature of light scattering. Future studies using these techniques should focus on achieving suitable acquisition times and lifetimes to ensure that a more robust and effective statistical analysis can be carried out on the resulting data.

Together this work uncovers a novel DNA binding mode displayed by UvrA and helps to further clarify the events that occur during the early stages of DNA damage detection within NER. We have shown that by utilising this DNA binding mode native levels of UvrA are able to realistically search the entirety of the *E. coli* genome within a single division cycle, without the need for the 10-fold increase that accompanies induction of the SOS response. This also simultaneously provides a search mechanism with a low-energetic cost, only requiring ATP hydrolysis upon binding of DNA damage.

## Future Work

### Furthering the work with UvrA to additionally consider the function of UvrB

Our work here has begun to further highlight the role of UvrA within the early stages of damage detection during prokaryotic NER, however a key next step would be to investigate further damage verification in the form of the recruitment of UvrB to form the $UvrA_2B_2$ complex at the site of damage.

It has been previously shown that the majority of UvrB molecules within the cell remain diffusive within solution (~85-90%), additionally of the static molecules only 4% were found to be UvrA-dependent (Stracy *et al.*, 2016). This suggests that rather than the

UvrA$_2$B$_2$ complex being the driver of damage detection, UvrB is instead recruited from solution by UvrA upon location of suspected damage. Therefore, direct imaging and understanding of this recruitment process of UvrB is key – this could be effectively achieved with differential labelling of UvrA and B within solution to allow for straightforward discrimination of both binder identity and stoichiometry. Further study of this process should allow us to further elucidate the function of both these molecules within the wider context of NER, and more specifically during the process of damage detection and confirmation. For example, we have noted a non-insignificant number of ATP-consuming UvrA interactions on undamaged detection which may indicate the promiscuity of UvrA damage detection (which would align well with previous observations regarding the wide-range of damage that can be recognised by the NER pathway (Van Houten *et al.,* 2005)). The recognition process may then be further refined upon recruitment of UvrB, before being either accepted or rejected as a site of damage. Our lack of understanding of these processes highlights the need for further study into the combinatorial work of UvrA and UvrB.

## Expanding iSCAT microscopy to further study protein-DNA interactions

Here we have described an effective methodology to examine both transient and long-lived protein-DNA interactions through the use of surface-tethered DNA molecules, providing a powerful and easily customisable method that can be tailored to fit most required experimental conditions. However, there are limitations to this method, for example the lack of ability to examine lateral motion of the bound protein(s) (however there is the possibility to combine this approach with 3D tracking of AuNP labelled proteins (Taylor *et al.*, 2019a; Gholami Mahmoodabadi *et al.*, 2020)). A method that has widely been used in the past for the study of protein-DNA interactions is DNA tightropes, however as previously discussed these present a number of experimental challenges when it comes to iSCAT microscopy. Firstly, the spatial separation between the suspended DNA molecules and the coverslip which gives rise to the reference wave, and

secondly the presence of large 5 µm beads which very effectively scatter light and lead to significant degradation of flat-field processed images.

To overcome the issues presented through the traditional methodology of DNA tightropes, we begun development of a surface-based assay revolving around the tethering of biotin-labelled λ-DNA molecules to a streptavidin-coated surface. This approach circumvents the issues present through the use of large diameter beads, and the spatial separation between the surface and the DNA tightropes.

Λ-DNA biotinylation is carried out as described previously (Ganji *et al.*, 2018), briefly, λ-DNA is heated to 65°C to denature the ends of the DNA molecules. Equimolar concentrations (33 µM) of dCTP, dGTP, dTTP, and Biotin-14-dATP are added, along with 1 unit of Klenow fragment, before being left to incubate at 25°C for 15 mins. The reaction is then stopped via heat and EDTA inactivation. This Klenow fill-in reaction results in λ-DNA molecules which are labelled with multiple Biotin-14-dATP nucleotides on both ends, allowing for surface-tethering via surface-immobilised streptavidin molecules. Flow cells are constructed as previously described and blocked with a 1:24 mg/mL ratio of Biotin-mPEG:mPEG overnight. These blocked flow cells are then washed with 400 µL MilliQ water, before addition of 0.1 mg/mL Streptavidin in TE buffer (10 mM Tris-HCl, 1 mM EDTA, pH 8) and incubated at 25°C for 5 minutes. 200 µL of 200 pM biotinylated λ-DNA is then introduced to the flow cell at a constant flow rate of 500 µL/min, followed by 10 mL TE buffer at the same flow rate. This results in full extension of biotinylated λ-DNA molecules which bind to the surface-tethered streptavidin. The primary challenges to overcome through the use of the method is ensuring effective surface-passivation to avoid additional contributions to noise which arise from the binding of non-specific items from solution (e.g., protein aggregates, contaminants, or bacteria). Due to the use of flat-field correction during image analysis these items are not removed during image processing and contribute significant levels of noise. This process could also be combined with recent

developments in nanofabricated microfluidic devices which allow for more effective surface immobilisation of DNA (Gorman, Fazio, *et al.*, 2010; Greene *et al.*, 2010).

We believe our work outline here highlights an exciting future for iSCAT microscopy within the study of protein-DNA interactions - with the further development of compatible assays, and combination with already established methods such as fluorescence microscopy, allowing for future biological investigations to be carried out with a level of speed and sensitivity which will exceed those currently in use.

# References

Abbe, E. (1873) 'Beiträge zur Theorie des Mikroskops und der mikroskopischen Wahrnehmung', *Archiv für Mikroskopische Anatomie*, 9, pp. 413–468.

Alhmoud, J. F. *et al.* (2020) 'DNA Damage / Repair Management in Cancers and'.

Ames, B. N., Shigenaga, M. K. and Hagen, T. M. (1993) 'Oxidants , antioxidants , and the degenerative diseases of aging', 90(September), pp. 7915–7922.

Ando, J. *et al.* (2018) 'Single-Nanoparticle Tracking with Angstrom Localization Precision and Microsecond Time Resolution', *Biophysical Journal*, 115(12), pp. 2413–2427. doi: 10.1016/j.bpj.2018.11.016.

Ando, J. *et al.* (2019) 'Multicolor High-Speed Tracking of Single Biomolecules with Silver, Gold, and Silver-Gold Alloy Nanoparticles', *ACS Photonics*, 6(11), pp. 2870–2883. doi: 10.1021/acsphotonics.9b00953.

Andrecka, J. *et al.* (2015) 'Structural dynamics of myosin 5 during processive motion revealed by interferometric scattering microscopy', *eLife*, 4. doi: 10.7554/eLife.05413.

Andrecka, J. *et al.* (2016) 'Label-free Imaging of Microtubules with Sub-nm Precision Using Interferometric Scattering Microscopy', *Biophysical Journal*, 110(1), pp. 214–217. doi: 10.1016/j.bpj.2015.10.055.

Asakura, S. and Oosawa, F. (1958) 'Interaction between particles suspended in solutions of macromolecules', *Journal of Polymer Science*, 33(126), pp. 183–192. doi: 10.1002/pol.1958.1203312618.

Ashkin, A. (1997) 'Optical trapping and manipulation of neutral particles using lasers.',

*Proceedings of the National Academy of Sciences of the United States of America*, 94(10), pp. 4853–60. doi: 10.1073/pnas.94.10.4853.

Axelrod, D. (1981) 'Cell-substrate contacts illuminated by total internal reflection fluorescence', *Journal of Cell Biology*, 89(1), pp. 141–145. doi: 10.1083/jcb.89.1.141.

Babcock, H. P. and Zhuang, X. (2017) 'Analyzing Single Molecule Localization Microscopy Data Using Cubic Splines', *Scientific Reports*, 7(1), p. 552. doi: 10.1038/s41598-017-00622-w.

Bagchi, B., Blainey, P. C. and Xie, X. S. (2008) 'Diffusion Constant of a Nonspecifically Bound Protein Undergoing Curvilinear Motion along DNA', *The Journal of Physical Chemistry B*, 112(19), pp. 6282–6284. doi: 10.1021/jp077568f.

Baird, G. S., Zacharias, D. A. and Tsien, R. Y. (2000) 'Biochemistry, mutagenesis, and oligomerization of DsRed, a red fluorescent protein from coral', *Proceedings of the National Academy of Sciences*, 97(22), pp. 11984–11989. doi: 10.1073/pnas.97.22.11984.

Barnett, J. T. and Kad, N. M. (2019) 'Understanding the coupling between DNA damage detection and UvrA's ATPase using bulk and single molecule kinetics', *The FASEB Journal*, 33(1), pp. 763–769. doi: 10.1096/fj.201800899R.

Baumann, C. G. *et al.* (1997) 'Ionic effects on the elasticity of single DNA molecules', *Proceedings of the National Academy of Sciences*, 94(12), pp. 6185–6190. doi: 10.1073/pnas.94.12.6185.

Berg, O. G. and Blomberg, C. (1976) 'Association kinetics with coupled diffusional flows', *Biophysical Chemistry*, 4(4), pp. 367–381. doi: 10.1016/0301-4622(76)80017-8.

Berg, O. G., Winter, R. B. and von Hippel, P. H. (1982) 'How do genome-regulatory

proteins locate their DNA target sites?', *Trends in Biochemical Sciences*, 7(2), pp. 52–55. doi: 10.1016/0968-0004(82)90075-5.

Bergqvist, S. *et al.* (2004) 'Heat Capacity Effects of Water Molecules and Ions at a Protein–DNA Interface', *Journal of Molecular Biology*, 336(4), pp. 829–842. doi: 10.1016/j.jmb.2003.12.061.

Blainey, P. C. *et al.* (2009) 'Nonspecifically bound proteins spin while diffusing along DNA', *Nature Structural & Molecular Biology*, 16(12), pp. 1224–1229. doi: 10.1038/nsmb.1716.

Bohren, C. F. and Huffman, D. R. (1998) *Absorption and Scattering of Light by Small Particles*. Wiley. doi: 10.1002/9783527618156.

Bonnet, I. *et al.* (2008) 'Sliding and jumping of single EcoRV restriction enzymes on non-cognate DNA', *Nucleic Acids Research*, 36(12), pp. 4118–4127. doi: 10.1093/nar/gkn376.

Bont, R. De and Larebeke, N. Van (2004) 'Endogenous DNA damage in humans : a review of quantitative data 1', 19(3), pp. 169–185. doi: 10.1093/mutage/geh025.

Bouwman, P. and Jonkers, J. (2012) 'Genomic instability in cancer: The effects of deregulated DNA damage signalling on cancer chemotherapy response and resistance', 12(September). doi: 10.1038/nrc3342.

Boyce, R. P. and Howard-Flanders, P. (1964) 'RELEASE OF ULTRAVIOLET LIGHT-INDUCED THYMINE DIMERS FROM DNA IN E. COLI K-12', *Proceedings of the National Academy of Sciences*, 51(2), pp. 293–300. doi: 10.1073/pnas.51.2.293.

De Brabander, M. *et al.* (1988) 'Dynamic behavior of the transferrin receptor followed in living epidermoid carcinoma (A431) cells with nanovid microscopy.', *Cell motility and the cytoskeleton*, 9(1), pp. 30–47. doi: 10.1002/cm.970090105.

Brackley, C. A., Cates, M. E. and Marenduzzo, D. (2013) 'Intracellular Facilitated Diffusion: Searchers, Crowders, and Blockers', *Physical Review Letters*, 111(10), p. 108101. doi: 10.1103/PhysRevLett.111.108101.

Brem, R. *et al.* (2017) 'Oxidative stress induced by UVA photoactivation of the tryptophan UVB photoproduct ( FICZ ) inhibits nucleotide excision repair in human cells', (January), pp. 1–9. doi: 10.1038/s41598-017-04614-8.

Brooks Shera, E. *et al.* (1990) 'Detection of single fluorescent molecules', *Chemical Physics Letters*, 174(6), pp. 553–557. doi: 10.1016/0009-2614(90)85485-U.

Brown, S. D. *et al.* (2010) 'Gold Nanoparticles for the Improved Anticancer Drug Delivery of the Active Component of Oxaliplatin', *Journal of the American Chemical Society*, 132(13), pp. 4678–4684. doi: 10.1021/ja908117a.

Cadet, J. *et al.* (2001) 'Effects of UV and visible radiations on cellular DNA.', *Current problems in dermatology*, 29, pp. 62–73. doi: 10.1159/000060654.

Cadet, J., Sage, E. and Douki, T. (2005) 'Ultraviolet radiation-mediated damage to cellular DNA', *Mutation Research - Fundamental and Molecular Mechanisms of Mutagenesis*, 571(1-2 SPEC. ISS.), pp. 3–17. doi: 10.1016/j.mrfmmm.2004.09.012.

Carter, A. R. *et al.* (2007) 'Stabilization of an optical microscope to 01 nm in three dimensions', *Applied Optics*, 46(3), p. 421. doi: 10.1364/AO.46.000421.

Case, B. C. *et al.* (2019) 'The ATPase mechanism of UvrA2 reveals the distinct roles of proximal and distal ATPase sites in nucleotide excision repair', *Nucleic Acids Research*, 47(8), pp. 4136–4152. doi: 10.1093/nar/gkz180.

Chalfie, M. *et al.* (1994) 'Green fluorescent protein as a marker for gene expression', *Science*, 263(5148), pp. 802–805. doi: 10.1126/science.8303295.

Chan, W. C. W. and Nie, S. (1998) 'Quantum dot bioconjugates for ultrasensitive nonisotopic detection', *Science*, 281(5385), pp. 2016–2018. doi: 10.1126/science.281.5385.2016.

Chatterjee, N. and Walker, G. C. (2017) 'Mechanisms of DNA Damage, Repair, and Mutagenesis', 00(February). doi: 10.1002/em.

Cheng, C. Y. and Hsieh, C. L. (2017) 'Background Estimation and Correction for High-Precision Localization Microscopy', *ACS Photonics*, 4(7), pp. 1730–1739. doi: 10.1021/acsphotonics.7b00238.

Cole, D. *et al.* (2017) 'Label-Free Single-Molecule Imaging with Numerical-Aperture-Shaped Interferometric Scattering Microscopy', *ACS Photonics*, 4(2), pp. 211–216. doi: 10.1021/acsphotonics.6b00912.

Costantini, L. M. and Snapp, E. L. (2013) 'Fluorescent Proteins in Cellular Organelles: Serious Pitfalls and Some Solutions', *DNA and Cell Biology*, 32(11), pp. 622–627. doi: 10.1089/dna.2013.2172.

Cravens, S. L. *et al.* (2015) 'Molecular crowding enhances facilitated diffusion of two human DNA glycosylases', *Nucleic Acids Research*, 43(8), pp. 4087–4097. doi: 10.1093/nar/gkv301.

Croteau, D. L. *et al.* (2006) 'The C-terminal Zinc Finger of UvrA Does Not Bind DNA Directly but Regulates Damage-specific DNA Binding', *Journal of Biological Chemistry*, 281(36), pp. 26370–26381. doi: 10.1074/jbc.M603093200.

Croteau, D. L. *et al.* (2008) 'Cooperative damage recognition by UvrA and UvrB: Identification of UvrA residues that mediate DNA binding', *DNA Repair*, 7(3), pp. 392–404. doi: 10.1016/j.dnarep.2007.11.013.

Curry, A., Hwang, W. L. and Wax, A. (2006) 'Epi-illumination through the microscope objective applied to darkfield imaging and microspectroscopy of nanoparticle interaction with cells in culture', *Optics Express*, 14(14), p. 6535. doi: 10.1364/OE.14.006535.

Curtis, A. S. G. (1964) 'THE MECHANISM OF ADHESION OF CELLS TO GLASS', *The Journal of Cell Biology*, 20(2), pp. 199–215. doi: 10.1083/jcb.20.2.199.

Deamer, D., Akeson, M. and Branton, D. (2016) 'Three decades of nanopore sequencing', *Nature Biotechnology*, 34(5), pp. 518–524. doi: 10.1038/nbt.3423.

DellaVecchia, M. J. *et al.* (2004) 'Analyzing the Handoff of DNA from UvrA to UvrB Utilizing DNA-Protein Photoaffinity Labeling', *Journal of Biological Chemistry*, 279(43), pp. 45245–45256. doi: 10.1074/jbc.M408659200.

Dépret, B., Verkerk, P. and Hennequin, D. (2002) 'Characterization and modelling of the hollow beam produced by a real conical lens', *Optics Communications*, 211(1–6), pp. 31–38. doi: 10.1016/S0030-4018(02)01900-4.

Dey, P. and Bhattacherjee, A. (2018) 'Role of Macromolecular Crowding on the Intracellular Diffusion of DNA Binding Proteins', *Scientific Reports*, 8(1), p. 844. doi: 10.1038/s41598-017-18933-3.

Dickson, R. M. *et al.* (1997) 'On/off blinking and switching behaviour of single molecules of green fluorescent protein', *Nature*, 388(6640), pp. 355–358. doi: 10.1038/41048.

Dikić, J. *et al.* (2012) 'The rotation-coupled sliding of EcoRV', *Nucleic Acids Research*, 40(9), pp. 4064–4070. doi: 10.1093/nar/gkr1309.

Dominguez, R. and Holmes, K. C. (2011) 'Actin Structure and Function', *Annual Review of Biophysics*, 40(1), pp. 169–186. doi: 10.1146/annurev-biophys-042910-155359.

Douki, T. and Sage, E. (2016) 'Dewar valence isomers, the third type of environmentally

relevant DNA photoproducts induced by solar radiation', *Photochemical and Photobiological Sciences*, 15(1), pp. 24–30. doi: 10.1039/c5pp00382b.

Dunn, A. R. *et al.* (2011) 'Single Qdot-labeled glycosylase molecules use a wedge amino acid to probe for lesions while scanning along DNA', *Nucleic Acids Research*, 39(17), pp. 7487–7498. doi: 10.1093/nar/gkr459.

Dunn, A. R. and Spudich, J. A. (2007) 'Dynamics of the unbound head during myosin V processive translocation', *Nature Structural & Molecular Biology*, 14(3), pp. 246–248. doi: 10.1038/nsmb1206.

Eiter, T. and Mannila, H. (1994) 'Computing discrete Frechet distance', *Technical Report CD-TR 94/64, Information Systems Department, Technical University of Vienna*.

El-Kurdi, R. and Patra, D. (2019) 'Gold and silver nanoparticles in resonance Rayleigh scattering techniques for chemical sensing and biosensing: a review', *Microchimica Acta*, 186(10), p. 667. doi: 10.1007/s00604-019-3755-4.

El-missiry, M. A. and Abou-seif, M. (2000) 'Photosensitization induced reactive oxygen species and oxidative damage in human erythrocytes', 158.

Elf, J., Li, G.-W. and Xie, X. S. (2007) 'Probing Transcription Factor Dynamics at the Single-Molecule Level in a Living Cell', *Science*, 1191(2007). doi: 10.1126/science.1141967.

Enoki, S. *et al.* (2012) 'Label-Free Single-Particle Imaging of the Influenza Virus by Objective-Type Total Internal Reflection Dark-Field Microscopy', *PLoS ONE*. Edited by P. Digard, 7(11), p. e49208. doi: 10.1371/journal.pone.0049208.

Eryilmaz, J. *et al.* (2006) 'Structural Insights into the Cryptic DNA-dependent ATPase Activity of UvrB', *Journal of Molecular Biology*, 357(1), pp. 62–72. doi:

10.1016/j.jmb.2005.12.059.

Ewers, H. *et al.* (2007) 'Label-free optical detection and tracking of single virions bound to their receptors in supported membrane bilayers', *Nano Letters*, 7(8), pp. 2263–2266. doi: 10.1021/nl070766y.

Fréchet, M. M. (1906) 'Sur quelques points du calcul fonctionnel', *Rendiconti del Circolo Matematico di Palermo*, 22(1), pp. 1–72. doi: 10.1007/BF03018603.

Ganji, M. *et al.* (2018) 'Real-time imaging of DNA loop extrusion by condensin', *Science*, 360(6384), pp. 102–105. doi: 10.1126/science.aar7831.

Garcés-Chávez, V. *et al.* (2002) 'Simultaneous micromanipulation in multiple planes using a self-reconstructing light beam', *Nature*, 419(6903), pp. 145–147. doi: 10.1038/nature01007.

Garmann, R. F., Goldfain, A. M. and Manoharan, V. N. (2019) 'Measurements of the self-assembly kinetics of individual viral capsids around their RNA genome', *Proceedings of the National Academy of Sciences of the United States of America*, 116(45), pp. 22485–22490. doi: 10.1073/pnas.1909223116.

Geerts, H. *et al.* (1987) 'Nanovid tracking: a new automatic method for the study of mobility in living cells based on colloidal gold and video microscopy', *Biophysical Journal*, 52(5), pp. 775–782. doi: 10.1016/S0006-3495(87)83271-X.

Gelles, Jeff, Schnapp, B. J. and Sheetz, M. P. (1988) 'Tracking kinesin-driven movements with nanometre-scale precision', *Nature*, 331(6155), pp. 450–453. doi: 10.1038/331450a0.

Gelles, J, Schnapp, B. J. and Sheetz, M. P. (1988) 'Tracking kinesin-driven movements with nanometre-scale precision', *Nature*, 331, pp. 450–453.

Gemeinhardt, A. *et al.* (2018) 'Label-free imaging of single proteins secreted from living

cells via iscat microscopy', *Journal of Visualized Experiments*, 2018(141), pp. 1–10. doi: 10.3791/58486.

Ghodke, H. *et al.* (2014) 'Single-molecule analysis reveals human UV-damaged DNA-binding protein (UV-DDB) dimerizes on DNA via multiple kinetic intermediates', *Proceedings of the National Academy of Sciences*, 111(18), pp. E1862–E1871. doi: 10.1073/pnas.1323856111.

Ghodke, H., Ho, H. N. and van Oijen, A. M. (2020) 'Single-molecule live-cell imaging visualizes parallel pathways of prokaryotic nucleotide excision repair', *Nature Communications*, 11(1), p. 1477. doi: 10.1038/s41467-020-15179-y.

Gholami Mahmoodabadi, R. *et al.* (2020) 'Point spread function in interferometric scattering microscopy (iSCAT) Part I: aberrations in defocusing and axial localization', *Optics Express*, 28(18), p. 25969. doi: 10.1364/OE.401374.

Goldfain, A. M. *et al.* (2016) 'Dynamic Measurements of the Position, Orientation, and DNA Content of Individual Unlabeled Bacteriophages', *Journal of Physical Chemistry B*, 120(26), pp. 6130–6138. doi: 10.1021/acs.jpcb.6b02153.

Goring, C. R. and Pritchard, A. (1837) *Micrographia*. Whitaker and Company.

Gorman, J., Chowdhury, A., *et al.* (2010) 'Dynamic Basis for One-Dimensional DNA Scanning by the Mismatch Repair Complex Msh2-Msh6', *Molecular Cell*, 28(3), pp. 359–370. doi: 10.1016/j.molcel.2007.09.008.Dynamic.

Gorman, J., Fazio, T., *et al.* (2010) 'Nanofabricated Racks of Aligned and Anchored DNA Substrates for Single-Molecule Imaging', *Langmuir*, 26(2), pp. 1372–1379. doi: 10.1021/la902443e.

Gorman, J. *et al.* (2011) 'Visualizing one-dimensional diffusion of eukaryotic DNA repair

factors along a chromatin lattice', *Nature Structural & Molecular Biology*, 17(8), pp. 932–938. doi: 10.1038/nsmb.1858.Visualizing.

Greene, E. C. *et al.* (2010) 'DNA Curtains for High-Throughput Single-Molecule Optical Imaging', in, pp. 293–315. doi: 10.1016/S0076-6879(10)72006-1.

Ha, T. *et al.* (1999) 'Ligand-induced conformational changes observed in single RNA molecules', *Proceedings of the National Academy of Sciences of the United States of America*, 96(16), pp. 9077–9082. doi: 10.1073/pnas.96.16.9077.

Ha, T. and Tinnefeld, P. (2012) 'Photophysics of Fluorescent Probes for Single-Molecule Biophysics and Super-Resolution Imaging', *Annual Review of Physical Chemistry*, 63(1), pp. 595–617. doi: 10.1146/annurev-physchem-032210-103340.

Hager, G., McNally, J. and Misteli, T. (2019) 'Transcription Dynamics', *Molecular Cell*, 35(6), pp. 741–753. doi: 10.1016/j.molcel.2009.09.005.Transcription.

Hakem, R. (2008) 'DNA-damage repair; the good, the bad, and the ugly', *The EMBO Journal*, (January), pp. 589–605. doi: 10.1038/emboj.2008.15.

Halford, S. E. (2004) 'How do site-specific DNA-binding proteins find their targets?', *Nucleic Acids Research*, 32(10), pp. 3040–3052. doi: 10.1093/nar/gkh624.

Hargreaves, V. V. and Schleif, R. F. (2008) 'The Salt Dependence of the Interferon Regulatory Factor 1 DNA Binding Domain Binding to DNA Reveals Ions Are Localized around Protein and DNA', *Biochemistry*, 47(13), pp. 4119–4128. doi: 10.1021/bi702082q.

Hecht, E. (1998) *Optics*. 3rd edn. Addison-Wesley.

Herman, R. M. and Wiggins, T. A. (1991) 'Production and uses of diffractionless beams', *Journal of the Optical Society of America A*, 8(6), p. 932. doi: 10.1364/JOSAA.8.000932.

Hess, S. T., Girirajan, T. P. K. and Mason, M. D. (2006) 'Ultra-High Resolution Imaging by Fluorescence Photoactivation Localization Microscopy', *Biophysical Journal*, 91(11), pp. 4258–4272. doi: 10.1529/biophysj.106.091116.

von Hippel, P. H. and Berg, O. G. (1989a) 'Facilitated target location in biological systems.', *The Journal of biological chemistry*, 264(2), pp. 675–8. Available at: http://www.ncbi.nlm.nih.gov/pubmed/2642903.

von Hippel, P. H. and Berg, O. G. (1989b) 'Facilitated Target Location in Biological Systems', *Journal of Biological Chemistry*, 264(2), pp. 675–678. doi: 10.1016/S0021-9258(19)84994-3.

Hirschfeld, T. (1976) 'Optical microscopic observation of single small molecules', *Applied Optics*, 15(12), pp. 2965–2966. doi: 10.1364/AO.15.002965.

Hopfield, J. J. (1974) 'Kinetic Proofreading: A New Mechanism for Reducing Errors in Biosynthetic Processes Requiring High Specificity', *Proceedings of the National Academy of Sciences*, 71(10), pp. 4135–4139. doi: 10.1073/pnas.71.10.4135.

Horio, T. and Hotani, H. (1986) 'Visualization of the dynamic instability of individual microtubules by dark-field microscopy', *Nature*, 321(6070), pp. 605–607. doi: 10.1038/321605a0.

Hoskins, A. A. *et al.* (2011) 'Ordered and Dynamic Assembly of Single Spliceosomes', *Science*, 331(6022), pp. 1289–1295. doi: 10.1126/science.1198830.

Hotani, H. and Horio, T. (1988) 'Dynamics of microtubules visualized by darkfield microscopy: treadmilling and dynamic instability.', *Cell motility and the cytoskeleton*, 10(1–2), pp. 229–236. doi: 10.1002/cm.970100127.

Van Houten, B. *et al.* (1987) 'DNase I footprint of ABC excinuclease.', *The Journal of*

*biological chemistry*, 262(27), pp. 13180–7. Available at:

http://www.ncbi.nlm.nih.gov/pubmed/3308871.

Van Houten, B. *et al.* (2005) '"Close-fitting sleeves": DNA damage recognition by the UvrABC nuclease system', *Mutation Research/Fundamental and Molecular Mechanisms of Mutagenesis*, 577(1–2), pp. 92–117. doi: 10.1016/j.mrfmmm.2005.03.013.

Van Houten, B. and Kad, N. (2014) 'Investigation of bacterial nucleotide excision repair using single-molecule techniques', *DNA Repair*, 20, pp. 41–48. doi: 10.1016/j.dnarep.2013.10.012.

Houten, B. Van and Kad, N. (2014) 'Investigation of bacterial nucleotide excision repair using single-molecule techniques', *DNA Repair*, pp. 41–48. doi: 10.1016/j.dnarep.2013.10.012.Investigation.

Hsu, D. S. *et al.* (1994) 'Flow Linear Dichroism and Electron Microscopic Analysis of Protein-DNA Complexes of a Mutant UvrB Protein that Binds to but cannot Kink DNA', *Journal of Molecular Biology*, 241(5), pp. 645–650. doi: 10.1006/jmbi.1994.1541.

Huang, F. *et al.* (2011) 'Simultaneous multiple-emitter fitting for single molecule super-resolution imaging', *Biomedical Optics Express*, 2(5), p. 1377. doi: 10.1364/BOE.2.001377.

Imashimizu, M. and Lukatsky, D. B. (2017) 'Transcription pausing : biological significance of thermal fluctuations biased by repetitive genomic sequences', 1264(November), pp. 0–18. doi: 10.1080/21541264.2017.1393492.

Inouye, S. and Tsuji, F. I. (1994) 'Aequorea green fluorescent protein. Expression of the gene and fluorescence characteristics of the recombinant protein', *FEBS Letters*, 341(2–3), pp. 277–280. doi: 10.1016/0014-5793(94)80472-9.

Jablonski, A. (1933) 'Efficiency of Anti-Stokes Fluorescence in Dyes', *Nature*, 363, pp. 839–840.

Jaciuk, M. *et al.* (2011) 'Structure of UvrA nucleotide excision repair protein in complex with modified DNA', *Nature Structural & Molecular Biology*, 18(2), pp. 191–197. doi: 10.1038/nsmb.1973.

Jaciuk, M. *et al.* (2020) 'A combined structural and biochemical approach reveals translocation and stalling of UvrB on the DNA lesion as a mechanism of damage verification in bacterial nucleotide excision repair', *DNA Repair*, 85, p. 102746. doi: 10.1016/j.dnarep.2019.102746.

Jacobsen, V. *et al.* (2006) 'Interferometric optical detection and tracking of very small gold nanoparticles at a water-glass interface', *Optics Express*, 14(1), p. 405. doi: 10.1364/opex.14.000405.

Jain, P. K. *et al.* (2006) 'Calculated Absorption and Scattering Properties of Gold Nanoparticles of Different Size, Shape, and Composition: Applications in Biological Imaging and Biomedicine', *The Journal of Physical Chemistry B*, 110(14), pp. 7238–7248. doi: 10.1021/jp057170o.

Jones, D. L. and Baxter, B. K. (2017) 'DNA repair and photoprotection: Mechanisms of overcoming environmental ultraviolet radiation exposure in halophilic archaea', *Frontiers in Microbiology*, 8(SEP), pp. 1–16. doi: 10.3389/fmicb.2017.01882.

Jones, R. R. *et al.* (2019) 'Raman Techniques: Fundamentals and Frontiers', *Nanoscale Research Letters*, 14(1), p. 231. doi: 10.1186/s11671-019-3039-2.

Jones, S. (2001) 'Protein-RNA interactions: a structural analysis', *Nucleic Acids Research*, 29(4), pp. 943–954. doi: 10.1093/nar/29.4.943.

Jünger, F., Olshausen, P. v. and Rohrbach, A. (2016) 'Fast, label-free super-resolution live-cell imaging using rotating coherent scattering (ROCS) microscopy', *Scientific Reports*, 6(1), p. 30393. doi: 10.1038/srep30393.

Jurdova, D. *et al.* (2019) 'Interferometric scattering (iSCAT) microscopy with optimized reference wave', in Lieberman, R. A., Baldini, F., and Homola, J. (eds) *Optical Sensors 2019*. SPIE, p. 106. doi: 10.1117/12.2522360.

Kad, N. M. *et al.* (2010) 'Collaborative Dynamic DNA Scanning by Nucleotide Excision Repair Proteins Investigated by Single- Molecule Imaging of Quantum-Dot-Labeled Proteins', *Molecular Cell*, 37(5), pp. 702–713. doi: 10.1016/j.molcel.2010.02.003.

Kampmann, M. (2005) 'Facilitated diffusion in chromatin lattices : mechanistic diversity and regulatory potential', *MicroReview*, 57, pp. 889–899. doi: 10.1111/j.1365-2958.2005.04707.x.

Karasawa, S. *et al.* (2004) 'Cyan-emitting and orange-emitting fluorescent proteins as a donor/acceptor pair for fluorescence resonance energy transfer', *Biochemical Journal*, 381(1), pp. 307–312. doi: 10.1042/BJ20040321.

Kastantin, M. and Schwartz, D. K. (2013) 'Identifying Multiple Populations from Single-Molecule Lifetime Distributions', *ChemPhysChem*, 14(2), pp. 374–380. doi: 10.1002/cphc.201200838.

Kawanishi, S. and Hiraku, Y. (2001) 'Sequence-specific DNA damage induced by UVA radiation in the presence of endogenous and exogenous photosensitizers.', *Current problems in dermatology*, 29, pp. 74–82. doi: 10.1159/000060655.

Kerber, F. *et al.* (2007) 'Control concepts for an active vibration isolation system', *Mechanical Systems and Signal Processing*, 21(8), pp. 3042–3059. doi: 10.1016/j.ymssp.2007.04.003.

Kerssemakers, J. W. J. *et al.* (2006) 'Assembly dynamics of microtubules at molecular resolution', *Nature*, 442(7103), pp. 709–712. doi: 10.1038/nature04928.

Kisker, C., Kuper, J. and Van Houten, B. (2013) 'Prokaryotic nucleotide excision repair', *Cold Spring Harbor Perspectives in Biology*, 5(3), pp. 1–18. doi: 10.1101/cshperspect.a012591.

Köhler, K. *et al.* (2016) *Regulation of the Initiation of DNA Replication upon DNA Damage in Eukaryotes*. 1st edn, *The Initiation of DNA Replication in Eukaryotes*. 1st edn. Edited by D. Kaplan. Springer International Publishing. doi: 10.1007/978-3-319-24696-3_22.

Koyama-Honda, I. *et al.* (2005) 'Fluorescence Imaging for Monitoring the Colocalization of Two Single Molecules in Living Cells', *Biophysical Journal*, 88(3), pp. 2126–2136. doi: 10.1529/biophysj.104.048967.

Kraithong, T. *et al.* (2017) 'Movement of the β-hairpin in the third zinc-binding module of UvrA is required for DNA damage recognition', *DNA Repair*, 51, pp. 60–69. doi: 10.1016/j.dnarep.2017.02.003.

Kraithong, T. *et al.* (2021) 'Real-time investigation of the roles of ATP hydrolysis by UvrA and UvrB during DNA damage recognition in nucleotide excision repair', *DNA Repair*, 97, p. 103024. doi: 10.1016/j.dnarep.2020.103024.

Krepel, D. and Levy, Y. (2017) 'Intersegmental transfer of proteins between DNA regions in the presence of crowding', *Physical Chemistry Chemical Physics*, 19(45), pp. 30562–30569. doi: 10.1039/C7CP05251K.

Kubitscheck, U. *et al.* (2000) 'Imaging and Tracking of Single GFP Molecules in Solution', *Biophysical Journal*, 78(4), pp. 2170–2179. doi: 10.1016/S0006-3495(00)76764-6.

Kukura, P. *et al.* (2009) 'Imaging a Single Quantum Dot When It Is Dark', *Nano Letters*,

9(3), pp. 926–929. doi: 10.1021/nl801735y.

Kumar, P. and Libchaber, A. (2013) 'Pressure and Temperature Dependence of Growth and Morphology of Escherichia coli: Experiments and Stochastic Model', *Biophysical Journal*, 105(3), pp. 783–793. doi: 10.1016/j.bpj.2013.06.029.

Lei, M. and Yao, B. (2004) 'Characteristics of beam profile of Gaussian beam passing through an axicon', *Optics Communications*, 239(4–6), pp. 367–372. doi: 10.1016/j.optcom.2004.05.048.

Lei, M. and Yao, B. (2008) 'Multifunctional darkfield microscopy using an axicon', *Journal of Biomedical Optics*, 13(4), p. 044024. doi: 10.1117/1.2960019.

Liebel, M., Hugall, J. T. and Van Hulst, N. F. (2017) 'Ultrasensitive Label-Free Nanosensing and High-Speed Tracking of Single Proteins', *Nano Letters*, 17(2), pp. 1277–1281. doi: 10.1021/acs.nanolett.6b05040.

Lindfors, K. *et al.* (2004) 'Detection and spectroscopy of gold nanoparticles using supercontinuum white light confocal microscopy', *Physical Review Letters*, 93(3), pp. 037401–1. doi: 10.1103/PhysRevLett.93.037401.

Lippincott-Schwartz, J. and Patterson, G. H. (2003) 'Development and use of fluorescent protein markers in living cells', *Science*, 300(5616), pp. 87–91. doi: 10.1126/science.1082520.

Lippincott-Schwartz, J. and Patterson, G. H. (2008) 'Fluorescent Proteins for Photoactivation Experiments', in, pp. 45–61. doi: 10.1016/S0091-679X(08)85003-0.

Lister, J. J. (1830) 'On some properties in achromatic object-glasses applicable to the improv ment of the micro', pp. 187–200.

Loeff, L. *et al.* (2021) 'AutoStepfinder: A fast and automated step detection method for

single-molecule analysis', *Patterns*, 2(5), p. 100256. doi: 10.1016/j.patter.2021.100256.

Lohman, T. M. *et al.* (1996) 'A Highly Salt-Dependent Enthalpy Change for Escherichia coli SSB Protein−Nucleic Acid Binding Due to Ion−Protein Interactions', *Biochemistry*, 35(16), pp. 5272–5279. doi: 10.1021/bi9527606.

Lowe, A. R. *et al.* (2010) 'Selectivity mechanism of the nuclear pore complex characterized by single cargo tracking', *Nature*, 467(7315), pp. 600–603. doi: 10.1038/nature09285.

Luscombe, N. M. (2001) 'Amino acid-base interactions: a three-dimensional analysis of protein-DNA interactions at an atomic level', *Nucleic Acids Research*, 29(13), pp. 2860–2874. doi: 10.1093/nar/29.13.2860.

Machius, M. *et al.* (1999) 'Crystal structure of the DNA nucleotide excision repair enzyme UvrB from Thermus thermophilus', *Proceedings of the National Academy of Sciences*, 96(21), pp. 11717–11722. doi: 10.1073/pnas.96.21.11717.

Madabhushi, R., Pan, L. and Tsai, L. (2014) 'Review DNA Damage and Its Links to Neurodegeneration', *Neuron*, 83(2), pp. 266–282. doi: 10.1016/j.neuron.2014.06.034.

Mahamdeh, M. *et al.* (2018) 'Label-free high-speed wide-field imaging of single microtubules using interference reflection microscopy', *Journal of Microscopy*, 272(1), pp. 60–66. doi: 10.1111/jmi.12744.

Mahamdeh, M. and Howard, J. (2019) 'Implementation of Interference Reflection Microscopy for Label-free, High-speed Imaging of Microtubules', *Journal of Visualized Experiments*, (150). doi: 10.3791/59520.

Malta, E. *et al.* (2008) 'Functions of base flipping in E. coli nucleotide excision repair', *DNA Repair*, 7(10), pp. 1647–1658. doi: 10.1016/j.dnarep.2008.06.011.

Malta, E., Moolenaar, G. F. and Goosen, N. (2006) 'Base Flipping in Nucleotide Excision Repair', *Journal of Biological Chemistry*, 281(4), pp. 2184–2194. doi: 10.1074/jbc.M508901200.

Malta, E., Moolenaar, G. F. and Goosen, N. (2007) 'Dynamics of the UvrABC Nucleotide Excision Repair Proteins Analyzed by Fluorescence Resonance Energy Transfer', *Biochemistry*, 46(31), pp. 9080–9088. doi: 10.1021/bi7002235.

Mamontova, A. V. *et al.* (2017) 'Struggle for photostability: Bleaching mechanisms of fluorescent proteins', *Russian Journal of Bioorganic Chemistry*, 43(6), pp. 625–633. doi: 10.1134/S1068162017060085.

Manning, G. S. (1978) 'The molecular theory of polyelectrolyte solutions with applications to the electrostatic properties of polynucleotides', *Quarterly Reviews of Biophysics*, 11(2), pp. 179–246. doi: 10.1017/S0033583500002031.

Manning, G. S. (1986) 'Polymer persistence length characterized as a critical length for instability caused by a fluctuating twist', *Physical Review A*, 34(1), pp. 668–670. doi: 10.1103/PhysRevA.34.668.

Manzo, C. *et al.* (2014) 'PSF decomposition of nanoscopy images via Bayesian analysis unravels distinct molecular organization of the cell membrane', *Scientific Reports*, 4, pp. 1–8. doi: 10.1038/srep04354.

Masters, B. R. (2020) *Superresolution Optical Microscopy: The Quest for Enhanced Resolution and Contrast.* Springer US.

McGorty, R., Kamiyama, D. and Huang, B. (2013) 'Active microscope stabilization in three dimensions using image correlation', *Optical Nanoscopy*, 2(1), p. 3. doi: 10.1186/2192-2853-2-3.

McLeod, J. H. (1954) 'The Axicon: A New Type of Optical Element', *Journal of the Optical Society of America*, 44(8), p. 592. doi: 10.1364/JOSA.44.000592.

Mickolajczyk, K. J. *et al.* (2019) 'Direct observation of individual tubulin dimers binding to growing microtubules', *Proceedings of the National Academy of Sciences of the United States of America*, 116(15), pp. 7314–7322. doi: 10.1073/pnas.1815823116.

Mie, G. (1908) 'Articles on the optical characteristics of turbid tubes, especially colloidal metal solutions', *Annalen der Physik*, 25(3), pp. 377–445.

Miranda, O. R. *et al.* (2010) 'Enzyme-Amplified Array Sensing of Proteins in Solution and in Biofluids', *Journal of the American Chemical Society*, 132(14), pp. 5285–5289. doi: 10.1021/ja1006756.

Mirny, L. *et al.* (2009) 'How a protein searches for its site on DNA: the mechanism of facilitated diffusion', *Journal of Physics A: Mathematical and Theoretical*, 42(43), p. 434013. doi: 10.1088/1751-8113/42/43/434013.

Misra, V. K. *et al.* (1998) 'Electrostatic Contributions to the Binding Free Energy of the λcI Repressor to DNA', *Biophysical Journal*, 75(5), pp. 2262–2273. doi: 10.1016/S0006-3495(98)77671-4.

Mitchell, D. L. and Rosenstein, B. S. (1987) 'the Use of Specific Radioimmunoassays To Determine Action Spectra for the Photolysis of (6-4) Photoproducts', *Photochemistry and Photobiology*, 45(6), pp. 781–786. doi: 10.1111/j.1751-1097.1987.tb07882.x.

Mosby, L. S. *et al.* (2020) 'Myosin II Filament Dynamics in Actin Networks Revealed with Interferometric Scattering Microscopy', *Biophysical Journal*. doi: 10.1016/j.bpj.2020.02.025.

Mouret, S. *et al.* (2006) 'Cyclobutane pyrimidine dimers are predominant DNA lesions in

whole human skin exposed to UVA radiation', 103(37), pp. 13765–13770.

Nakagawa, N. *et al.* (1999) 'Crystal Structure of Thermus thermophilus HB8 UvrB Protein, a Key Enzyme of Nucleotide Excision Repair', *Journal of Biochemistry*, 126(6), pp. 986–990. doi: 10.1093/oxfordjournals.jbchem.a022566.

Nelson, P. C. (2008) *Biological Physics*.

Niekamp, S., Stuurman, N. and Vale, R. D. (2020) 'A 6-nm ultra-photostable DNA FluoroCube for fluorescence imaging', *Nature Methods*, 17(4), pp. 437–441. doi: 10.1038/s41592-020-0782-3.

Ninio, J. (1975) 'Kinetic amplification of enzyme discrimination', *Biochimie*, 57(5), pp. 587–595. doi: 10.1016/S0300-9084(75)80139-8.

Normarski, G. (1950) 'Dispositif Oculaire a Contraste De phase pour microscope', *J. De Physique Et le Radiu*, 11(12), pp. 9–10.

O'Brien, R. *et al.* (1998) 'The effects of salt on the TATA binding protein-DNA interaction from a hyperthermophilic archaeon 1 1Edited by I. Tinoco', *Journal of Molecular Biology*, 279(1), pp. 117–125. doi: 10.1006/jmbi.1998.1743.

Olerinyova, A. *et al.* (2020) 'Mass Photometry of Membrane Proteins (Pre-Print)', *bioRxiv*. doi: 10.1101/2020.02.28.969287.

von Olshausen, P. and Rohrbach, A. (2013) 'Coherent total internal reflection dark-field microscopy: label-free imaging beyond the diffraction limit', *Optics Letters*, 38(20), p. 4066. doi: 10.1364/OL.38.004066.

Orren, D. K. and Sancar, A. (1989) 'The (A)BC excinuclease of Escherichia coli has only the UvrB and UvrC subunits in the incision complex.', *Proceedings of the National Academy of Sciences*, 86(14), pp. 5237–5241. doi: 10.1073/pnas.86.14.5237.

Ortega-Arroyo, J. and Kukura, P. (2012) 'Interferometric scattering microscopy (iSCAT): new frontiers in ultrafast and ultrasensitive optical microscopy', *Physical Chemistry Chemical Physics*, 14(45), p. 15625. doi: 10.1039/c2cp41013c.

Ortega Arroyo, J. *et al.* (2014) 'Label-free, all-optical detection, imaging, and tracking of a single protein', *Nano Letters*, 14(4), pp. 2065–2070. doi: 10.1021/nl500234t.

Ortega Arroyo, J., Cole, D. and Kukura, P. (2016) 'Interferometric scattering microscopy and its combination with single-molecule fluorescence imaging', *Nature Protocols*, 11(4), pp. 617–633. doi: 10.1038/nprot.2016.022.

Pakotiprapha, D. *et al.* (2008) 'Crystal Structure of Bacillus stearothermophilus UvrA Provides Insight into ATP-Modulated Dimerization, UvrB Interaction, and DNA Binding', *Molecular Cell*, 29(1), pp. 122–133. doi: 10.1016/j.molcel.2007.10.026.

Pakotiprapha, D. *et al.* (2009) 'A Structural Model for the Damage-sensing Complex in Bacterial Nucleotide Excision Repair', *Journal of Biological Chemistry*, 284(19), pp. 12837–12844. doi: 10.1074/jbc.M900571200.

Pakotiprapha, D. *et al.* (2012) 'Structure and mechanism of the UvrA–UvrB DNA damage sensor', *Nature Structural & Molecular Biology*, 19(3), pp. 291–298. doi: 10.1038/nsmb.2240.

Park, J. S. *et al.* (2018) 'Label-free and live cell imaging by interferometric scattering microscopy', *Chemical Science*, 9(10), pp. 2690–2697. doi: 10.1039/c7sc04733a.

Piliarik, M. and Sandoghdar, V. (2014a) 'Direct optical sensing of single unlabeled small proteins and super-resolution microscopy of their binding sites', *Nature communications*, 5, p. 4495.

Piliarik, M. and Sandoghdar, V. (2014b) 'Direct optical sensing of single unlabelled

proteins and super-resolution imaging of their binding sites', *Nature Communications*, 5, pp. 1–8. doi: 10.1038/ncomms5495.

Podestà, A. *et al.* (2005) 'Positively Charged Surfaces Increase the Flexibility of DNA', *Biophysical Journal*, 89(4), pp. 2558–2563. doi: 10.1529/biophysj.105.064667.

Porschke, D. (1986) 'Structure and Dynamics of Double Helices in Solution: Modes of DNA Bending', *Journal of Biomolecular Structure and Dynamics*, 4(3), pp. 373–389. doi: 10.1080/07391102.1986.10506356.

Quekett, J. (1848) *A Practical Treatise on the Use of the Microscope*.

Rao, K. S. (2007) 'Mechanisms of Disease : DNA repair defects', 3(3). doi: 10.1038/ncpneuro0448.

Record, M. T., Anderson, C. F. and Lohman, T. M. (1978) 'Thermodynamic analysis of ion effects on the binding and conformational equilibria of proteins and nucleic acids: the roles of ion association or release, screening, and ion effects on water activity', *Quarterly Reviews of Biophysics*, 11(2), pp. 103–178. doi: 10.1017/S003358350000202X.

Renz, M. (2013) 'Fluorescence microscopy-A historical and technical perspective', *Cytometry Part A*, 83(9), pp. 767–779. doi: 10.1002/cyto.a.22295.

Richter, P. H. and Eigen, M. (1974) 'Diffusion controlled reaction rates in spheroidal geometry', *Biophysical Chemistry*, 2(3), pp. 255–263. doi: 10.1016/0301-4622(74)80050-5.

Riggs, A. D., Bourgeois, S. and Cohn, M. (1970) 'The lac represser-operator interaction', *Journal of Molecular Biology*, 53(3), pp. 401–417. doi: 10.1016/0022-2836(70)90074-4.

Rivin, E. I. (1995) 'Vibration isolation of precision equipment', *Precision Engineering*, 17(1), pp. 41–56. doi: 10.1016/0141-6359(94)00006-L.

Rotman, B. (1961) 'Measurement of activity of single molecules of beta-D-galactosidase.', *Proceedings of the National Academy of Sciences of the United States of*, 47, pp. 1981–1991. doi: 10.1073/pnas.47.12.1981.

Rust, M. J., Bates, M. and Zhuang, X. (2006) 'Sub-diffraction-limit imaging by stochastic optical reconstruction microscopy (STORM)', *Nature Methods*, 3(10), pp. 793–796. doi: 10.1038/nmeth929.

Sancar, A. *et al.* (1981) 'Identification of the uvrC gene product.', *Proceedings of the National Academy of Sciences*, 78(9), pp. 5450–5454. doi: 10.1073/pnas.78.9.5450.

Sancar, A., Franklin, K. A. and Sancar, G. B. (1984) 'Escherichia coli DNA photolyase stimulates uvrABC excision nuclease in vitro.', *Proceedings of the National Academy of Sciences*, 81(23), pp. 7397–7401. doi: 10.1073/pnas.81.23.7397.

Sancar, A. and Rupp, W. D. (1983) 'A novel repair enzyme: UVRABC excision nuclease of Escherichia coli cuts a DNA strand on both sides of the damaged region', *Cell*, 33(1), pp. 249–260. doi: 10.1016/0092-8674(83)90354-9.

Sancar, A. and Sancar, G. B. (1988) 'DNA Repair Enzymes', *Annual Review of Biochemistry*, 57(1), pp. 29–67. doi: 10.1146/annurev.bi.57.070188.000333.

Savir, Y. and Tlusty, T. (2007) 'Conformational Proofreading: The Impact of Conformational Changes on the Specificity of Molecular Recognition', *PLoS ONE*. Edited by E. Scalas, 2(5), p. e468. doi: 10.1371/journal.pone.0000468.

Schmidt, A. *et al.* (2016) 'The quantitative and condition-dependent Escherichia coli proteome', *Nature Biotechnology*, 34(1), pp. 104–110. doi: 10.1038/nbt.3418.

Schmidt, P. D. *et al.* (2018) 'Method for high frequency tracking and sub-nm sample stabilization in single molecule fluorescence microscopy', *Scientific Reports*, 8(1), p.

13912. doi: 10.1038/s41598-018-32012-1.

Schmidt, T. *et al.* (1996) 'Imaging of single molecule diffusion.', *Proceedings of the National Academy of Sciences of the United States of America*, 93(7), pp. 2926–9. doi: 10.1073/pnas.93.7.2926.

Schmoranzer, J. *et al.* (2000) 'Imaging constitutive exocytosis with total internal reflection fluorescence microscopy', *Journal of Cell Biology*, 149(1), pp. 23–31. doi: 10.1083/jcb.149.1.23.

Schurr, J. M. (1979) 'The one-dimensional diffusion coefficient of proteins absorbed on DNA. Hydrodynamic considerations.', *Biophysical chemistry*, 9(4), pp. 413–4. doi: 380674.

Seeberg, E. and Steinum, A. L. (1982) 'Purification and properties of the uvrA protein from Escherichia coli.', *Proceedings of the National Academy of Sciences*, 79(4), pp. 988–992. doi: 10.1073/pnas.79.4.988.

Setlow, R. B. and Carrier, W. L. (1964) 'THE DISAPPEARANCE OF THYMINE DIMERS FROM DNA: AN ERROR-CORRECTING MECHANISM', *Proceedings of the National Academy of Sciences*, 51(2), pp. 226–231. doi: 10.1073/pnas.51.2.226.

Shaner, N. C. *et al.* (2004) 'Improved monomeric red, orange and yellow fluorescent proteins derived from Discosoma sp. red fluorescent protein', *Nature Biotechnology*, 22(12), pp. 1567–1572. doi: 10.1038/nbt1037.

Shi, Q. *et al.* (1992) 'Electron microscopic study of (A)BC excinuclease', *Journal of Molecular Biology*, 226(2), pp. 425–432. doi: 10.1016/0022-2836(92)90957-L.

Shimamoto, N. (1999) 'One-dimensional Diffusion of Proteins along DNA', *Journal of Biological Chemistry*, 274(22), pp. 15293–15296. doi: 10.1074/jbc.274.22.15293.

Shimomura, O., Johnson, F. H. and Saiga, Y. (1962) 'Extraction, Purification and

Properties of Aequorin, a Bioluminescent Protein from the Luminous

Hydromedusan,Aequorea', *Journal of Cellular and Comparative Physiology*, 59(3), pp.

223–239. doi: 10.1002/jcp.1030590302.

Simmert, S. *et al.* (2018) 'LED-based interference-reflection microscopy combined with

optical tweezers for quantitative three-dimensional microtubule imaging', *Optics Express*,

26(11), p. 14499. doi: 10.1364/OE.26.014499.

Singh, P. *et al.* (2017) 'Ultrafast spectroscopy on DNA-cleavage by endonuclease in

molecular crowding', *International Journal of Biological Macromolecules*, 103, pp. 395–

402. doi: 10.1016/j.ijbiomac.2017.05.058.

Sinha, R. P. and Häder, D. P. (2002) 'UV-induced DNA damage and repair: A review',

*Photochemical and Photobiological Sciences*, 1(4), pp. 225–236. doi: 10.1039/b201230h.

Skorvaga, M. *et al.* (2002) 'The β-Hairpin Motif of UvrB Is Essential for DNA Binding,

Damage Processing, and UvrC-mediated Incisions', *Journal of Biological Chemistry*,

277(2), pp. 1553–1559. doi: 10.1074/jbc.M108847200.

Slutsky, M. and Mirny, L. A. (2004) 'Kinetics of Protein-DNA Interaction : Facilitated Target

Location in Sequence-Dependent Potential', *Biophysical Journal*, 87(6), pp. 4021–4035.

doi: 10.1529/biophysj.104.050765.

Soltermann, F. *et al.* (2020) 'Quantifying protein-protein interactions by molecular counting

with mass photometry', *Angewandte Chemie*, p. ange.202001578. doi:

10.1002/ange.202001578.

Sonn-Segev, A. *et al.* (2020) 'Quantifying the heterogeneity of macromolecular machines

by mass photometry (Pre-Print)'. doi: 10.1101/864553.

Springall, L. *et al.* (2018) 'Recruitment of UvrBC complexes to UV-induced damage in the

absence of UvrA increases cell survival', 46(3), pp. 1256–1265. doi: 10.1093/nar/gkx1244.

Stracy, M. *et al.* (2016) 'Single-molecule imaging of UvrA and UvrB recruitment to DNA lesions in living Escherichia coli', *Nature Communications*, 7(1), p. 12568. doi: 10.1038/ncomms12568.

Svechkarev, D. and Mohs, A. M. (2019) 'Organic Fluorescent Dye-based Nanomaterials: Advances in the Rational Design for Imaging and Sensing Applications', *Current Medicinal Chemistry*, 26(21), pp. 4042–4064. doi: 10.2174/0929867325666180226111716.

Tafvizi, A. *et al.* (2011) 'A single-molecule characterization of p53 search on DNA', *Proceedings of the National Academy of Sciences*, 108(2), pp. 563–568. doi: 10.1073/pnas.1016020107.

Talà, L. *et al.* (2019) 'Pseudomonas aeruginosa orchestrates twitching motility by sequential control of type IV pili movements', *Nature Microbiology*, 4(5), pp. 774–780. doi: 10.1038/s41564-019-0378-9.

Tanner, N. A. *et al.* (2009) 'Real-time single-molecule observation of rolling-circle DNA replication', *Nucleic Acids Research*, 37(4), pp. e27–e27. doi: 10.1093/nar/gkp006.

Taylor, R. W. *et al.* (2019a) 'Interferometric scattering microscopy reveals microsecond nanoscopic protein motion on a live cell membrane', *Nature Photonics*, 13(7), pp. 480–487. doi: 10.1038/s41566-019-0414-6.

Taylor, R. W. *et al.* (2019b) 'Interferometric scattering microscopy reveals microsecond nanoscopic protein motion on a live cell membrane', *Nature Photonics*, 13(7), pp. 480–487. doi: 10.1038/s41566-019-0414-6.

Taylor, R. W. *et al.* (2020) 'High-Precision Protein-Tracking With Interferometric Scattering Microscopy', *Frontiers in Cell and Developmental Biology*, 8. doi:

10.3389/fcell.2020.590158.

Theis, K. (1999) 'Crystal structure of UvrB, a DNA helicase adapted for nucleotide excision repair', *The EMBO Journal*, 18(24), pp. 6899–6907. doi: 10.1093/emboj/18.24.6899.

Theis, K. *et al.* (2000) 'The nucleotide excision repair protein UvrB, a helicase-like enzyme with a catch', *Mutation Research/DNA Repair*, 460(3–4), pp. 277–300. doi: 10.1016/S0921-8777(00)00032-X.

Thériault, G., De Koninck, Y. and McCarthy, N. (2013) 'Extended depth of field microscopy for rapid volumetric two-photon imaging', *Optics Express*, 21(8), p. 10095. doi: 10.1364/OE.21.010095.

Thomas, D. C., Levy, M. and Sancar, A. (1985) 'Amplification and purification of UvrA, UvrB, and UvrC proteins of Escherichia coli', *Journal of Biological Chemistry*, 260(17), pp. 9875–9883.

Thompson, R. E., Larson, D. R. and Webb, W. W. (2002) 'Precise nanometer localization analysis for individual fluorescent probes', *Biophysical Journal*, 82(5), pp. 2775–2783. doi: 10.1016/S0006-3495(02)75618-X.

Thyagarajan, K. and Ghatak, A. . (1981) *Lasers: Theory and Applications*. Plenum Press.

Timmins, J. *et al.* (2009) 'Structural and Mutational Analyses of Deinococcus radiodurans UvrA2 Provide Insight into DNA Binding and Damage Recognition by UvrAs', *Structure*, 17(4), pp. 547–558. doi: 10.1016/j.str.2009.02.008.

Truglio, J. J. *et al.* (2004) 'Interactions between UvrA and UvrB: the role of UvrB's domain 2 in nucleotide excision repair', *The EMBO Journal*, 23(13), pp. 2498–2509. doi: 10.1038/sj.emboj.7600263.

Ueno, H. *et al.* (2010) 'Simple Dark-Field Microscopy with Nanometer Spatial Precision and Microsecond Temporal Resolution', *Biophysical Journal*, 98(9), pp. 2014–2023. doi: 10.1016/j.bpj.2010.01.011.

Ulbrich, M. H. and Isacoff, E. Y. (2007) 'Subunit counting in membrane-bound proteins', *Nature Methods*, 4(4), pp. 319–321. doi: 10.1038/nmeth1024.

Verhoeven, E. E. A. (2002) 'The presence of two UvrB subunits in the UvrAB complex ensures damage detection in both DNA strands', *The EMBO Journal*, 21(15), pp. 4196–4205. doi: 10.1093/emboj/cdf396.

Waggoner, A. (1995) 'Covalent labeling of proteins and nucleic acids with fluorophores', in, pp. 362–373. doi: 10.1016/0076-6879(95)46017-9.

Wagner, K., Moolenaar, G. F. and Goosen, N. (2011) 'Role of the insertion domain and the zinc-finger motif of Escherichia coli UvrA in damage recognition and ATP hydrolysis', *DNA Repair*, 10(5), pp. 483–496. doi: 10.1016/j.dnarep.2011.02.002.

Wan, X. Y. *et al.* (2014) 'Real-time light scattering tracking of gold nanoparticles-bioconjugated respiratory syncytial virus infecting HEp-2 cells', *Scientific Reports*, 4, pp. 1–7. doi: 10.1038/srep04529.

Wang, H. *et al.* (2006) 'UvrB Domain 4, an Autoinhibitory Gate for Regulation of DNA Binding and ATPase Activity', *Journal of Biological Chemistry*, 281(22), pp. 15227–15237. doi: 10.1074/jbc.M601476200.

Wang, H. *et al.* (2009) 'DNA wrapping is required for DNA damage recognition in the Escherichia coli DNA nucleotide excision repair pathway', *Proceedings of the National Academy of Sciences*, 106(31), pp. 12849–12854. doi: 10.1073/pnas.0902281106.

Wang, X. *et al.* (2009) 'Non-blinking semiconductor nanocrystals', *Nature*, 459(7247), pp.

686–689. doi: 10.1038/nature08072.

Waters, T. R. *et al.* (2006) 'Damage detection by the UvrABC pathway: Crystal structure of UvrB bound to fluorescein-adducted DNA', *FEBS Letters*, 580(27), pp. 6423–6427. doi: 10.1016/j.febslet.2006.10.051.

Weigel, A., Sebesta, A. and Kukura, P. (2014) 'Dark Field Microspectroscopy with Single Molecule Fluorescence Sensitivity', *ACS Photonics*, 1(9), pp. 848–856. doi: 10.1021/ph500138u.

de Wit, G. *et al.* (2018) 'Revealing Compartmentalized Diffusion in Living Cells with Interferometric Scattering Microscopy', *Biophysical Journal*, 114(12), pp. 2945–2950. doi: 10.1016/j.bpj.2018.05.007.

Wolf, E. (2007) *Introduction to the Theory of Coherence and Polarization of Light*. New York: Cambridge U. Press.

Wolters, S. *et al.* (2013) 'Genome maintenance and transcription integrity in aging and disease', 4(February), pp. 1–10. doi: 10.3389/fgene.2013.00019.

Xie, X. S. and Trautman, J. K. (1998) 'Optical Studies of Single Molecules At Room Temperature', *Annual Review of Physical Chemistry*, 49(1), pp. 441–480. doi: 10.1146/annurev.physchem.49.1.441.

Yasuda, R. *et al.* (2001) 'Resolution of distinct rotational substeps by submillisecond kinetic analysis of F1-ATPase', *Nature*, 410(6831), pp. 898–904. doi: 10.1038/35073513.

Yeh, Y.-C., Creran, B. and Rotello, V. M. (2012) 'Gold nanoparticles: preparation, properties, and applications in bionanotechnology', *Nanoscale*, 4(6), pp. 1871–1880. doi: 10.1039/C1NR11188D.

Yeung, A. T. *et al.* (1983) 'Enzymatic properties of purified Escherichia coli uvrABC

proteins.', *Proceedings of the National Academy of Sciences*, 80(20), pp. 6157–6161. doi: 10.1073/pnas.80.20.6157.

Yildiz, A. *et al.* (2003) 'Myosin V walks hand-over-hand: Single fluorophore imaging with 1.5-nm localization', *Science*, 300(5628), pp. 2061–2065. doi: 10.1126/science.1084398.

Yin, H., Landick, R. and Gelles, J. (1994) 'Tethered particle motion method for studying transcript elongation by a single RNA polymerase molecule', *Biophysical Journal*, 67(6), pp. 2468–2478. doi: 10.1016/S0006-3495(94)80735-0.

Yiwen, L., Struwe, W. B. and Kukura, P. (2020) 'Single molecule mass photometry of nucleic acids (Pre-Print)', *bioRxiv*. doi: 10.1101/2020.01.14.904755.

Yoon, J. H. *et al.* (2000) 'The DNA damage spectrum produced by simulated sunlight', *Journal of Molecular Biology*, 299(3), pp. 681–693. doi: 10.1006/jmbi.2000.3771.

Yoon, Y. Z. and Cicuta, P. (2010) 'Optical trapping of colloidal particles and cells by focused evanescent fields using conical lenses', *Optics Express*, 18(7), p. 7076. doi: 10.1364/OE.18.007076.

Young, G. *et al.* (2018) 'Quantitative mass imaging of single biological macromolecules', *Science*, 360(6387), pp. 423–427. doi: 10.1126/science.aar5839.

Young, G. and Kukura, P. (2019) 'Interferometric Scattering Microscopy', *Annual Review of Physical Chemistry*, 70(1), pp. 301–322. doi: 10.1146/annurev-physchem-050317-021247.

Yu, B., Pettitt, B. M. and Iwahara, J. (2020) 'Dynamics of Ionic Interactions at Protein–Nucleic Acid Interfaces', *Accounts of Chemical Research*, 53(9), pp. 1802–1810. doi: 10.1021/acs.accounts.0c00212.

Zernike, F. (1942a) 'Phase contrast, a new method for the microscopic observation of

transparent objects', *Physica*, 9(7), pp. 686–698. doi: 10.1016/S0031-8914(42)80035-X.

Zernike, F. (1942b) 'Phase contrast, a new method for the microscopic observation of transparent objects part II', *Physica*, 9(10), pp. 974–986. doi: 10.1016/S0031-8914(42)80079-8.

Zernike, F. and Stratton, F. J. M. (1934) 'Diffraction Theory of the Knife-Edge Test and its Improved Form, The Phase-Contrast Method', *Monthly Notices of the Royal Astronomical Society*, 94(5), pp. 377–384. doi: 10.1093/mnras/94.5.377.

Zsigmondy, R. (1926) 'Richard Zsigmondy - Nobel Lecutre: Properties of Colloids', in *Nobel Lecture*. Nobel Media AB 2014. Available at: https://www.nobelpirze.org/uploads/2018/06/zsigmondy-lecture.pdf.

# Acknowledgements

First and foremost, I would like to thank my supervisor, Dr Neil Kad, for his constant support and encouragement throughout my PhD. The environment in and around the lab that he has developed has made even the most challenging parts of this PhD enjoyable. Thanks to his guidance and motivation, these past few years have been some of the most rewarding I have ever experienced.

I want to thank all members of the Kad Lab, past and present, who together made the lab such an enjoyable place to work, study, and discuss. Thank you to Dr Jamie Barnett, for always being happy to discuss any part of my work, and for working with me on developing the surface-based DNA assay. Also, for the many jam sessions and Tuesday evening pub trips. Thank you to Dr Luke Springall, and Dr Alessio Inchingolo, and whilst I didn't get to spend much time in the lab with them, I'll always be grateful for making me feel so welcome. Thank you to Dr Alex Moores, Dr James Leech, Laurens Heling, Quentin Smith, and Dr Arya Gupta for all their help and friendship across many years. And last but not least, thank you to Antoine Paris, Matvey Pilagov, Lorenzo Bernachia, and Roman Urban for making lab life during many lockdowns so much fun – and for somehow making 15-hour road trips seem like a good idea. Additionally, thank you to everyone who I've met inside and outside the lab along the way and shared in all these experiences, including Joe, Diego, Alex, Elliot.

I want to express my absolute gratitude to my friends and family who have supported me throughout these last 4 years. In particular, thank you to my parents, as without their continuing support, care, and kindness, I would not be able to chase my passions and interests as I do now. Finally, thank you to my long-suffering partner Lauren, who has had been by my side every step of the way – and has unconditionally supported and encouraged me through the highest highs and lowest lows throughout.